

Magnetic measurements on single-phase and composite multiferroics

Von der Fakultät für Physik der Universität Duisburg-Essen
zur Erlangung des akademischen Grades eines Doktors der
Naturwissenschaften (Dr. rer. nat.) genehmigte Dissertation

vorgelegt von

Soma Salamon

aus

Budapest

1. Gutachter: Prof. Dr. Heiko Wende
 2. Gutachter: Prof. Dr. Martina Müller
- Datum der Einreichung: 13.08.18
Datum der Disputation: 29.10.18

Abstract

This thesis focuses on the detailed characterization of multiferroic phenomena in single-phase and composite materials, which have become a key aspect of research interest due to their numerous possible uses for application purposes. The main topic deals with the interplay of electric and magnetic material properties, linked either intrinsically in single-phase materials or via a mediator such as strain coupling in purposefully engineered biphasic composites. The influence of different material compositions, synthesis techniques and resulting morphologies was analyzed in order to obtain a detailed overview of the physical phenomena that govern the strength of magnetoelectric (ME) coupling. The main methods used for this purpose include Mössbauer spectroscopy, a non-destructive nuclear physical method utilizing resonant absorption of γ -radiation, as well as a magnetoelectric measurement setup. Latter is based on a modified SQUID AC susceptometer, making it possible to record the magnetic response of ceramic samples exposed to electric fields with high precision.

One section of this thesis is devoted to the single-phase material bismuth ferrite (BiFeO_3), which is antiferromagnetic and ferroelectric. This multiferroic property was never utilized for applications, as its antiferromagnetic nature leads to zero net magnetic moment. It was discovered that BiFeO_3 contains a long range modulation of magnetic moments (spin cycloid), which is incommensurable with the crystal lattice. Furthermore, weak ferromagnetism was observed in nanoparticles, which was the main motivation for our measurements. Using Mössbauer spectroscopy, we examined the behavior of this spin cycloid in great detail while recording spectra in a large temperature range (4 K - 800 K), for different particle sizes (54 nm - 1 μm). This allowed us to assess the temperature dependence of the spin cycloid, which was distorted towards an anharmonic state at lower temperatures, while no significant influence of the particle size was witnessed. This work represents the first instance of the anharmonic cycloid being characterized in detail for nanoparticle samples in a wide temperature range.

The second section deals with a number of composite ceramics that combine magnetostrictive and piezoelectric materials with different constituents and connectivity schemes. These were characterized with our converse ME measurement setup at different temperatures (4 K - 350 K) and applied magnetic fields (± 5 T), in order to ascertain their behavior, and to optimize the measurement parameters. This was followed by the recording of the electric field dependence of sample magnetization, providing direct access to the converse ME coupling coefficient, which provides a measure for the strength of ME coupling in our samples. Through the course of our work, we were able to significantly increase the coupling coefficient by modifications of the sample composition, preparation and constituents. Our studies also provide information about the underlying physical driving forces that affect the strength of the ME coupling, while also uncovering possible pitfalls of the measurement setup. The knowledge of these factors made it possible to effectively optimize our samples, allowing us to increase coupling coefficients nearly fourfold relative to our initial work.

Kurzfassung

Diese Arbeit beschäftigt sich mit der detaillierten Charakterisierung multiferroischer Phänomene in einphasigen Materialien und Verbundmaterialien, die wegen ihrer möglichen Anwendungen in den Fokus der Wissenschaft gerückt sind. Das Hauptaugenmerk liegt auf dem Zusammenspiel elektrischer und magnetischer Eigenschaften, welche entweder intrinsisch oder über Vermittler, wie die mechanische Spannung, miteinander gekoppelt sind. Der Einfluss verschiedener Materialzusammensetzungen, Synthesemethoden und daraus resultierender Morphologien wurde analysiert, um eine Übersicht der physikalischen Phänomene zu erhalten, welche die Stärke der magnetoelektrischen (ME) Kopplung bestimmen. Bei den hauptsächlich verwendeten Methoden handelt es sich um Mössbauerspektroskopie, einer zerstörungsfreien kernphysikalischen Messmethode, die auf der resonanten Absorption von γ -Strahlung beruht, und um einen Aufbau für ME Messungen. Letzterer basiert auf einem modifizierten SQUID AC Suszeptometer, was die Messung der magnetischen Reaktion auf elektrische Felder erlaubt.

Ein Abschnitt der Arbeit ist dem einphasigen Material Bismutferrit (BiFeO_3) gewidmet, welches gleichzeitig antiferromagnetisch und ferroelektrisch ist. Diese multiferroische Eigenschaft wurde nie genutzt, da das antiferromagnetische Material keine Nettomagnetisierung besitzt. Es ist bekannt, dass BiFeO_3 eine langreichweitige, mit dem Kristallgitter inkommensurable Modulation der magnetischen Momente aufweist (Spin-Zykloide). Weiterhin wurde schwach ferromagnetisches Verhalten in BiFeO_3 -Nanopartikeln beobachtet, was die Hauptmotivation für unsere Messungen war. Mittels Mössbauerspektroskopie konnten wir das Verhalten dieser Spinzykloide im Detail beobachten, während Spektren in einem sehr weiten Temperaturbereich (4 K - 800 K) für verschieden große (54 nm - 1 μm) Partikel aufgenommen wurden. Dies erlaubte uns die Observierung der Temperaturabhängigkeit der Spinzykloide, welche bei tiefen Temperaturen zunehmend verzerrt und anharmonisch wurde, während kein nennenswerter Einfluss der Partikelgröße zu sehen war. Im Zuge dieser Arbeit wurde erstmalig die anharmonische Zykloide in Nanopartikeln im Detail temperaturabhängig charakterisiert.

Im zweiten Abschnitt beschäftigen wir uns mit Kompositen, welche aus einer magnetostriktiven und piezoelektrischen Phase mit verschiedenen Bestandteilen und Konnektivitäten bestehen. Diese wurden bei verschiedenen Temperaturen (4 K - 350 K) und angelegten Magnetfeldern (± 5 T) charakterisiert, sodass ihr Verhalten beobachtet und die Messparameter optimiert werden konnten. Es folgte die Aufnahme des magnetischen Signals in Abhängigkeit von angelegten elektrischen Feldern, was die Berechnung des konversen ME Koeffizienten erlaubt, der ein Maß für die Stärke der ME Kopplung darstellt. Somit konnten wir den Kopplungskoeffizienten durch Modifikation der Probenbestandteile, Präparation und Zusammensetzung stark erhöhen. Wir erhielten so Informationen über die zugrundeliegenden physikalischen Phänomene des ME Effekts, während auch potentielle Probleme des Messaufbaus erkannt wurden. Das Wissen über diese Faktoren ermöglichte die Optimierung der Probeneigenschaften, sodass der Kopplungskoeffizient verglichen mit unseren ersten Arbeiten um etwa den Faktor 4 erhöht werden konnte.

Contents

1	Introduction	1
2	Theoretical foundations	5
2.1	Magnetism	5
2.1.1	Ferromagnetism	5
2.1.2	Ferrimagnetism	7
2.1.3	Antiferromagnetism	8
2.1.4	Magnetostriction	8
2.2	Electric material properties	15
2.2.1	Polarization and dielectric permittivity	15
2.2.2	Piezoelectric properties	21
2.2.3	Ferroelectrics and poling	22
2.2.4	Landau-theory of phase transitions	23
2.3	Magnetoelectric coupling coefficient	25
2.3.1	Connectivity schemes for magnetoelectric ceramics	32
3	Physical properties of the constituents	35
3.1	Bismuth ferrite	35
3.2	Cobalt ferrite	37
3.3	Nickel ferrite	39
3.4	Barium titanate	39
3.5	Barium calcium zirconate titanate	40
4	Scientific instrumentation	44
4.1	Cooperative measurement techniques	46
4.1.1	X-ray diffraction	46
4.1.2	Microscopy methods	47
4.1.3	Electrical characterization methods	50
4.1.4	Time of flight secondary ion mass spectroscopy	52
4.1.5	Measurement of the direct ME effect	53
4.2	Mössbauer spectroscopy: Theoretical framework	55
4.2.1	Isomer shift	58
4.2.2	Quadrupole interaction	62
4.2.3	Magnetic interaction	64
4.3	Mössbauer spectroscopy: Experimental details	66
4.3.1	Evaluation of Mössbauer data	69
4.4	SQUID magnetometry: Theoretical basics	71

4.5	Principle of AC susceptometry measurements	82
4.6	Converse ME measurement setup	83
4.7	Description of the converse ME measurement methodology	89
4.7.1	Temperature dependence	90
4.7.2	Magnetic field dependence	90
4.7.3	Electric field dependence	91
4.8	Pitfalls of the converse ME setup	92
4.8.1	Apparent ME signal from conductivity	92
4.8.2	Excessive Joule heating	95
4.8.3	Lack of ME signal due to frequency doubling	95
4.8.4	Effects of measurement frequency	97
5	Sample synthesis methods and precursor characterization	100
5.1	Wet chemical synthesis and characterization of BFO nanoparticles	100
5.2	Synthesis and characterization of CFO-BTO core-shell nanoparticles	102
5.3	Solid state fabrication route for BCZT-based ceramics	107
5.4	Fabrication techniques for ceramics	112
5.4.1	Conventional sintering procedure	112
5.4.2	Spark plasma sintering method	112
5.4.3	Poling procedure	113
6	Results	114
6.1	BFO nanoparticles	114
6.1.1	Precharacterization	114
6.1.2	Mössbauer spectroscopy results	123
6.1.3	Modeling of the cycloidal spin structure	127
6.2	Magnetoelectric ceramics	135
6.2.1	Analysis of measurement data	136
6.2.2	Error estimation	137
6.2.3	CFO-BTO composites with different connectivity schemes	138
6.2.4	Direct and converse effect in CFO-BTO (0-3) composites	150
6.2.5	BCZT-CFO composites	169
6.2.6	Al-modification of BCZT-CFO composites	179
6.2.7	BCZT-NFO composites	191
7	Conclusion	207
7.1	BFO nanoparticles	207
7.2	CFO-BTO ceramic composites	208
7.3	BCZT-based ceramic composites	209
7.4	Converse ME measurement setup	211

7.5 Summary	212
8 Outlook	214
8.1 Magnetoelectric ceramics via industrial route	214
8.2 Magnetoelectric ceramics with Terfenol-D	214
8.3 Thin film ME samples via PLD	215
Bibliography	218
List of Figures	240
List of Tables	244
List of Abbreviations	245
Publications	246
Acknowledgements	251

1 Introduction

The topic of multiferroic materials is not a new one, but after a decade or two of relative inactivity, this field has become incredibly popular over the last ten years, with a large and continuously increasing number of publications being put forward. In fact, some of the comprehensive reviews often talk of a "Revival of the magnetoelectric effect"¹ or of "The renaissance of magnetoelectric multiferroics".² With this, it's already clear where the topic of this thesis will be heading. Multiferroics as such are a rather wide ranging subject that deals with a great number of material systems. This makes it necessary to, at first, define what a multiferroic material is in the context of this work, and to observe the history of how this effect was discovered and characterized.

The generally accepted modern-day definition of a multiferroic is that it exhibits two or more of the primary ferroic properties, which are ferromagnetism, ferroelectricity, ferroelasticity and ferrotoroidicity. Naturally, one of the most sought after combination is that of magnetoelectric multiferroics, which are simultaneously ferromagnetic and ferroelectric. In this work, we will be dealing with materials that are ferroelectric, as well as ferri- and antiferromagnetic, with the above definition having been expanded to include these other types of magnetic ordering, in addition to ferromagnetism.

If we stick to only magnetoelectric (ME) materials, we can define them as materials that show a coupling between electric and magnetic properties, with an applied electric field leading to induced magnetization, while an applied magnetic field leads to induced polarization. The contributions to this effect can be observed in detail by the expansion of the free energy with regard to the electric or magnetic field, which will be dealt with in detail in section 2.3.

When observing how the ME effect was discovered, we come across some rather famous scientists who all partially contributed to the overall level of knowledge. The first theoretical prediction of the effect is attributed to Pierre Curie, who, in 1894, was the first to describe symmetry considerations necessary for the effect to occur in crystals.³ Even earlier, in 1888, Wilhelm Conrad Röntgen discovered that a dielectric material became magnetized when placed in an electric field,⁴ while also becoming polarized when moved into a magnetic field. Despite this being a very interesting experimental observation, the fundamental principles behind these effects were not understood at the time. In the 1920s, several attempts were made to demonstrate the effect experimentally, and it was also at this time that Peter Debye introduced the term 'magnetoelectric' in 1926.⁵ It was only much later that a greater understanding of symmetry was obtained, with several publications noting that time-asymmetry is a necessary prerequisite for the ME effect to occur, either induced through the application of external fields⁶ or by

physically moving a sample into a field, as it was done by Röntgen. Arriving in 1959, we come to perhaps the most well-known two studies on magnetoelectric materials, namely the publication by Igor Dzyaloshinskii, who was able to show, theoretically, a violation of time-reversal symmetry for antiferromagnetic chromium oxide (III) (Cr_2O_3).⁷ The reason for it being popularly known within the community is the fact that less than a year thereafter, an experimental proof was brought forward by D. N. Astrov, who was able to measure the electric-field induced magnetization on a sample of this material.^{8,9} In fact, it is with Cr_2O_3 that our own converse ME measurement setup was first tested,¹⁰ being a well-known model system that has been extensively characterized, including the reverse effect of inducing polarization via magnetic field application.^{11,12}

After a peak in the number of publications per year around 1973, the interest in this topic declined, as the coupling coefficient for intrinsic magnetoelectrics was estimated to only reach a maximum of 0.1 ps/m after the microscopic mechanisms behind the coupling were uncovered.^{13,14} Apart from the overall low effect, single-phase multiferroics had other drawbacks. As the number of compounds that showed ME effects was rather small and required a specific, discrete composition, there was almost no room for improvement via doping or variations in composition. Often, the physical properties of the materials, their stability, or cost were further obstacles that stalled the initial excitement for this topic. Indeed, one of the materials we will be characterizing in detail, bismuth ferrite, is a classic case in point: While it is ferroelectric, the intrinsic magnetic ordering is of an antiferromagnetic type, leaving no effective net magnetic moment, making this material unsuitable for technical applications, at least at first glance. Furthermore, the ordering temperatures of many single-phase magnetoelectrics were often well below room temperature, which is not problematic for experiments, but makes the respective materials unsuitable from an applications point of view. Because of these factors, the number of publications waned, with the late 70s and 80s leaving the topic of magnetoelectrics mostly dormant.

The often cited renaissance, heralding a renewed interest in magnetoelectric materials, was brought about by the possibility of using synergy effects to overcome the difficulties described above. Ironically, this idea was not new, in fact, it had been proposed by Bernhard Tellegen of the Philips Research Laboratories¹⁵ in 1948, more than a decade before the ME effect in a single-phase material was first measured by Astrov. However, it needs to be mentioned that it's only the principle as such that was valid, while the route proposed by Tellegen, comprised of a suspension of macroscopic particles that carry both electric and magnetic dipole moments, was not feasible. In essence, the main idea revolves around the combination of two or more compounds, with the resulting composite showing effects that would not be possible to attain with the single constituents. As described by M. Fiebig,¹ there are three classes of effects that can be distinguished: The sum property, resulting from the weighted sum of the contributions

from all constituent phases, with well-known examples being density and resistivity. The scaling property, representing effects that occur in higher strength in a composite compared to the effect seen in the individual constituents, and finally the product property, denoting effects that are only present in the composite but not in any of the constituents.

It is this last effect that we want to concentrate on. In our case, we will be combining ferroelectric and ferrimagnetic materials, which, in their pure form, don't show any magnetoelectric coupling. However, when combined appropriately, a coupling mechanism via strain enables the composite to show magnetic response to electric fields and electric response to magnetic fields. Generally speaking, the use of composite materials offers several advantages, as outlined by J. van den Boomgard and R. A. J. Born,¹⁶ such as the free choice of the mole ratio of the constituent phases, the independent choice of grain size of the respective phases, and also the free choice of the sintering temperature during sample formation. The most generally understandable advantage is of course the ability to individually tune the properties of the magnetic and electric constituent, which was not possible with single phase magnetoelectrics. It was observed early on that the sample preparation methodology has a major influence on the quality of the samples¹⁶ and the resulting ME effect, which is why the preparation steps of the samples used in this thesis are also outlined in their own chapter 5.

Pioneering work that made use of the product property was performed by J. van Suchtelen¹⁷ and J. van den Boomgard et al.¹⁸ on composites of $\text{CoFe}_2\text{O}_4 - \text{BaTiO}_3$ (CFO-BTO) that became a well-known model system for a biphasic magnetoelectric composite. Further works on this system followed, in addition to various modifications thereof.^{19,20} Due to the well characterized nature of this material system, we will also start off with attempts of optimization and improvement of the ME coupling coefficient in CFO-BTO before moving on to other materials.

The main motivation behind this thesis was the desire to obtain a greater understanding of both intrinsic and composite sample systems with regards to their multiferroic properties, and how one could potentially improve them. As a result, this work is subdivided into two main parts. In the first half, we will be dealing extensively with bismuth ferrite, BiFeO_3 (BFO), a single-phase, intrinsic multiferroic, which has not seen any widespread use due to its inherent antiferromagnetic ordering. In the course of the work outlined in the following, we will perform a detailed characterization of the magnetic properties intrinsic to this material, observing the effects of a long range magnetic ordering, and discuss how these results may be utilized to improve the properties of BFO through different constraints of sample dimensions, from nanoparticles to thin films.

The second half will deal with a number of strain-coupled ME composites on which a large number of measurements have been performed, starting out with the classic CFO-BTO sys-

tem. This is a continuation of a preceding work,²¹ with the measurements shown in this thesis being performed with the aim of improving the converse magnetoelectric coupling coefficients by modifications of the sample synthesis and ceramic forming techniques. Through the course of our cooperations, we will see the replacement of both magnetic and electric constituents, with the overall aim always being the improvement of the magnetoelectric coupling coefficient. We will see how our converse ME measurement setup performs during this large array of measurements, learn about the possible pitfalls, and observe numerous nuances and clues in our measurement results that will help us to place them in a proper context when making comparisons to literature values. In the end, our understanding of the ME effect will be significantly augmented as we gather more and more knowledge about the behavior of the systems at hand.

This thesis is structured in a way to allow each chapter to logically follow the previous ones, starting off with the theoretical physical principles we need to adequately explain our methods and results in chapter 2, followed by a description of the sample systems, their properties, prior results in literature, and of course the reasoning behind their usage for our purposes in chapter 3. Next, the utilized scientific instrumentation is reviewed in chapter 4, with our own specialized methods being discussed in greater detail, while cooperative or conventional methods are described briefly. The short chapter 5 is devoted to the synthesis and sintering techniques with which our samples were produced. While not the main topic of this work, this provides crucial information that is necessary for understanding the behavior of samples that were formed through different synthesis routes. Finally, the results are presented in chapter 6, followed by the conclusion and outlook in chapters 7 and 8, respectively. The aim is to present a concise picture of all results on magnetoelectric multiferroics that have been obtained in the past four years.

2 Theoretical foundations

This chapter summarizes the theoretical background necessary for the understanding and later evaluation of the effects and sample systems we are dealing with.

2.1 Magnetism

A general understanding of the underlying magnetism in the samples that will be measured is of utmost importance for proper interpretation of the experimental data. The major types of magnetic interaction and ordering present in our samples will be discussed individually in order to achieve a solid overview of the possible ways of magnetic interaction.

As a rule of thumb, all materials are magnetic, but not all types of magnetism are of interest for experimental purposes, technical applications and indeed the ME effect. To discuss this, materials are classified according to their response to an external magnetic field, described by the magnetic susceptibility. It comes from latin *susceptibilis*, "receptive", and in case of the volume susceptibility, is described by

$$M = \chi H. \tag{2.1}$$

M is the magnetization of the material, usually given in emu/g or Am²/kg in case of mass or A/m in case of volume normalization, while H is the magnetic field strength. The susceptibility χ is a dimensionless quantity, with a positive susceptibility denoting para-, ferro- and ferrimagnetic materials (strengthening of the magnetic field in the material due to induced magnetization) and a negative susceptibility denoting diamagnetic materials (magnetic field weakened by the induced magnetization). Materials that are described as non-magnetic in layman's terms are usually para- or diamagnetic, as they don't possess any spontaneous magnetization without an external magnetic field present.

2.1.1 Ferromagnetism

Conversely, the materials most interesting for our purpose are those that still show magnetic properties even after an external magnetic field has been reduced to zero, referred to as remanence or remanent magnetization. Beginning with ferromagnets, the most well-known class of magnetic materials, it becomes clear that their properties cannot be described by a solely classical approach, as they were determined to be a quantum mechanical effect. The basis lies in the magnetic dipole moment of the electron, caused by its quantum mechanical spin, which in turn can only exist in one of two states, "up" and "down". If an atom has partially filled electron shells, it leads to the existence of unpaired spins, which allows the occurrence of

spontaneous magnetization without an applied magnetic field. There is a complex interplay of different interactions that are responsible for the parallel orientation of spins, with the main driving force being provided by the exchange interaction. The temperature is also an important factor, as thermal energy can overcome the parallel orientation of spins when the material is heated above its Curie temperature.

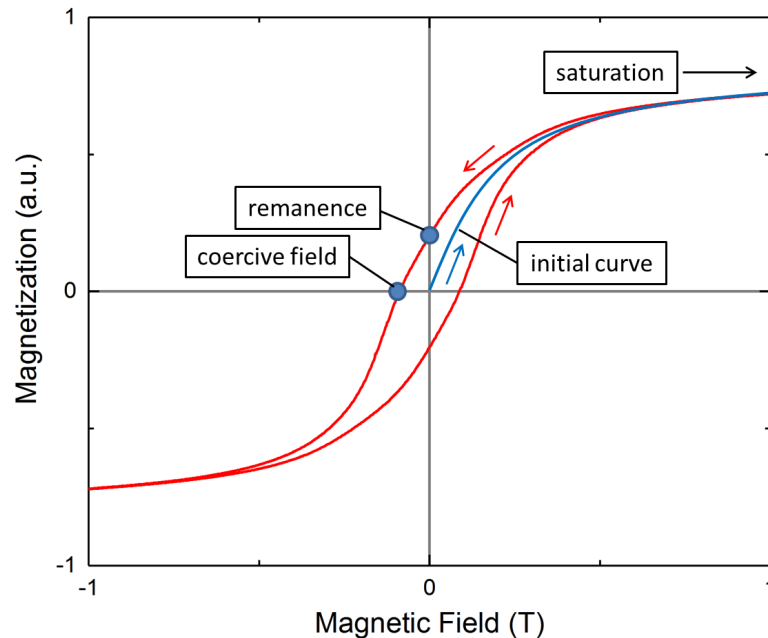


Figure 2.1: Field dependent magnetization curve showing typical ferromagnetic hysteresis (red), starting with the initial curve from a demagnetized state (blue).

As a macroscopic ferromagnet would create a large magnetic stray field that would extend into the surrounding space, it would lead to an unfavorably high magnetostatic energy, with the system striving to reduce this. The formation of magnetic domains directly follows, with regions of parallel spins forming in the macroscopic ferromagnet, separated by domain walls. For a ferromagnet that is heated above its Curie temperature and then cooled down again, the random orientation of these domains leads to zero net magnetic moment when measured from the outside, even though the parallel orientation of the spins is still present within the domains. The behavior that is regarded as typical for a ferromagnet can be observed when starting from such a demagnetized material, through the recording of $M(H)$ hysteresis curves. By exposing the ferromagnet to an increasing external field while recording the magnetization, one can witness the strong increase and saturation of the magnetization, followed by the irreversible change brought on by the exposure to the external field when latter is ramped back to zero. In this case, the magnetization does not return to zero, but retains a so called remanent magnetization, requiring a certain field strength, referred to as coercive field, in order to and reduce it to zero (see Fig. 2.1). It is this behavior that is most directly associated with ferromagnetism: High saturation magnetization, a significant remanence and coercive field.²²

2.1.2 Ferrimagnetism

A ferrimagnet, while showing spontaneous magnetization and similar behavior as shown in Fig. 2.1, is not equivalent to the parallel orientation of all spins as it is the case for a ferromagnet at 0 K. This phenomenon can be best described by a popular example, magnetite, Fe_3O_4 , which is in many ways rather similar to the Co and Ni ferrites that will be described later on. One formula unit of magnetite contains three Fe ions, in the form of $\text{Fe}^{2+}\text{Fe}_2^3+\text{O}_4^{2-}$, with electron configurations of $[\text{Ar}]3d^5$ for Fe^{3+} leading to a magnetic moment of $5 \mu_{\text{B}}$, while Fe^{2+} has a configuration of $[\text{Ar}]3d^6$ and a resulting magnetic moment of $4 \mu_{\text{B}}$. Oxygen with its filled p-orbital does not show any magnetic moment. One would normally assume that the net magnetic moment for a formula unit would result from the addition of all ion magnetic moments, which, when considering only spin moments as first approximation, would give us $14 \mu_{\text{B}}$. In reality however, the theoretical value is only $4 \mu_{\text{B}}$, which closely matches the experimentally determined value of $4.1 \mu_{\text{B}}$.²³ This can be explained by the moments of the Fe^{3+} ions being aligned antiparallel to each other, with this arrangement being caused by the superexchange interaction between Fe^{3+} and O^{2-} ions. This is shown schematically in Fig. 2.2, with the Fe^{3+} magnetic moments canceling each other out. The residual net magnetic moment is provided solely by the remaining Fe^{2+} ions, which have their moments oriented in parallel to the neighboring Fe^{3+} due to double-exchange interaction. These findings were brought forward by L. Néel^{24,25} and are of significant importance for the AB_2O_4 system of ferrites²⁶ used in this work with divalent metal cations (A) such as Co^{2+} or Ni^{2+} being combined with Fe^{3+} (B) that we will discuss in detail in the following chapter. Indeed, the term ferrimagnetism was coined because it was originally used to describe the spin arrangement of such ferrites.

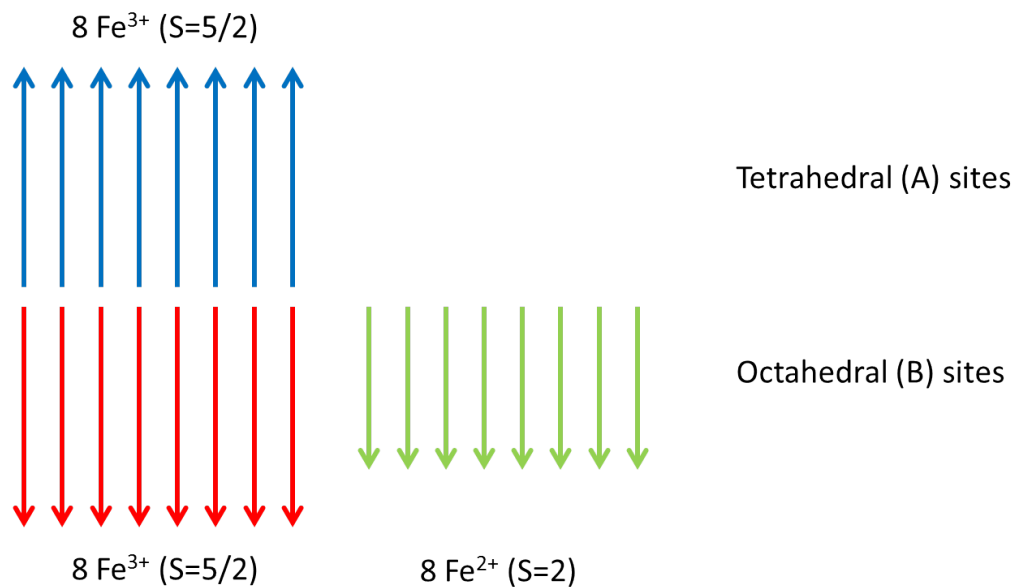


Figure 2.2: Schematic representation of the sublattice magnetization in magnetite, which contains 8 Fe^{2+} and 16 Fe^{3+} ions per unit cell.

2.1.3 Antiferromagnetism

Antiferromagnetism is conceptually similar to ferromagnetism and can be regarded as a special case of it, with sublattices of spins that are aligned antiparallel to each other. In this case though, the two sublattices have equal saturation magnetization, which means that the spins cancel each other out completely, so that the material as such has no net magnetization. This is problematic for magnetometry measurements, making characterizations much harder. It is however not a problem for one of our chiefly used methods, Mössbauer spectroscopy, which will be explained in detail in section 4.2. With this method, the magnetic order in antiferromagnets leads to the typical sextet spectrum that is also seen for ferromagnets, thus making a detailed characterization possible. Furthermore, thermal agitation can also neutralize this ordering if the material is heated above a specific temperature, referred to as the Néel temperature in case of antiferromagnets. An interesting example for such a material is bismuth ferrite, BiFeO_3 (BFO). It was considered as a candidate for magnetoelectric applications as it's one of the few materials that can be regarded as a single-phase intrinsic multiferroic, with a magnetoelectric coupling of its antiferromagnetically ordered spins to its polarization. However, due to the fact that it's an antiferromagnet, there was never a large scale usage of BFO for ME applications such as sensors or electrically written and magnetically read memory, for example. This might change in the near future though: During the course of this work, we will see that this material, once its magnetic characteristics have been unraveled, may yet be of some practical use when certain size constraints are applied.

2.1.4 Magnetostriction

An important attribute for our ME applications is the phenomenon of magnetostriction, a material property caused by small anisotropic changes of interatomic distance as a result of a change of the material's magnetization. The underlying mechanism is the spin-orbit coupling, leading to a slight change in the electron cloud in the presence of a magnetic field, with this small change in orbital motion causing the mentioned change in interatomic distance via orbit-lattice coupling. This leads to a macroscopic change of shape or dimension of a solid body due to elastic strain, which can be brought on by externally induced magnetization, e.g. by application of magnetic fields to the sample. Characterized by J. P. Joule²⁷ in 1847, one of its most well-known effects in everyday life is the characteristic hum of electrical transformers, caused by magnetostriction of their iron core due to the sinusoidal AC field produced by mains electricity flowing through the solenoid. To quantify this phenomenon, it is regarded as a strain that leads to a fractional change in length Δl , such that

$$\lambda = \frac{\Delta l}{l}, \quad (2.2)$$

with the special symbol λ being used to set it apart from strain produced by applied mechanical

stress. Generally speaking, it is an elastic strain, with the material returning to its original state when the external field is switched off. However, there are still hysteresis effects that are brought on by the magnetic characteristics of the material itself, such as remanence. The strain can reach a maximum value at magnetic saturation, thus referred to as saturation magnetostriction λ_S . While occurring in most substances, the effect of magnetostriction is unfortunately rather small, roughly of the order of 10^{-5} even in otherwise strongly magnetic substances. A fitting comparison was made by B. D. Cullity and C. D. Graham,²³ who compared the magnitude of the strain induced by magnetostriction to that induced by thermal expansion of alloys and metals. Using typical expansion coefficients for such materials, a strain of 10^{-5} would result from a temperature change of only 0.5 K, aptly showing that we are dealing with very small effects here.

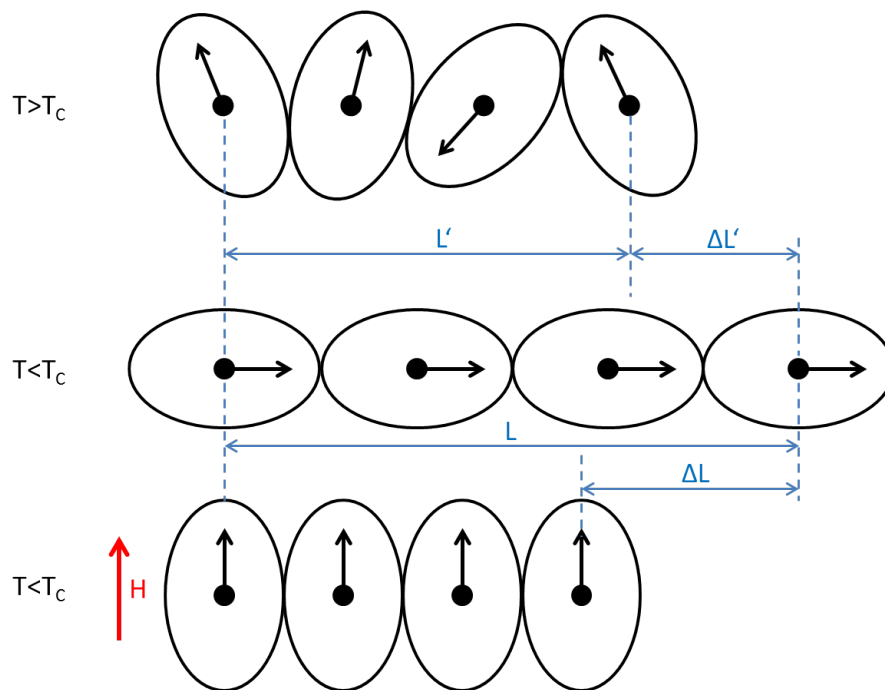


Figure 2.3: Schematic representation of the mechanism of magnetostriction, adapted from Ref. 23, reprinted with permission.

For most cases, when talking about magnetostriction, one usually refers to the saturation value λ_s , which can be positive, negative and also zero under certain circumstances. This value is also strongly dependent on the magnetization of the material, and thus on the applied external field. For the purpose of our experiments, this property is of high importance, as we will later on tune the ME effect in our composites using an external static magnetic field H_{DC} . When taking into account the phenomena that take place during the process of magnetization, the major part of the length change is caused by the alignment of magnetic domains in the material. This is shown schematically in Fig. 2.3 by a row of atoms within a crystal, with us regarding only one dimension for simplicity. The black dots represent atomic nuclei, the arrows

show their net magnetic moment, while the oval lines around both represent the nonspherically distributed electrons. We use an idealized case of a paramagnet, starting off above the Curie temperature T_C , assuming an extremely strong spin-orbit coupling. We can observe two effects: The spontaneous magnetostriction $\Delta L'$ resulting from magnetocrystalline anisotropy, caused by the alignment of the electron clouds along the easy axis, forcing the nuclei further apart, as well as the forced magnetostriction ΔL . This is achieved by applying a strong magnetic field H , in this case perpendicular to the easy axis, leading to field induced magnetostriction. As mentioned, this is an extremely exaggerated schematic depiction, with electron clouds of real materials only being reoriented to a much smaller extent.

For a more realistic approach, one would also need to consider that magnetic domains are aligned such that the stray field of a crystal is minimized. This leads to a structure that is schematically shown in Fig. 2.4, which depicts a material with positive magnetostriction under the influence of tensile stress, leading to domain wall motion.

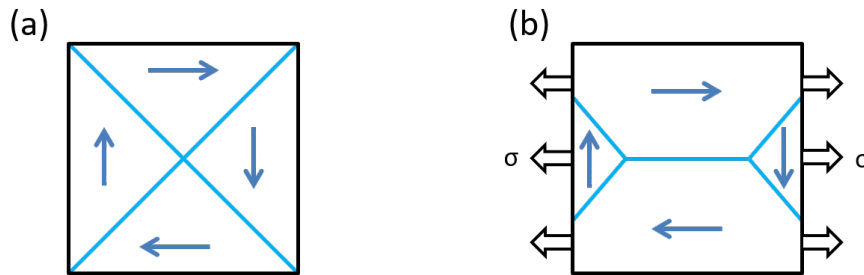


Figure 2.4: Schematic representation of the magnetic domain structure of a material with positive magnetostriction (a) under tensile stress σ (b). Adapted from Ref. 23, reprinted with permission.

After discussing the general character of magnetostriction, we can have a closer look at its dependence not only on external stress, but also on an applied magnetic field. It will be an applied mechanical stress that will induce the magnetization in our samples, while an applied external magnetic field H_{DC} will be used to tune the ME coupling. When coming from a fully demagnetized state, such as a material that has been heated above its Curie temperature, to a fully saturated state, there is hardly any change in the volume of a material sample. It is in this region that the magnetostriction undergoes its most dramatic rise, up to magnetic saturation. If the field is ramped even higher, one enters the region of forced magnetostriction, in which a further field increase causes an increasing but small amount of further strain, as depicted in Fig. 2.5. The underlying cause is the degree of spin order induced by high magnetic fields. A small volume change of the material occurs when going beyond saturation, which leads to the designation of this effect as volume magnetostriction, being responsible for an equal expansion (or contraction, depending on the sign of the coefficient) in all directions. For technical applications, this region is usually not of interest. On the one hand, the effect is very small compared

to λ_s , while on the other hand, high magnetic fields are not practical, as these usually require superconducting magnets. However, since the measurement setup described later on is capable of providing fields of up to 5 T, which have been used during our experiments, we want to keep this effect in mind for later evaluation.

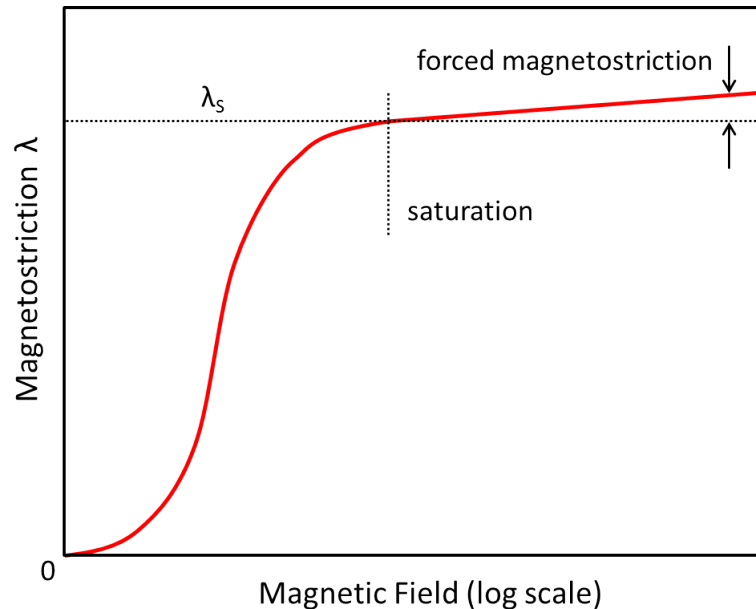


Figure 2.5: Magnetic field dependence of magnetostriction (schematic), adapted from Ref. 23, reprinted with permission.

When applying theoretical calculations to the samples that will be used in this study, one must take into account their crystalline properties first. There are a number of expressions for different types of single crystals, however, our samples are mixtures of two constituents that were sintered, rather than grown, thus having an unordered polycrystalline structure. In general, the saturation magnetostriction of a polycrystalline sample, measured parallel to the magnetization as is the case for our setup, can be characterized by a single constant λ_P . The value is dependent on the magnetostrictive properties and arrangement of individual crystals, for which we assume no preferred domain or grain orientation. For such a random arrangement, the overall saturation magnetostriction of the polycrystalline sample can be defined as an average over all crystallographic orientations. There is some debate on how to perform this averaging, with the two alternatives consisting of uniform stress but varying strain throughout the sample from grain to grain, or uniform strain and varying stress.

If we look at the saturation magnetostriction in a cubic crystal in a bit more detail, it quickly becomes apparent that we always want to know the strain relative to the direction of the magnetization. In our case, this is defined by the orientation of the sample in the magnetometer. For polycrystalline samples, an example of field dependent magnetostriction is given in Fig. 2.6,

but it was noted that the shape of such curves can vary quite widely, depending on the investigator who performed the experiment.²³ It is therefore difficult to precisely characterize or model the magnetostriction in the systems we are going to discuss, and indeed, measurements of magnetostriction usually don't contain information about the type and degree of preferred orientation. Most works usually show only the strain plotted against the field, although it would also be appropriate to plot it against the magnetization, as that is the parameter on which it depends directly. Nevertheless, we can clearly see the saturation behavior in Fig. 2.6, as well as the strong increase of magnetostriction in the small field range around to 100 Oe.

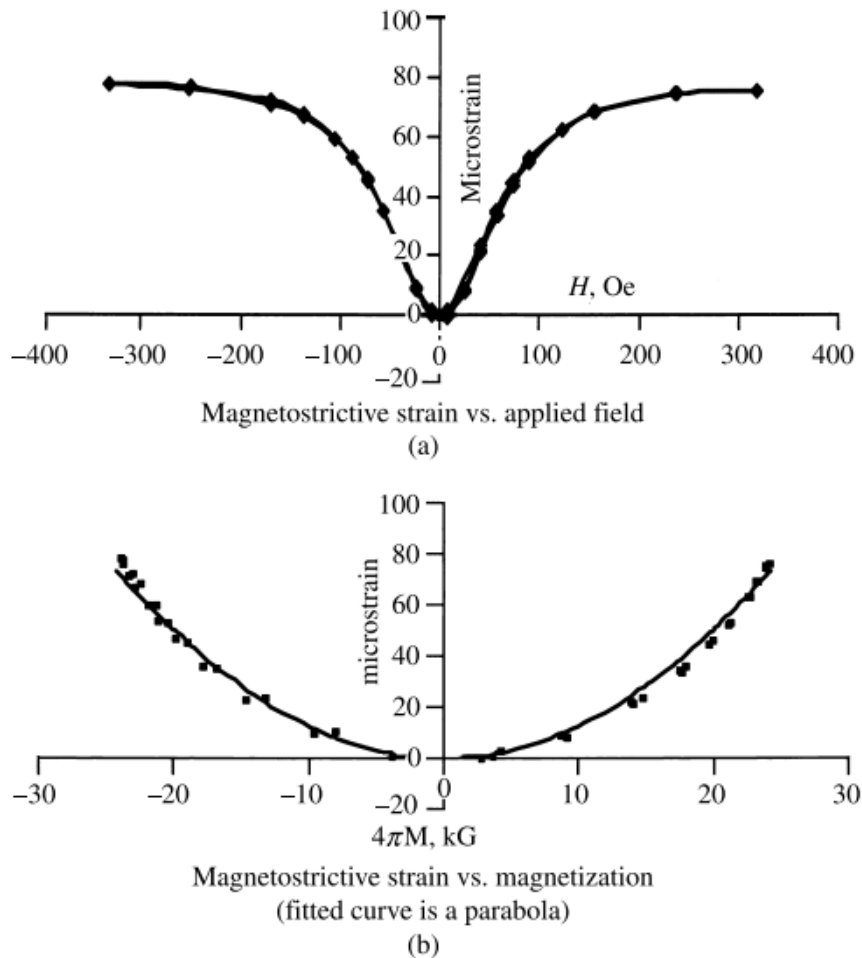


Figure 2.6: Magnetic field dependence of magnetostriction at room temperature in a polycrystalline sample of FeCo with 2% V doping, adapted from Ref. 23, data taken from Ref. 28, reprinted with permission.

If we want to obtain a rough understanding of the general shape of the magnetostriction curve, we can start off with the definition of saturation magnetostriction λ_s in a cubic crystal as explained in Ref. 23, when measured in the directions $\langle 100 \rangle$ and $\langle 111 \rangle$, thus referred to as λ_{100} and λ_{111} , respectively, with the equation

$$\lambda_s = \frac{2}{3}\lambda_{100}(\alpha_1^2\beta_1^2 + \alpha_2^2\beta_2^2 + \alpha_3^2\beta_3^2 - \frac{1}{3}) + 3\lambda_{111}(\alpha_1\alpha_2\beta_1\beta_2 + \alpha_2\alpha_3\beta_2\beta_3 + \alpha_3\alpha_1\beta_3\beta_1) \quad (2.3)$$

being valid for crystals having either $\langle 100 \rangle$ or $\langle 111 \rangle$ as easy directions. In it, the saturation magnetostriction is given in a direction defined by the direction cosines β_i relative to the crystal axes when the crystal goes from a demagnetized state to a saturated state, in a direction defined by the direction cosines α_i . This equation is obviously rather unwieldy, and as it will also be seen during the derivation of the magnetoelectric coupling coefficient, our polycrystalline composites allow for some simplification. At first, the general relation

$$(\alpha_1^2 + \alpha_2^2 + \alpha_3^2)^2 = (\alpha_1^4 + \alpha_2^4 + \alpha_3^4) + 2(\alpha_1^2\alpha_2^2 + \alpha_2^2\alpha_3^2 + \alpha_3^2\alpha_1^2) = 1 \quad (2.4)$$

can be used to reduce Eq. 2.3 to the form

$$\lambda_s = \lambda_{100} + 3(\lambda_{111} - \lambda_{100})(\alpha_1^2\alpha_2^2 + \alpha_2^2\alpha_3^2 + \alpha_3^2\alpha_1^2) \quad (2.5)$$

referred to as the "two-constant" equation for magnetostriction. Cullity and Graham do warn that this equation gives the field-induced strain when a crystal is brought from a demagnetized to a fully saturated state, which would of course mean that the entire sample needs to consist of one domain, which is never the case for our own samples. Furthermore, the demagnetized state is not properly defined, as it only requires the sum of the domain magnetizations to be zero, which can be reached through a large number of different domain orientations. Therefore, we will only use these equations to qualitatively discuss the behavior of our samples, not to numerically evaluate any results.

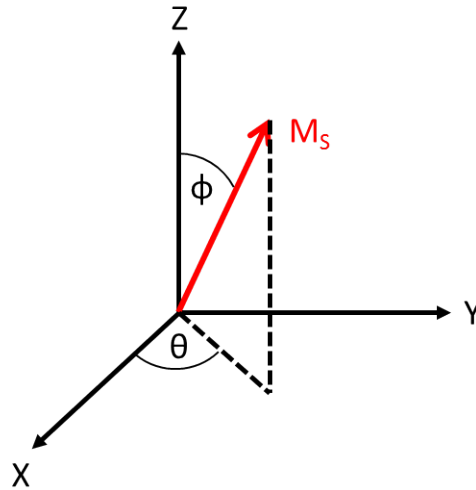


Figure 2.7: Definition of the angles θ and ϕ .

Returning to our initially introduced method of using λ_P to denote the magnetostrictive properties of a polycrystalline specimen, it should be noted that the saturation magnetization of

said specimen should be given as an average over all crystalline orientations in the sample, although it is not entirely clear how this is best performed.

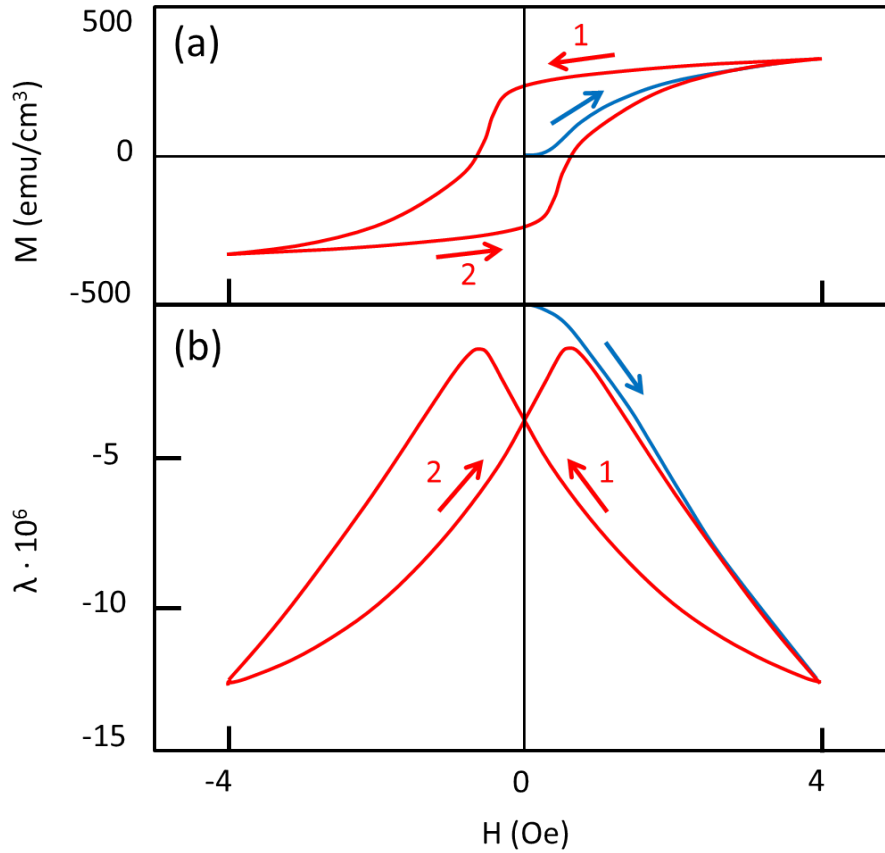


Figure 2.8: Magnetic field dependence of magnetization (a) and magnetostriction (b) in polycrystalline Ni, with initial magnetization shown in blue. Adapted from Ref. 23, data taken from Ref. 29, reprinted with permission.

Generally speaking, when applying a strong field to a polycrystal, the grains will strain in the direction of the field due to magnetostriction, but each grain produces a different value depending on its orientation relative to the applied field. Looking back to page 11, it is generally considered as more realistic to consider the strain to be uniform throughout the sample, while the stress varies. We therefore need to average the magnetostriction in field direction over all crystal orientations, for which we use Eq. 2.5 and express the α terms through the angles as shown in Fig. 2.7 allowing us to write

$$\alpha_1 = \sin(\phi) \cos(\theta), \quad \alpha_2 = \sin(\phi) \sin(\theta), \quad \alpha_3 = \cos(\phi). \quad (2.6)$$

so the surface of a sphere can be utilized, with the area $dA = \sin(\phi) d\phi d\theta$. Averaging over the upper hemisphere provides an average value for λ_s :

$$\overline{\lambda_s} = \frac{1}{2\pi} \int_{\theta=0}^{\theta/2} \int_{\phi=0}^{\phi/2} \lambda_s \sin(\phi) d\phi d\theta \quad (2.7)$$

If we then go ahead and substitute Eq. 2.5 for λ_s , integration results in the form

$$\overline{\lambda_s} = \frac{2\lambda_{100} + 3\lambda_{111}}{5} \quad (2.8)$$

that gives us a rough idea of the behavior of the magnetostriction in dependence of the two crystal orientations. There are other ways to present this,³⁰ but for our purposes, we were mainly looking for a general depiction. We now have an understanding of the mechanism and forms in which magnetostriction occurs, and could also see in Fig. 2.8 that just as the magnetization itself, the magnetostriction shows hysteresis behavior, with the value depending on the previous history of field exposure of the sample. As we will see in chapter 6, such effects become visible in our samples, with slight deviations in peak positions and amplitudes depending on the prior field exposure.

2.2 Electric material properties

The electric properties of our samples represent the equivalent of the magnetic properties, in terms of both effects needing to be present in order to achieve proper ME coupling. Due to the fact that many electrical properties are more easily measured and characterized than the magnetic properties, this section delves somewhat deeper into theoretical calculations than the previous section.

2.2.1 Polarization and dielectric permittivity

Our main goal in the topic of ferroelectric properties is to understand the interaction between an external electric field with the interior of a crystal we expose to this field, as will be done in the converse ME measurements. When starting off from the Maxwell equations, we arrive at the definition of polarization p , defined as the dipole moment per volume unit, averaged across the volume of a unit cell.

$$\vec{p} = \sum q_i \vec{r}_i \quad (2.9)$$

Basically, it's the sum of all point charges q at the respective positions r . Of interest for us is the reaction of this system to the application of an external electric field. However, the polarization as such, depending on the material in question, can itself be the sum of different types of effects altogether. For a better overview, the different types of polarization processes shall be discussed separately, as it was described in Ref. 31. The electronic polarization (Fig.2.9 (a)) can arise in materials that are electronically neutral if no electric field is present. Upon application of such a field, the electric charge of the atomic shell is shifted relative to the nucleus, with this displacement of the charges leading to an induced polarization. This is possible due to the comparatively small mass of electrons relative to the nucleus, enabling them to follow

even high frequency stimuli. For slower processes, like the frequencies used in our converse ME measurements, this effect can be considered as instantaneous. It remains in effect to frequencies up to 10^{15} Hz, with a polarization occurring during every cycle of the applied field, making this effect interesting for applications that require high frequencies. This type of polarization is not temperature dependent, while being proportional to the applied electric field strength. For this and the other polarization mechanisms described in the following, the frequency dependence is displayed in Fig 2.10.

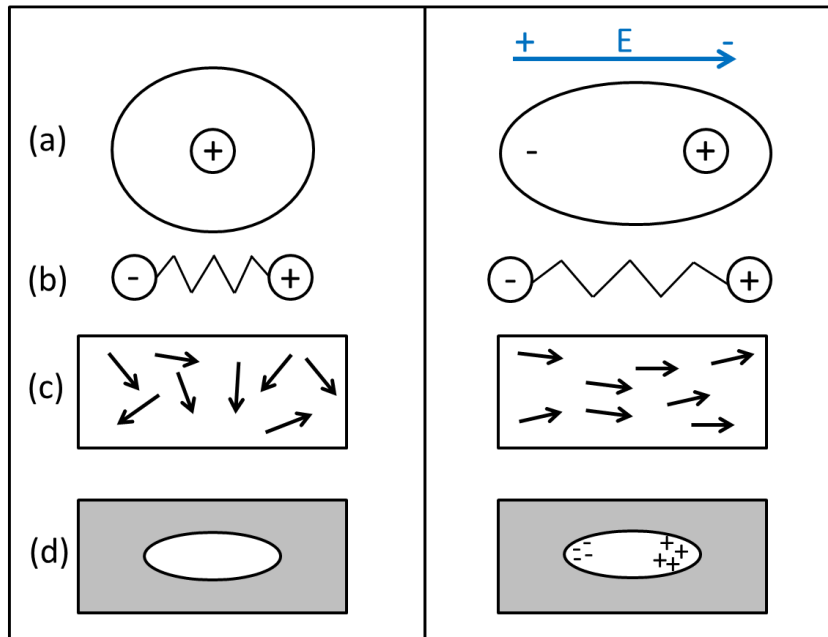


Figure 2.9: Different polarization processes without (left) and with (right) applied electric field: (a) electronic polarization, (b) ionic polarization, (c) orientational polarization, (d) space charge polarization, adapted from Ref. 31, reprinted with permission.

In case of an ionic crystal (Fig. 2.9 (b)), the applied electric field has an effect on both positive and negative ions, moving them out of their equilibrium positions. Positive ions are moved in field direction, while negative ions are moved in the opposite direction, with the resulting displacement leading to the so called ionic polarization. Its strength mainly depends on the binding energies involved and is independent of temperature. As we will see later on, this type of polarization will be of great importance, as the BaTiO_3 used here is generally viewed as a model system not only for ionic polarization but also with regards to strain and piezoelectricity.

If a molecule is composed of different atoms (Fig. 2.9 (c)), this can also lead to an asymmetric charge distribution, with water being the most well-known example. Under an applied electric field, these dipoles, if they are free to move, will rotate and align themselves in field direction and thus contribute to the overall polarization. This is referred to as orientational polarization. Similarly to magnetic moments, thermal agitation plays a role in this type of ordering, causing it to be temperature dependent.

In heterogeneous materials (Fig. 2.9 (d)), there is also the possibility of space charge polarization, caused by free charges in a more complex crystal system that contains boundaries or defects that stop these charges from freely moving through the material. This clustering of the charges at certain positions can lead to a dipole moment that contributes to the polarization of the material, in addition to other possible effects that can occur at the same time. Similarly to orientational polarization, the space charge polarization shows temperature dependence.

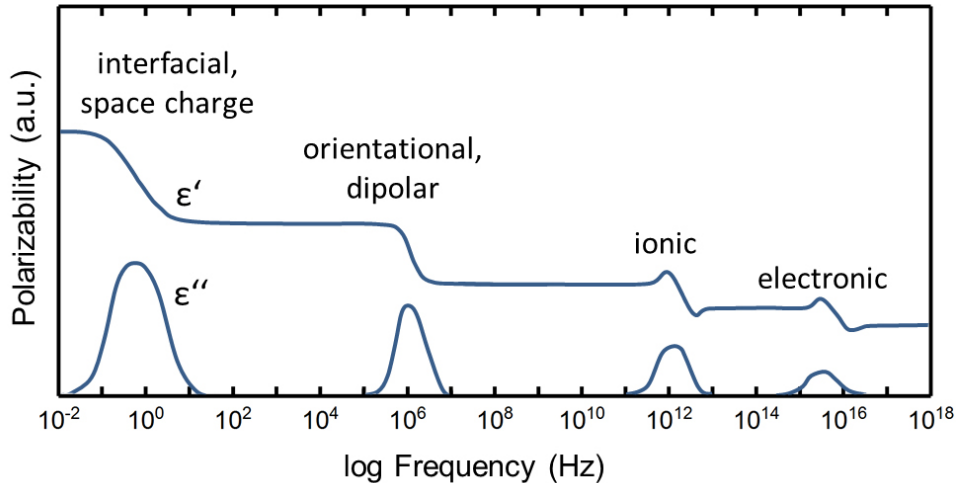


Figure 2.10: Frequency dependence of polarizability, represented by the real (ϵ') and imaginary part (ϵ'') of permittivity, adapted from Ref. 31, reprinted with permission.

Under the assumption that these effects do not have a direct influence on each other, they can be regarded as independent and thus allow a simple description as a sum. However, when wanting to make a distinction between the spontaneous polarization that is already present in some materials, such as in the case of dipolar bonds, the total polarization can be split between these two. The spontaneous polarization P_{sp} can be defined as the overall polarization present in a volume V of material

$$P_{sp} = \frac{p}{V}. \quad (2.10)$$

If we want to observe the two types of polarization separately, we can simply write the total polarization as a sum of the induced polarization P_E and the spontaneous polarization P_S , ending up with

$$P_i = P_{Ei} + P_{Si}. \quad (2.11)$$

We can further specify that the induced polarization, assuming that the electric field is not too strong so that the linear relationship holds true, can be written as

$$P_{Ei} = \epsilon_0 \chi_{ij} E_j \quad (2.12)$$

with χ_{ij} representing the dielectric susceptibility tensor and ε_0 the free space (vacuum) permittivity. If we then introduce the electric flux density D , which we write as

$$D_i = \varepsilon_0 E_i + P_i \quad (2.13)$$

then we can combine this with Eq. 2.12 to form

$$D_i = \varepsilon_0(\delta_{ij} + \chi_{ij})E_j + P_{Si} \equiv \epsilon_{ij}E_j + P_{Si}. \quad (2.14)$$

Here we introduce the dielectric permittivity tensor ϵ_{ij} , the first of many terms that appear in tensor notation in our theoretical derivations. With χ_{ij} and the Kronecker delta function δ_{ij} forming the dielectric permittivity tensor ϵ_{ij} together with the vacuum permittivity ε_0 we can write it as

$$\epsilon_{ij} = \varepsilon_0(\delta_{ij} + \chi_{ij}). \quad (2.15)$$

As done in Ref. 32, due to the fact that ε_0 is a scalar constant, we can introduce the dimensionless tensor

$$\varepsilon_{ij} = \frac{\epsilon_{ij}}{\varepsilon_0} \quad (2.16)$$

which can be referred to as the relative-dielectric-permittivity tensor, or more simply, as the dielectric constant tensor. Combining Eq. 2.12 and 2.15 gives us the relationship between polarization, electric field and dielectric constant, which we can write as

$$\varepsilon_0(\varepsilon_{ij} - \delta_{ij}) = \frac{P_{Ei}}{E_j} \quad (2.17)$$

or in scalar form for isotropic media:

$$P_E = \varepsilon_0(\varepsilon - 1)E. \quad (2.18)$$

Having established a definition of the electric polarization in dependence of applied electric field through usage of the dielectric permittivity, we have to look at one more factor, namely the frequency dependence of the polarization. Alternating electric fields will often be used in complementary measurements in order to probe the real and imaginary part of the dielectric permittivity, so their mathematical derivation shall be explained here.

We start off with a time-varying field $E(t)$ that is applied to a dielectric material, which invokes a delayed response due to the fact that, like many physical properties, the response of the polarization is subject to a certain inertia. Generalizing Eq. 2.13 for the electric flux, we can write it in a time dependent form as

$$D(t) = \varepsilon_0 E + P(t). \quad (2.19)$$

The susceptibility we have introduced earlier becomes the dielectric response function $\chi(t)$ that we use to define a relation between it and $P(t)$ for a delta-function type of perturbation so that

$$P(t) = \varepsilon_0 (E\Delta t)\chi(t) \quad (2.20)$$

with $E\Delta t$ approaching a constant value if Δt approaches zero. We further assume the applicability of linear response theory, which gives us the time dependence of the polarization:

$$P(t) = \varepsilon_0 \int_{-\infty}^t dt' \chi(t') E(t-t'). \quad (2.21)$$

If we then write the electric field as a general function of time using the Fourier integral

$$E(t) = \frac{1}{2\pi} \int_{-\infty}^{\infty} E(\omega) e^{i\omega t} d\omega \quad (2.22)$$

and then Fourier-invert it, we end up with

$$E(\omega) = \int_{-\infty}^{\infty} E(t) e^{-i\omega t} dt. \quad (2.23)$$

The same procedure can be performed for $P(t)$ that can be inverted to $P(\omega)$

$$P(\omega) = \int_{-\infty}^{\infty} P(t) e^{-i\omega t} dt. \quad (2.24)$$

In order to obtain the Fourier transform of Eq. 2.21, we can substitute it into Eq. 2.24 and use 2.22 in order to arrive at

$$P(\omega) = \varepsilon_0 \chi(\omega) E(\omega). \quad (2.25)$$

We then also perform the Fourier transform of the response function $\chi(t)$ to express it as the frequency dependent susceptibility $\chi(\omega)$:

$$\chi(\omega) = \int_{-\infty}^{\infty} \chi(t) e^{i\omega t} dt \equiv \chi'(\omega) + i\chi''(\omega) \quad (2.26)$$

This function, as shown by the right side, follows the real and imaginary part of the dielectric susceptibility, χ' and χ'' , respectively, which are defined as follows:

$$\chi'(\omega) = \int_0^{\infty} \chi(t) \cos(\omega t) dt \quad (2.27)$$

$$\chi''(\omega) = \int_0^{\infty} \chi(t) \sin(\omega t) dt. \quad (2.28)$$

From these, we can use the Kramers-Kronig dispersion relation to arrive at expressions for the

respective real and imaginary part of the dielectric permittivity that is also responsible for the frequency dependence of the polarizability we saw in Fig. 2.10. Going one step further, we can also take into account any dielectric losses that occur during the application of alternating fields, with the two main mechanisms being non-zero resistivity and non-zero inertia. Especially the former will play a role in our experiments, as it leads to problems for samples that have excessive conductivity and thus do not allow full polarization. If we again assume a linear response behavior, we can use time dependent terms for polarization and electric field, namely

$$E = E_0 e^{i\omega t} \quad (2.29)$$

and

$$P = P_0 e^{i\omega t + \psi}. \quad (2.30)$$

We can again use Eq. 2.12 in order to write the dielectric susceptibility as

$$\chi = P_0 / (\varepsilon_0 E_0) e^{i\psi} = (P_0 / (\varepsilon_0 E_0)) (\cos(\psi) + i \sin(\psi)) \quad (2.31)$$

and then, after a comparison with Eq. 2.26, we arrive at

$$\tan(\psi) = \frac{\chi''}{\chi'}. \quad (2.32)$$

Returning to the flux density or electric displacement, we can take into account a shift of the displacement vector by an angle δ relative to the applied electric field, which means that D can be written as

$$D = D e^{i(\omega t + \delta)}. \quad (2.33)$$

If we now go ahead and Fourier invert Eq. 2.14, we can use Eq. 2.26 to obtain

$$D(\omega) = \varepsilon_0 (1 + \chi'(\omega) + i\chi''(\omega)) E(\omega) = \epsilon(\omega) E(\omega). \quad (2.34)$$

Then, assuming that the overall susceptibility is the result of a contribution from several mechanisms, we can generalize this equation to:

$$D(\omega) = \varepsilon_0 \left(1 + \sum_m \chi'_m(\omega) + i \sum_m \chi''_m(\omega) \right) E(\omega) = \epsilon(\omega) E(\omega) \quad (2.35)$$

From this, we can thus deduce that the dielectric function itself, akin to the susceptibility, is a complex quantity with a real and imaginary part.

$$\epsilon(\omega) \equiv \epsilon'(\omega) + i\epsilon''(\omega) \quad (2.36)$$

$$\epsilon'(\omega) = \epsilon_0(1 + \sum_m \chi'(\omega)) \quad (2.37)$$

$$\epsilon''(\omega) = \epsilon_0 \sum_m \chi''(\omega) \quad (2.38)$$

These are the two quantities that we will often encounter when discussing the results from permittivity measurements that were performed on the samples that were also later utilized for magnetoelectric measurements. To avoid any confusion, I have kept the scalar and tensor notation of ϵ and ϵ , respectively, to keep these derivations in line with their source.³² For the discussion of the real and imaginary components obtained via measurements, the regular ϵ will be utilized in future sections.

2.2.2 Piezoelectric properties

The phenomenon of piezoelectricity can be observed in all crystals that are also ferroelectric. As described in Ref. 33, if we apply a mechanical strain Z to a crystal, it results in the change of electric polarization, while the application of an external electric field, which induces additional polarization, will also induce mechanical strain and deformation. The most well-known everyday item that makes use of this phenomenon is the piezo ignition element found in lighters or gas stoves, which use a spring loaded hammer to strike a piezoelectric crystal, often lead zirconate titanate (PZT) or quartz. The sudden and forceful deformation of these crystals produces a high voltage, which, through appropriate contacting, is used to generate the spark needed for ignition.

Using the schematic one dimensional notation found in Ref. 33, we can write the piezoelectric equations as:

$$P = Zd + E\epsilon_0\chi \quad (2.39)$$

$$e = Zs + Ed \quad (2.40)$$

Here, P is the polarization, Z the mechanical strain, d the piezoelectric coefficient, E the electric field, χ the dielectric susceptibility we have talked about above, e the elastic expansion and s the elasticity coefficient. If we go to the tensor notation of the piezoelectric coefficient as used in Ref. 32, we can write

$$e_{ij} = d_{kij}E_k \quad (2.41)$$

to obtain a relation between elastic elongation e_{ij} and piezoelectric tensor d_{kij} with the electric field E . Similar to the notation we will see for magnetoelectric effects, this equation represents

the converse piezoelectric effect, with mechanical strain being generated by the application of an electric field. The direct piezoelectric effect, the generation of polarization through the application of strain, can be more clearly shown by the following equation

$$D_i = d_{ijk}\sigma_{jk} \quad (2.42)$$

containing the uniaxial stress σ . The piezoelectric effect as such is a linear effect, but there can also be quadratic effects, referred to as electrostriction, which is present in all crystals. The single time we saw signs of only electrostriction and not just the much larger ME coupling was during problems that were encountered during our converse ME measurement, as mentioned in section 4.8.3.

2.2.3 Ferroelectrics and poling

Now that we know the principles behind polarization and piezoelectricity, there is one last important material property that we must look at, namely the phenomenon of ferroelectricity. In layman's terms, it describes materials that display spontaneous polarization, but also allow a reversal or switching of this polarization by the application of external electric fields, similar to the concept of ferromagnetism that was described earlier. As explained in Ref. 32, of the 32 possible crystal classes, ferroelectricity can only occur in 10 of them, namely the polar classes from the subset 21 noncentrosymmetric classes, of which all but one show piezoelectricity, but not ferroelectricity. Conveniently, all (non-semiconductor) ferroelectrics are also insulators; they are often referred to as ceramic ferroelectrics, rather than polycrystalline ferroelectrics. These are the materials that will be utilized to form the ferroelectric phase in our magnetoelectric composites. One important property that will be talked about in the sample preparation and the results section is the ability to pole the samples. This is usually not explained in depth in publications, so it shall be mentioned here in order to have a clear understanding of it when it comes to its use for our ceramics. When a piezoelectric ceramic is formed, as will be done from precursor powders in the synthesis section, we end up with randomly oriented grains as far as their electric properties are concerned. Therefore, an untreated, freshly sintered material is effectively a centrosymmetric material that cannot exhibit a piezoelectric effect, as explained previously. In order to overcome this problem, the ceramic needs to be poled. This is achieved by heating it above its ferroelectric Curie temperature, applying a strong external field, and then cooling the sample down in the applied field. This leads to a switching of the electric domains into directions that are more closely aligned to an external poling field. Obviously, a material needs to be ferroelectric in order to be poled, so nonferroic piezoelectrics for example cannot be poled. In our work, the poling is always performed in the same direction in which the electric field will be applied (or the polarization measured) during the magnetoelectric characterization, so that the majority of domain switching occurs in the direction the measurement setups are most sensitive in.

2.2.4 Landau-theory of phase transitions

In this thesis, we will often be dealing with phase transitions of ferroelectric constituents. In order to understand their character, as to why we see 'smooth' peaks and transitions rather than abrupt ones, we must consider the different types of phase transitions that can be encountered. The following explanations are based on Charles Kittel's well-known textbook "Introduction to Solid State Physics".³³

To obtain a consistent thermodynamic theory for the behavior of such crystals, we will utilize the free energy, as it will also be seen in the description of the magnetoelectric effect itself. More precisely, we expand the Landau free energy with regard to the polarization P in one dimension. We can write

$$F(P, T, E) = -EP + g_0 + \frac{1}{2}g_2P^2 + \frac{1}{4}g_4P^4 + \frac{1}{6}g_6P^6 + \dots \quad (2.43)$$

with the temperature dependent coefficients g_n , assuming that we're not dealing with materials that have non-analytical ranks in the vicinity of the phase transition, or singularities etc. As the value of P is given by the minimum of $F(P)$ in thermal equilibrium, we can set the differential to zero and write

$$\frac{\partial F}{\partial P} = 0 = -E + g_2P + g_4P^3 + g_6P^5 + \dots \quad (2.44)$$

to obtain the equilibrium polarization in an applied electric field E . As described by Cullity and Graham,²³ we assume the sample to be a long bar in this case, with the electric field being applied parallel to the longitudinal side. In order to attain a ferroelectric state, we need to assume that the coefficient g_2 from Eq. 2.43 goes through zero at a specific temperature, which we will here refer to as T_0 in order to avoid confusion with the Curie temperature T_C used elsewhere in this thesis. We can therefore write

$$g_2 = \gamma(T - T_0) \quad (2.45)$$

with the positive constant γ . As previously mentioned, coefficients like g_2 are temperature dependent, which can be traced back to thermal expansion and other anharmonic lattice interactions. In this case, a small value of g_2 indicates a softer lattice that is easily destabilized, while a negative value points towards the unpolarized lattice becoming unstable.

Second order phase transitions

With the groundwork having been established, we can now observe the two different types of phase transitions. For the second order phase transition, we assume g_4 in Eq. 2.43 to be positive, in which case g_6 has no influence and can be neglected. Further assuming no external applied field, Eq. 2.44 gives us the following relation

$$\gamma(T - T_0)P_S + g_4P_S^3 = 0 \quad (2.46)$$

such that the two cases

$$P_S = 0 \quad (2.47)$$

and

$$P_S^2 = \frac{\gamma}{g_4}(T_0 - T) \quad (2.48)$$

exist to solve this equation. In the case of $T \leq T_0$ there is only one real solution to Eq. 2.46 which lies at $P_S = 0$ due to the fact that γ and g_4 are both positive. In this case, it means that T_0 is in fact the Curie temperature and we have $T_0 = T_C$. In case of lower temperatures when $T \geq T_0$ is valid, the minimum of the free energy is given by:

$$|P_S| = \frac{\gamma}{g_4}{}^{\frac{1}{2}}(T_0 - T)^{\frac{1}{2}} \quad (2.49)$$

This is generally referred to as a second order phase transition, characterized by a discontinuous jump upon reaching T_C .

First order phase transitions

If g_4 in Eq. 2.43 becomes negative, then g_6 can no longer be neglected, as otherwise, F would tend towards negative infinity. Using Eq. 2.44 with $E = 0$, we arrive at

$$\gamma(T - T_0)P_S - |g_4|P_S^3 + g_6P_S^5 = 0 \quad (2.50)$$

and again have two possibilities to solve it, either by setting P_S to zero like in 2.47 or by the relation

$$\gamma(T - T_0) - |g_4|P_S^2 + g_6P_S^4 = 0. \quad (2.51)$$

For our phase transition, this means that the free energy F for the paraelectric phase above T_C and the ferroelectric phase below it must become equal at T_C . Effectively, the value for F at the point $P_S = 0$ must be equal to the value we obtain at the minimum of Eq. 2.51. This is characterized by an abrupt change upon reaching the transition temperature. One well-known example is the Curie temperature of BTO, as shown in Ref. 33, which is logical when we consider that the cubic phase above T_C has no inherent polarization. It is this phase transition that causes the sharp peaks to appear in electric permittivity measurements on our composite samples, for example in Fig. 6.43.

2.3 Magnetoelectric coupling coefficient

We have now obtained a general overview of basic magnetic and electric sample properties, some of which we will directly measure, and many of which have a direct influence on the ME coupling. The next step is the development of a model for the coupling itself, which we can then use to analyze our data. For this purpose, we will now derive the necessary mathematical correlation that is going to be used to evaluate the results from our converse magnetoelectric measurements, which are described in detail in chapter 6. The main body of the following explanations is based on the compact but comprehensive review by Eerenstein et al.,³⁴ which is a highly recommended read for all those wishing to obtain a general overview of the developments of magnetoelectrics in the past decades.

As always with theoretical derivations, we will start out with well-defined model systems in order to build up the main body of mathematical relations, and then adapt it to our samples. These are of course complex and polycrystalline, enabling certain simplifications, allowing us to end up with the straightforward model of calculating the converse coefficient that will be described in section 6.2.1. Starting off with the ME effect in single-phase crystals, we again describe it in terms of Landau theory, as it is often done in literature,^{35,36} using the free energy F in dependence of the applied magnetic and electric field H and E , respectively, with their i -th components being given by H_i and E_i . We further assume that the material is non-ferroic, and that in the absence of applied electric or magnetic fields, both the temperature dependent electrical polarization $P_i(T)$ as well as the magnetization $M_i(T)$ are zero, with no hysteresis effects being considered. Furthermore, we assume a stress free medium that is infinite and homogeneous, thus being able to write the free energy as

$$-F(E, H) = \frac{1}{2}\varepsilon_0\varepsilon_{ij}E_iE_j + \frac{1}{2}\mu_0\mu_{ij}H_iH_j + \alpha_{ij}E_iH_j + \frac{1}{2}\beta_{ijk}E_iH_jH_k + \frac{1}{2}\gamma_{ijk}H_iE_jE_k + \dots \quad (2.52)$$

using the Einstein summation convention in S.I. units. In essence, it is the first three terms that are of importance to us, with the third one being the decisive factor we are after. All of these factors, as visible by the ij notation, are second rank tensors, with the following third rank tensors β_{ijk} and γ_{ijk} representing higher-order magnetoelectric coefficients. Going through them, we start with the first term, which describes the overall contribution that stems from the electrical response of the system to an electric field, with the well-known dielectric permittivity of free space ε_0 and the relative permittivity $\varepsilon_{ij}(T)$ that we will also directly measure later on. In non-ferroic materials, it can be assumed to be independent of E_i . The second term gives us the magnetic response to an applied magnetic field, basically representing the magnetic equivalent to the first term, with the permeability of free space μ_0 also being a well-known physical constant, while the relative permeability is given by μ_{ij} . The part we are most interested in is α_{ij} in the third term, representing the linear magnetoelectric coupling, which is exactly what

we will measure on our composite samples.

When we look ahead at how the ME effect is measured, namely by the application of electric or magnetic fields in order to observe the resulting magnetic and electric response, it is obvious that we want to obtain our above relation in the form of either $P_i(H_j)$ for the direct or $M_i(E_j)$ for the converse ME effect. We will mainly deal with the latter, so we differentiate F with respect to H_i and then set $H_i = 0$, arriving at the more familiar form

$$\mu_0 M_i = \alpha_{ij} E_j + \frac{1}{2} \gamma_{ijk} E_j E_k + \dots \quad (2.53)$$

The complementary relation for polarization can be written in the same manner:

$$P_i = \alpha_{ij} H_j + \frac{1}{2} \beta_{ijk} H_j H_k + \dots \quad (2.54)$$

We can now include some valid assumptions regarding the systems we are going to measure, which are ferroic materials, in which ε_{ij} as well as μ_{ij} display field hysteresis, while it also has to be observed that such materials can be better parameterized in terms of resultant rather than applied fields.^{34,37} The cause behind this, which will also be discussed in the results section, is the significant demagnetizing field that is present in finite media, being strongly dependent on their shape. We can therefore use an approximation³⁸ in which we represent the resultant electric and magnetic field by the polarization and magnetization in our samples, which are obtainable through established measurement methods.

We already know that the materials, on which we will perform quantitative magnetoelectric measurements, are ferrimagnetic as well as ferroelectric, which often means that these materials have a large permittivity ε and permeability μ . It results in a boundary condition for α_{ij} through the diagonalized tensors ε_{ij} and μ_{ij} , which can thus be written as³⁹

$$\alpha_{ij}^2 \leq \varepsilon_0 \mu_0 \varepsilon_{ij} \mu_{ij}. \quad (2.55)$$

This equation can be obtained directly from Eq. 2.52 by ignoring the higher-order coupling terms and thereby forcing the sum of the first three terms to be greater than zero.

There is of course the possibility of non-linear coupling, which would necessitate the use of higher order coupling terms. In some materials, like in certain piezoelectric paramagnets,⁴⁰ β_{ijk} can indeed be of greater magnitude than α_{ij} and play a dominant role in the overall effect. In our case however, we shall only deal with materials in which the linear effect is clearly dominant. As mentioned in Ref. 1, the great majority of the measurements concern only the linear ME effect, and it has become acceptable to omit the 'linear' prefix when referring to the ME effect in general, as it's clear that it's almost always the linear one that is of interest. While it is theoretically possible to also characterize higher order effects, it would require some

experimental effort¹⁰ that negates the practicality of our setup, so no such attempts were undertaken this far. Also, it was suggested in Ref. 34 that the proper investigation of such effects should be performed with magnetic materials of reduced dimensionality, which would make our composites with their complex 3D structures less suitable.

Another factor we need to look out for is the type of coupling present in our samples. As it was mentioned in the introduction, our composites make use of strain coupling between the piezoelectric and piezomagnetic constituents, which is an indirect type of coupling. If we want to take this into consideration, we would need to add cross terms in Eq. 2.52 to account for magnetostriction, and the modification of strain by the applied magnetic field, for which theoretical calculations predicted further mixed terms.⁴¹ However, the boundary conditions set by Eq. 2.55 do not restrict the strength of such indirect coupling, and indeed, much greater effects have been measured when compared to single-phase systems.⁴² It is for this reason, among others, that we will only evaluate results from these indirectly coupled composite materials numerically.

We now want to arrive at a simple formula that we can use to determine the coupling coefficient in our materials. As correctly noted by Eerenstein et al.,³⁴ in order to perform experimental magnetoelectric measurements, a number of challenges need to be addressed, the most important issue being the conductivity of the sample leading to leakage currents, which has to be overcome by the use of sufficiently insulating samples. Even in the preliminary measurements we will present later on in chapter 6, excessive conductivity poses a problem for the recording of ferroelectric $P(E)$ loops, as it was already discovered in earlier works.^{37,43} We will discuss this problem extensively in section 4.8.1, and explain how it may influence the outcome of our measurements, while also showing ways on how to detect any stray signals from conductivity effects. For indirect measurement methods, Eerenstein et al.³⁴ also warned of effects when measuring dielectric constants near magnetic transition temperatures, as any results may come from magnetoresistance effects alone, rather than magnetoelectric coupling, which was described in an article by Catalan et al. that is aptly titled "Magnetocapacitance without magnetoelectric coupling".⁴⁴ We, however, are going to measure the effect as a magnetic response to an applied electric field, referred to as the converse ME effect, while some measurements of the direct effect, the electric response to applied magnetic fields, were performed in the group of Prof. Doru C. Lupascu (University of Duisburg-Essen). In such measurements, the time-integrated current per unit area from Eq. 2.54 directly represents the magnetically induced change of polarization, which would give us dP/dH when referring to the change of polarization or dE/dH when referring to the change of electric field. The latter results in the expression for the direct ME coupling coefficient α_D , also known as the magnetoelectric voltage coefficient, written as

$$\alpha_D = \frac{dE}{dH}. \quad (2.56)$$

The same is also true for the complementary Eq. 2.53, so that we end up with the simple equation

$$\alpha_C = \mu_0 \frac{dM}{dE}, \quad (2.57)$$

in which we henceforth use α_C to denote the converse ME coupling coefficient, in order to set it apart from the direct coefficient that results from the magnetic field induced polarization. In a simple linear approximation, the direct and converse coefficients are identical due to Maxwell's relations, as explained in Ref. 45, with purely piezoelectric cases being shown in Ref. 37 while the magnetoelectric coefficients were also discussed in Ref. 36.

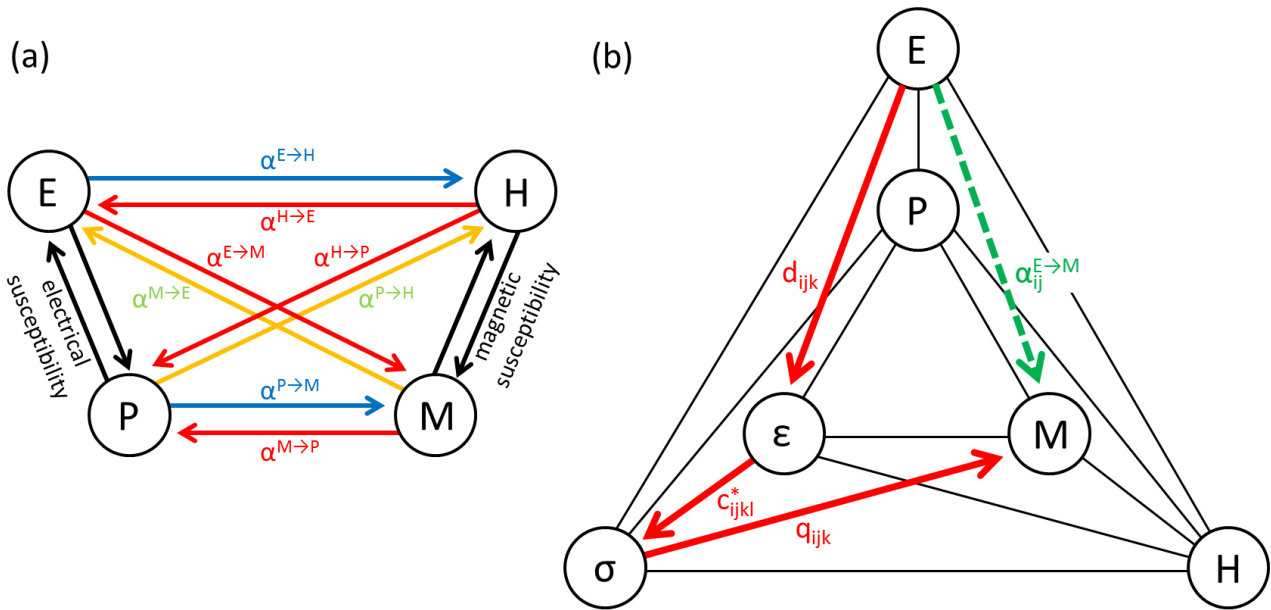


Figure 2.11: Heckmann diagrams showing magnetolectric coupling coefficients and their inverse (a) and the product properties (b). The dashed green line represents the relation given by Eq. 2.57 while the red lines show the indirect path of strain coupling as utilized in the composites discussed here, via the piezoelectric coefficient d , the stiffness c^* , and the piezomagnetic coefficient q . Adapted from Ref. 45.

To obtain a clearer picture of our indirect path via strain coupling, one can take a look at Fig. 2.11 that showcases the relation between electric, mechanical and magnetic properties, as well as the interrelation between the thermodynamic material fields. It is based on the original textbook-based Heckmann-diagram⁴⁶ using the form that was implemented by Spaldin and Fiebig² with added parameters as used in Fig. 12 of our joint GAMM-Mitteilungen.⁴⁵ In this publication, all eight possible coefficients are differentiated, which, in the linear case, are pairwise identical. To make it clear, the coefficients were written in a slightly different $A \rightarrow B$ notation in order to showcase which action A yields the response B ,

$$\alpha_{ij}^{H \rightarrow P} = \alpha_{ij}^P \quad (2.58)$$

and in the same manner

$$\alpha_{ji}^{E \rightarrow M} = \alpha_{ji}^M \quad (2.59)$$

while we can state that the two coefficients are equivalent such that

$$\alpha_{ij}^{H \rightarrow P} \equiv \alpha_{ji}^{E \rightarrow M}. \quad (2.60)$$

This was included just to clearly show the relation between the two coefficients in the case of our system. In the literature, there are works that clearly state that the direct and converse coupling coefficients are equivalent,^{47,48} while others state the opposite.^{49,50} Works that state the latter are often performed on laminate systems at high frequencies to make use of resonance effects, while we will be using low frequencies in our work. Even so, despite considerable numerical differences between the two coefficients being reported, the magnetic and frequency dependent curves show equivalent shapes (see Fig. 5 and 6 in Ref. 49) and are often described to be very similar to each other.⁵¹ We can therefore state that our assumption of equivalence of α_C and α_D holds true and we'll be able to compare their qualitative dependence on external parameters.

In terms of being able to convert the direct to the converse coefficient and vice versa, we refer to the work of Wu et al.⁵² who compared the direct and converse ME effect in laminated composites. As also explained in Ref. 21, they determined that for the direct effect, the ME voltage coefficient can be expressed through α_D as

$$\alpha_D = \frac{dE}{dH} = \frac{\alpha}{\varepsilon_0 \varepsilon} \quad (2.61)$$

while the converse coefficient is given by

$$\alpha_C = \frac{dB}{dE} = \alpha. \quad (2.62)$$

This leads to the conversion formula

$$\alpha_D = \frac{\alpha_C}{\varepsilon_0 \varepsilon}. \quad (2.63)$$

As we can see, this conversion strongly depends on the permittivity ε , which provides the main factor between α_D and α_C , while introducing a strong frequency dependence. This also explains the striking difference that some authors^{49,50} saw in their results, especially when high frequency measurements of laminate samples in resonance are concerned. We will therefore only make a qualitative comparison between direct and converse ME results in this work, as only one sample has the full set of results from both measurement methods, while the majority of the results is based only on the converse ME coupling coefficient. Furthermore, instead of using the more cumbersome notation of $\alpha_{ij}^{E \rightarrow M}$, we will instead keep using α_C as an indicator that the converse coefficient is being given for experimental results, determined from the mag-

netization that was induced by the application of an electric field. Going further, we need to consider the orientation of our sample relative to the electric and magnetic fields, which also includes the direction of polarization and magnetization. As explained above, we moved away from the tensor notation due to the complexity of our ceramics, but that makes it necessary to somehow define the orientations through our experimental procedure. In the case of a polycrystalline or multidomain material, as explained in Ref. 45, the orientation of polarization (or magnetization) is not defined by the crystal orientation, but becomes a function of the effective polarization state. We thus use the notation α_{33} and α_{31} to denote orientations of the sample with respect to the polarization direction and the applied magnetic field, with latter being turned from its out of plane direction (3) into the in plane direction (1) during the course of our experiments. This is also referred to as the longitudinal and transverse magnetoelectric measurement, with the former being performed with all fields parallel to each other and perpendicular to the sample surface, while the latter uses a perpendicular magnetic field parallel to the sample surface. As we will only discuss this for one sample set in the results section, we will not use any extra notation for the other sample sets we will characterize in the following.

Eerenstein et al.³⁴ also mentioned that the strategy we use here of purposefully engineering composites that show high ME coupling through indirect strain transfer offers several advantages. Apart from the coupling limit of Eq. 2.55 being lifted, it allows one to individually optimize each phase separately, which is not possible with single phase materials. They go on to explain that epitaxial thin films offer the potential for precise ME studies due to their well defined nature thanks to precise control of thickness, interfacial quality and crystallographic orientation. However, measurements of α in such systems have not been forthcoming, often due to the effect of clamping from the underlying epitaxial structure as well as the substrate. Still, we should keep the potential of thin films in mind for our final discussion in chapter 8.

If we consider our chances of properly modeling the behavior of our complex composite systems, it quickly becomes apparent that this is an extremely difficult task,⁵³⁻⁵⁶ although it has been attempted for one of our sample systems.⁵⁷ We will therefore use our experimental definitions for sample orientation and resulting converse coupling coefficient without detailed calculations. Finally, we must also take note of remanent polarization and magnetization effects that can alter the response of the system, which, for example, cause the coupling coefficient to become a function of the orientation of the poling state.

$$\alpha_{ij}^P = \alpha_{ij}^P(P_{rem}, M_{rem}) \quad (2.64)$$

The same is true for any remanent magnetization that may be present in the system. This is mainly valid for composite samples, as the crystal orientation itself determines the orientation and value of the coupling tensor in intrinsic multiferroics. However, experimentally, we will not

have any problems with these remanences, as both the electric and magnetic field are externally applied to the sample, with their magnitudes overpowering any potential remanent fields, at least in the field ranges we will be using for our studies. Some effects through remanence and self-biasing will be discussed in the results section, but these effects are usually not of interest for potential technical applications, and are often superimposed by other effects such as the trapped flux in the superconducting magnet of our setup.

Generally speaking, we now know that we can determine α_C with the simple Eq. 2.57 for our system of magnetolectric composites. Although thin films would be much more adequate for precise ME studies, their low ME effect and the more complicated fabrication methods make our composites a more suitable candidate for studies that may not have the highest mathematical precision, but are based on robust and reliable measurement methods, as we will see in chapter 4.

One last factor we need to take into consideration is the dependence of the magnetolectric coefficient on the magnetostriction. Although we have introduced the effect of magnetostriction in section 2.1.4, we need some additional knowledge to interpret the field dependent curves of the induced ME magnetization, referred to as $ME(H)$ in the following. If we briefly return to the tensor notation, we can write Eq. 2.59 as follows, using the external stress σ :

$$\alpha_{ij}^{E \rightarrow M} = \alpha_{ij}^M(H) = \frac{\mu_0 dM_i(H)}{dE_j} = \frac{\mu_0 dM_i(H)}{d\sigma_{mn}} \cdot \frac{d\sigma_{mn}}{d\varepsilon_{kl}} \cdot \frac{d\varepsilon_{kl}}{dE_j} = q_{imn} \cdot c_{mnkl}^* \cdot d_{jkl}. \quad (2.65)$$

This is equal to the effective magnetolectric coefficient $\alpha^{E \rightarrow M}$ that is shown in Fig. 2.11. We are thus able to see that the ME response tracks the magnetic field dependence of the magnetostrictive strain coefficient, which, thanks to Maxwell's relations, can be written as

$$q_{ikl}(H) = \frac{d\lambda_{kl}(H)}{dH_i} = \frac{\mu_0 dM_i(H)}{d\sigma_{kl}}, \quad (2.66)$$

with λ_{kl} being the magnetostrictive strain coefficient⁵⁸ that we introduced in section 2.1.4 while d_{jkl} represents the piezoelectric tensor. Normally, one can assume that λ_{kl} and ε_{kl} are equivalent, which certainly holds true at phase boundaries between magnetostrictive and piezoelectric phases. However, as we will see in microscopy images in the results section, the vast majority of the material is not at the interface but in a volume around it, while still experiencing an effective stress upon electric or magnetic field applications. Therefore, as it was included in the previous Eq. 2.65, we need an effective stiffness $c_{mnkl}^* = d\sigma_{mn}/d\varepsilon_{kl}$ that provides the transfer of interface constraint to the material volume, thus giving us the overall response of our sample system to external field applications. Regarding the question of how to include this into our evaluation, we again face the problem of our composites being rather difficult to properly model. This also has to do with the connectivity scheme, which will be dealt with in the next section, followed by the final explanation of its effects on our modeling.

2.3.1 Connectivity schemes for magnetoelectric ceramics

Connectivity is a very critical parameter for magnetoelectrics, basically giving us a rough representation of the dimensionality of connectivity patterns within the sample. The notation we use here is valid for biphasic solids,⁵⁹ which represent the magnetoelectric composites that we are going to be dealing with in this thesis. In total, there are ten important connectivity patterns, but we will concentrate on the ones that are of significance to our experimental work. Denoted in the form of (x-y), the first digit gives us the magnetostrictive constituent, while the second digit represents the ferroelectric one, with the possible numbers 0, 1, 2, and 3 displaying what can be described as the number of dimensions in which the material has continuous connections.

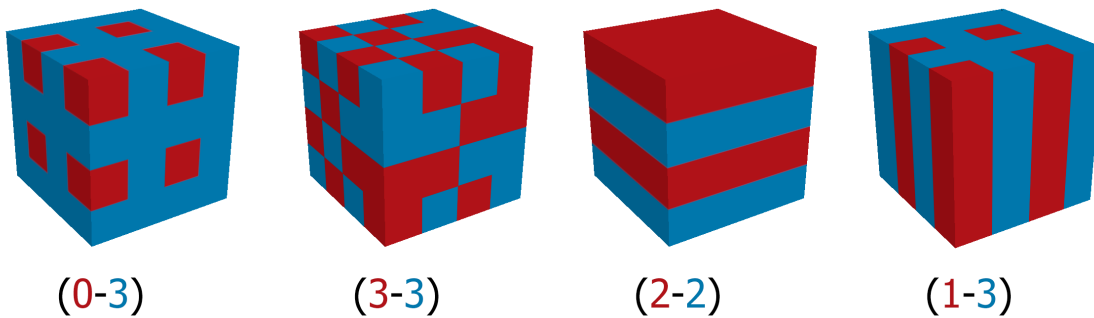


Figure 2.12: Examples of connectivity schemes in biphasic composites, with the first digit representing the dimensionality of the magnetostrictive (red), and the second digit of the piezoelectric phase (blue).

A digit 0 therefore represents no significant spreading in any direction, valid for nanoparticles or comparatively small grains, while the digit 3 points towards a material that shows significant expansion in all directions (matrix material). Similarly, a digit 1 would indicate an expansion in only one direction, such as thin bars that were also the subject of previous cooperations,⁶⁰ while a digit 2 stands for a spread in two dimensions, such as a thin film layer. Therefore, a (0-3) connectivity would consist of magnetostrictive nanoparticles embedded in a ferroelectric matrix, while the (3-3) connectivity stands for a completely mixed phase system in which both constituents extend in all dimensions. A schematic representation of these examples is given in Fig. 2.12. The decision on the use of different schemes rests in the question of which aspects one wants to look at, either maximizing the interface, or making use of certain shape anisotropies for specialized applications. Each scheme has its own advantages and drawbacks, the decisive factor always being the specific properties of the two constituents. In our case, for example with the CFO-BTO system, the (0-3) scheme was highly advantageous, as the high electric resistance of the BTO phase allowed effective electrical poling, while upon reversal to (3-0), it was observed that a CFO matrix had excessive conductivity, rendering certain measurements impossible. Nevertheless, due to the fact that applications exist for such a system,^{61,62} attempts were made to obtain ME results for (3-0) samples as well.

With the different connectivity schemes established, we can return to the topic of the previous section and formulate our final remark on the possibility of modeling the response of our composite ceramics to applied external fields, as it was performed in Ref. 45. The main question revolved around the effective stiffness c_{mnkl}^* and how one might take it into account. Looking through the literature, we find analytical expressions for the overall coupling coefficient α_{33} in longitudinal direction,⁵⁸ as the volume fractions and numerous elastic constants were attainable due to the well defined nature of the samples used. There were also theoretical predictions for (1-3) connectivities⁵³ that represent magnetostrictive pillars in a ferroelectric matrix, which were also successfully measured⁶⁰ in the course of a previous cooperation of our group.

However, when we arrive at (0-3) or (3-3) connectivities, it becomes extremely difficult to properly determine c_{mnkl}^* . There are possibilities through finite element structures⁵⁷ and by embedding the respective materials in an insulating matrix in order to achieve converging models,^{53,54} but this would certainly go beyond the scope of both this work, and our main goal to measure and improve the magnetolectric coupling in our sample sets via macroscopic measurement methods.

Instead, we can make assumptions based on our experimental work, in which we will deal with only two sample orientations, longitudinal and transverse, as previously discussed. If we apply these limitations to Eq. 2.65, it breaks down to a scalar equation. Using only the longitudinal case as an example, we arrive at

$$\alpha_{33}^L = c_{l,effective}^* \cdot q_l \cdot d_l \quad (2.67)$$

in which an applied electric AC field E_{AC} leads to the magnetolectrically induced magnetic moment $M_{ME,AC}$. In strain coupled multiferroics, we can thus write

$$M_{ME,AC} = c_{l,effective}^* \cdot q_l \cdot d_l \cdot E_{AC} \quad (2.68)$$

where d_l is the longitudinal piezoelectric coefficient of the ferroelectric phase while q_l is the equivalent piezomagnetic coefficient of the magnetostrictive phase.⁵² As before, due to the effective stiffness not being readily obtainable, it is common in experiments to use a simple proportionality between electric field and magnetic moment, such that

$$M_{ME,AC} \propto q_l d_l E_{AC} = \alpha_C E_{AC}. \quad (2.69)$$

Indeed, our determination of the converse ME effect is based on the straightforward proportionality that is offered by Eq. 2.57, summing up the proportionality from the respective coefficients into one overall parameter α_C that is used to judge the quality of the respective ME composite ceramic. As previously mentioned, we will not delve into higher order effects, as they are strongly overpowered by the linear effects in our samples. We can thus conclude that although

we may lack the detailed theoretical possibilities that other connectivity types would allow to be used, our composites, albeit complex and not straightforward to model, provide a simple and robust method of obtaining a good overall idea of the strength of magnetoelectric coupling.

3 Physical properties of the constituents

This chapter contains information on the basic crystalline, electric and magnetic properties of the sample systems that were examined in this thesis, providing insight as to why these systems were chosen for our studies to begin with. It will also provide references to the most important publications and gives a general overview of the current knowledge base for these systems and their advantages as well as the inherent problems associated with their use.

3.1 Bismuth ferrite

Bismuth ferrite, BiFeO_3 (BFO) has been a material of great interest for a long time, but until now, still has not seen any widespread use in applications. For the best overview from a single publication, I can recommend the extensive review by G. Catalan and J. F. Scott on the physics and applications of bismuth ferrite,⁶³ while Park et al.⁶⁴ provide the most detailed information on the influence of nanoparticle sizes on the properties of BFO. It is a G-type antiferromagnet up to a Néel temperature of 653 K,⁶⁵ often misquoted to be 640 K,⁶⁶ and is ferroelectric up to 1100 K,⁶⁷ placing its ordering temperatures high above room temperature. For application purposes, this means that we won't see any significant temperature dependent variation in electric and magnetic properties in the range around room temperature. It crystallizes in a rhombohedrally distorted perovskite crystal structure (space group $R3c$), which is generally regarded as the underlying structure behind its ferroelectricity. The Bi^{3+} and Fe^{3+} cations are displaced along the hexagonal $[001]$ axis, which leads to a spontaneous polarization in this direction. An overview of this crystal structure is given in Fig. 3.1.

The Fe^{3+} cations in BFO are characterized by a canted antiferromagnetic ordering, with a magnetoelectric coupling to the polarization having been identified as the cause for the small canting angle by Kadomtseva et al.,⁶⁸ who were the first to refer to the potential for BFO to become the "single phase, room temperature magnetoelectric 'holy grail'". One of the decisive Mössbauer works by Blaauw et al.⁶⁹ had already discussed that there must be some kind of inherent magnetic structure in addition to antiferromagnetism as such, discovered by nuclear magnetic resonance (NMR) and Mössbauer spectroscopy, which will be discussed in the results section. However, no complete characterization was possible at that time, and it was only much later that a long range ordering in the form of a cycloidal spin structure of the Fe^{3+} magnetic moments had been discovered by Sosnowska et al.,^{70,71} who characterized it in detail for the first time via neutron diffraction studies. It was thus known that this spin cycloid, which has a length of about 62 nm and is incommensurate with the crystal structure, propagates along the hexagonal $[110]$ direction, with the magnetic moments being located in a plane defined by the propagation direction and the polarization vector. This is shown schematically in Fig. 3.1,

with the magnetic moments being represented by arrows, revealing their rotation in the plane defined by the hexagonal $[110]$ axis (propagation direction) and the polarization axis $[001]$. This rotation is strongly exaggerated to more easily visualize this behavior. It is this spin structure and its magnetoelectric origin that our own Mössbauer studies will focus on.

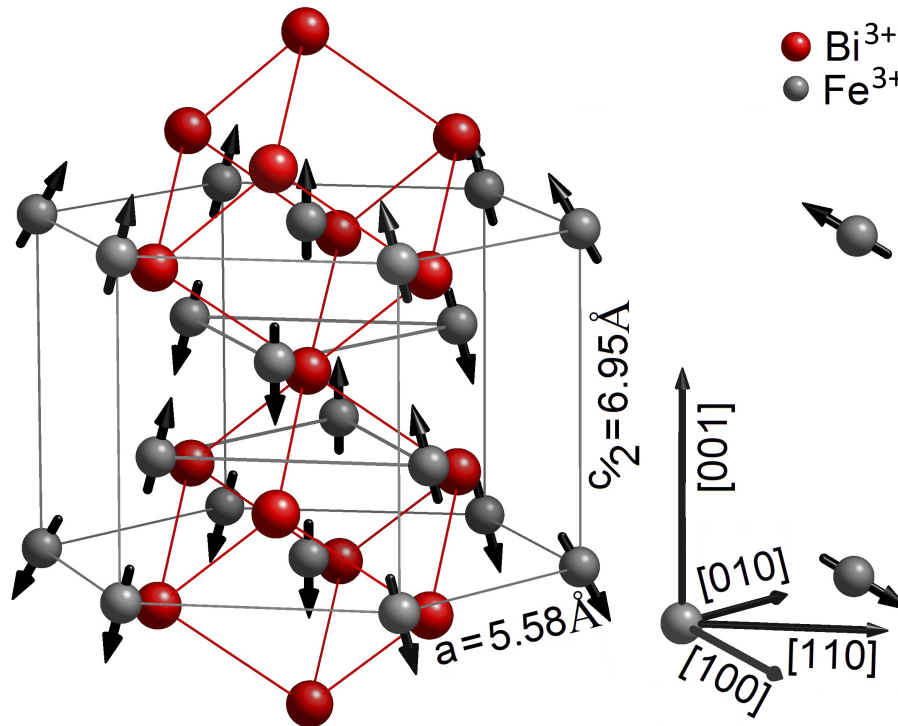


Figure 3.1: Crystal structure of BFO with arrows depicting the magnetic moments of individual Fe³⁺ ions and the (exaggerated) rotation of these while moving along the $[110]$ direction. O²⁻ ions have been omitted for clarity. Adapted from Ref. 72, reprinted with permission.

The main motivation for our use of nanoparticles was a number of recent publications that showed the magnetic properties of BFO to be significantly altered when in the form of thin films or nanoparticle samples, or in other words, when the dimensions are constrained so much that they approach the length of the cycloid.^{73–78} A number of explanations have been put forward, as we have summarized in our own publication,⁷² such as oxygen vacancy effects,⁷⁹ modified spin canting by lattice strain^{76,78,79} and uncompensated magnetic moments.⁶⁴ It was especially the latter publication by Park et al.⁶⁴ that discussed higher than expected saturation magnetizations of ca. $1.5 \text{ Am}^2/\text{kg}$ for nanoparticles with diameters smaller than 62 nm that seemed extremely promising. Spurred by these results, we were aiming to find the key to BFO with not just spontaneous polarization, but also magnetization, with the additional hope for the ability to use ferroelectric switching to influence the magnetic properties. Due to the fact that one of our samples had a mean diameter of 54 nm, we wanted to obtain a thorough understanding of the influence of the small particle size on the spin cycloid, which was to be achieved through a detailed Mössbauer study.

3.2 Cobalt ferrite

In order to understand the coupling phenomena of magnetoelectric composites, it's necessary to familiarize oneself with the basic properties of the main materials used. Cobalt ferrite, CoFe_2O_4 (CFO) is a very popular constituent in magnetic applications and thus also in magnetoelectric composites due to its high saturation magnetization, high coercive field and large magnetostriction. In the following, some light will be shed on its magnetic and structural characteristics.

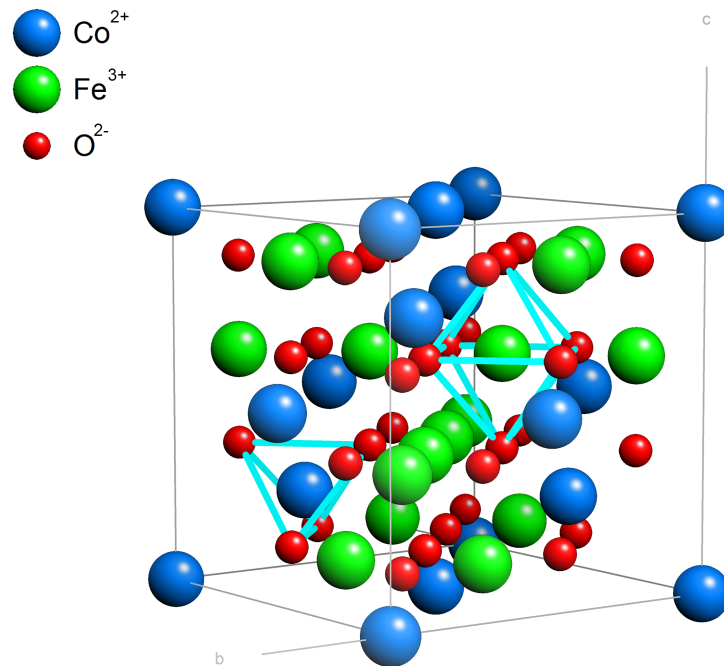


Figure 3.2: Crystal structure of CFO showing a Co^{2+} ion on an A- and a Fe^{3+} ion on a B-site, being tetragonally and octahedrally (blue lines) surrounded by O^{2-} ions, respectively.

CFO crystallizes as an inverse spinel (space group $\text{Fd}\bar{3}\text{m}$), corresponding to a cubic crystal structure with oxide anions arranged in a cubic close packed lattice (lattice parameter 8.392 \AA). As shown in Fig. 3.2, Fe^{3+} cations of the standard AB_2O_4 unit cell are placed on sites where they are either tetragonally (A-site) or octahedrally (B-site) surrounded by oxygen, with the distribution of the ions across these sites defining the degree of inversion. In a normal spinel, the Fe^{3+} ions are found only on B-sites, while an inverse spinel is characterized by Fe^{3+} ions being distributed equally across A- and B-sites. As the ferrimagnetic properties are dependent on the distribution of magnetic moments of the Fe ions across these two sites, it's obvious that the magnetic properties of a spinel system are strongly influenced by the degree of inversion.^{80,81} Below its relatively high Curie Temperature of 860 K , bulk-CFO is known to possess a long-range collinear order due to antiferromagnetic superexchange interactions. As described in detail by Kim et al.,⁸² there are several different types of exchange interaction in CFO that were characterized in detail via Mössbauer spectroscopy. For samples that were

cooled slowly during synthesis, giving them enough time to achieve thermal equilibrium for good crystalline ordering, the main interactions were represented by the intersublattice A-B superexchange interaction, as well as the intrasublattice A-A superexchange interaction, with respective strengths of $J_{AB} = -25 k_B$ and $J_{AA} = -19.8 k_B$. Generally speaking, Mössbauer spectroscopy is a valuable tool to determine not only exchange interactions in spinels but also to precisely determine their degree of spin canting and the inversion parameter. For bulk-CFO, these properties provide a positive first-order magnetocrystalline anisotropy constant K_1 of $2 \cdot 10^6$ ergs/cm³, greater than that of other spinel ferrites by about an order of magnitude. Furthermore, it has a high saturation magnetization⁸³ of 80 Am²/kg, in addition to a coercive field as high as 0.58 T.⁸⁴

If we want to look at the magnetic structure of CFO in detail, we can refer to the extensive Mössbauer studies of Kim et al.,⁸² who applied the Néel theory of ferrimagnetism to more closely understand the superexchange interactions intrinsic to this material. For a more general overview, there are a number of well-known publications that deal with superexchange interactions in ferrites.^{85,86}

Further interesting properties of CFO include hardness, resistance against mechanical wear, and quite critically, electrical insulation, making it suitable for application as constituent for a magnetoelectric composite. However, as we will see later on, the conductivity of this material is still sufficient to cause problems during our measurements. Going further down this route to usability, it has long been known that CFO has a relatively large saturation magnetostriction λ_{100} of $800 \cdot 10^{-6}$ as determined by Bozorth et al.⁸⁷ in their well-known 1955 review of anisotropy and magnetostriction in ferrites, allowing its use in strain-coupled systems, in which magnetically induced deformation of CFO is used to exert a force on another constituent at the respective interfaces. Conversely, a piezoelectric constituent can be used to apply forces to the CFO phase, inducing a net magnetization.

Furthermore, when dealing with CFO nanoparticles, size effects also come into play, with decreasing particle sizes leading to a lower high field magnetization due to strong surface spin frustration, as well as to a more complex size dependence of the coercive field.⁸⁸⁻⁹⁰ While this seems to go against our goals at first, nanoparticles also offer the advantage of providing a very large surface area per volume, with the goal being the maximization of the overall interface between CFO and a piezoelectric phase. However, as we will see in the synthesis chapter, particles are subject to agglomeration, which often hinders such efforts. The overall aim is therefore to make use of the advantageous properties of CFO for the formation of multiferroic composites, attempting to utilize nanosized particles to maximize the interface, while avoiding the shortcomings such as reduced magnetization and potential agglomeration.

3.3 Nickel ferrite

Used at the very end of our experimental history, nickel ferrite, NiFe_2O_4 (NFO), is rather similar to cobalt ferrite, with the obvious difference that the respective lattice positions are occupied by Ni^{2+} rather than Co^{2+} ions. It also crystallizes as an inverse spinel, with a similarly high Curie temperature of 858 K.⁸³ It's a soft magnetic material that shows some advantageous properties for ME applications, such as a high magnetomechanical coupling factor⁹¹ and a large change of field dependent magnetostriction. Latter is caused by the lower anisotropy constant for nickel ferrites ($K_{\text{eff}} = 1 \cdot 10^4 \text{ J/m}^3$)⁹² compared to cobalt ferrite ($K_{\text{eff}} = 1 - 4 \cdot 10^5 \text{ J/m}^3$),⁹² leading to fast magnetic alignment (low coercive field). Furthermore, the importance of the magnetomechanical coupling factor was only uncovered at a later stage of our research, which explains why NFO was only used in the last sample set that was evaluated.

3.4 Barium titanate

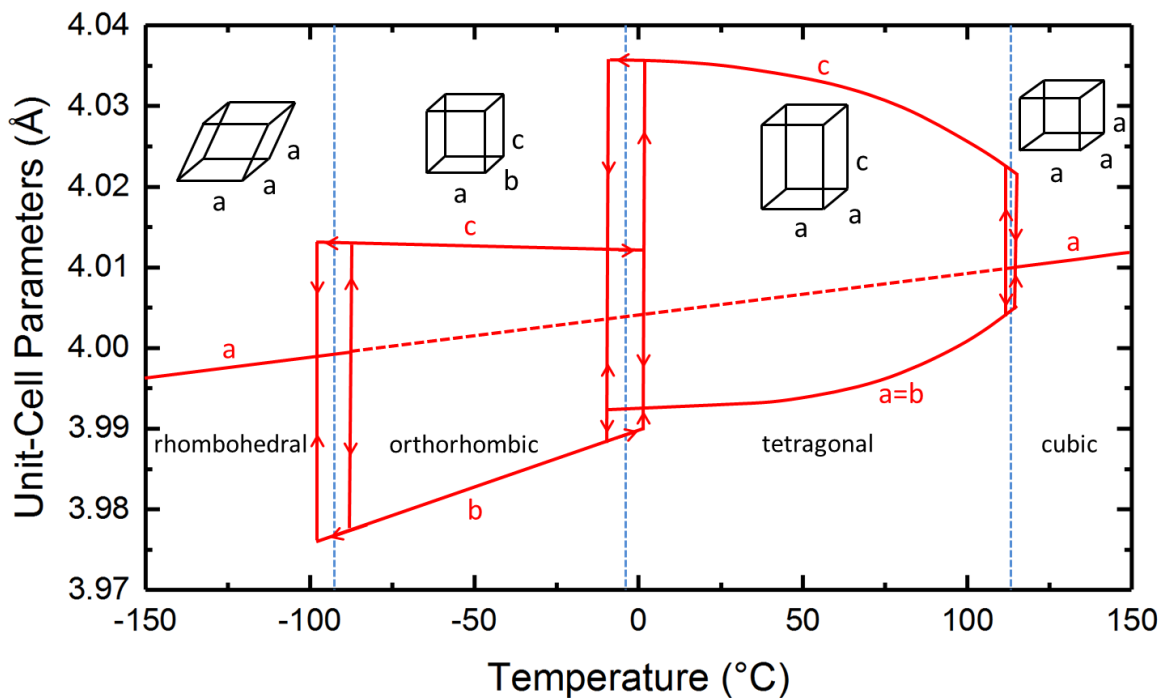


Figure 3.3: Variation of cell parameters with temperature in BaTiO_3 crystals, data taken from Ref. 93, reprinted with permission.

Barium titanate, BaTiO_3 (BTO), is a piezoelectric material with ferroelectric character, making it highly suitable for our use in magnetoelectric composites. It crystallizes in a perovskite structure, depicted in Fig. 3.4, with unit cell parameters consisting of $a = b = 3.992 \text{ \AA}$, $c = 4.036 \text{ \AA}$ and a tetragonality value of $c/a = 1.1011$, and undergoes a number of phase transitions in its bulk form, as shown in Fig 3.3. It is rhombohedral at temperatures below -90°C , orthorhombic from -90°C up to 5°C , tetragonal between 5°C and 120°C , and cubic above 120°C , as sum-

marized in Ref. 93. The high temperature cubic phase is of no interest for our purposes, as no spontaneous polarization exists in this phase, and although an external electric field can induce a polarization in the same direction, it reverts to zero when the field is removed. However, the tetragonal phase causes the Ti^{4+} ions to move in the $[001]$ direction, inducing a dipole moment in the unit cell. We can explain this microscopically by regarding the ionic radii of Ti^{4+} and O^{2-} : The sum of both radii is roughly 0.196 nm while the distance between the nuclei is 0.2005 nm, which means that there is a residual space between the ions of $4.5 \cdot 10^{-3}$ nm that allows for movement of the Ti^{4+} . It is this movement that allows for polarization along six possible $[001]$ directions, which means that the most interesting phase for ME applications is the tetragonal one. It furthermore covers the area near room temperature, which is of course highly practical from an application point of view. It is in this temperature range where most of our measurements on composite systems took place.

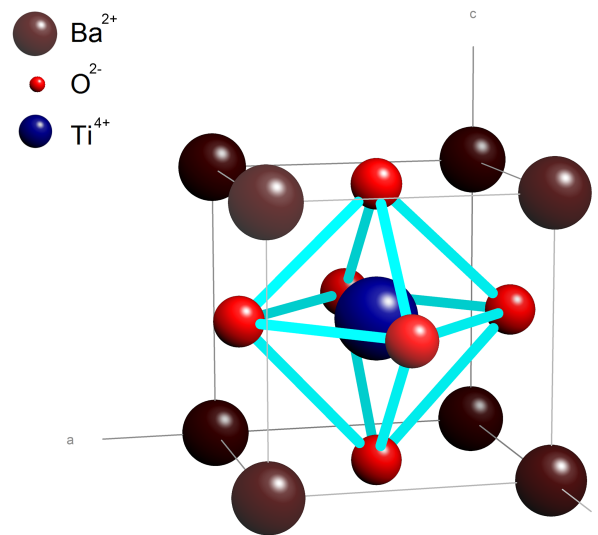
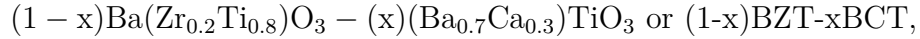


Figure 3.4: Crystal structure of BTO.

3.5 Barium calcium zirconate titanate

Used at a later stage in the experimental history behind this thesis, the barium calcium zirconate titanate $(\text{Ba,Ca})(\text{Ti,Zr})\text{O}_3$ or BCZT system was the result of BTO being doped with Ca and Zr ions, with the aim of modifying the phase boundaries described in the previous section (3.4). The main motivation behind its usage was the desire to obtain higher ME effects using different constituents, after the possible improvements to the classic CFO-BTO system through connectivity and morphology modifications seemed to have been exhausted. Another reason were the restrictions imposed on the usage of Pb-based piezoelectric constituents through the Restriction of Hazardous Substances Directive (RoHS) and European Union (EU) regulations, as explained in Ref. 94. This means that the well-known and excellent piezoelectrics $\text{Pb}(\text{Zr}_{1-x}\text{Ti}_x)\text{O}_3$ (PZT) and $(1-x)\text{Pb}(\text{Mg}_{1/3}\text{Nb}_{2/3})\text{O}_3 - x\text{PbTiO}_3$ (PMN-PT) as described in

Ref. 95 and 96, respectively, could not be utilized. While not of large concern for experiments, the Pb content would prohibit any use for application purposes. In a large number of rather recent publications,^{97–103} it was reported that a very high piezoelectric effect had been observed in the system



making it a very promising candidate for the replacement of pure BTO and an alternative to Pb-based systems as a piezoelectric constituent in ME composite ceramics. Its longitudinal piezoelectric coefficient d_{33} has been reported⁹⁷ to be over 600 pC/N, which is even higher than that of the Pb-based PZT^{97,104} and also higher than the 191 pC/N of BTO.¹⁰⁵

Like with BTO, we are also interested in the structural phase transitions that are intrinsic to this material, and its possible modifications. The phase transitions and their characteristic impact on converse ME measurements are a valuable tool not only to optimize the ME effect, as will be shown in section 4.7.1, but also allow us to check for any stray signals produced by conductivity effects that might lead to an 'apparent' ME coupling, as explained in 4.8.1.

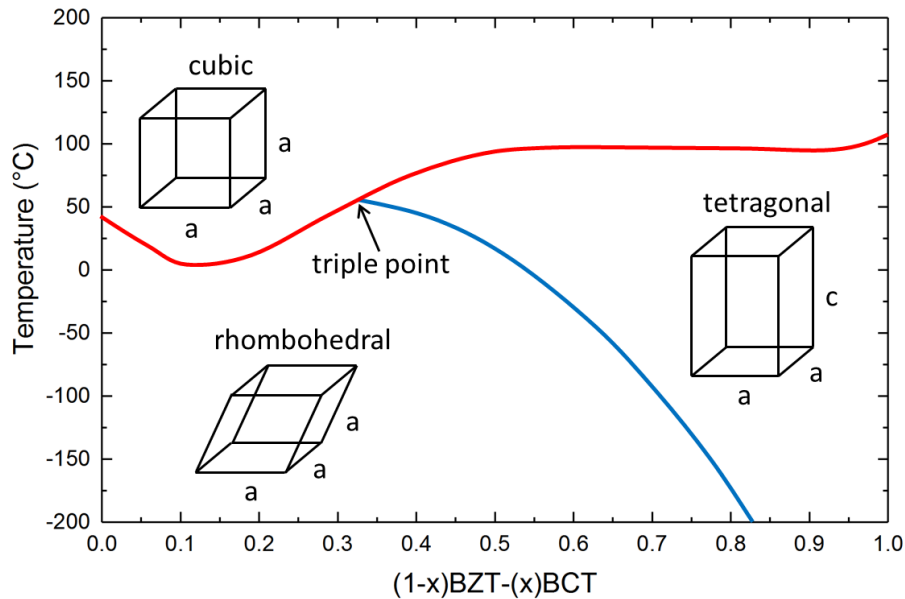


Figure 3.5: Temperature and composition dependent phase transitions of BCZT with polymorphic (red line) and morphotropic (blue line) phase boundaries, adapted from Ref. 106, reprinted with permission.

When regarding the influence of the dopants, it was found, with regards to the parent phase BTO, that the addition of Zr shifts the tetragonal-orthorhombic as well as the orthorhombic-octahedral phase boundaries towards higher temperatures. However, in case of solid solution that contains both dopants, these relations become more complex.^{104,107} We can visualize this by looking at the phase diagram shown in Fig. 3.5, which contains both polymorphic (red line)

and morphotropic (blue line) phase boundaries (MPB), with studies having been performed on the piezoelectric properties and energy barriers of ceramics with compositions near the MBP.⁹⁸ In literature, a polymorphic boundary is known to be driven by thermodynamic variables,¹⁰⁸ while a morphotropic boundary is driven mainly by the material's composition.

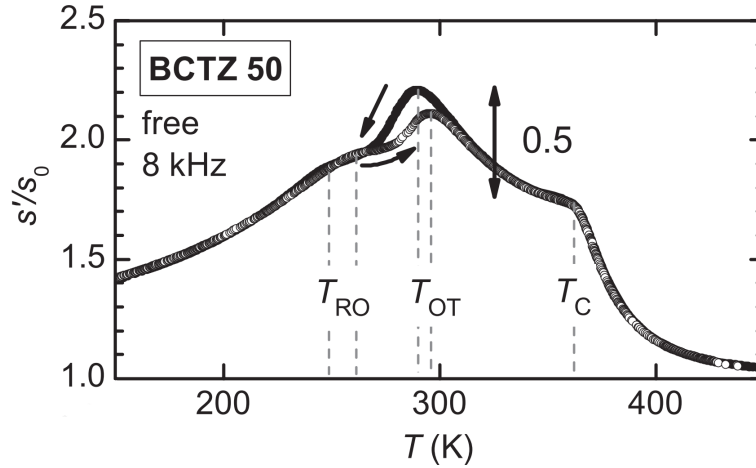


Figure 3.6: Temperature dependence of the elastic compliance of 0.5BZT-0.5BCT, taken from Ref. 109, reprinted with permission.

At this point, we refer to the work of Cordero et al.¹⁰⁹ who recorded the elastic response of BCZT with different compositions. They observed that the MPBs separate phases with different orientations of polarization, expecting to see exceptionally high piezoelectric activity near such boundaries. They remarked that the flattening of the free energy with respect to the polarization direction is responsible for the enhancement of the piezoelectric coefficient, as it was discussed in other works,^{110,111} while the precise mechanism is not quite clear yet. Two explanations were proposed: The existence of an intermediate monoclinic phase, allowing a continuous transition between the tetragonal and rhombohedral phase via a continuous rotation of the polarization,^{112,113} which was also elucidated in preceding works by Cordero et al.^{114,115} The other possibility is based on the notion that the monoclinic phase is adaptive, with mobile walls between rhombohedral and tetragonal domains that have extremely high density and mobility. While the previous explanation is based on an intrinsic property of the material, this explanation describes the increased piezoelectric coefficient via the extrinsic effect of easy wall motion.¹¹⁶ As such, this is a very wide ranging topic on its own, with a complete commentary not being possible within the scope of this thesis. Indeed, many reports have been published in the past few years, due to the importance of replacement materials for Pb-based piezoelectrics, with initial publications reporting on a rhombohedral-tetragonal border, attributing the crossing of this border to the high piezoelectric coupling at $x=0.5$, which corresponds to the composition we are going to use.^{97,117} This is at odds with the tetragonal-orthorhombic border that we know from BTO, which has been reported to be causing a more limited enhancement of piezoelectric coupling.¹¹⁸

In order to more closely monitor these phase transitions, which are also of interest for our work, Cordero et al. measured the elastic compliance of samples with different composition from $x = 0.45 - 0.55$, also including a sample with $x = 0.5$ that we will utilize. The elastic compliance is basically the mechanical analogue of the dielectric susceptibility, with the added advantage that it's not directly coupled to the polarization, thus not being dominated by the ferroelectric transition, thereby allowing a clearer insight into the nature of other underlying phase transitions. If we observe the results for the real part of the compliance obtained on BCZT($x = 0.5$) from Ref. 109, the tetragonal-orthorhombic phase transitions is clearly visible, with a small thermal hysteresis, caused by the direction in which the measurement was performed.

We can thus keep in mind that BCZT, while showing promising results in terms of its usability for our piezoelectric constituent, also displays a highly complex nature in terms of its structural phase transitions, with their immediate effect on the piezoresponse near said phase transitions not always being completely clear. Attention must be paid to the precise control of the composition, as any deviation will easily shift the phase transition temperatures. Fortunately, all of them are located within the close vicinity of room temperature, easily accessible by our converse ME setup and of good practical use for any future application purposes.

4 Scientific instrumentation

This section will deal with the devices and setups that were utilized in order to obtain the data, used for both the precharacterization of the precursor materials in the synthesis chapter 5, as well as for the characterization of the final ceramic samples and their structural, electronic, magnetic and finally multiferroic properties in chapter 6. This work is predominantly experimental in nature, and as such, a great emphasis is placed on the measurement methods that are exclusive to our group, such as Mössbauer spectroscopy and the converse ME measurement setup. Because of this, we need to make a distinction between the importance of certain measurement methods, and their role in this work, which is the result of long running cooperations that culminated in a number of publications.^{72,94,119–126} The majority of these are directly based on the results and measurements that will be presented here. As one would expect, a rather large number of methods and devices were used in our pursuit of fabricating and characterizing multiferroics. Describing all of them in detail would go beyond the scope of this thesis, wherefore the measurement methods exclusive to our own group are described in greater detail in section 4.2, as these were obviously the main scope of our work.

However, one method cannot be used purely on its own; it has to be complemented by other techniques for characterization of both precursor and finished sample materials, as well as for the purpose of crosschecking results. With this in mind, the main focus of this work will be on magnetometry, including the specialized setup for converse ME measurements, and on Mössbauer spectroscopy, which was used extensively in the initial part of our work on BFO nanoparticles, as well as for the characterization of some of the precursors for magnetoelectric composites. The remainder of the utilized characterization methods, most of them having been performed in the group of Prof. Lupascu, will be discussed and summarized briefly in the first section 4.1 of cooperative measurement techniques, to give sufficient insight into their workings, and to help properly understand the data that was obtained. The results of these methods will be outlined in the results section 6 alongside the Mössbauer and magnetometry data. At times, not all of the obtained measurement data is shown for certain sample sets, as some samples received more complementary measurements than others, with some results also being of higher significance than others.

Throughout this thesis, I will usually use the plural "we" when talking about the performance of experiments and the observation and evaluation of results. This is due to the fact that scientific research is never done alone, and to claim otherwise would be unfair for all those who contributed to this work. To briefly sum up the individual competences: The chemical synthesis of the used ferrites, as well as the formation of ceramic composites and their structural and electric characterization was performed in the group of Prof. Lupascu at the Essen campus. My

main points of contact were Dr. Marianela Escobar Castillo for the BFO sample set (section 6.1), Dr. Morad Etier for the CFO-BTO ceramics (sections 6.2.3 and 6.2.4) and Dr. Muhammad Naveed-Ul-Haq for the BCZT-based composites (sections 6.2.5 to 6.2.7). Our group of Prof. Wende at the Duisburg campus was mainly responsible for all magnetic characterizations that were performed during these cooperations. My main experimental contribution consisted of performing the numerous high and low temperature Mössbauer spectroscopy measurements (section 6.1), with support and guidance from Dr. Joachim Landers, while also undertaking standard magnetometry measurements. My most important contribution by far was the improvement and supervision of the converse ME setup (section 4.6), the execution of all of the converse ME measurements that are shown in section 6.2, their evaluation, and the continuous adjustment of the measurement methodology.

4.1 Cooperative measurement techniques

We start off with measurement techniques that were mainly utilized by or performed in conjunction with the group of Prof. Lupascu, with short descriptions to give sufficient insight into the basic workings of these methods.

4.1.1 X-ray diffraction

XRD is a standard method that was used in all of our collaborative works to check the structure and phase purity of both powder and ceramic samples, performed by both the groups of Prof. Lupascu and Wende, using a Siemens D5000 and Philips PW1730, respectively. In general, an XRD device contains a cathode ray tube to produce X-rays, with filters and collimators being utilized to produce a fine and monochromatic beam that can be used for experiments. For this purpose, both devices use Cu as the target material of the cathode ray tube, producing Cu-K α radiation with a wavelength of 1.5406 Å. This beam is aimed at the sample, with powder samples generally being affixed to a suitable substrate or pressed into disks for such measurements. As our samples are (poly)crystalline, containing regular arrays of atoms, the incoming X-rays are scattered by these, producing secondary waves from the interaction of the X-rays with the electrons, which is known as elastic scattering. If we assume a regular array of atoms, they will also produce a regular array of waves, which cancel each other out in most directions. To still be able to observe and characterize them, Bragg's law is utilized:

$$2d \sin(\theta) = n\lambda \quad (4.1)$$

It forms a relationship between the spacing of the diffracting planes d , the incident angle θ , and the wavelength λ , with n being an integer. This makes it necessary to modify θ , which is achieved by rotating the sample relative to the X-ray source, while the detector is also moved along by 2θ . The detector records the count rate at each angle, usually between 5° and 90°, as that's where most materials have all of their interesting X-ray peaks that are necessary for their evaluation. The evaluation of the spectra is often performed by comparing them to reference diffractograms found in literature, which of course always assumes a rough knowledge of the general chemical composition of the sample. With the constituents known, fitting procedures can be employed to clarify whether all peaks are accounted for by the constituents that the sample is supposed to contain, or whether there are ones that can't be fitted and point towards a parasitic phase.

Generally speaking, the diffraction pattern one obtains from XRD is determined partly by the crystal structure, with the makeup of the unit cell providing the positions of the diffraction lines at certain angles, while the arrangement of the different atoms within the crystal structure determine the relative intensity of the diffraction lines. This allows the simultaneous determina-

tion of structure and chemical composition, providing that the lines can be properly evaluated. This must not always be the case for very small crystallites, which lead to a broadening of the diffraction lines. In this case, the Scherrer equation can be used, which provides information on the size of crystallites or particles in the powder.

4.1.2 Microscopy methods

Microscopy is generally used in almost all of the publications that are the foundation of this thesis, as it allows a wide range of characterization methods and modes that provide a very comprehensive overview of local sample properties. With the range of microscopy methods used here, it was possible to characterize the sample morphology, crystalline ordering, as well as the electric and magnetic response to external fields. A short overview shall be given for each of the methods used in the following, with the two overall main types being divided between electron (SEM, TEM) and atomic force microscopy (AFM), with the latter containing subdivisions for electric (PFM) and magnetic field dependence (MFM). The main idea of these methods is to be able to resolve the microscopic structures, down to the nanometer range, which would not be possible with optical microscopy methods, as well as to probe the response to external fields.

SEM

Scanning electron microscopy relies on the interaction of the sample material with a focused electron beam, which is scanned over the surface of a sample in order to produce an image from the recorded signals.

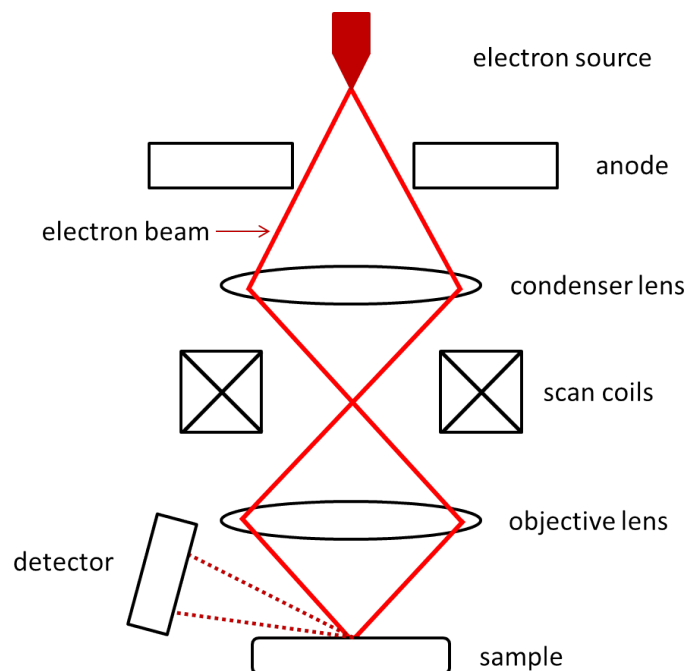


Figure 4.1: Schematic image of a standard SEM measurement setup.

These are made up of secondary as well as backscattered and transmitted electrons, and also characteristic X-ray lines and light emission. Depending on the type of emission that is to be detected, one can record and characterize different aspects of the sample. For example, elastically scattered electrons are usually utilized to profile the sample surface, while back-scattered electrons emerge from deeper within the sample, allowing one to determine the makeup of the sample up to a certain depth in terms of the distribution of different elements. A schematic image of a standard SEM setup is shown in Fig. 4.1.

Thanks to the highly focused beam, SEM has a large depth of field, similar in principle to a photographic lens being used with a very small aperture. The distinct 3-dimensional micrographs are very useful for the determination of nanoparticle shape and size distribution, as it will be shown for BFO samples in Fig. 6.2. SEM micrographs have also been recorded for CFO-BTO composite samples, as shown in Fig. 6.25, allowing the observation of the distribution of the CFO grains within the BTO matrix. The images shown in this work were recorded with a FEI Quanta 400 FEG, which has a maximum specified resolution of 2 nm.

TEM

Transmission electron microscopy, as the name suggests, is also based on the interaction of an electron beam with the sample matter, but is performed in transmission geometry. This technique was mainly used for the characterization of the BFO nanoparticles used in the first half of this thesis. For this purpose, the nanoparticles of the BFO study were deposited onto a TEM support mesh (grid) in order to be measured, which constitutes the standard method of sample preparation for this method. In addition to nanoparticle size and its distribution, TEM can also provide valuable data on the underlying crystal structure. With the correct settings, diffraction patterns can be produced, with a pattern of dots indicating a single crystal, while polycrystals produce a series of circles. TEM is therefore not only able to provide information about the size of our BFO nanoparticles, but also allowed us to check their crystallinity.

The TEM micrographs in the BFO section 6.1 were recorded with a Philips Tecnai F20 by Dr. Anna Elsukova from the group of Prof. Michael Farle.

AFM

Atomic force microscopy was used in three different modes during the course of this thesis, both in its standard form, as well as in conjunction with applied electric and magnetic fields. The standard form is utilized to characterize the topography of a sample using a nanometer sized probing tip attached to a flexible cantilever that acts like a spring, the deflection of which is measured using a laser and photodiode setup, as shown in Fig. 4.2. The interaction between the tip and the sample produces a deformation of the cantilever, which can be recorded and combined into a 3-dimensional image if the entire surface has been scanned.

There are several modes of operation, such as contact mode, lateral force mode or wave mode, differing mainly in how the height of the tip is regulated, which doesn't change the basic working principle. For our purposes, the main focus lies with the measurement of electric and magnetic field responses from the sample. Because of this, all samples were polished before these measurements, so that any influence from the topography could be ruled out. The basic mode of AFM was mainly used to search for certain grains, in order to later on check their response to applied electric and magnetic fields. In the case of measurements on BFO nanoparticles, they were embedded in epoxy resin which was then polished, so that individual particles could be selected and characterized (see Ref. 119).

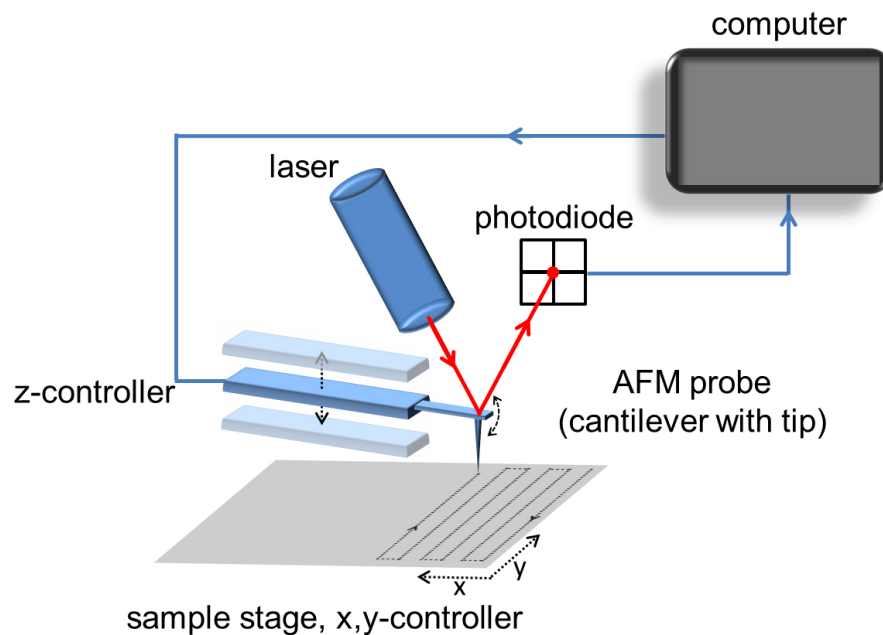


Figure 4.2: Schematic representation of a standard atomic force microscope setup.

PFM

Being a subgroup of AFM techniques, piezoresponse force microscopy allows the imaging of ferroelectric domains, representing a mixture between topographic and electric measurements. It's based on the converse piezoelectric effect present in a sample, using an AC bias voltage applied to a conductive probe tip to produce a deformation of the samples via the piezoelectric effect. Just as in the regular AFM, the tip height can be adjusted, allowing the measurement of both topography and piezoresponse at the same time. As a way to improve resolution, since the changes in terms of absolute length are in the range of tens of picometers per volt, a lock-in amplifier is used. The applied AC signal is modulated with a certain frequency, with the lock-in amplifier being sensitive to this frequency alone, thus being able to reject any environmental noise that may be present. Thanks to the ability to detect phase shifts between the driving voltage and the measured piezoresponse, it's possible to determine the direction of the piezoresponse und thus of the orientation of polarization.

MFM

The last of the microscopy methods is magnetic force microscopy, which is similar to PFM in terms of using the standard AFM setup as its base, while recording the influence of an applied magnetic field. This is achieved by the use of a sharp, magnetized tip being scanned over the surface of the sample, with the interaction between the magnetic moment of the tip and the magnetic stray field from the sample surface exerting a force on the tip and thus on the cantilever. For this purpose, the probe tips are usually coated with high coercivity materials such as Ni or Co, which are of course the same materials that are utilized in the ME composites studied here. The typical resolution is around 30 nm,¹²⁷ though one has to be careful regarding magnetic interactions between the sample stray field and the tip, and vice versa. In extreme cases, it can happen that the magnetic field of the tip undesirably influences the properties of a soft magnetic sample.¹²⁸ Furthermore, AFM methods in general are rather sensitive to the shape of the probe tip, requiring it to be of the correct geometry to be able to properly evaluate results. This is especially true for MFM, which is strongly affected by deformed or worn tips. In order to minimize these stray effects, it's good practice to keep the magnetization of the tip small, so that the disturbance of sample magnetization is kept to a minimum. Due to the fact that similar results can be obtained for different magnetic patterns, results from MFM must always be evaluated with caution. It's because of this that we consider our macroscopic ME data via the converse ME measurement setup to be so crucial.

4.1.3 Electrical characterization methods

This section deals with devices and setups that are used exclusively for macroscopic electrical characterization of the ceramic samples. This distinction is made due to the fact that certain microscopy methods such as PFM are used to probe microscopic electric properties, so the boundaries between structural and electrical characterization became a bit blurred in this case. Two main methods were utilized here, both of them being performed in the group of Prof. Lupascu: The recording of $P(E)$ loops, as well as dielectric measurements to determine the sample's permittivity.

P(E) loops by Sawyer-Tower method

A standard method for recording $P(E)$ loops is a Sawyer-Tower circuit, conceived by C. Sawyer and C. Tower in 1930.¹²⁹ There are other methods that can be used for this purpose, such as pulse-switching¹³⁰ or constant current polarization measurements,¹³¹ but in this work, only results from the Sawyer-Tower method are used.

The setup is technically straightforward, with the device used here being self-built by the group of Prof. Lupascu, shown schematically in Fig. 4.3. It is based on two capacitors being connected in series, with one of them having a known capacitance C_{ref} and being used as a reference (blue).

The other capacitor is represented by the sample (red), prepared in the same manner as for ME measurements, with silver paste electrodes attached to the top and bottom surface. A waveform generator is used to apply a triangular AC voltage in the frequency range of 5- 100 Hz through an amplifier, with both the input voltage and the measured voltage across the capacitors being recorded by a two channel oscilloscope. According to basic rules of electricity, while the voltage and capacitance need to be added as inverse values, the charge stored in the two capacitors must always be equal. One can therefore determine the charge Q in the unknown capacitor, in this case the sample, by using the voltage V_{ref} and capacitance C_{ref} of the reference capacitor, using the equation

$$V_{ref} \cdot C_{ref} = Q = V_{sample} \cdot C_{sample} \quad (4.2)$$

and thereby obtaining an expression for the polarization P

$$P = \frac{(V_{ref} \cdot C_{ref})}{A} \quad (4.3)$$

with A being the surface area of the sample that needs to be determined before or after the measurement. The $P(E)$ loops shown in the results section of the respective sample sets were recorded by plotting the applied electric field against the polarization. The only requirements to the setup are that one must keep the reference capacitance larger than that of the sample, in order to minimize the voltage drop at the sample.

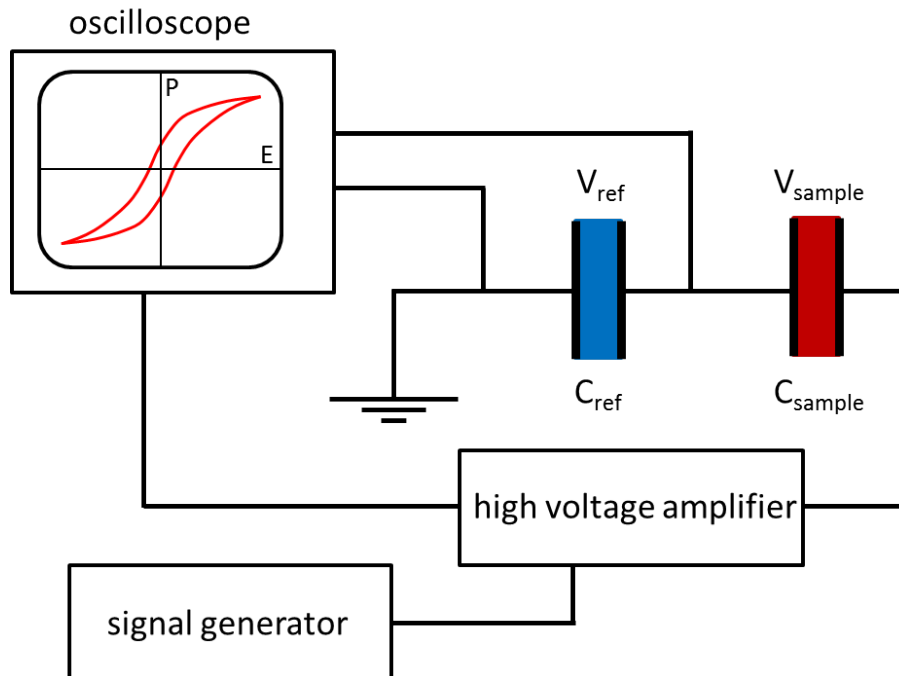


Figure 4.3: Schematic representation of the Sawyer-Tower setup used for the measurement of $P(E)$ loops, with reference capacitance (blue) and sample (red).

Dielectric measurements

In the same manner as it was done for the Sawyer-Tower method, we again use the capacitance of our contacted ceramic sample, though in this case, we need to observe that the capacitance can be expressed as a complex number in the form of $C^* = C' - iC''$ with C' being the real and C'' the imaginary part. We can then use the standard formula for the dielectric permittivity ε

$$\varepsilon = C \cdot \frac{d}{A} \quad (4.4)$$

with d being the thickness of the sample, representing the distance between the two electrodes that represent capacitor plates, just like in ME measurements (see section 4.7), while A again gives the surface area of the sample and its electrodes. Keeping in mind that the dielectric permittivity can also be written as a complex number, we can express it as

$$\varepsilon^* = \varepsilon' - i\varepsilon'' \quad (4.5)$$

The capacitance described above cannot be measured directly, but is determined through the value of the complex AC resistance, known as the impedance Z^* :

$$C^* = \frac{1}{j\omega Z^*} \quad (4.6)$$

In the same way as for DC resistance, we can write $Z^* = u/i$ with u and i being the complex valued alternating voltage and current, respectively. The ability to measure these parameters provides direct access to the real and imaginary part of the electric permittivity, which in turn enables the calculation of the low field electric permittivity $\varepsilon_r = \varepsilon'/\varepsilon_0$ as well as the loss tangent $\tan(\delta) = \varepsilon''/\varepsilon' = C''/C'$, two parameters that are routinely measured and compared for dielectric samples. It's a generally known rule in electrics that a capacitance shows a phase difference of 90° between current and voltage, with δ giving us the deviation from this rule, indicative of power loss or energy dissipation in the sample, hence the term loss tangent. Such measurements were mostly performed in the early stage of our studies, with the last sample set results concentrating more on the converse magnetoelectric effect in combination with PFM and MFM. Generally speaking, such studies are very commonly found in publications dealing with magnetoelectrics. In our case, a commercially available Solartron Impedance Analyzer with temperature control capabilities was utilized, with measurements being performed between 300 and 440 K at an electric frequency range of 1 Hz - 1 MHz.

4.1.4 Time of flight secondary ion mass spectroscopy

Although it was only used in one of our cooperative works,¹²⁶ TOF-SIMS produced very interesting results in terms of visualizing the 3D structure of samples with different compositions, enabling a very clear view of the changes in morphology and modification of connectivity. The contributions from Ba^{2+} and Fe^{3+} ions can be deconvoluted, making it possible to clearly dis-

tinguish between the two phases of the biphasic composite.

This method utilizes primary ions such as Au^+ that are accelerated towards the surface of a sample, usually at energies of several keV. These ions enter the sample and transfer their energy through collisions with the sample atoms, which then also collide among each other, leading to a cascade that carries a small part of the energy back to the surface, which in turn leads to the emission of electrons, neutral particles and secondary ions. It's these secondary ions that are relevant for our measurement, as they can be analyzed in terms of mass and charge using for example a time of flight mass spectrometer, but other methods such as quadrupole mass filters and sector mass spectrometers can also be utilized.

As made obvious by the large number of particles being ejected from the sample, this is a destructive method, essentially sputtering away sample material while measuring. Nevertheless, it's a highly sensitive method to profile the elemental composition of the sample surface, with the added benefit of depth selective measurements.¹³² These are achieved by the use of higher ion energies that led to an increased sputtering rate, so that the sample surface is removed in a controlled manner while continuing to record mass and energy data. In our measurements, the depth was profiled down to 200 nm into the sample, with the recorded 2D sweeps being combined into a 3D image of the sample's interior.

4.1.5 Measurement of the direct ME effect

The most interesting cooperative method in terms of comparability is the measurement of the direct magnetoelectric effect, which is the counterpart of the converse effect. This allows one group to crosscheck the results of the other, in case the samples are suitable for both methods. However, this setup is unfortunately limited to room temperature, and can thus not always be used at the temperature dependent maximum of the ME effect.

As depicted in the schematic diagram in Fig. 4.4, the sample is contacted on both sides, in the same way as for converse ME measurements, and placed in a small magnetic AC field coil that is located between the pole shoes of a large electromagnet. The former is used to apply a DC bias field in order to check the magnetic field dependence of the ME effect, while the small field coil is used to generate the measurement signal. The polarization of the contacted sample is recorded through a lock-in amplifier and evaluated by the computer used to control the setup. As we will see later on, this is akin to the converse ME setup, which uses the same principle, but applies an electric field while recording the magnetization with a lock-in amplifier. In both cases, any stray signals that do not match the frequency of the original AC field are ignored, leading to a strong reduction in noise.

The two basic measurement modes of this setup consist of the recording of $ME(H_{DC})$ curves to observe the behavior of the sample in large DC magnetic fields, while the dependence on the amplitude of the applied AC magnetic field $ME(H_{AC})$ allows the recording of polarization vs. field amplitude. In the case of the linear ME effect, this should result in a linear function, the slope of which provides direct access to the magnetoelectric coupling coefficient.

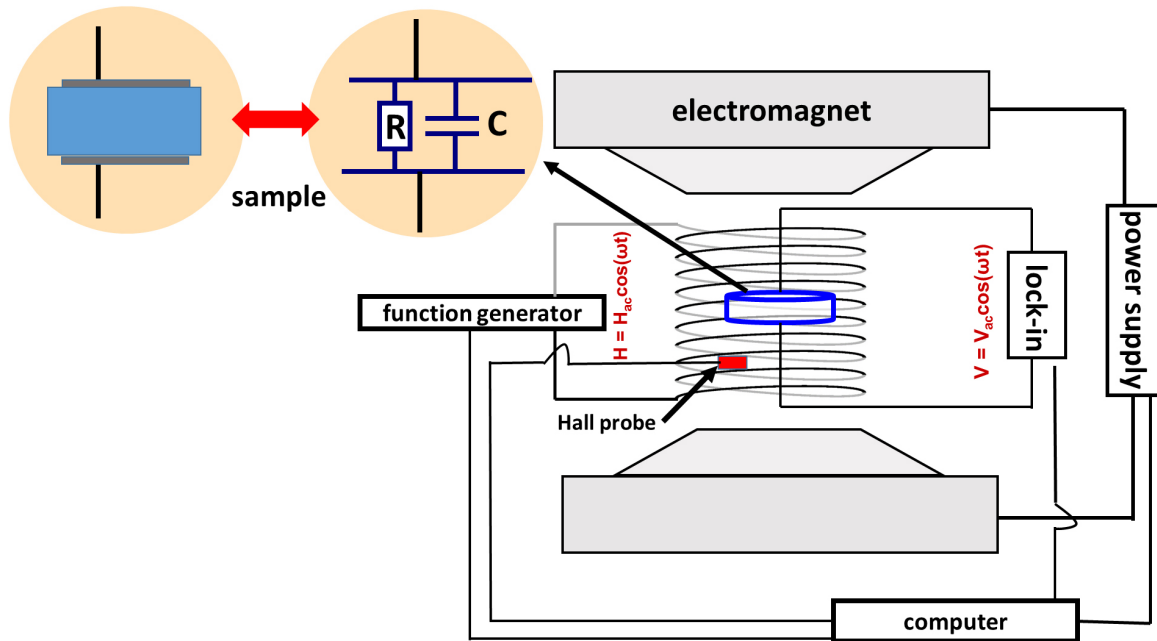


Figure 4.4: Schematic diagram of the direct ME measurement setup, with the sample being represented by its capacitance C and resistance R , taken from Ref. 45, reprinted with permission.

One drawback of this setup, apart from the lack of temperature control, lies in the necessity of the sample to have a high resistance, as it otherwise becomes impossible to measure the polarization. This is the reason for most of our works to rely on the converse setup, as some samples, like the ones prepared by spark plasma sintering, were rather leaky due to their low resistance. While the converse setup was able to cope with these, albeit with difficulties, no successful measurements of the direct ME effect were performed.

This concludes our short description of the cooperative measurement methods. The next section deals with the techniques that were used only by our group, namely Mössbauer spectroscopy and magnetometry, as well as the converse ME measurement setup. These will be described in greater depth, as they represent the core of our expertise. We will delve into the basic physical principles behind each measurement method in order to understand their principle of operation, and how the data has to be evaluated in order to arrive at the results presented in chapter 6.

4.2 Mössbauer spectroscopy: Theoretical framework

One of the principal methods used in this thesis is Mössbauer spectroscopy, an element-specific, non-destructive measurement method that utilizes the resonant emission and absorption of γ -rays to probe extremely small nuclear energy changes in the range of a few neV. It is named after Rudolf L. Mössbauer, who discovered this effect while working on his dissertation, titled "Kernresonanzfluoreszenz von Gammastrahlen in Ir191".¹³³ After his first observation of this effect, an experimental proof was obtained in 1958, for which he received the Nobel Prize in physics in 1961, together with Robert Hofstaedter. Following its discovery, the Mössbauer effect was used extensively in solid state physics, but also in material sciences, metallurgy, chemistry, geology and even archeology. One of the most prominent and well-known applications was in astronomy, with the inclusion of miniaturized Mössbauer spectrometers in the scientific payloads of the Mars exploration rovers *Spirit* and *Opportunity*, providing data that foreshadowed the discovery of water on the surface of Mars. Clearly, this is a very powerful method to probe deep into local properties, able to record fine structures resulting from the alignment and distribution of spins, which makes it highly suitable for the experiments that were performed in the course of this thesis.

The Mössbauer effect as such describes that there is a certain probability for γ -quanta to be emitted and absorbed by atomic nuclei without the associated loss of energy due to the conservation of momentum. This mechanism shall be explained in further detail in the following. In this work, we only deal with ^{57}Fe Mössbauer spectroscopy, and while the general descriptions are valid for all isotopes, the transitions and energy values mentioned here refer only to this widely used isotope. As a matter of fact, there are more than 100 isotopes in which the Mössbauer effect has been observed, but only a small number of these are realistically suitable for use in spectroscopy, partly due to some of the parent isotopes having very short half-lives, which poses logistical/financial problem of the source material activity decaying too rapidly for efficient usage. When regarding the excited state, $I = 3/2$ in the case of ^{57}Fe , an overly short half-life would lead to excessive line broadening. Conversely, undesirably long half-lives lead to lines that are too sharp and cannot overlap sufficiently, requiring much greater effort in terms of instrumentation in order to be recorded or evaluated.¹³⁴ The isotopes that are utilized by our lab are ^{57}Fe and ^{119}Sn , while ^{121}Sb and ^{125}Te are also common, in addition to a number of lanthanides. However, the overwhelming majority of publications usually deals with ^{57}Fe . This is due to the highly suitable half-life, sharp lines, long usage period, and due to the abundance of Fe in minerals with interesting magnetic properties such as ferrites, which themselves see very widespread technological and scientific applications.

The source material consists of ^{57}Co embedded in Rh, with the according nuclear transitions shown in Fig. 4.5. ^{57}Co , which has a half-life of 270 days, decays into an excited $I=5/2$ state

of 136 keV via electron capture, and can further decay to the $I=1/2$ ground state after an 8.7 ns half-life via two routes. One of those routes goes through an intermediate $I=3/2$ state of 14.41 keV with a 97.8 ns half-life.¹³⁴ This transition leads to the emission of the 14.41 keV γ -photons that we are interested in, with the mentioned half-life leading to a natural line width of ca. 5 neV, as it follows from the time-energy uncertainty equation:

$$\Delta E \Delta t \geq \frac{\hbar}{2} \quad (4.7)$$

This half-life can be considered as the sweet spot for our purposes, being neither too short, which would lead to excessive line broadening, nor too long, as this would prove difficult to measure with standard instrumentation, as mentioned previously.

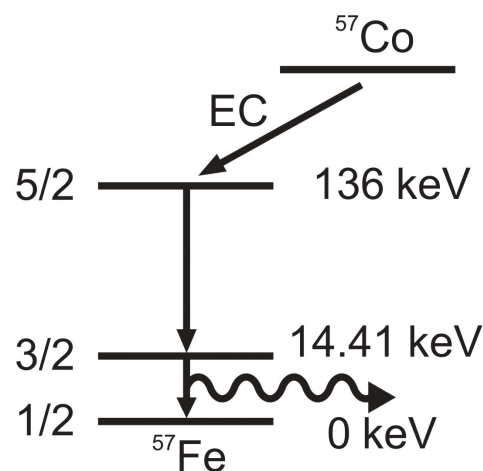


Figure 4.5: Decay scheme of ^{57}Co via electron capture (EC) to ^{57}Fe and associated emission of the 14.41 keV γ -photon used for Mössbauer spectroscopy.

For easier understanding, the quantum mechanical Mössbauer effect can be described through classical mechanics, assuming atoms that can freely move: During the emission of a γ -photon from the nucleus, the conservation of momentum stipulates that any momentum of the emitted photon must also be transferred to the nucleus. This is comparable to the recoil of a gun, which moves in the opposite direction upon being fired, albeit to a much lesser extent than the bullet, due to the greater mass of the gun. The same happens to the nucleus, it moves in a direction opposite to the emitted photon due to the recoil. Because of this, the energy of the photon is lowered by the amount of energy that was transferred to the nucleus. This poses a problem: In order to perform actual spectroscopy measurements, the photon has to be absorbed by a nucleus of the same element as the one it was emitted from. But if the energy of the photon has been reduced by the recoil energy, the total energy carried by the photon will not be sufficient to be absorbed by the other nucleus. This is shown schematically in Fig. 4.6.

If we want to quantify this problem, a few simple equations can be used to put these energies in relation to each other. We define E_R as the recoil energy received by the nucleus, causing

the original emitted γ -photon energy E_0 to be reduced by E_R , giving the actual energy of the emitted photon $E_{\gamma e}$. In the same manner, the energy of an incoming photon, if it is to be absorbed by a nucleus, must contain the energy E_R in addition to its original energy E_0 in order to be absorbed despite the transfer of momentum to the nucleus.

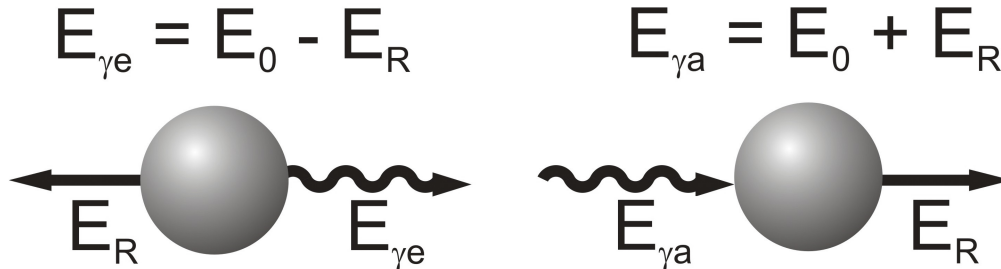


Figure 4.6: Schematic representation of the transfer of momentum during the emission (left) and absorption (right) of a γ -quantum by a nucleus. Adapted from Ref. 135.

To deduce this relation, we define the initial energy E_i prior to emission using the energy of the excited nucleus E_e , its impulse p and mass M :

$$E_i = E_e + \frac{p^2}{2M} \quad (4.8)$$

Accordingly, the final energy E_f after emission with the nucleus in the ground state E_g can be written as

$$E_f = E_g + \frac{(p - \hbar k)^2}{2M}. \quad (4.9)$$

The impulse of the γ -photon is given by $\hbar k$, with the energy difference being

$$E_i - E_f = \hbar\omega = \hbar\omega_0 + \hbar(k \cdot v) - \frac{\hbar^2 k^2}{2M}. \quad (4.10)$$

Here, $\hbar(k \cdot v)$ is the velocity dependent Doppler-effect, which takes on values in the range of 0 - 10^{-2} eV. When inserting the mass of a ^{57}Fe nucleus for M into the recoil term $\frac{\hbar k^2}{2M} = \frac{E_0^2}{2Mc^2}$, the problem becomes apparent: The recoil term takes on the value of $2 \cdot 10^{-3}$ eV, which is 6 orders of magnitude higher than the natural line width of the γ -photon energy (Eq. 4.7). As a result, almost no absorption can be expected. Another way to display this problem is by usage of the emission and absorption line, calculated by usage of the Breit-Wigner-equation, taking into account the mentioned natural line width caused by the underlying energy uncertainty. Absorption can only occur when there is an overlap between the two lines, but when we consider our result of the energies being pushed apart by 6 orders of magnitude relative to their line width, it's obvious that the probability for absorption processes is rather low.

Now we arrive at the quantum mechanical phenomenon that allowed Mössbauer to overcome this problem. During his experiments, he tried to heat up his samples, thinking that the

additional, thermally induced motion of the nuclei would help to reintroduce the energy to the system that was lost to recoil, thus increasing the rate at which absorption takes place. However, the results contradicted his findings. It was in fact when he cooled his sample down that the absorption rate went up. As it later turned out, this is due to quantized lattice vibrations, phonons, which can only take on discrete energy values. In the case of a recoil energy that has no matching phonon energy, no transfer of momentum takes place, and the photon is emitted with no energy loss, the same being valid for the absorption process. This is thus referred to as resonant absorption, or recoilless nuclear resonance, with the probability for this process taking place being given by the Debye-Waller factor, also used to define the ratio of elastic diffraction in X-ray studies. In Mössbauer spectroscopy, the analogous factor is often referred to as the Lamb-Mössbauer factor, or simply f-factor. Described by Eq. 4.11, it denotes the fraction of γ -emissions or absorptions occurring without recoil, also known as the recoil free fraction,¹³⁴ with the wave number k of the γ -photons and the mean square atomic displacement $\langle x^2 \rangle$ giving us

$$f = e^{-k^2 \langle x^2 \rangle}. \quad (4.11)$$

Now that the basics of the Mössbauer effect have been elucidated, we can turn to the actual, practical application, which is not concerned with the observation of the Mössbauer effect as such, but with the effects caused by the interaction of the sample's internal electric and magnetic fields with the energy of the nuclear states. Due to the extremely small energies in the neV range that define these effects, they are commonly known as hyperfine interactions. These enable us to observe and evaluate the variation of nuclear energies, which in turn makes it possible to characterize these in dependence of factors such as temperature, particle size and composition etc. The three main types of interaction will be described here, using theoretical spectra that only possess one type of interaction, to clearly show the kind of effect each of these interactions has on the spectral shape. In reality, it is of course common that these effects appear superimposed, often requiring the use of several subspectra for evaluation. Hence, the spectra shown here, with fixed, idealized parameters, are used only for clarity, not to represent actual samples.

4.2.1 Isomer shift

As the name suggests, this effect causes the entire spectrum to be shifted along the velocity (energy) axis, the designation of which will be explained in the description of the experimental measurement technique. The basic cause of this phenomenon is the different local surroundings of ^{57}Fe nuclei in the source and absorber material. One usually refers to the isomer shift as the energy difference between two identical nuclei that have the same charge and mass, but are in different nuclear (excitation) states.

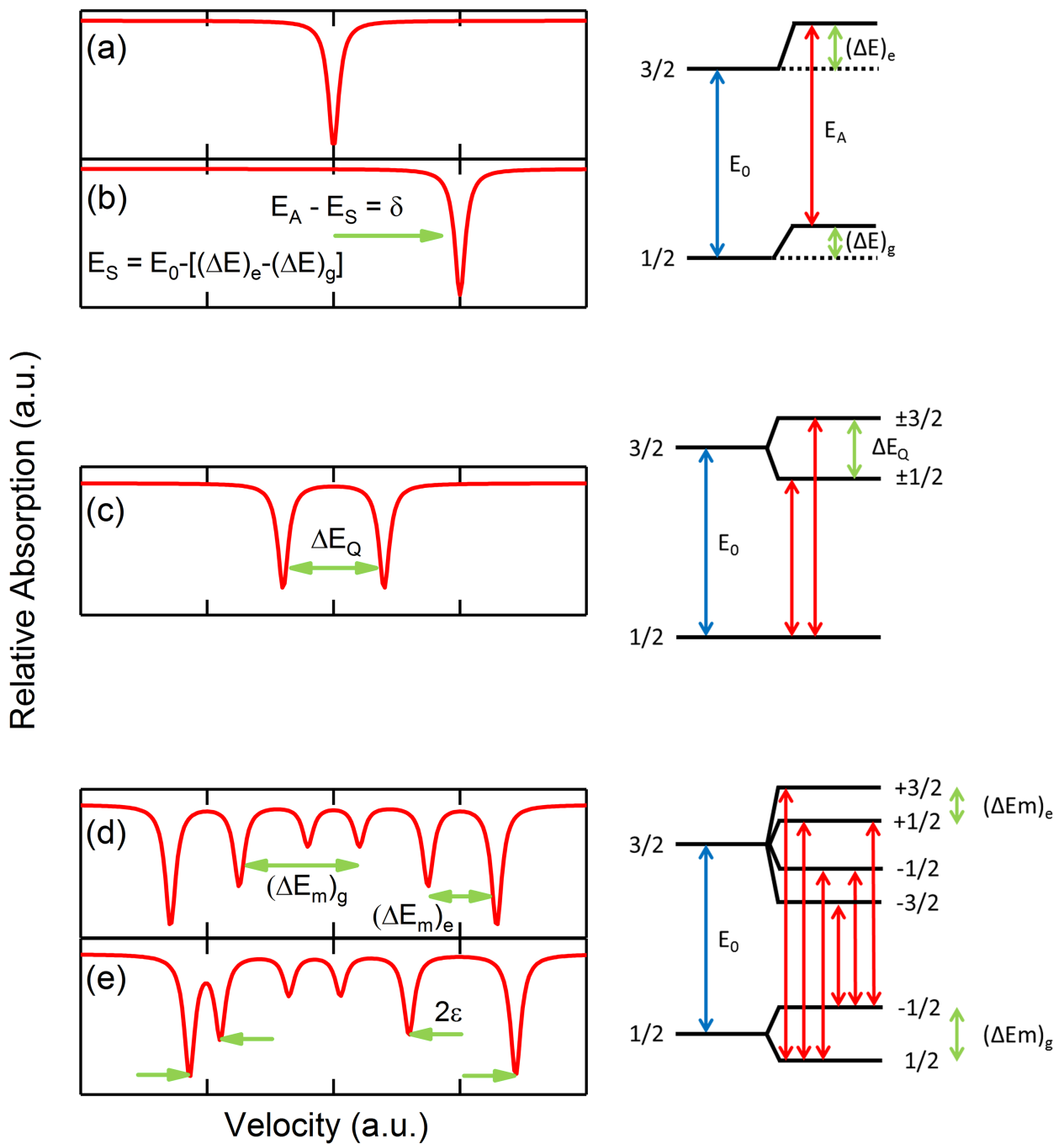


Figure 4.7: Schematic representation of the effect of hyperfine interactions on Mössbauer spectra (strongly exaggerated for clarity), showing no interaction (a), electric monopole interaction (b), electric quadrupole (splitting) interaction (c), magnetic dipole interaction (d) and magnetic dipole interaction under the influence of electric quadrupole (shift) interaction (e). Adapted from Ref. 135.

This is mainly due to the fact that nuclei in excited and ground states have different radii, which in turn influences the interaction with the local potential of the electrons. To obtain a mathematical relation, one has to first consider the basic electric interaction and the interaction energy that follows from it. Using the route described by Barb,¹³⁵ we regard the charge of the nucleus $\rho(r)$, which is inside an electric field, described by the potential $V(r)$, with the origin of the coordinate system being inside the nuclear charge distribution. The classical formula for the interaction energy between this charge distribution and potential can be written as

$$E = \int \rho(r)V(r)d\tau \quad (4.12)$$

with τ being the volume element while integration is performed over the entire space in which $\rho(r)$ is defined. If we assume that the electric field produced by the potential $V(r)$ weakly varies within the distribution defined by $\rho(r)$, we can perform an expansion of $V(r)$ in a Taylor series around the coordinate origin of r , giving us

$$V(r) = V(0) + \sum_{\alpha} X^{\alpha} \left(\frac{\partial V}{\partial X^{\alpha}} \right) + \frac{1}{2!} \sum_{\alpha, \beta} X^{\alpha} X^{\beta} \left(\frac{\partial^2 V}{\partial X^{\alpha} \partial X^{\beta}} \right) + \dots \quad (4.13)$$

with X^{α} with $\alpha = 1, 2, 3$ being the Cartesian coordinates x, y and z . Utilizing the approach of substituting

$$V_{\alpha} = \left(\frac{\partial V}{\partial X^{\alpha}} \right)_0, \quad V_{\alpha\beta} = \left(\frac{\partial^2 V}{\partial X^{\alpha} \partial X^{\beta}} \right)_0 \quad (4.14)$$

we arrive at the interaction energy in the form of

$$E = V(0) \int \rho(r)d\tau + \sum_{\alpha} V_{\alpha} \int X^{\alpha} \rho(r)d\tau + \frac{1}{2!} \sum_{\alpha, \beta} V_{\alpha\beta} \int X^{\alpha} X^{\beta} \rho(r)d\tau + \dots \quad (4.15)$$

This term can now be further simplified by the following assumptions: The first member represents the electrostatic energy of the point-shaped charge of the nucleus, which is of no interest here, as it doesn't have any effect on the splitting or shift of different nuclear levels. The second member contains the electric dipole moment of the nucleus, but the integral becomes zero due to symmetry, under the condition that $\rho(r)$ is an even function, which is logical when starting at the origin of a charge density of a point charge. The third, most interesting member, consists of the electric quadrupole term:

$$E = \frac{1}{2} \sum_{\alpha, \beta} V_{\alpha\beta} \int X^{\alpha} X^{\beta} \rho(r)d\tau \quad (4.16)$$

By the addition and subtraction of $\frac{1}{3} \delta_{\alpha\beta} r^2 \rho(r)$, which is independent of the orientation of the nucleus, we arrive at the energy term

$$E = \frac{1}{6} \sum_{\alpha, \beta} \left[\int (3X^{\alpha} X^{\beta} - \delta_{\alpha\beta} r^2) \rho(r) + \delta_{\alpha\beta} V_{\alpha\beta} \int r^2 \rho(r)d\tau \right]. \quad (4.17)$$

Following these deductions, we can now regard the groundwork for the isomer shift. For this, we again regard a potential $V(r)$ caused by electric charges such as electrons, which permeate the nucleus, and can be described by the Poisson equation

$$\sum_{\alpha} V_{\alpha\alpha} = -4\pi q |\Psi(0)|^2. \quad (4.18)$$

Here, q is the inner charge and $|\Psi(0)|^2$ the probability density of the charges q near the nucleus. Using this relation, the second member of 4.17 can be simplified down to

$$E_D = -\frac{2\pi}{3} Z q e |\Psi(0)|^2 \langle R^2 \rangle \quad (4.19)$$

with

$$\langle R^2 \rangle = \frac{1}{Z} \int r^2 \rho' d\tau, \quad \rho' = \frac{\rho}{e} \quad (4.20)$$

giving us the mean square nuclear radius, Z the nuclear charge and ρ' the number of electric charges per volume unit. A further obvious assumption that can be made here is that q is of course e , the charge of an electron, enabling us to write its interaction with a spherical and homogeneously nuclear charge distribution through the equation

$$E_D = -\frac{2\pi}{3} Z e^2 |\Psi(0)|^2 \langle R^2 \rangle \quad (4.21)$$

We arrive at an important and decisive conclusion: The interaction we have now described leads to a shift of the nuclear energy level, which takes on different values for nuclei that have the same total charge, but are subjected to different distributions of electric charges that permeate the nucleus. The same is also true for two nuclei that have the same charge but different masses, or are equal in all terms except for being in different nuclear states, as can be witnessed in isomers. Using s to represent the source and a the absorber material, and e and g to denote excited and ground state, respectively, the isomer shift

$$\delta = E_s - E_a \quad (4.22)$$

can be written as

$$\delta = [(E_D)_e - (E_d)_g]_s - [(E_D)_e - (E_D)_g]_a. \quad (4.23)$$

One can further assume that $\langle R^2 \rangle$ is not dependent on the surrounding of the nucleus, while $|\Psi(0)|^2$ is independent of its excited state, the equation can be written in its well-known textbook form

$$\delta = \frac{2\pi}{3} Z e^2 S(Z) [\langle R^2 \rangle_e - \langle R^2 \rangle_g] [|\Psi(0)|_a^2 - |\Psi(0)|_s^2]. \quad (4.24)$$

Here, $S(Z)$ is a relativistic factor, which can be obtained from tables for the respective isotopes, with $S(26) = 1.32$ for Fe.^{135,136} It's important to note that, as is visible by the derivations above, we never measure the isomer shift of a single material, as δ is always a difference value of the interaction energies from the emitting and absorbing nucleus. In order to be able to make comparisons to literature values, some kind of standard needs to be established for the isomer shift to be referenced against. This is achieved by calibration of the spectrometers using an α -Fe sample, which enables the scaling of other spectra to this value. This allows one to normalize them to zero, as also described in the experimental section 4.3.

Even more important is what we can obtain from the observation of the isomer shift: The direct dependence of δ on the electron density $|\Psi(0)|^2$ is mostly carried by s-electron interactions, as these are closest to the nucleus. Nevertheless, due to electron screening effects from p- and d-shells still significantly influencing the s-electrons, one can obtain information on the valence state and chemical bonding, among others. A popular application is the differentiation between Fe^{3+} and Fe^{2+} , with the different valence states leading to different isomer shifts, enabling, for example, the separation of spectral contributions from magnetite and maghemite. Generally speaking, a decreasing isomer shift is indicative of an increase of the s-electron density in the sample being observed, which points towards an increase in electronegativity in the direct surrounding. An obvious example would be the task to decide which of two samples is made up of pure iron and which one contains iron bound to electronegative elements such as chlorine.

In general, we can use the isomer shift to observe any changes in the binding, valence state and surrounding of the Fe-atoms in our sample, in addition to the less commonly studied difference in nuclear radii due to different nuclear states in emitter and absorber. In this work, the isomer shift will only play a minor role, being used mainly to observe any unwanted changes of the sample's chemical composition during the progression of high temperature measurements. The choice to include the entirety of the derivation was made due to the fact that it is also necessary for the explanation of the quadrupole interaction, as shown in the next section.

An additional modification of the isomer shift, or rather, the shift of the centroid of the Mössbauer spectrum we need to keep in mind that isn't caused by the change of the chemical surrounding of the sample, but by the thermally induced motion of the nuclei in the sample material (thermal redshift), called the second order Doppler shift.¹³⁴

4.2.2 Quadrupole interaction

To establish the groundwork for the electric quadrupole interaction, we can use the first part of our previous derivations and take Eq. 4.17 as a starting point. First, we assume that the Laplace equation is valid for the case of a potential V outside of the charge distribution $\rho(r)$,

so that we can write

$$\sum_{\alpha} V_{\alpha\alpha} = 0. \quad (4.25)$$

This cancels the second term of Eq. 4.17 so that we are left with the interaction energy of a nucleus with the potential of an external charge distribution:

$$E_Q = \frac{1}{6} \sum_{\alpha,\beta} V_{\alpha\beta} \int (3X^{\alpha}X^{\beta} - \delta_{\alpha\beta}r^2)\rho(r)d\tau \quad (4.26)$$

Using the quantum mechanical route, we need to replace the classic density function $\rho(r)$ with the quantum mechanical operator, so that

$$p(r) \rightarrow \hat{\rho} = \sum_p \delta(r - r_p) \quad (4.27)$$

with a summation over all nucleons $p = 1, \dots, n$ while e_p can take on the value e for protons and zero for neutrons. With this, we can define our Hamilton operator, which is simplified to

$$\hat{H}_Q^{hf} = \frac{e}{6} \sum_{\alpha\beta} V_{\alpha\beta} \sum_p (3X_p^{\alpha}X_p^{\beta} - \delta_{\alpha\beta}r_p^2) \quad (4.28)$$

if we take into account the properties of the delta function. A number of assumptions need to be made from here onwards, but the full derivation would take up considerable space. Instead, we refer to page 113 in Ref. 135 for the simplifications made to Eq. 4.28 by the usage of the Wigner-Eckart theorem to express the matrix elements of the tensor operators. In the end, we arrive at the term

$$\hat{H}_Q^{hf} = \frac{eQ}{4I(2I-1)} \left[V_{zz}(3I_z^2 - I^2) + \frac{1}{2}(V_{xx} - V_{yy})(I_-^2 + I_+^2) \right] \quad (4.29)$$

using the tensor of the electric field gradient $V_{\alpha\beta}$, which, with the appropriate coordinate system (x,y,z) , can be written in diagonal form, using only the non-zero components V_{xx} , V_{yy} and V_{zz} . I is the nuclear spin quantum number, while I_{\pm} are shift operators, with I_z being the operator of the nuclear spin projection onto one of the principal axes. Using the asymmetry parameter

$$\eta = \frac{V_{xx} - V_{yy}}{V_{zz}} \quad (4.30)$$

the operator can be further simplified to

$$\hat{H}_Q^{hf} = \frac{eQV_{zz}}{4I(2I-1)} \left[3I_z^2 + I(I+1) + \frac{\eta}{2}(I_+^2 + I_-^2) \right] \quad (4.31)$$

with Q denoting the nuclear quadrupole moment and V_{zz} representing the z component of the electric field gradient, with the entire term eQV_{zz} often being referred to as the nuclear quadrupole coupling constant. In its general form, Q is an irreducible second rank tensor,

however, the nuclear charge distribution has cylindrical symmetry, allowing its use in scalar form. Furthermore, in our case, the excited state of ^{57}Fe has a nuclear spin of $I = 3/2$, allowing us to write our equation as

$$\Delta E_Q(I = 3/2, m_I) = \frac{eQV_{zz}}{4I(2I + 1)} [3m_I^2 - I(I + 1)] \sqrt{1 + \frac{\eta^2}{3}} \quad (4.32)$$

with the magnetic quantum number m_I . If we assume the simplest case of an axial electric field gradient, it brings the asymmetry parameter to zero and we end up with

$$\Delta E_Q(m_I) = \frac{eQV_{zz}}{4I(2I + 1)} [3m_I^2 - I(I + 1)]. \quad (4.33)$$

So in essence, for experimental purposes, this derivation and the final equation describe the following: If a nucleus has a nuclear quadrupole moment Q , which is the case if the nuclear spin is greater than $1/2$, and if there is an inhomogeneous electric field at the nucleus (electric field gradient is non-zero), then we will see a precession of the quadrupole moment around the axis of the electric field gradient. This causes a splitting of the $I = 3/2$ level into two sublevels with the magnetic quantum numbers $m_I = \pm 3/2$ and $\pm 1/2$. It is the energy difference between these two states that is given by ΔE_Q from the equation above, which, in the absence of nuclear Zeeman splitting, is characterized by the splitting of a single absorption line into a doublet, with the energetic distance between the two lines given by ΔE_Q . In general, the quadrupole splitting is of great importance for chemical applications of the Mössbauer effect, providing information on bond properties and local symmetry of the iron site. This is easily understood when considering that for example the electric field gradient as such is being generated by valence electrons not conforming to cubic symmetry.

However, for our purposes, the main objective of the detailed measurement of quadrupole interaction lies in the connection between this electronic property and the magnetic characteristics of our sample system. To gain more understanding on this, we need to look at the third form of hyperfine interaction found in Mössbauer spectroscopy, explained in the following.

4.2.3 Magnetic interaction

There are several names by which this interaction is known, such as magnetic dipole interaction, magnetic splitting, nuclear Zeeman splitting and so forth. It's arguably the most important of the three when considering that it's the only one directly providing us with information regarding the magnetic state of the sample, with magnetically ordered ferro-, ferri- and anti-ferromagnets producing a characteristic sextet structure in their absorption lines, while para- and diamagnetic materials produce doublets or singlets, depending on presence or absence of quadrupole interaction.

The derivation of the appropriate notation is a bit shorter than for the electronic interactions. We can use the Hamiltonian¹³⁴ that describes the interaction of a nucleus with a spin quantum number $I > 0$ interacting with a magnetic field via its magnetic dipole moment μ :

$$\hat{H}_m^{hf} = -\hat{\mu} \cdot \hat{B} = -g_N \mu_N \hat{I} \cdot \hat{B}. \quad (4.34)$$

Here, B represents the magnetic induction, g_N the nuclear Landé factor and $\mu_N = e\hbar/2M_p c$ as the nuclear magneton using the proton mass M_p . If we diagonalize the Hamilton matrix, we end up with the eigenvalues:

$$E_M^{hf} = -\mu B m_I / I = -g_N \mu_N B m_I \quad (4.35)$$

This interaction is present as soon as the nuclear spin quantum number I is at least $1/2$, which is valid for both the ground state $I=1/2$ as well as the excited state $I=3/2$ for ^{57}Fe . The effect of the interaction is the splitting of the nuclear state I into $2I + 1$ equally spaced, non-degenerate substates, characterized by the sign and magnitude of the nuclear magnetic spin quantum number m_I .¹³⁴ If we observe the schematic Mössbauer spectrum in Fig. 4.7 (d), we can see that the ground state is split into two magnetic substates, while the excited state is split into four. Due to the dipole selection rule $|m_I| \leq 1$, we end up with a total of six allowed transitions from eight possible ones, with their energy differences being directly responsible for the line positions in the Mössbauer spectra.

What we can also see from Eq. 4.35 is that the magnitude of the splitting and thus the "width" of the entire sextet depends directly on the magnetic field B that we need to look at in more detail. It is generally referred to as the effective magnetic field, which can be the superposition of an applied field B_{ext} and internal field B_{int} induced by the valence electrons. There are a number of causes for the latter, as described in Ref. 134, with the total field often being described as a superposition of the isotropic Fermi contact field, arising from spin polarization of s-electrons by unpaired valence electrons,¹³⁷ the anisotropic contribution from the orbital motion of valence electrons, as well as the anisotropic spin-dipolar contribution from nonspherical distribution of the electron spin density. Generally speaking, the Fermi contact field is the dominant of the three, with values as high as 50 T clearly showing that the majority of the hyperfine field contribution comes from this source. Indeed, we can see that measurements in our high field cryostat using up to 5 T produce comparatively small fields when directly compared to the magnitude of the nuclear hyperfine fields. We have thus derived and explained the three major hyperfine interactions that are commonly observed in Mössbauer spectroscopy.

Foreshadowing our evaluation, we need to consider the effect when several types of interaction take place simultaneously, as this will be the main tool for our theoretical model. As a matter of fact, it is rather rare for these effects to occur only individually, so the general perturbation

of the nuclear state can be described by the Hamiltonian

$$\hat{H} = \delta E + \hat{H}_Q + \hat{H}_M \quad (4.36)$$

with the interaction terms in the order of their introduction. The isomer shift δE is not of concern here, as it simply shifts the entire spectrum, regardless of what other types of interactions are present. Its influence is therefore additive, not interfering with any other hyperfine parameters. With quadrupole and magnetic dipole interaction though, things become somewhat complex, as both of them act upon the magnetic quantum numbers of nuclear spin, making their combined Hamiltonian rather difficult to evaluate.¹³⁴ In our case, we make the valid assumption that ΔE_Q is much smaller than E_M , enabling us to use a superposition of the two contributions. In this case, we no longer refer to the quadrupole splitting ΔE_Q , but to the quadrupole level shift 2ε , as it leads to a shift of the inner four absorption lines relative to the outer two, as displayed in Fig. 4.7 (e). It is this effect that, together with the underlying hyperfine field distribution, gives rise to the characteristic asymmetric (non-Lorentzian) peaks in Mössbauer spectra of BFO, if an anisotropic magnetic hyperfine field B_{hf} is present. We can obtain a relation between shift and splitting if we observe the angle θ between the principal axis of the electric field gradient and the spin direction, arriving at the equation

$$2\varepsilon = \Delta E_Q \frac{3 \cos^2(\theta) - 1}{2}. \quad (4.37)$$

It is this equation that will be the basis of our Mössbauer evaluation, with the detailed elucidation of our theoretical model being described in the results section.

4.3 Mössbauer spectroscopy: Experimental details

There are several different methods that can be utilized to obtain Mössbauer spectra. The by far most common one is referred to as transmission geometry, with a sample being placed between the γ -ray source and the detector, enabling the measurement of transmission spectra that show characteristic negative peaks at energies where resonant absorption takes place. Other methods include backscattering, as was used in the famous MIMOS 2 spectrometers aboard the Mars exploration rovers, as well as conversion electron Mössbauer spectroscopy (CEMS) and depth selective conversion electron Mössbauer spectroscopy (DCEMS), all of which have been performed in our group in the past. As the name of the latter two suggests, the secondary process of internal conversion is utilized, requiring a different detection setup. In this thesis, we only deal with transmission geometry, so only this type of measurement setup is explained here, schematically represented in Fig. 4.8. In order to observe the spectra that were shown exemplarily in the previous section, it's obvious that the photon energy needs to be modulated. This is accomplished by making use of the Doppler shift: The radioactive ^{57}Co source is mounted on a Mössbauer drive, an electromechanical linear motor that can move the source back and

forth in different modes. During the early days of Mössbauer spectroscopy, these were often home built from low frequency speakers (woofers), while most contemporary laboratories use specially built units that are commercially available, for example from WissEl, referred to as Mössbauer Velocity Transducers.¹³⁸ It is because of this type of modulation that the energy axis in Mössbauer spectroscopy is always labeled in terms of velocity rather than energy. An important factor is the mode of motion that is used, as a physical oscillator would normally be expected to move in a sinusoidal fashion. But, as one realizes when looking at the velocity scale of the previously shown spectra, this would lead to a high number of data points to be recorded near the two outer regions of the spectrum, which consists of background noise, while much fewer points are recorded in the region that contains the absorption peaks, leading to a much longer data acquisition time.

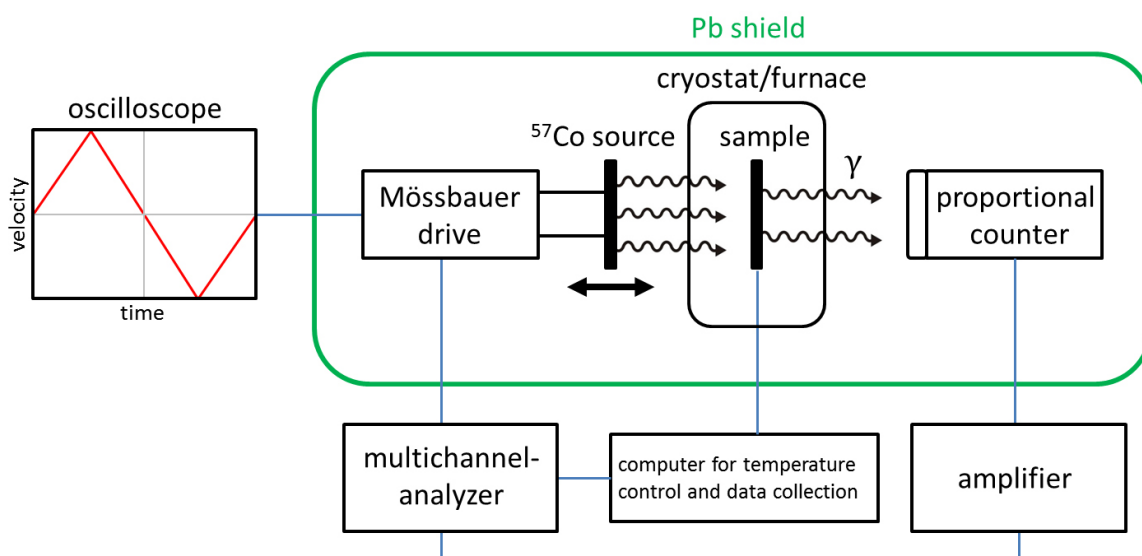


Figure 4.8: Schematic depiction of a standard setup for Mössbauer spectroscopy measurements in transmission geometry, with the sample placed in furnace or cryostat for high or low temperature measurements, respectively.

To overcome this problem, Mössbauer drives are usually always operated in constant acceleration mode, resulting in a triangular velocity function as shown schematically on the left in Fig. 4.8. This mode also results in the same number of data points for each section along the velocity curve, allowing easier analysis of the data. There is, however, a problem that may arise from this: Operation in constant acceleration mode leads to very abrupt changes of direction at the point of highest velocity, in contrast to the naturally occurring sinusoidal motion. In order to ensure that no errors result from potential deviations from the desired velocity, Mössbauer drive units always incorporate a pickup coil in order to check the actual motion of the source against the velocity signal being fed to the drive coil. The difference signal between the drive and the pickup coil signal is output as an error function, allowing the operator to ensure that no considerable deviations take place. In the spectra that are shown in this thesis, the error of the Mössbauer drive was always checked before measurements and remained in the range

of 0.5% or smaller. It can thus be considered as insignificant, not contributing to the overall errors that are given for hyperfine parameters.

The next component of our measurement setup is the proportional counter, consisting of a conductive tube filled with krypton, the outer shell representing the cathode and a coaxial wire inside the cylinder representing the anode. A beryllium entrance window provides an airtight seal while allowing γ -photons to enter with minimal losses. This geometry is identical to a standard Geiger-Müller counter, with the main difference being the applied voltage. When increasing the voltage of a counter tube, one moves through different regions that have different characteristics and uses. Generally speaking, incoming radiation leads to ionization of the gas atoms, producing free electrons that move towards the anode. The charge that is generated is proportional to the energy of the incident photon, which is what we are mainly interested in. With voltages being too low, many electrons recombine on their way to the anode, making it necessary to increase the voltage. Starting at 100 V, all electrons reach the anode, marking the ionization chamber region. Further increasing the voltage now causes an acceleration of the electrons towards the anode to be so high that these electrons ionize further atoms on their way, referred to as avalanche effect. This only takes place in a volume very close to the anode, which means that the height of the measured electric pulse is independent from the point of initial ionization while still being proportional to the photon energy. This means that a much higher sensitivity can be obtained by keeping the voltage in the proportional region. This section of the curve is very steep, making it necessary to use specialized power supplies that keep the voltage highly constant and free of fluctuations.

Another task at the beginning of a Mössbauer measurement series is the correct setup of the counter tube voltage, which is performed manually. The correct setting can be found by performing a pulse height analysis to determine the position of the 14.4 keV peak. Additional K_{α} lines from secondary processes are also visible, such as from Fe and Co (6.4- 6.9 keV)¹³⁹ and Rh (20.2 keV)¹³⁹ into which the ^{57}Co source material is embedded. With these numbers known, it's easy to find the correct peak once the voltage has been adjusted until the three peaks appear side by side. Then it's just a question of using the discriminator of the multichannel analyzer to block all peaks except for the "Mössbauer peak" at 14.4 keV. Finally, in order to achieve a valid calibration for all recorded spectra, the energy scale, in this case the velocity scale, needs to be fixed relative to a reference sample. For ^{57}Fe Mössbauer spectroscopy, α -Fe is used, in our case in the shape of a very thin foil, with the measurement being performed at room temperature. Using the known hyperfine parameters of this reference sample,¹³⁴ the velocity scale can be precisely set for all measurements that are performed with that spectrometer. A calibration via laser interferometer is also possible, and often used for higher velocities. It's important to keep this in mind, as a change of the velocity scale also requires this calibration measurement to be performed again. Although one can also use factors between two velocity settings to adjust the

potentiometer of the drive unit, this is not regarded as a sufficiently reliable method for proper evaluation of Mössbauer spectra. Because of this, in virtually all publications that utilize ^{57}Fe Mössbauer spectroscopy, it should ideally always be stated in the experimental section that all spectra were normalized against a reference sample.

This methodology is valid for all setups used here, be it a simple room temperature spectrometer, or one involving a cryostat for low temperature or an oven for high temperature measurements. The sample preparation, in the case of the BFO powder samples, must take into account the high amount of nonresonant absorption caused by Bi, which is a high-Z element like the Pb used for radiation shielding. In order to have sufficient sample volume without absorbing too much radiation nonresonantly, the sample material was mixed with chemically inert boron nitride (BN), with the optimum ratio having been determined experimentally before the series of measurements were performed. For the CFO-BTO samples, this was not an issue, and the pure powder was used. For high temperature measurements, a Mössbauer oven was utilized, with the sample powder, mixed with BN, being pressed into a disk shaped pellet, held in place between two beryllium plates, which themselves were attached to a ring-shaped heater within the vacuum oven. This permits sufficient transmission while allowing the desired temperatures to be reached, while the oven itself consists of a metal tube with aluminized Mylar windows, providing sufficient transmittance to the γ -photons while being able to hold a vacuum against ambient air. Low temperature measurements were performed using the same sample holder and transmission geometry, utilizing bath cryostats with liquid nitrogen or liquid helium. Field-dependent measurements on BFO were performed with a magnet cryostat, which contains a superconducting magnet in split-pair geometry, able to apply a homogenous magnetic field of 5 T at the sample position, with the field direction being parallel to the γ -ray propagation direction.

4.3.1 Evaluation of Mössbauer data

The recorded Mössbauer spectra were evaluated with the "Pi" program package by Dipl.-Ing. Ulrich von Hörsten, which is publicly accessible.¹⁴⁰ It traces its roots back to the NORMOS program that was originally developed for MS-DOS by P. D. Richard A. Brand, commercially available for Windows operating systems through WissEl.¹³⁸ The evaluation is performed by fitting the raw experimental data with the appropriate theoretical subspectra, using a least-squares procedure to minimize the error between theoretical function and experimental spectrum. A large number of parameters can be directly manipulated, such as the well-known hyperfine interactions consisting of isomer shift, quadrupole shift or splitting, as well as the magnetic hyperfine field. In addition, the line ratios and line widths can be taken into account, allowing the specification of certain maximum and minimum values to keep the fit physically sensible. For example, it would not make sense to use a sextet with extremely broad lines to fit

a spectrum that contains hyperfine field distributions. By setting a certain maximum value for the line width, one can clearly observe that no satisfactory fit can be achieved with this type of theoretical spectrum, and thus utilize a different solution. Furthermore, due to the fact that the software has a completely open environment, it's possible to implement custom functions of any kind for the fitting procedure. This was done in our case for the functions described in the results section, so that we were able to model the cycloidal spin structure in detail.

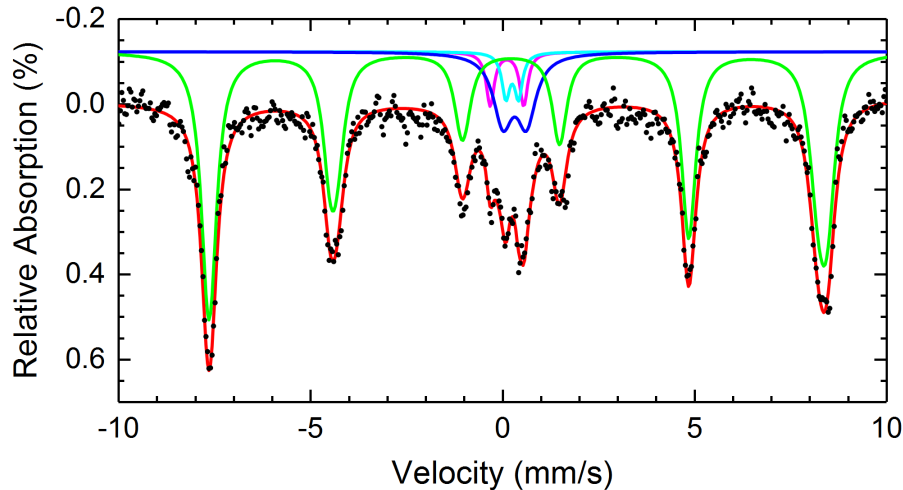


Figure 4.9: Exemplary Mössbauer spectrum showing the typical output after the finished fit routine. Experimental data is represented by black dots (error bars omitted for clarity) while theoretical subspectra, after optimization through a fitting process, are given by lines. The red line shows the overall fit, while the green sextet and the blue, cyan and magenta doublets represent the subspectra that, in superposition, form the overall fit. Adapted from Ref. 141, reprinted with permission.

An exemplary spectrum is shown in Fig. 4.9 of a BFO sample at room temperature. It contains the experimental data (black dots) as well as the overall fit function (red line), which is itself a superposition of several subspectra. In this case, the sample contains both magnetically ordered (sextet) as well as (super)paramagnetic (doublet) phases. The selection of appropriate subspectra and fitting routines ensures a physically vested approximation of the experimental data, which in turn makes it possible to extract the desired hyperfine parameters from the optimized fits. All spectra in this thesis are represented in this manner, by a superposition of one or more subspectra onto the experimentally obtained Mössbauer spectrum, with the fit routine providing the associated hyperfine parameters and their respective errors and deviations. This of course requires prior knowledge of sample properties, such as chemical composition (obtainable by XRD) or particle size distribution (via microscopy methods) for nanoparticle samples. Otherwise, it would, for example, not be clear whether we are dealing with a paramagnetic phase, or superparamagnetic Néel relaxation of an otherwise magnetically ordered material. Due to this, a sufficient amount of precharacterization results were included in chapter 6 in order to properly evaluate the obtained Mössbauer data.

4.4 SQUID magnetometry: Theoretical basics

As already mentioned at the beginning of section 4.1.3, there is a certain overlap between methods such as MFM and magnetometry. It was therefore elected to keep the microscopy methods separate from the pure magnetic characterization, even though one is able to measure microscopic magnetic properties via microscopy methods. In the same fashion, Mössbauer spectroscopy is also sensitive to magnetic properties, and even though it measures in terms of local nuclear effects, the results are always superimposed, and can only be given for the overall sample or certain identical ion types like Fe^{2+} and Fe^{3+} . The chapter we start here will therefore deal with conventional magnetometry, which is concerned with the macroscopic measurement of the magnetic moment over the entirety of powder or ceramic samples.

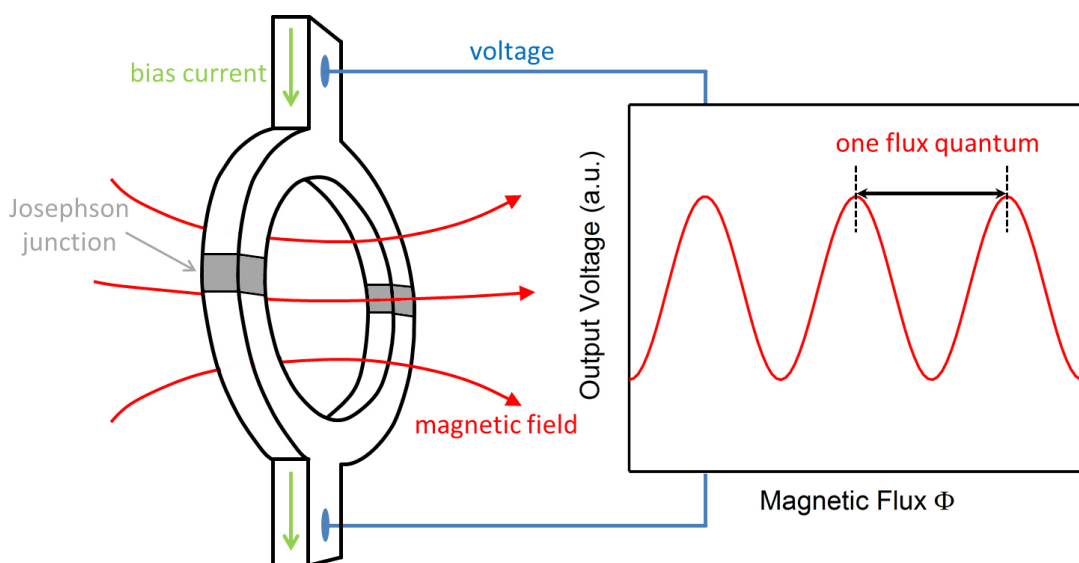


Figure 4.10: Schematic representation of a double junction SQUID (left) with the output voltage as a response to a change of flux (right).

The superconducting quantum interference device (SQUID) has been a mainstay of magnetic characterization since becoming commercially available from the 1980s onwards in the shape of standalone magnetometers from different manufacturers. These devices allow basic and advanced magnetic characterization of small amounts of sample material, from standard field dependent magnetization curves all the way to the measurement of the magnetoelectric coupling coefficient, as we will see later on. Since this device is among the most important instruments that were used here, the physical principles behind it are discussed in greater detail. To sum it up very shortly, a SQUID is a flux to voltage converter, as represented in Fig. 4.10, allowing a highly precise measurement of the change of magnetic flux through a superconducting loop.

The device used in the course of this thesis is a magnetic property measurement system from Quantum Design, designated as MPMS-5S, manufactured in 1996. Representing a typical

configuration that is also used by other suppliers, it features a large liquid helium Dewar to enable the cooling of the SQUID sensor below its critical temperature. At the same time, the liquid helium bath is also used to cool the superconducting solenoid in order to apply high magnetic fields, while a small capillary tube enables the sample chamber to be cooled to low temperatures in a controlled manner. In combination with a gas heater, this setup allows temperatures between 2.3 K and 400 K to be set, while static and homogenous magnetic fields of up to $\pm 5\text{T}$ can be applied at the sample position. At the heart of every magnetometer lies the actual SQUID sensor, a superconducting ring with one or two Josephson junctions, depending on the type of SQUID used, which combines the quantum mechanical phenomena of flux quantization as well as tunneling. It's based on the discovery made by R. Doll and M. Näbauer, who found that the flux contained in a closed superconducting loop is quantized in units of the flux quantum.¹⁴² Regarding the wave function of the electrons circling such a superconducting loop, in the form of Cooper pairs, the integral around the closed path of the ring can be written as

$$\oint d\theta = n2\pi, \quad (4.38)$$

showing that the function must be an integral number, which in turn means that the phase cannot vary by a fraction of $n2\pi$. Furthermore, the Cooper pairs in the loop have the same angular momentum, only being able to take on a discrete set of states, according to the Bohr quantization rule. As a result, the total flux threading the loop can be expressed as

$$\phi = h/2e \quad (4.39)$$

with $h = 2\pi\hbar$ being the Planck constant and $2e$ the electron charge, accounting for electrons traveling in Cooper pairs. If such a simple superconducting ring, cooled below its critical temperature, is exposed to an external magnetic flux, a persistent supercurrent is induced in the loop, to keep the inside of the loop free of flux. This is due to the Meißner-Ochsenfeld-effect, which describes how superconductors behave like ideal diamagnets, expelling all magnetic flux from their interior. This so called Meißner state persists even when the external flux is varied, as the supercurrent will vary accordingly. However, this state breaks down if the applied field is too large. The supercurrent can't become infinitely large, as all materials have a critical current that cannot be exceeded without the material returning to its normal conductive state. If we imagine an external flux that is constantly increased, upon the point of the critical current being reached, the supercurrent collapses, and one flux quantum can enter the ring. This process repeats itself periodically, every time the critical current is reached, one flux quantum can enter the ring. Fig. 4.11 aptly shows this behavior with the critical current being reached at $0.75 \Phi_0$ in this example. One can see the steadily increasing external flux (a) and the increasing supercurrent (b), showing a sudden drop every time a flux quantum enters the ring, which is also shown in (d).

What we can gather from this is the fact that a superconducting ring is sufficient to observe the effects of flux quantization. However, for application purposes, the required critical fields are too large to build sensitive magnetometers, and the size of the loop is further constrained by thermal energy considerations, also lowering its sensitivity. The solution lies in the usage of Josephson junctions, very thin sections of insulating or normal conducting material that interrupt the ring. When made thin enough (in the range of nanometers), the Cooper pairs can tunnel through these junctions, which can be described by their wave function needing to be single valued when going around a superconducting loop. In case of a sufficiently thin junction within the loop, the wave functions on either side can overlap, making it possible for Cooper pairs to tunnel. This setup allows much lower critical currents, which means that the flux switching explained earlier will occur at much smaller applied fields, making the device much more sensitive.

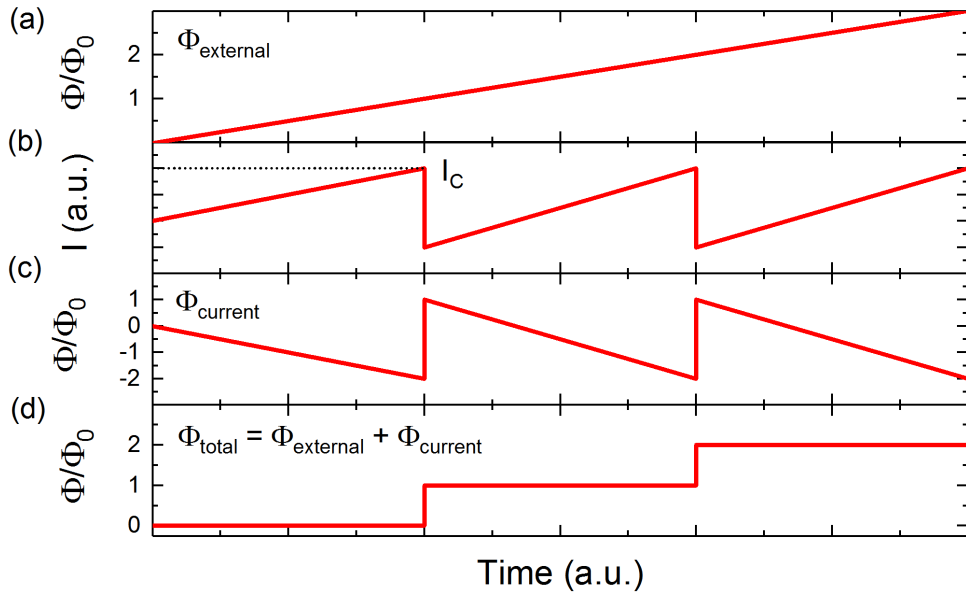


Figure 4.11: Behavior of a superconducting loop when exposed to a steadily increasing external flux Φ_{external} (a), which generates a supercurrent (b) inducing an equal and opposite flux Φ_{current} (c), with the critical current I_C of this ring being reached at $\Phi = 0.75 \Phi_0$, the resulting total flux Φ_{total} in the loop being shown in (d). Adapted from Ref. 143.

The current flowing across the Josephson junction is dependent on the critical current I_C and also on the phase difference δ between the wave functions of the electrons in the superconductors on either side:

$$I = I_C \sin(\delta). \quad (4.40)$$

Known as the DC Josephson effect, this phenomenon can be described by Eq. 4.40 from Ref. 143. Furthermore, the phase around the closed loop must be an integral number, according to Eq. 4.38 we saw earlier, which is still valid after a Josephson junction is inserted into the loop. It therefore follows that the total phase difference can be described using Eq. 4.41 with the

total flux Φ_T and with $2\pi\Phi_T/\Phi_0$ representing the phase difference.

$$\delta + 2\pi \frac{\Phi_T}{\Phi_0} = 2\pi \quad (4.41)$$

We arrive at the conclusion that with the addition a Josephson junction to our superconducting loop, the basic principles of flux quantization are still valid, however, the phase difference across the junction allows for the fact that the flux is no longer precisely quantized.¹⁴⁴

With everything assembled that is needed for the basics of a magnetometer, we can now observe the two underlying methods of building one as far as the actual SQUID is concerned. Generally speaking, there are two varieties of SQUID sensors, the DC SQUID, which features two Josephson junctions in its superconducting ring, and the radio frequency (RF) or AC SQUID, which has only one. This naming also takes into account whether the SQUID sensor is biased with a DC or AC current. Curiously, the RF SQUID does not feature interference between two wave functions, as there is only one, so if we're picky, it doesn't deserve the name Quantum Interference Device. However, with the appropriate external circuitry, it can be made to behave similar to a DC SQUID, as we will see in the following.

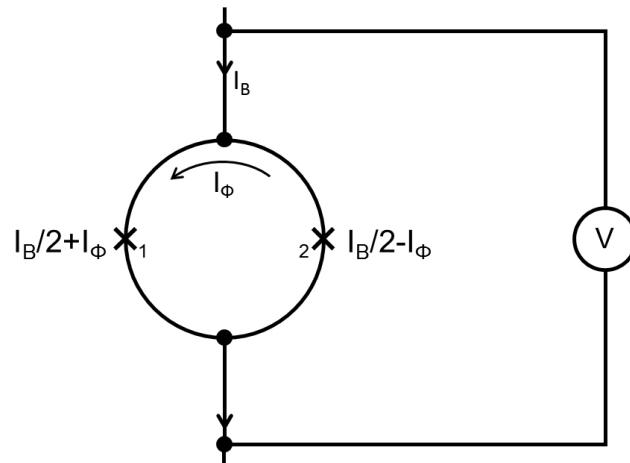


Figure 4.12: Schematic representation of a DC SQUID, adapted from Ref. 145, reprinted with permission.

We first look at the DC SQUID, represented in Fig. 4.12, which, for application as a magnetometer, is subjected to an external bias current I_B . Each of the two Josephson junctions has its own critical current, and with no external flux present, half of the bias current flows through either of the two junctions, assuming that the bias current itself does not exceed the critical currents of the junctions. When this ring is exposed to an external flux, a circulating supercurrent forms in the ring to counter the applied flux, keeping the inside of the ring flux-free according to the Meißner-Ochsenfeld-effect. Due to the applied bias current, one junction will now experience the supercurrent added to the already flowing bias current, while the other junction will experience a bias current lowered by the supercurrent. As a result of this constel-

lation, the left junction will reach its critical current before the right one does. When this takes place, the ring will momentarily become normal conducting, absorb a flux quantum, and the circulating current reverses, as shown in Fig. 4.13. The critical current for the entire setup is therefore $I_C = 2I_0 + 2I\Phi$ and shows a periodic variation when the external flux is continuously ramped up, caused by the interference of the two junctions with each other.

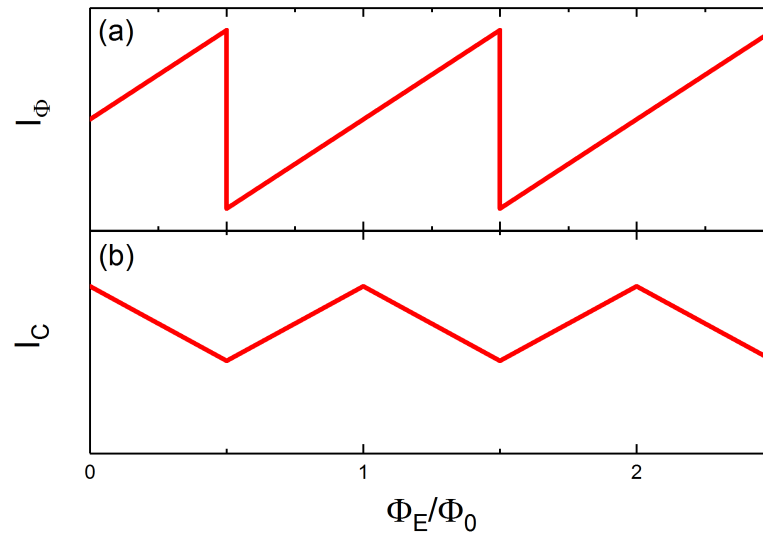


Figure 4.13: Induced circulating current I_Φ in a DC SQUID as a function of applied flux Φ_E (a) and variation of the critical current I_C (b) caused by interference between the two junctions, adapted from Ref. 146, reprinted with permission.

This is what gave the SQUID its name, and is often compared to the double slit experiment. The SQUID itself is regarded as the double slit in this case; splitting a single wave function and having the two resulting waves interfere with each other, modulating the critical current of the device. In practice, the measurement is performed by recording the voltage across the entire 2-junction setup with a constant bias current, the selection of which is based on the behavior of the SQUID shown in Fig. 4.14 (a). Such devices are usually operated at bias currents that are greater than I_C , which is shown by point *A* in Fig. 4.14 (a). In this mode, the measured voltage is a function of both the bias current as well as the external flux, reaching a maximum when I_C is minimized at $(n + \frac{1}{2})\Phi_0$ and a minimum where I_C is maximized at $n\Phi_0$. Due to the fact that I_C varies with flux, as shown in Fig. 4.13 (b), the output voltage also varies periodically, depicted in Fig. 4.14 (b).

This characteristic periodic voltage output can be evaluated to determine the amount of flux quanta that have entered the ring. Already, we can see that a SQUID isn't capable of measuring the absolute value of a sample's magnetization. It can only measure changes in flux, which requires any magnetometer setup to, in some way, introduce sample and thus its magnetic flux into the sensor, with the total magnetic moment being determined by calculating it from the change in flux the sample caused.

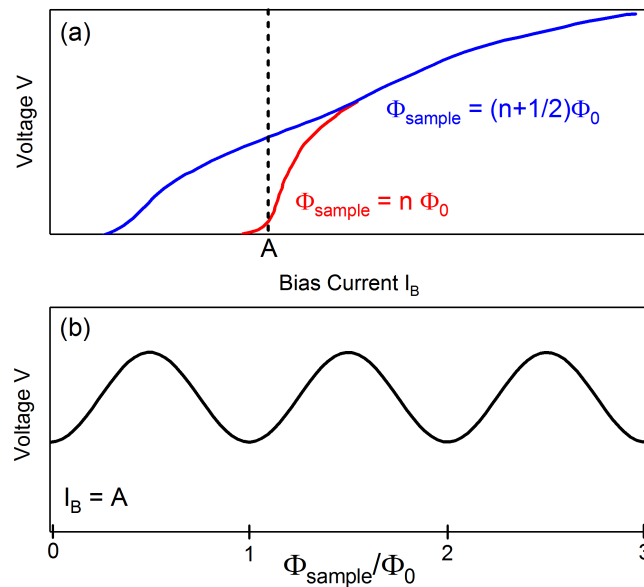


Figure 4.14: Voltage as a function of bias current I_B for a DC SQUID (a) and voltage as a function of sample flux Φ_{sample} (b), adapted from Ref. 145, reprinted with permission.

We now come to the single junction RF SQUID that was the first of the two that saw widespread use, mostly due to the ease and lower cost of manufacturing. As mentioned previously, it's not actually a SQUID, as there is only one junction, and no interference between two wave functions. Instead, the RF SQUID is inductively coupled to a resonant tank circuit (Fig. 4.15) that is driven near its resonant frequency, with the device output being provided by measuring the voltage across the resonant circuit (voltmeter not shown in figure).

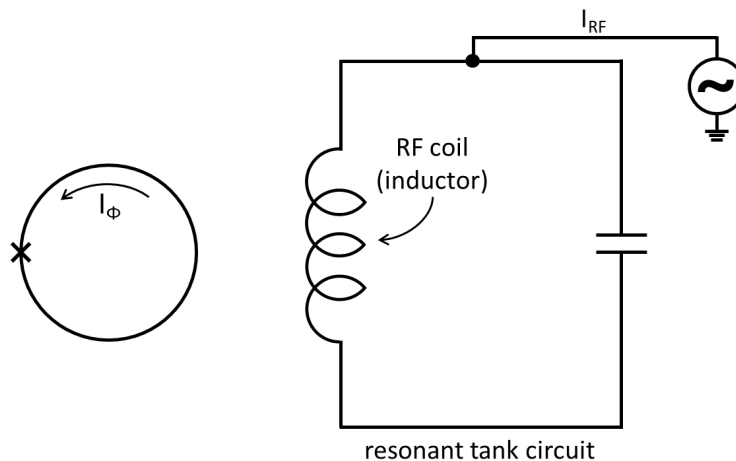


Figure 4.15: Schematic representation of an RF SQUID (voltmeter not shown), adapted from Ref. 145, reprinted with permission.

Users of Quantum Design MPMS devices will remember the necessity of tuning the SQUID amplifier after performing the initial cooldown of the device, which is akin to the tuning of the resonant tank circuit. To describe the current flowing across the junction, we can again use

Eq. 4.40 and 4.41 and receive

$$I_{\Phi} = -I_C \sin\left(2\pi \frac{\Phi_T}{\Phi_0}\right). \quad (4.42)$$

As before, we can plot the relation between the externally applied flux Φ_E and the flux within the ring Φ_T , as displayed in Fig. 4.16. If we regard only the influence of the flux from the RF-field ($\Phi_E = \Phi_{RF}$) and disregard any flux from a sample, we can examine the somewhat more complex behavior of the RF SQUID in more detail: The behavior of the device is depicted as a dashed green line, with only the positively sloping segments being stable,¹⁴³ as flux will enter or exit the ring if the alternating external flux is sufficiently large for the induced supercurrent to exceed the critical current ($I_{\Phi} > I_C$). This behavior is shown by the thick red lines in Fig. 4.16, with the resulting peak output voltage ($V_{RF,max}$) measured across the tank circuit against the drive current being shown by the red line in Fig. 4.17 (a).

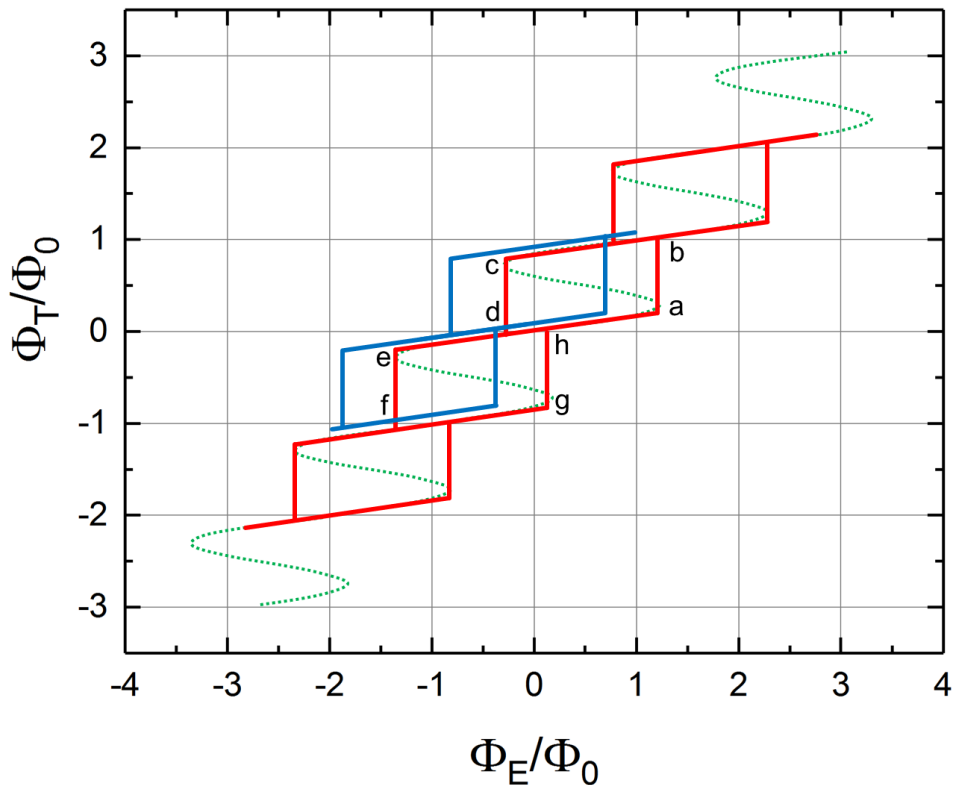


Figure 4.16: Behavior of the total flux Φ_T in an RF SQUID when exposed to an external flux Φ_E (dotted green line), with influence of different drive currents (see Fig. 4.17) being shown by red and blue lines. Adapted from Refs. 143, 145, reprinted with permission.

If we continue with our assumption of there being no sample flux, we can observe the behavior to depend solely on the current I_{RF} that we can use to modify the response of the device. If the current is sufficiently small, not enough flux is induced to exceed the critical current of the loop, with the SQUID remaining in the "zero" quantum state, moving back and forth along the $\bar{a}\bar{e}$ line. In this region, the increase of I_{RF} causes a linear rise of the measured voltage $V_{RF,max}$

as denoted by point A in Fig. 4.17 (a). When the drive current is sufficiently high to exceed the critical current (B), one flux quantum is temporarily admitted into the loop, which now follows the paths \overline{abcd} or \overline{efgh} , which in turn causes energy to dissipate in the resonant circuit. Due to this energy loss, the device isn't able to reach the \overline{ab} or \overline{ef} transition any more, despite I_{RF} still being at B , instead staying in the initial state on path \overline{ae} , building up energy over the course of many RF cycles, until Φ_{RF} again becomes sufficient to reach the \overline{ab} or \overline{ef} transition. This process occurs more frequently if we increase I_{RF} past A , and if we increase it all the way to D , every RF cycle causes a complete double hysteresis loop $\overline{abcdefgh}$. Increasing I_{RF} to E causes I_C to be exceeded twice, with two flux quanta being admitted to the loop, which can be continued onwards for higher currents. If we now consider the sample flux, it becomes clear that the response of the device can be adjusted by varying I_{RF} .

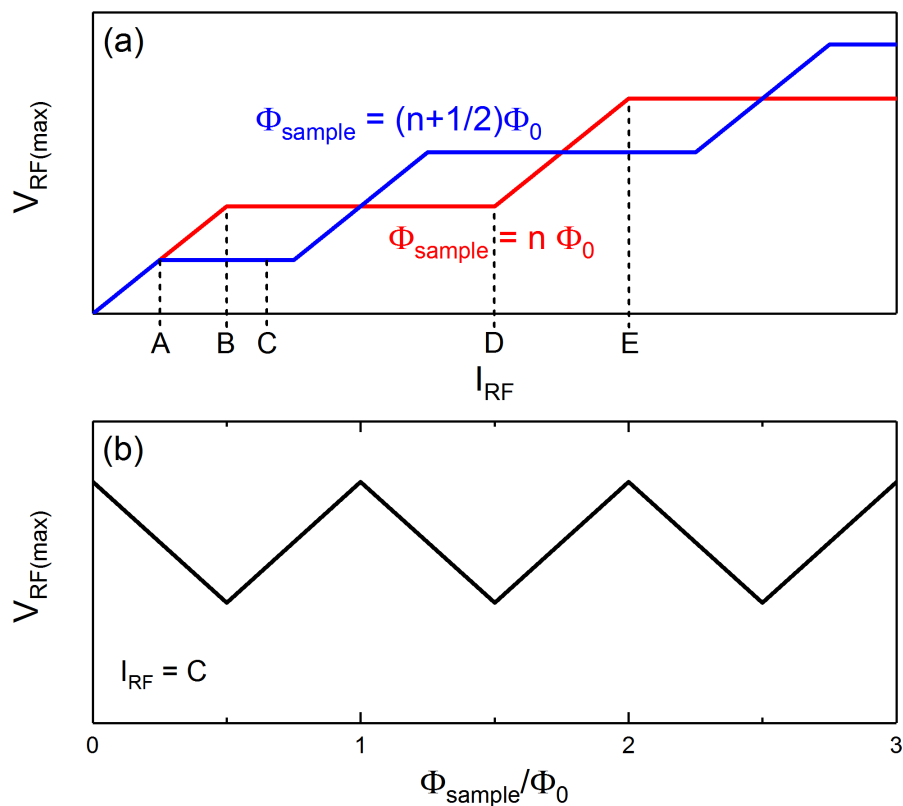


Figure 4.17: Peak voltage achieved across the resonant circuit as a function of RF drive current (a) and voltage as a function of applied flux (b) using constant drive current C , adapted from Ref. 145, reprinted with permission.

At the same time, the strength of the sample flux Φ_{sample} relative to Φ_0 also plays a role. For $\Phi_{\text{sample}} = n\Phi_0$, the red line is obtained in Figs. 4.16 and 4.17, while the blue line represents the relationship for $\Phi_{\text{sample}} = n + \frac{1}{2}\Phi_0$, causing a shift of the transitions in Fig. 4.17 so that a higher flux state can occur at a lower drive current A . We can conclude that the RF bias current I_{RF} is adjusted so that the voltage change caused by a change of Φ_{sample} is maximized in order to obtain a high sensitivity. In most cases, these devices are operated with a constant RF bias current, in this example set to C , which leads to the output voltage depicted in Fig. 4.17 (b).

We can therefore utilize the SQUID to generate a voltage signal that oscillates with increasing flux quanta being admitted into the ring, allowing an evaluation of this signal in order to actually measure the sample flux Φ_{sample} .

To sum up these findings, we can conclude that a SQUID is a comparatively simple yet highly sensitive flux to voltage converter that allows high precision measurements, although only of a change of flux, with the absolute value having to be determined from this change.

After this short review of the physical principles upon which SQUID magnetometers are based, let's now take a short look at the actual measurement geometry used in practical devices. As we have seen earlier, the size and shape of the superconducting ring has to be carefully controlled, which severely restricts its usage to directly measure a change of flux by the common method of moving a sample through the SQUID itself. Instead, a set of detection coils are used to achieve a separation between the SQUID and the sample positioning, in order to allow for the standard measurement method as described below. The schematic sensing circuitry for our device clearly shows this separation between sensing coils and the actual SQUID, as depicted in Fig. 4.18, also including the RF tank circuit on the right side.

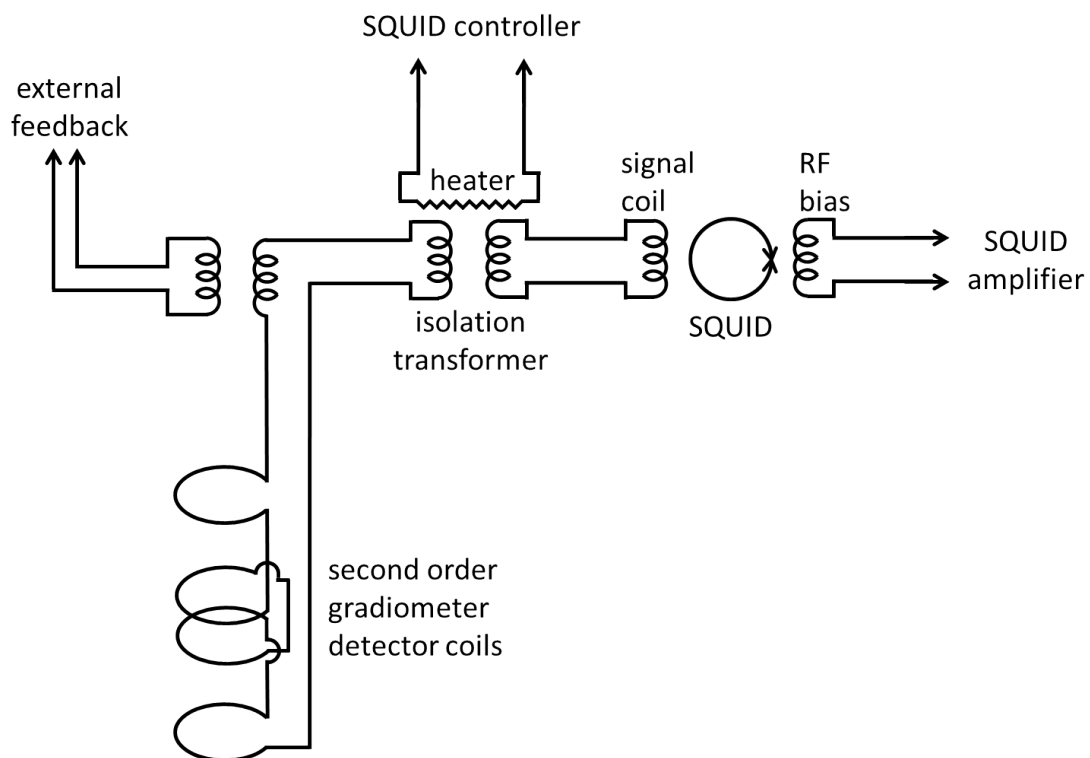


Figure 4.18: Longitudinal SQUID system schematic, based on Fig. 8-1 from Ref. 147.

In modern day devices, the desired change in magnetization is brought about by physically moving the sample through a set of detection coils, which themselves are also superconducting to minimize noise and current losses. The geometry of our device is shown in Fig. 4.19 consisting

of three coils, one at the top and bottom, wound once anticlockwise, and a central coil, with two clockwise windings (or vice-versa). This unit forms an axial second order gradiometer, able to detect a change in magnetization, while also making it possible to obtain a centering position for the sample within the coilset. The measurement is performed by moving the sample through the coilset while recording the output voltage, determined from the amount of detected flux quanta, on which the device software performs a fitting procedure to determine the amplitude and thus the magnetization of the sample.

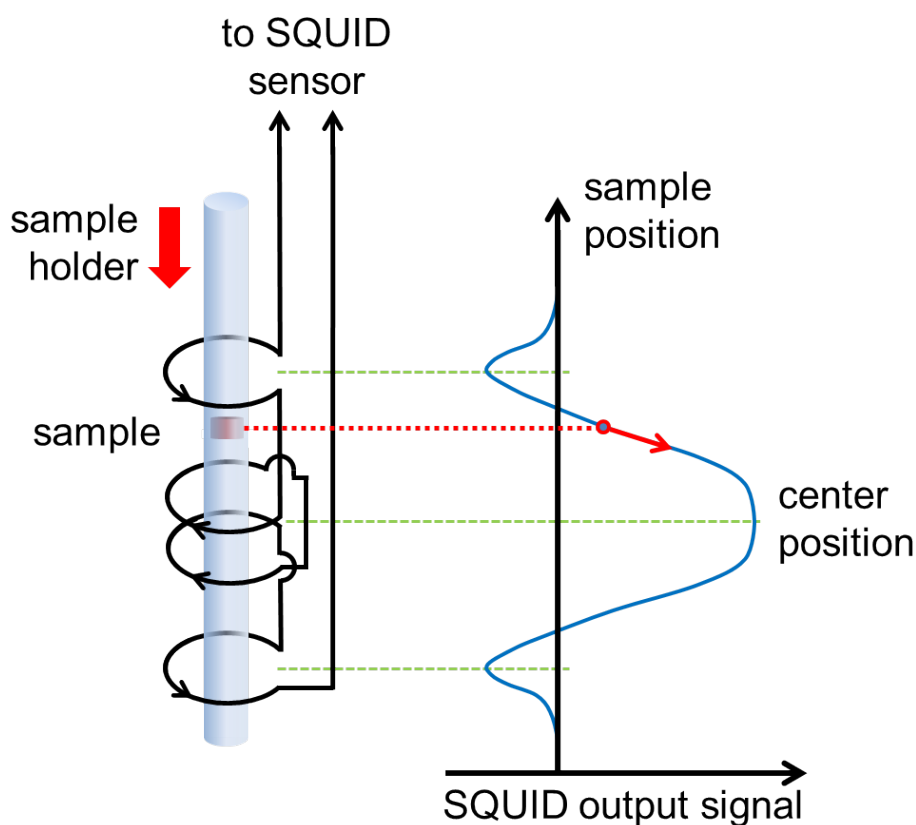


Figure 4.19: Schematic representation of the measurement geometry utilized by our SQUID magnetometer, with the sample being moved through a second order gradiometer, resulting in a characteristic W-shaped curve, the amplitude of which is proportional to the sample magnetic moment.

The characteristic W-shaped curve shown in Fig. 4.19 allows the device to detect the position of the sample relative to the coils by simply locating the position of the large, central peak, while the symmetric nature of the gradiometer rejects any linear background drifts of the magnetic field. This is especially important for magnetic field dependent measurements, with the associated creep of the magnetic field in the superconducting solenoid after large field sweeps being a commonly known source for errors. Thanks to the gradiometer geometry, such field creeps, and any unwanted external magnetic fields, can be reliably filtered out, as any linear background to the W-curve is disregarded by the fitting algorithm. The entire procedure is automated and doesn't require any further inputs from the user. The device automatically sets

the appropriate sensitivity in the SQUID amplifier to make use of the most optimal settings that are suitable for the respective sample signal.

With the described setup, using the integrated temperature controller of the cryostat, standard measurements such as $M(H)$ and $M(T)$ curves can be recorded using automated sequences that the user can combine as appropriate. Such measurements have been performed for a large number of the publications that deal with the overall sample system of this thesis, including the characterization of precursor materials and finished composites, representing an important reference to obtain an understanding of the magnetic properties. However, the largest role of SQUID magnetometry was played by its usage to directly determine the converse magnetoelectric effect using a modified sample holder and the integrated AC susceptibility measurement option. The reason for the use of this option rather than the preexisting capabilities of the SQUID lay in the problem of measuring the very small influence of the ME effect while it's superimposed onto the static magnetic moment of the sample. One would normally expect it to be possible to simply contact a ceramic sample on either side, and then apply a voltage while measuring the magnetic moment. In theory, after normalization, one should then be able to plot the increase of magnetization caused by increased electric field amplitudes, with the fitting of the electric field vs. magnetization curve giving direct access to the magnetoelectric coupling coefficient. However, when putting this idea into practice, one quickly realizes that very little can be seen in the magnetization data. As we saw in the theory of the ME effect, it's strongly dependent on the magnetostriction of the magnetically active constituent of the composite. This necessitates the application of different magnetic fields so that the optimum field for the highest magnetostriction can be determined. When doing this, even at small fields, it becomes painfully obvious that the static magnetic moment of the ceramic sample is simply huge compared to the induced magnetic moment from the ME effect. In the last few sample sets that were measured, with ceramic samples weighing about 200 mg, the static moment was in the range of several emu while the ME effect at optimum parameters usually went as high as several 10^{-5} emu, being five orders of magnitude smaller than the static sample magnetic moment. The device automatically adjusts the settings of the SQUID amplifier to account for the magnitude of the signal, doing so to avoid a saturation of the sensor that would distort the measurement value. As a result, a sample with a large signal directly leads to the least sensitive amplifier settings, with any potential additional signal arising from ME coupling disappearing completely in background noise. This problem is further exacerbated when the magnetic field dependence of the ME effect is to be characterized by $ME(H)$ sweeps at higher fields. To overcome these issues, a different methodology was utilized, which shall be explained in section 4.6. To obtain a general understanding of this methodology, the well-established AC susceptibility measurement method shall be described beforehand, as it is on the basis of this method that our specialized converse ME measurement setup was built.

4.5 Principle of AC susceptometry measurements

As we learned from the previous section, a SQUID can only measure a change in magnetization, with absolute values being calculated against a reference calibration. While regular measurements, usually referred to as static or DC measurements, make use of a mechanical linear movement of the sample through the gradiometer to achieve this change in magnetization, there are also other methods to obtain the same effect.

Referred to as AC or dynamic magnetometry, this method utilizes a magnetic AC field of comparatively small amplitude to modify the magnetization of the sample. In the case of our device, this is achieved with an additional non-superconducting solenoid that surrounds the sample space at the position of the second order gradiometer, able to apply a homogenous field of up to 0.52 mT^{148} in a usable frequency range of ca. 0.01 - 1500 Hz. As a result, we not only utilize this type of measurement method to determine temperature dependent phase transitions,¹⁴⁹ but also to observe the relaxation behavior of nanoparticles in fluids and gels,^{150, 151} as it provides direct information on the dynamics of a sample. The measurement output consists of the real and imaginary part of the measured magnetic moment, while it can also be displayed as an amplitude signal with accompanying phase shift relative to the original input signal. The name stems from the fact that this method can be used to directly obtain the magnetic susceptibility of a material at a set temperature and applied static field, with latter being supplied by the large superconducting solenoid. While the susceptibility can be calculated from the measurement data by normalizing it with the applied field value, we will utilize the direct output of the machine, which provides the measured magnetic moment of the sample, from which we can determine the magnetization by normalizing to sample volume or mass.

The major advantage of this setup lies in its high sensitivity (10^{-8} emu) and low noise, which is achieved by a number of proprietary steps that are performed during a standard two point measurement. The line and drive nulling procedure ensures that all stray signals are eradicated before performing the actual measurement, which itself is based on the use of a lock-in amplifier in conjunction with the SQUID sensor. The former is only sensitive to signals that match the frequency of the applied AC magnetic field, and is thus able to reject any stray signals that do not correspond to the measurement frequency. The only disadvantage of this system is the considerable time it takes, up to 10 minutes per data point, depending on device settings and the strength of the sample signal.

4.6 Converse ME measurement setup

Now that we have dealt with the functionality of the standard SQUID magnetometer, as well as the AC susceptometry fundamentals, it is time to delve into the custom built setup that will be used in the following to measure the converse magnetoelectric effect of ceramic samples. This method was devised by Dr. Pavel Borisov in 2007 while he was working on his PhD in the group of Prof. W. Kleemann, with the general description having been published in the Review of Scientific Instruments.¹⁰ Since then, several other groups have copied this method, as it can be applied to all "classic" Quantum Design MPMS and MPMS-XL systems that predate the current MPMS3 (formerly known as SQUID-VSM). The biggest advantage of this system is the ease of implementation, with just minor modifications being needed to transform a regular SQUID magnetometer into one that can be used for magnetoelectric measurements. The only requirement is for the SQUID to be equipped with the AC susceptibility measurement hardware, which can be added to existing machines in case it was not selected as an option when the system was ordered.

To sum it up very briefly: The signal that would normally be sent to the magnetic AC field solenoid is diverted and instead used to apply an electric field to the sample, with the SQUID recording the resultant change of magnetization through a lock-in amplifier.

For this purpose, one of the main leads that connects the SQUID probe to the J-C5 socket of the electronics cabinet is used. Instead of connecting it to the cabinet, is it plugged into a junction box, as shown in Fig. 4.20, which simply splices out pin no. 17 and 18 while letting all other wires pass through without interference. These would normally be connected to the AC magnetic field solenoid. The main lead that emerges from this box can be connected to J-C5 again to allow all other functions of the SQUID to work normally, while the two spliced out pins are now available for their alternative use. One could directly use the output signal at these pins to apply a voltage to the sample, but in order to protect the AC electronics from short circuits, and to more freely set higher applied voltages, we instead connect them to the input side of a wide band amplifier (Krohn-Hite Model 7602) shown in Fig. 4.22 (h). Latter has two inputs, A and B, with us using the mode A-B that generates an output signal from the difference of the two input signals. With the grounding switch of the amplifier set to floating instead of chassis, we can rule out any possibility of current flow to ground from the AC pins, thereby making sure that measurements can be performed without any harm to the device in case of short circuits or leaky samples.

The wide band amplifier will be our main power source for measurements, able to supply AC voltages up to ± 200 V, with the same voltage also being available as DC offset that is added to the AC signal. The combined voltage cannot exceed the specified 200 V, so lower AC amplitudes

It is a standard MPMS sample rod that had its top seal removed so that a pair of 0.2 mm manganin wires could be run through its length, as all sample rods are hollow. Manganin was chosen as it minimizes thermal conductance throughout the sample rod. The top was sealed with wax, as this part remains at room temperature and doesn't undergo any significant thermocycling, and a BNC connector with a small metal tube was added, affixed to the silver knurl at the very top of the sample holder. This is normally intended to slide off the rod in case latter becomes mechanically jammed for some reason. In our case, it was tightened with pliers in order to stop that from happening. Otherwise, in case the sample rod jams, the fixture would pull out the wires and with them the wax plug, opening the sample space to ambient air. Since the device would attempt to maintain a low pressure atmosphere, a lot of air would be pumped through this opening, which could freeze out if the sample chamber were at low temperature at that time. If this happens, even if the leak is small and not readily noticeable, the resulting ice formation can easily damage the sample holder, which is rather brittle at low temperatures. Because of this, the low temperature region was often avoided in the later parts of this work, as described in section 6.2.5.

It has to be mentioned that Quantum Design offers their own sample rod with electrical contacts, designated as "Manual Insertion Utility Probe", but the hardware at the bottom end doesn't make it ideally suitable for sensitive magnetic measurements. We therefore elected to keep using this home-built sample rod, despite the seal at the top being a clear weak point.

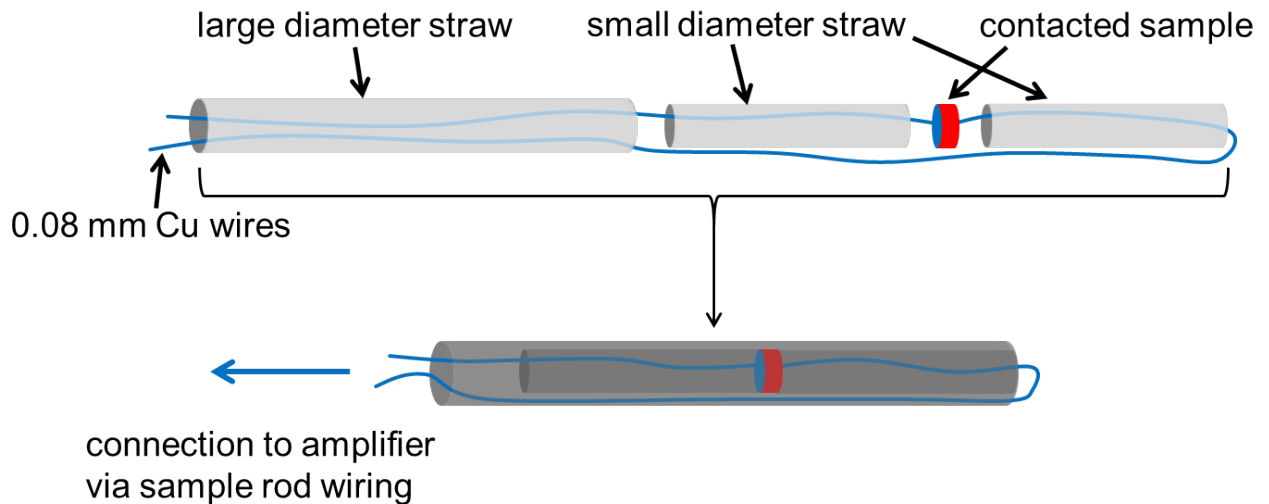


Figure 4.21: Schematic representation of the converse ME SQUID sample holder before (top) and after assembly (bottom). The ends of the small diameter straws facing the sample are blocked by small pieces of adhesive tape, which locate the sample.

Following the sample rod down to the sample holder, we arrive at the final part of the measurement setup, displayed in Fig. 4.21. Regular SQUID users will recognize the clear, plastic drinking straws that are used for standard sample mounting on these older systems. We de-

cided to use the same method, mostly due to the fact that it allows standard DC magnetometry measurements to be performed in addition to the intended ME measurements.

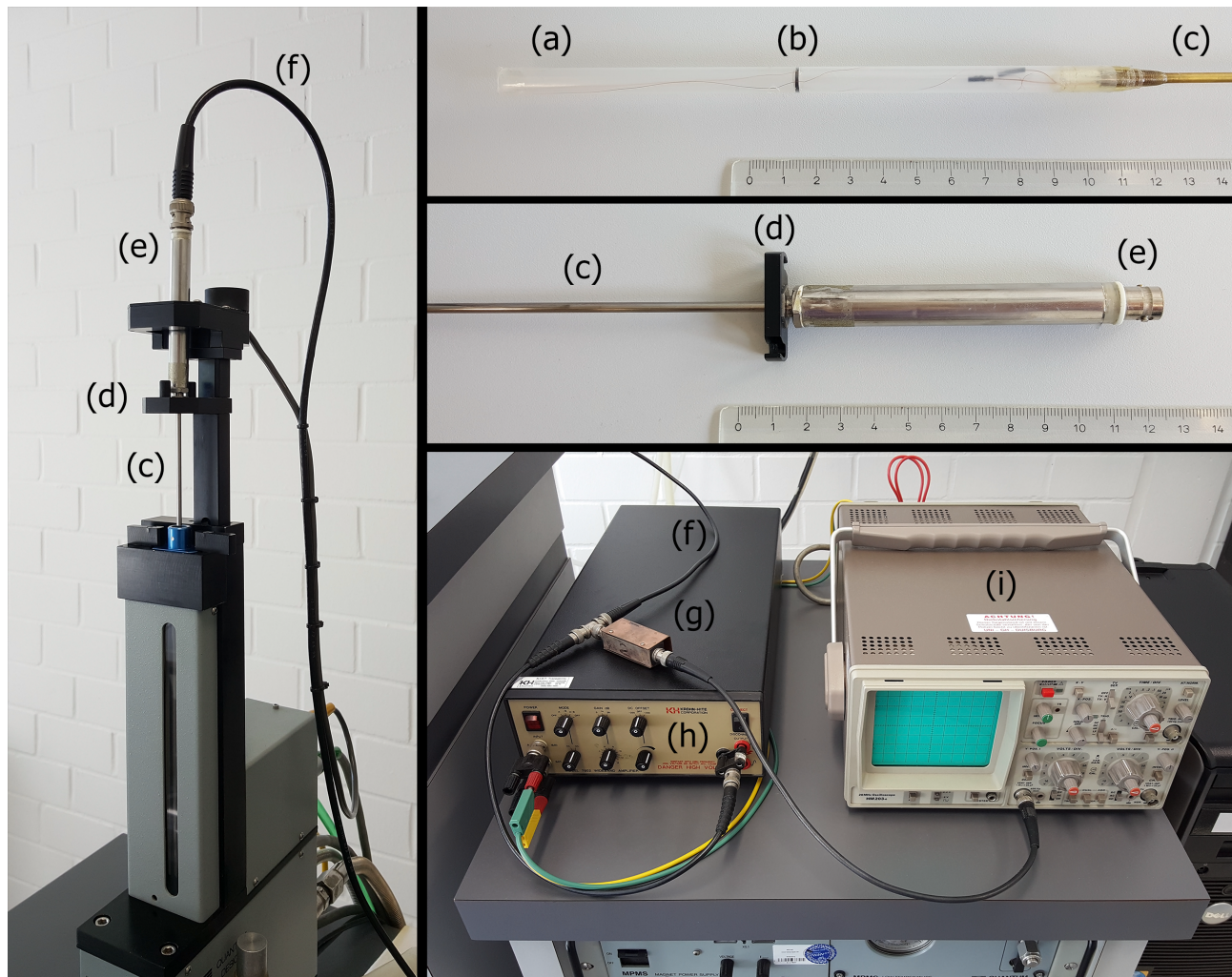


Figure 4.22: Overview of the converse ME measurement components, with the sample holder (a) and an installed sample (b), as shown in detail in Fig. 4.21. This is attached to the bottom end of the 1.5 m sample rod (c), which has an attachment at the top end (d) to the linear motion of the SQUID magnetometer. A BNC connector (e) allows the sample to be directly wired (f) via a voltage switch (g) to the output side of the wide band amplifier (h). The yellow and green wires are pins 17 and 18 from J-C5, as shown in Fig. 4.20. The oscilloscope (i) is used to check the shape and amplitude of the applied voltage so that the setup can be calibrated.

Therefore, the main goal is the mounting of the sample with a minimal amount of magnetic background signal from the sample holder. To achieve this, the sample holder is built in a way that no or only minimal inhomogeneities are present, apart from those that cannot be avoided at the sample position. The sample itself is held in place by the two small diameter straw segments visible in Fig. 4.21 that had their ends closed by small sections of adhesive tape, with the straws and the sample being slid into a slightly larger straw with an inner diameter of 8 mm. Their diameters are similar enough to allow the entire stack to be relatively stable

by friction alone, with almost nonexistent play between them. The attachment to the sample rod is provided by a roll of adhesive tape that has the correct thickness to allow the outer straw to be pushed onto it, with friction being sufficient to hold it in place. This measurement geometry, with magnetic and electric fields both being perpendicular to the sample surface, is the standard way of mounting samples for the measurement of the longitudinal ME effect. Unless otherwise stated, the sample is always oriented in this manner.

The 0.2mm wires running along the length of the sample rod terminate just below the attachment point of the sample holder, being soldered to much thinner 0.08mm copper wires for the last few centimeters to the sample, to minimize the mass of non-sample material at this stage. To achieve symmetry in the sample holder, one of the wires runs directly from one of the terminals to the sample, while the other one runs down the entire length of the sample holder, in the small space between inner and outer straws, then makes a 180° turn at the bottom of the assembly to connect to the sample from below. This way, as far as magnetic signals are concerned, the wires represent a homogenous background along the entire scan region, with the only inhomogeneity being the ends of the inner straws and the sample with the electrodes. Care must be taken when assembling the entire stack, making sure that there are no loops near the top where a small but unavoidable length of excess wire is bunched up when sliding the straws into each other. As the wires are lacquered, no short circuits should occur, but if the wire bunch takes on a certain geometry, one or several small solenoids can be formed inadvertently. These would introduce a small magnetic field to the sample environment that the lock-in amplifier wouldn't be able to filter out, as the resulting field would have the exact same frequency as the applied signal and thus also the sample signal. These problems are discussed in detail in section 4.8.1.

This description represents the current iteration of the sample holder and rod assembly. The previous iteration was burdened with excessive lengths of unshielded wires connecting the sample rod to the amplifier, as well as sections of badly insulated wires within the sample rod, causing numerous problems that had a detrimental impact on the reliability of the measurement. After a lot of trial & error, the wiring in its entirety was completely replaced, enabling the performance of reliable and reproducible measurements. Other small improvements were made, following the advice of Dr. Pavel Borisov, such as the removal of the load resistor that is shown in Ref. 10, which proved to be unnecessary.

The final contacting of the sample to the wires was achieved by the simple application of silver paste onto the sample faces, making sure to evenly coat the entire surface, while placing the wire on the still wet silver paste. When dried, this results in an electrode that acts as a capacitor plate with no air gap between electrode and sample, while also affixing the wire at the same time. Care must be taken to remove the lacquer coating of the wire prior to electrode

application, with a standard multimeter being utilized to test the continuity between the BNC connector and the electrode on the sample surface. Measurements of $P(E)$ loops or the direct ME effect use the same electrode configuration, allowing its re-use in the converse ME setup.

When all is satisfactory, a high sensitivity electrometer (Keithley Model 617) is connected to the assembled setup to determine the resistivity of the sample. This serves a dual purpose: On the one hand, the resistance of each sample in a set can be used for later explanations of trends seen in the following measurements. On the other hand, a very low resistance (in the low $M\Omega$ range) is indicative of a leaky sample that has excessive conductivity. With such samples, a current flow can occur through the ceramic, which is a rather complex material with grain boundaries and discontinuities. As a result, current loops can form, leading to a parasitic signal that is caused only by conductivity and not by the ME effect. This will be discussed in the pitfalls (4.8.1) and evaluation section (6.2.3) later on. Another, more straightforward problem is the resistive heating of the sample, which can quickly become excessive. Depending on the properties of the material, porosity or general stability, it can happen that the sample bursts, contaminating the sample chamber and damaging the sample holder, also explained in detail in the section 4.8.1. As a result, samples with questionably low resistivity are subjected to the maximum voltage before the sample holder is assembled, to mitigate any damage or contamination. This also avoids the risk of one of the unlaquered wire ends touching the inside of the sample chamber, as it has been observed that in case of badly insulated wiring, the voltage takes the path of least resistance, in this case via the wiring of the temperature sensor that is built into the sample chamber walls. This can lead to wildly fluctuating temperature readings, with the temperature controller attempting to work against it, despite the actual chamber temperature not having changed, usually causing an automatic shutdown of the controller to mitigate any damage. In the worst case, the wiring between the control cabinet and the SQUID probe can be damaged, which must be avoided at all costs, hence the pre-measurement high voltage check.

This concludes the detailed description of the measurement setup that will be used in the following to obtain the entirety of the converse ME data.

4.7 Description of the converse ME measurement methodology

In this chapter, the methodology of the converse ME measurement setup is described, to make it clear how the data shown in the upcoming chapters has been obtained. This section only describes the methodology itself, to provide the reader with a general idea of the course of such measurements, while the evaluation and interpretation of the data takes place afterwards. After going through the sample mounting steps outlined in the previous chapter, we end up with the sample rod installed in the magnetometer, the BNC connector linked to the output side of the amplifier, which in turn was previously calibrated, so that the desired voltage can be set by using predetermined field values.

At this point, one usually performs a test measurement with parameters known from previously used sample sets. In our case, the transition temperatures for BTO are close to room temperature, so that no variation of the temperature needs to take place for a first test. The magnetic field is usually set in the range of 0.1 to 0.15 mT, and if the sample has shown sufficient resistance, the largest possible voltage of 200 V can be used, with the resulting electric field depending on the sample thickness, usually being in the range of 1-2 kV/cm. The frequency is normally kept slightly below 10 Hz, a value that was also learned from numerous previous measurements. After making sure that all these parameters are correct, a single measurement is performed, usually with two scans per measurement, so that the software can produce an error bar based on the deviation of two points relative to each other. Once the measurement is completed, which can take up to ten minutes depending on signal strength and device settings, a single data point is produced. It can be analyzed in terms of the signal amplitude relative to the error bar, which is a quick indicator of whether or not there is any ME effect present in the sample, or rather, whether we are currently able to measure it.

If the data point is of the same magnitude as the error, in the range of 10^{-7} to 10^{-8} emu, there is usually a problem with either the sample or its contacting. If we do have a sufficiently large signal, one has to take a look at the raw data that is always saved for the last recorded data point. It shows the relative voltages that are recorded in the course of the pre-programmed two-point measurement, which are subtracted from each other to form the final measurement signal. If everything performs as expected, and as the ME effect in our samples is expected to be linear, we should end up with a sinusoidal wave that would ideally be a close match to the applied signal, with a slightly deviating phase and an amplitude dependent on the sample properties. An example of such a raw data plot is depicted in Fig. 4.25 of section 4.8.1, while this output from the SQUID is also available via a BNC connector at the back panel of the device. If needed, it can be connected to the second channel of the oscilloscope shown in Fig. 4.22 to directly observe the input and output signals simultaneously, while the measurement is being

performed. One must be cautious if the signal shows strong signs of distortion or spurious artifacts. The device performs a fit routine using a sinusoidal wave to produce a data point from the raw data output, with the Regression Fit value being the indicator of the fit's goodness. This is also an important factor when considering the validity of obtained data. Once all the prerequisites are met, we may commence with the first type of measurement that is usually performed on the sample sets we have investigated, although these steps may be different for other magnetoelectric systems.

4.7.1 Temperature dependence

This stage of the measurement serves to obtain the maximum of the ME effect in dependence of sample temperature, with the change in the effect usually being associated with the structural phase transitions of the BTO phase. This would be equally interesting for other constituents that have phase transitions within the range of measured temperatures, or other parameters of importance that show temperature dependence. The behavior of BTO is well-known in its bulk form, but can shift depending on the crystallite size present in the composites. As the recording of one point takes considerable time compared to a standard DC magnetometry measurement, this sequence can only be performed in "settle" mode, with the temperature being stopped and stabilized at each set point before the measurement commences. Faster measurement types usually utilize the "sweep" routine whereby the temperature is ramped at a constant small rate such as 2 K/min while measurements are performed at predetermined points that the sample temperature passes through. In addition to using the "settle" mode, it has to be ensured that the sample remains centered in the sensing coils of the gradiometer. While DC measurements can account for a shift of the W-curve with every measurement, this is not the case for our ME measurements, as the change in magnetic flux is not brought along by moving the sample through the entire coilset. To avoid an unwanted drop in the signal amplitude due to the thermal expansion or contraction of the 1.5 m long sample rod, a centering scan is performed at every temperature point. These consist of a single movement of the sample through the coilset, using the static magnetization to determine and re-adjust the sample position. This ensures that for every temperature dependent ME measurement, the sample always remains perfectly centered in the coilset, avoiding an unwanted drop in the magnitude of our values due to thermal expansion of the sample rod.

4.7.2 Magnetic field dependence

After establishing the temperature for the highest ME effect, the next step consists of doing the same for the applied static magnetic field. The easiest way to accomplish this is by using a standard $M(H)$ magnetometry sequence, but in addition to recording the static magnetic moment, the ME measurement is also performed at each field step. This allows the recording of two curves, $M(H)$ and $ME(H)$, using just one field sweep. In the case of the samples discussed

in this thesis, we are looking at the properties of the ferrimagnetic constituent, namely the field dependence of its magnetostriction, which influences the strength of ME coupling, while also recording the standard parameters of magnetometry such as saturation magnetization, coercive field and remanence. Due to effects of remanence, slightly different maxima are visible, depending on the previous history of the sample (arriving from high positive or high negative fields). We usually elected the maximum with the higher amplitude as our optimum magnetic field for subsequent measurements.

4.7.3 Electric field dependence

The last measurement type can be considered as the most important one, as it provides the data from which we obtain our quantitative analysis of the coupling. Once the temperature and magnetic field dependence have been determined, it's rather straightforward: Using the optimum temperature and optimum magnetic field, provided they make physical sense (such as not using high temperatures in the case of suspected leakage currents generating the signal), we simply ramp down the electric field amplitude from the maximum value to almost zero, recording 10-40 data points in between. These data points, once analyzed via linear fitting, provide the slope, which can be directly translated into the converse ME coupling coefficient. Further information on this is provided in the upcoming section 6.2.1 while section 6.2.2 provides insight into our error estimation for this procedure.

4.8 Pitfalls of the converse ME setup

When using this setup, it's very important to consider the validity of the data, in terms of determining whether the values we measure are really based on the magnetoelectric coupling we want to characterize, or are the result of any stray or parasitic effects. Due to the fact that the setup is self-built, no manual exists to tell the user what to look out for, so the following explanations are based on experience and a lot of trial & error that went on during the characterization of these samples, especially at the beginning of our cooperations.

4.8.1 Apparent ME signal from conductivity

The process of the temperature dependent measurement has been explained in section 4.7.1, its purpose being the characterization of the ME effect with regards to structural phase transitions, so that the optimum temperature for later measurements can be determined. This step, however, is even more important than it seems at first: The knowledge of the phase transitions, in this case of BTO, as shown in Fig. 3.3, allows us to make sure that the ME effect we can see in the raw data and also the measurement data, is in fact a signal caused by strain coupling between the piezoelectric and magnetostrictive constituents. It can occur that a stray signal also plays a part in these measurements, which can happen for two reasons. The most obvious one is the presence of a wire loop in the vicinity of the sample, which acts as a small solenoid. Any magnetic field generated by it will have the exact same frequency of the input signal, and thus also of the signal from actual ME effects, if those are present in the sample. This poses a significant problem: The main method of noise rejection utilized by the measurement process inherent to the MPMS relies on a lock-in amplifier. With the stray signal having the exact same frequency as the input and measurement signal, it can completely bypass the lock-in filtering and distort our measurement data. Thankfully, there is a simple solution to this problem, as contained in the general description of the setup (4.6): One has to make sure that no loops are present in the wiring when assembling the sample holder. If loops keep appearing, the wires have excessive length and need to be shortened. This of course decreases the margin for error when performing the assembly of the sample holder, since the thin wires are easily severed. Still, it's an important and straightforward precaution.

The second large source of signal from conductivity is of a more complex nature: It's caused by excessive leakage currents through the ceramic sample, which was most apparent in some of the spark plasma sintered (SPS) samples (see section 6.2.3), due to the (3-0) connectivity scheme giving rise to an interconnected network of CFO structures that propagate through the sample. The complex structure of the ME ceramics used in this work is nicely illustrated in the TOF-SIMS images of the BCZT-NFO sample shown in Fig. 6.58 from Ref. 126. We can see that there is a very complex, and irregular pattern of the phases, which in the case of that sample set was not a problem, as it mostly crystallized in the (0-3) pattern, with the

more conductive NFO grains being surrounded by the BCZT matrix. If this were the other way around, as in the case for the SPS samples, we have a large number of paths that offer higher conductivity, so that a small current will flow through the sample when a voltage is applied during the converse ME measurement. If we assume a perfect sample that simply consists of a homogenous material of a certain conductivity, the current would flow directly from one electrode to the other, in z -direction relative to our second order gradiometer, and thus not induce any magnetic flux that the SQUID would pick up. However, in reality, the samples are not ideal, and it can easily happen, through grain boundaries, defects, or the general shape and morphology of the two constituents, that small current loops are present in the sample. The superposition of a multitude of these is sufficient for the SQUID to see a signal of significant strength, which is itself superimposed onto any signal stemming from actual ME effects. Even if the sample is not magnetoelectric, we would be able to see these effects from conductivity. And just as it was the case for the small wire loops, the lock-in amplifier is unable to reject this kind of stray signal, as it has the exact same frequency as the applied voltage.

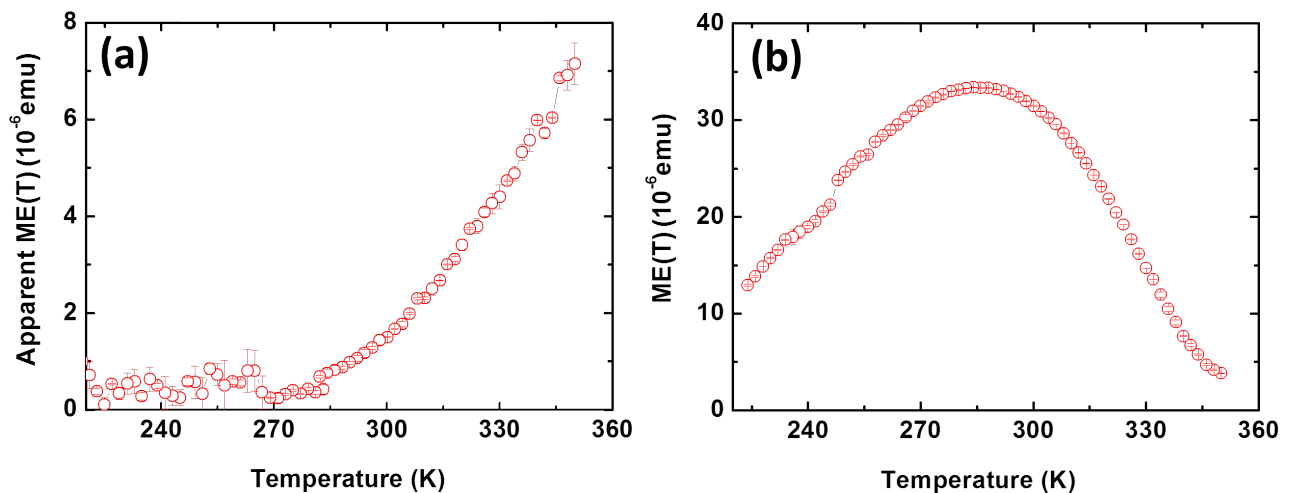


Figure 4.23: Apparent ME signal from leakage currents in a temperature dependent converse ME measurement for a CFO-BTO 50-50 sample produced by SPS (a) compared to a ceramic of the same composition with higher resistivity from conventional sintering (b), adapted from Ref. 45, reprinted with permission.

This pitfall was discussed briefly in Ref. 45, from which Fig. 4.23 is taken. It shows a comparison between two samples of equal 50-50 CFO-BTO wt% composition, with the curve in (a) representing an early attempt at the SPS fabrication technique, while the curve in (b) was recorded on a sample that was conventionally sintered. There are two telltale signs of the signal we see in (a) not being generated by a magnetoelectric coupling in the sample: At low temperatures, the signal is very low and noisy, being indicative of the non-poled state of the sample, caused by its conductive nature preventing effective poling. More importantly, at high temperatures, the signal shows a very strong and monotonous increase, with no sign of

the BTO phase transition near 285 K being visible. Meanwhile, the sample in (b) shows the expected peak at this temperature, with the data points being characterized by low noise and variance. These observations are strong indicators for a stray signal caused by current flow through a leaky sample in (a), with the increase at high temperatures being caused by the increasing number of charge carriers that become available due to thermal excitation. Because of this, the temperature dependence of the magnetoelectric effect, even when it's not shown in publications, was always recorded for every sample that is discussed in the results section.

Additionally, the magnetic field dependence, $ME(H)$, is also an important indicator, as the lack of a characteristic peak, caused by the magnetic field dependence of the magnetostriction λ in the sample, can also be an indicator for the signal being caused solely by conductivity effects. In this case, a more or less constant signal is observed, which, in theory, would still allow one to observe ME signals, as the effects from magnetoelectric coupling and conductivity are superimposed. However, it's often the case that very leaky samples also make it impossible to perform proper poling, with the residual ME effect therefore being rather small. One very recent example of a sample with strong leakage current is a composite made from Terfenol-D and BTO in 40-60 wt% composition, as mentioned in the outlook, for which the electric and magnetic field dependence of the induced magnetic moment is shown in Fig. 4.24. This sample represents a textbook case of strong conductivity effects, with an exponential increase of the apparent ME signal with rising temperature (a), and with no discernible reaction to magnetic field application (b).

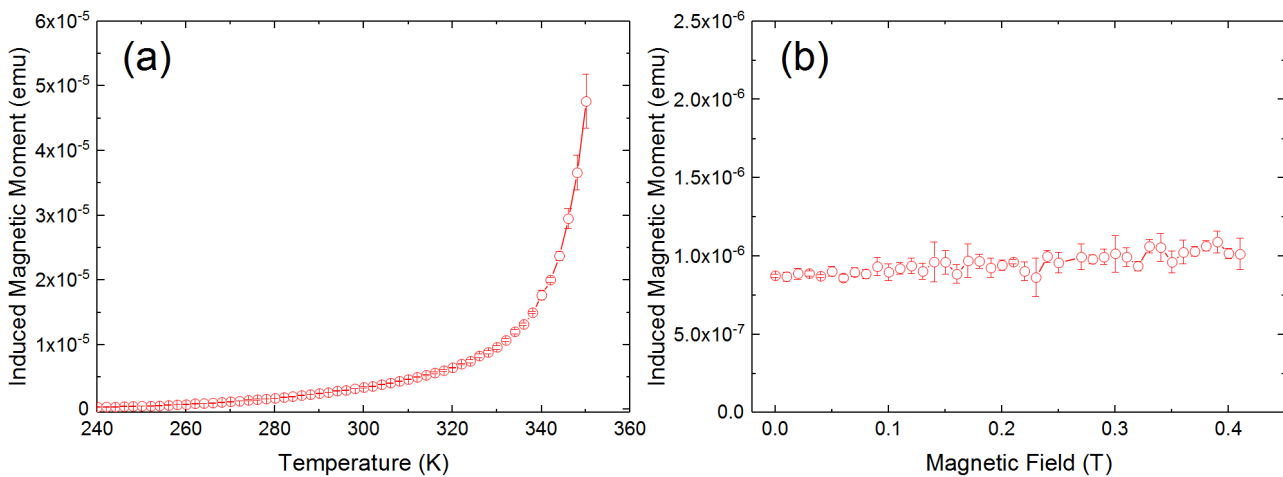


Figure 4.24: Apparent ME signal from leakage currents in temperature (a) and magnetic field dependent (b) measurements of a Terfenol-D - BTO 40 - 60 composite sample.

As described in the results chapter, we will encounter a sample that shows temperature dependent results that are highly indicative of leakage currents, but were still able to see the typical magnetic field dependence of the magnetostrictive phase in section 6.2.3. This clearly shows that the underlying ME coupling can sometimes still be characterized due to the superposition

with stray signals from current flow, unless the latter is so large that it completely overshadows the ME coupling.

4.8.2 Excessive Joule heating

Furthermore, not being a pitfall as such but a very obvious problem: If a sample has such a low resistance that the current flow through it becomes substantial, it can happen that the sample is subjected to significant resistive heating, since the amplifier is able to output 34 W in total. This can lead to two outcomes: Either the sample simply becomes hot and melts the sample holder around it until the electrodes or wires become detached, or it heats up so quickly that it disintegrates explosively. We assume that the latter is caused by the inherent porosity of sintered ceramics, with the sudden heating and the expansion of gas within the pores forcing the sample apart from inside. Both of these cases can lead to a destruction of the sample holder assembly and a contamination of the SQUID sample chamber, both of which are time consuming to rectify. This shows how important it is to check the sample resistance before measurements are performed. Due to the complex crystalline nature of our samples, we cannot give a certain resistance value down to which ME measurements are safely possible, as it always depends on the applied voltage. As a rough ballpark figure, if a sample has a resistivity of 100 M Ω or lower, we usually test it by contacting the sample but not yet inserting it into the sample holder or the SQUID. By connecting the sample holder to the output side of the amplifier and starting a dummy measurement, we can easily test whether the sample can deal with the maximum voltage that will be applied during the course of the measurements, additionally checking its temperature with an infrared thermometer. If the sample does explosively shatter, it does so on the workbench, without causing contamination or damage to our experimental setup. If leaky samples need to be measured, this problem can also be avoided by using very low voltages and thus making sure that only minimal heating occurs.

4.8.3 Lack of ME signal due to frequency doubling

This effect was discovered during the measurements of the CFO-BTO composites from the first two publications on magnetoelectric ceramics^{123,124} that concern this thesis. We observed no satisfactory ME signal on a sample that had been previously characterized by the direct measurement of the ME effect in the group of Prof. Lupascu, while the converse ME setup produced only data points that were on the same level as the background noise. After extensive searches for errors in the wiring and sample contacting, the problem was discovered in the raw data: The frequency of the raw signal showed twice as many peaks as expected, as if the frequency of the ME response was doubled relative to the frequency of the applied electric field, which of course meant that the lock-in amplifier was hardly able to see any signal at the frequency it was set to.

At the time, we explained this behavior by samples that weren't fully poled, so not all domains were aligned fully in the electric field direction. This can cause the piezoelectric strain of different grains to have opposing signs, effectively canceling out the linear ME response. The electrostrictive strain would still be present, being proportional to the square of the electric field, and as the response through coupling to the magnetostrictive phase would be present for both positive and negative applied fields, it would effectively double the resulting signal frequency. Following an idea from Dr. Joachim Landers, the problem was solved by using an offset DC electric field, which can be manually set with the standard controls of the amplifier. This was tested on a CFO-BTO 40-60 sample that showed complete frequency doubling, depicted in Fig. 4.25 (a). Some samples only show a certain degree of a phase shifted signal, while this sample had an almost perfectly frequency doubled signal. Testing the offset led to a stepwise reduction of the doubled fraction until it disappeared at roughly equal DC and AC voltages. For peace of mind, the DC voltage was increased to 150 V, with no further changes being visible (Fig. 4.25 (b)).

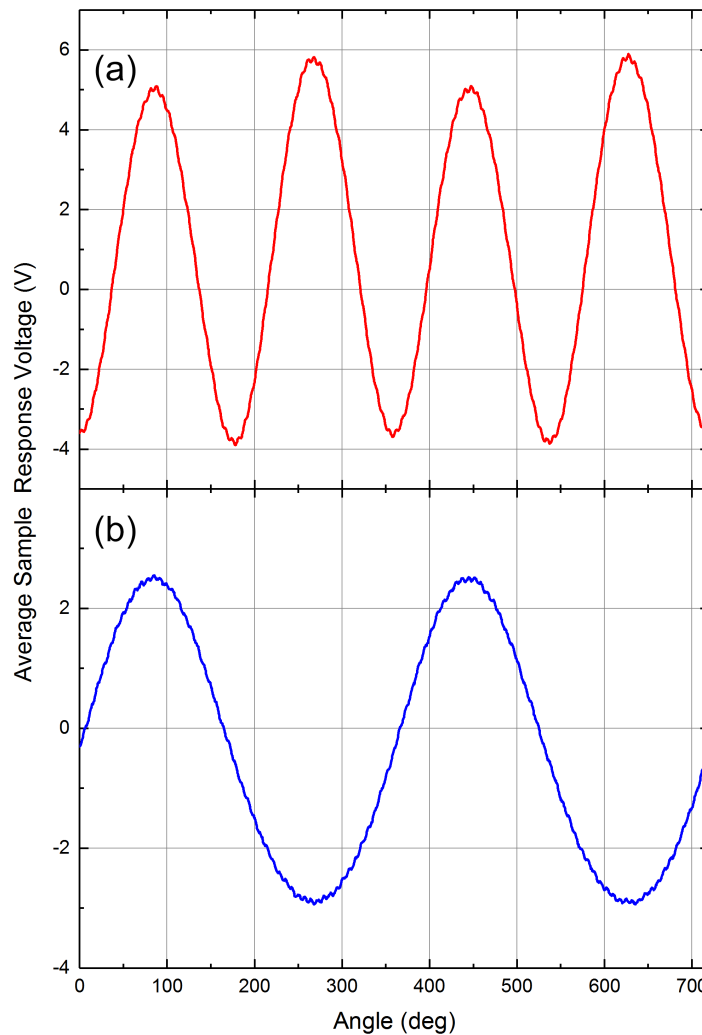


Figure 4.25: Frequency doubling in the raw data of a CFO-BTO 40-60 sample with 200 V AC and no DC offset (a) and with a 150V DC offset and an AC voltage of 50 V (b).

We assume that the DC electric field also helps to at least partially pole the sample. In case of an imperfectly poled sample, or one that cannot be poled due to high conductivity, this enables the measurement of ME coupling, although not under optimum conditions of course. After these initial tests, the usage of an offset was established as standard procedure in order to rule out any errors like this in the future: For all subsequent samples, the standard settings consisted of a DC offset of 100 V in conjunction with a 100 V amplitude of the applied AC electric signal. We thus turned a bipolar signal into a unipolar one, which oscillates between 200 V and 0 V around the 100 V DC offset. To make sure that this doesn't change the magnitude of the recorded measurements, it was tested with several samples. Whenever the samples did not suffer from frequency doubling, the application of the DC offset did not change the strength of the induced magnetization, which we deemed satisfactory to assume that this is valid for all samples. In fact, it was discovered that while some samples didn't display frequency doubling as such, a degree of distortion of the raw signal was sometimes visible, an effect that was also cured by the DC offset, which avoided any distortion and produced near perfect sinusoidal signals for samples that showed ample ME coupling. It therefore became the regular method for sample characterization from that point onward. For peace of mind, we can also refer to the $P(E)$ measurement results that will be described in chapter 6, which are usually measured with electric fields up to tens of kV/cm, with the 1-2 kV/cm maximum fields used for these converse ME measurements being within the linear parts of the polarization response. We therefore do not expect any issues to arise from our offset procedure, or from the general magnitude of electric fields used here.

4.8.4 Effects of measurement frequency

It was discovered fairly early in our work that the frequency at which the AC electric field is applied plays some role in terms of measurement signal stability. Throughout our measurements, the AC frequency was kept between 1 Hz and 11 Hz, as experience dictated that this frequency range was the most optimal for our purposes. However, being experimenters, we wanted to know what would happen if we went to higher (or lower) frequencies, if there is any obvious change in the measured parameters, why these might occur, and why certain frequencies should be avoided. Generally speaking, a check of the frequency dependence was usually performed for at least one sample per set. In some cases, depending on complementary measurements, the frequency was chosen based on the requirements of other experiments, so that for example the same frequency could be used for the measurement of the direct and converse ME effect. In such cases, we sacrifice some signal strength for comparability, as is also done during the selection of measurement temperatures for certain samples.

One comprehensive frequency survey is shown as an example in Fig. 4.26, recorded on a sample from the last set, namely BCZT-NFO 60-40 at 310 K, 0.04 T and 100 V AC amplitude with a

100 V DC offset, for reasons described in the previous section 4.8.3. The AC and DC designation in Fig. 4.26 refers to the setting of the amplifier, with one mode obviously intended for AC and the other for DC signal amplification. We can see that on the AC setting, the amplifier seems to have problems with very low frequencies, which show a stark decrease of the signal, correlated with a similar decrease in voltage that's visible on the oscilloscope. It is therefore a machine property, easily avoided by using only DC mode for our low frequency regime.

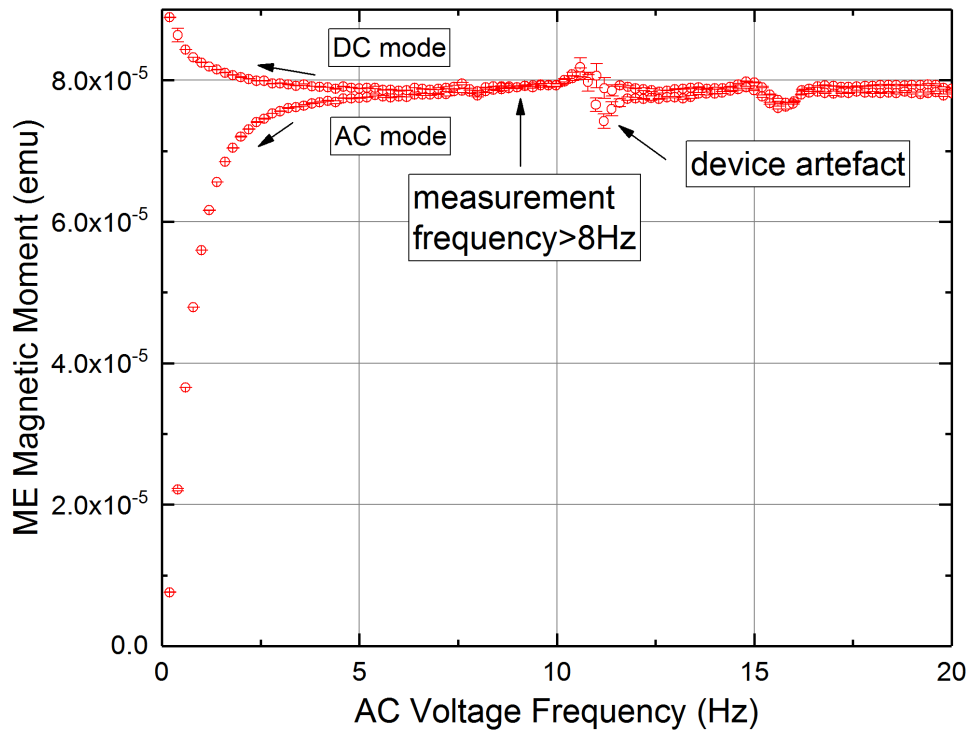


Figure 4.26: Frequency dependence of measurement signal recorded on a BCZT-NFO 60-40 ceramic sample with AC and DC amplifier settings with indicated commonly used measurement frequency.

However, when using the DC setting, an increase of the signal at very low frequencies can be observed. We attribute this to influence from interfacial and space charge (see Fig. 2.10), such as the Maxwell-Wagner effect.¹⁵² It describes a charge buildup in dielectrics with layered or inhomogeneous interfaces, for which sintered composites are a good example. This effect is caused by different permittivities and conductivities of the two constituents at interfaces, leading to a charge accumulation. Generally speaking, the dielectric losses observed in our samples, for example in Fig. 6.44, show a strong increase at low frequencies, which is usually indicative of effects from conductivity. We can thus assume that our samples, especially with higher ferrite content, are susceptible to stray signals from conductivity, which is what we see here at low frequencies. For this sample, which contains 40 wt% NFO, the effect is fairly moderate. However, an increase of this content by 10 wt% has led to an increase of the ME signal by a factor of nearly 3.4 from a frequency of 8 Hz down to 1.7 Hz. It is because of such behavior that the measurement frequency needs to be carefully controlled. We therefore

utilized AC frequencies between 8 Hz and 9 Hz for the majority of the measurements shown here. This way, we could avoid any potential influences from the amplifier or conductivity effects, while also steering clear of the artefact above 10 Hz, which is intrinsic to our device. Going towards higher frequencies, there isn't much observable change in the magnitude of the signal at first, while frequencies above 100 Hz (not shown here) lead to a drop of the measured signal. We attribute this to the fact that this is a self-built setup, with the long, unshielded wires going down the sample rod potentially acting as antennae, with the associated energy loss. Indeed, one could argue that we are susceptible to picking up all kinds of stray signals from the environment. However, this is completely mitigated by the lock-in technique that was described in section 4.6. We also need to keep in mind that our low frequencies are sufficiently far away from known stray signal sources such as 50 Hz from mains electricity, or 16.7 Hz from railway overhead lines, both of course depending on the locally used voltage systems, and the proximity of the device to stray signal sources. This leaves only conductivity effects as a main source for stray measurement signals.

5 Sample synthesis methods and precursor characterization

The focus of this work clearly lies in the experimental characterization of samples for the determination of the converse magnetoelectric effect. Before these experiments can even begin, the samples need to be synthesized first. It is without question that this first step carries with it a lot of significance, as the consistency and quality of the samples decide on the successful outcome of the experiment. As such, a short overview shall be given for each of the techniques that were used to produce the samples used for this thesis. The synthesis was performed in the group of Prof. Lupascu in Essen, and was thus not the main topic in this work, but its importance dictates its inclusion, so that a comprehensive overview can be formed of this topic.

Here, we run into the problem of the boundaries between synthesis and characterization becoming somewhat blurred, as a number of measurements have been performed on the precursor materials after their initial synthesis but before the formation of ceramics via sintering. It was on these ceramics that the most important measurements were performed, but the precharacterization results are still vital to the understanding of the peculiarities of these sample sets. A decision had to be made on how to divide these closely intertwined topics, whether to keep a pure synthesis chapter completely separate from initial measurements or whether to include a number of measurement results in this chapter. I decided to opt for the latter, enabling the reader to more clearly understand the progress and decisions that were made with regards to the synthesis methods following some of the initial precharacterization results. This way, the results chapter can be devoted mainly to the data obtained from magnetoelectric measurements and Mössbauer spectroscopy. This is also done to differentiate between the extensive preliminary characterization that was performed in the group of Prof. Lupascu, allowing us to concentrate only on our specialty topics in greater detail.

5.1 Wet chemical synthesis and characterization of BFO nanoparticles

There are a number of possible methods that can be used to synthesize BFO, each with their own advantages and also problems. These include solid state reaction,¹⁵³ rapid liquid phase sintering,¹⁵⁴ simple carbonate precipitation,¹⁵⁵ chemical solution deposition,¹⁵⁶ high energy ball milling,¹⁵⁷ sol-gel,¹⁵⁸ coprecipitation¹⁵⁹ and pulsed laser deposition.^{160,161} While many of these share some common features, one can divide them into two general groups, one consisting of solid state reactions that involve mixing stoichiometric amounts of precursors, followed by dif-

ferent mixing or milling steps as well as subsequent calcination. The other routes are chemical or soft chemical in nature, with latter denoting the comparatively low temperature required for the reaction to take place. We will concentrate on these, as the particles described in the following were synthesized by a chemical route. Pulsed laser deposition, while a very interesting technique for multiferroics overall, is in a league of its own, as it's strictly speaking not a synthesis technique. The production of samples with this method, while promising good quality and possible applications,⁷⁸ requires a target material of pure BFO to begin with. As such, it's a method that is useful for the production of thin films, but less so for material synthesis and nanoparticle formation.

It becomes obvious when researching BFO synthesis that the goodness or suitability of synthesis routes depend strongly on the individual application. One example is Pechini's autocombustion method, which was originally patented in 1967 to produce lead and alkaline earth titanates and niobates.¹⁶² The method was successfully applied to the production of BFO, with some groups claiming that it fails to produce phase pure BFO in order to promote their own methodology,¹⁶³ while others were able to use this method with good results.¹⁶⁴ We must therefore always remember that the method is only as good as the skill of the experimenter who is applying it, while also depending strongly on the quality and shelf-life of the precursor materials that are used. One has to keep in mind that the method described in the following is one of many, and not without alternatives.

With that said, the sample set we are concerned about was produced by a low temperature and thus soft chemical route that was proposed by Ghosh et al.¹⁶³ This choice was made due to the fact that this preceding work¹¹⁹ had the main purpose of investigating the effect of particle size on the magnetic and ferroelectric properties of BFO. As such, small, monodisperse particles were required, which are not easily obtainable by other, more common methods. Conventional solid state synthesis is performed by mixing Bi_2O_3 and Fe_2O_3 and then heating them to 800°C - 830°C , which often leads to varying amounts of unwanted or unreacted phases such as Bi_2O_3 or $\text{Bi}_2\text{Fe}_4\text{O}_9$. While these can be removed by washing with nitric acid (HNO_3), this leaching of unwanted phases with an acid leads to coarser powder and poor reproducibility.¹⁶³ In contrast, chemical processes have the advantage that the homogeneity of an aqueous solution of salts is preserved, although care has to be taken since such solutions tend to be hygroscopic, which can lead to an unwanted off-stoichiometry.¹⁶⁴

In total, two different wet chemical methods were employed. In the first one, stoichiometric amounts of the Bi and Fe precursors were mixed. In this case, they were dissolved in the form of nitrates $\text{Bi}(\text{NO}_3)_3 \cdot 5\text{H}_2\text{O}$ and $\text{Fe}(\text{NO}_3)_3 \cdot 9\text{H}_2\text{O}$ in 2N HNO_3 under constant magnetic stirring.¹¹⁹ In the first approach, tartaric acid was added to the solution (molar ratio 1:1 with respect to the cations), which was then heated to 80°C until evaporation lead to a viscous

mixture that was then further dried at 150 °C. When all liquid has evaporated, the dry material was ground to a powder and calcinated at either 500 °C or 600 °C for 2 h. In the second approach, the same procedure was performed, but with citric acid in place of tartaric acid, and subsequent calcination at 600 °C as well as 825 °C. As no optimization of the synthesis method based on the characterization of the samples took place, all measurement results recorded on these powders are located in chapter 6, section 6.1.1.

5.2 Synthesis and characterization of CFO-BTO core-shell nanoparticles

The synthesis of precursor materials as well as the manufacturing of ceramic composites from these precursors also took place in the laboratories of the group of Prof. Lupascu in Essen, which shall be briefly described here. This includes some of the measurement methods described in the previous chapter, such as magnetometry and Mössbauer spectroscopy, which have been applied to the precursor materials. This chapter here is intended to show the groundwork behind the finished ceramics, and how the final synthesis and calcination routes were developed according to the results of previous studies.

Preliminary works

An important factor is of course the rather obvious question: Why even bother going through the complex chemical synthesis to form core-shell nanoparticles? To answer this question, we have to look back at previous works that had the same goal of obtaining CFO-BTO ceramics, but noticed quality issues with the samples that were formed. These experiments were performed by V. V. Shvartsman et al.²¹ in 2011, serving as our guide for the described approach to sample preparation and subsequent characterization. The main goal of that work was the synthesis of CFO-BTO ceramic composites and the measurement of the converse ME effect on said composites, with the latter being performed by Dr. Pavel Borisov (University of Liverpool at that time).

The synthesis route used in the approach by Shvartsman et al.²¹ was the sol-gel technique, in which a sol was formed by mixing barium acetate with titanium (IV) isopropoxide at 90 °C. A commercially available CFO powder was acquired by Pi-KEM LTD with a nominal particle diameter of ca. 40 nm, which was then added at a molar ratio of 1:1 of CFO and BTO. The gel formation was initiated by the addition of ethylene glycol to the mixture. After drying and grinding steps, the material was pressed into small discs of 5-7 mm diameter that are of an appropriate size for the ME sample holder setup of the SQUID magnetometer, which has an inner diameter of 8 mm. Further preparation steps included sintering at 1200 °C for 12 h as well as the application of silver paste to the sample faces in order to form the electrodes for ME and

other measurements. The samples formed by this method were analyzed by a number of different measurement methods such as XRD, PFM and MFM, while the electric field dependence of polarization was also measured with a self-built Sawyer-Tower circuit. We will concentrate on the two results that indicated some issues with these samples: MFM results showed "sizes of a few microns indicating strong agglomeration of the initial CoFe_2O_4 nanoparticles."²¹ while polarization hysteresis loops measured at room temperature showed no saturation of the polarization and small remanence compared to bulk BTO, a result considered typical for leaky ferroelectrics. This was a telltale indication of an ineffective coverage of the CFO clusters with BTO, which means that some amount of percolation between the clusters had taken place, providing paths for electrical conductance through the ceramic. There are two problems this causes: It's difficult to pole the sample, which reduces the measured ME effect, and it also leads to erroneous signals during ME measurements. Such phenomena have been discussed in detail in section 4.8.1. Due to the complex nature of such samples, small current loops can easily form, and the small fields these cause have the same frequency as the applied electric field. As a result, the noise-reducing automation and lock-in amplifier of the setup is unable to differentiate this stray signal from an actual ME induced magnetization. Nevertheless, successful measurements have been performed on this sample, with the temperature dependence indicating that the signal does indeed stem from ME coupling rather than from current flow (see Fig. 4 in Ref. 21 and section 4.7.1 for explanation), with the recorded converse magnetoelectric coefficient α_C of 20 ps/m being rather high, surpassing previously reported values for similar structures at the time. Still, the problem of strong particle agglomeration was acknowledged, as the SEM and MFM measurements also showed that the formerly 40 nm particles have grown to micron sized clusters during the sample fabrication process. It was proposed that a more efficient poling process and thus a higher ME effect could be obtained by reducing the degree of agglomeration, which necessitated other synthesis routes than the sol-gel method. This leads us directly to the next step.

In order to try and curb the issues caused by particle agglomeration, it was decided to follow a different routine: Instead of using ready-made CFO particles for subsequent coating, the aim was shifted to the synthesis of core-shell particles. It was hoped that a reduction of agglomeration effects was achievable by this method, ending up with core-shell particles that, come time for sintering, will not be able to agglomerate to such a high degree due to the separation of the CFO grains provided by the BTO shell. The main goal is the utilization of these particles to form a composite consisting of CFO clusters in a BTO matrix, which will be achieved by the fusing of the shells during sintering.

The first step in the overall process was the synthesis of CFO nanoparticles and the avoidance of particle agglomeration, as described in Ref. 121. This was achieved by a synthesis route similar to the co-precipitation method described by Zhang et al.¹⁶⁵ using precursor solutions

containing both Fe and Co, namely $\text{Fe}(\text{NO}_3)_3 \cdot \text{H}_2\text{O}$ and $\text{Co}(\text{NO}_3)_2 \cdot 6\text{H}_2\text{O}$ that were dissolved in distilled water and heated to 90°C under stirring. Particle formation was initiated by the dropwise adding of NaOH until black precipitate appears, indicating that particle formation is taking place. Four different samples were produced using different amounts of NaOH from 0.1 mol up to 2.5 mol. What followed was sonification and drying of the resulting particle precipitate, with repeated grinding and washing steps making sure that no contaminants of the synthesis such as NaOH remained, as well as avoiding particle agglomeration.

In summary, as shown in Ref. 121, analysis of the obtained CFO particles via XRD confirmed the presence of a pure CFO phase, with a crystallite size of 20 nm being determined via the Scherrer equation. Energy dispersive spectroscopy showed that the particle powder contained only the desired elements with nominal ratios, while SEM provided the sample sizes that resulted from different NaOH concentrations. A trend was visible, with the lowest concentration of 0.1 mol providing a mean particle diameter of 38(6) nm while the highest concentration of 2.5 mol resulted in 24(4) nm particles. The magnetic properties were evaluated through $M(H)$ curves, revealing that all samples had coercive fields below 25 mT, lower than the literature value for bulk CFO and agreeing well with reports for similar sized particles.¹⁶⁶ The magnetization at an applied field of 1 T was in the range of 30-50 Am^2/kg , significantly lower than the literature value of 80 Am^2/kg ,²³ a behavior that is typical for nanoparticles of this size range.⁹⁰

These results were deemed as satisfactory in order to continue towards the overall goal, namely the formation of multiferroic ceramics. The most important step in the CFO particle synthesis was the repeated grinding and sonification in order to prevent particle agglomeration, which was identified as the main culprit behind excessive conductivity of earlier attempts at particle formation.²¹ What then followed was the utilization of the synthesized CFO particles for the formation of CFO-BTO core-shell particles, which shall be described next.

Precursor synthesis

Arriving at the synthesis of the precursor materials used for the CFO-BTO composites discussed in the results section, we will take a short look at the first effort that was successful in the synthesis of CFO-BTO core-shell nanoparticles. The first preceding work to achieve this goal and to establish a new fabrication and improved fabrication methodology was completed in 2012 with the synthesis of CFO-BTO core-shell nanoparticles.¹²¹ This publication follows what has become the standard route of synthesis, microscopy and electric property evaluation being performed in the group of Prof. Lupascu, while magnetometry and Mössbauer spectroscopy was contributed by the group of Prof. Wende. This route of sample preparation via core-shell nanoparticles was chosen due to the importance of a well-defined interface between magnetic and electric constituents for the strain coupling and resulting ME effect. The underlying idea was that if the precursor material is composed of ready-made core-shell particles, there will no

longer be a problem regarding the complete coverage of the CFO clusters by the BTO matrix in the ceramic, and no need for the difficult de-agglomeration of hard agglomerates. With the CFO nanoparticle being enclosed by a BTO shell, it was just a question of successfully sintering the material to produce ceramics with low amounts of percolation, in contrast to the previously described sample.

A short description of the synthesis methodology shall be given here, with the fully detailed description being contained in the respective publications.^{120,121} This section is intended to provide a general overview of the manner in which the core-shell nanoparticles were formed, which were then sintered to ceramics in subsequent steps described in section 5.4.

The coating of the CFO particles with BTO shells was accomplished by a two-step process, with the first step being the dispersion of CFO particles in a solution. For this purpose, the particles synthesized in the previous section were added to toluene, heated to 80 °C under stirring and mixed with 30 wt% of oleic acid and oleylamine. This was followed by rotation milling for 12 hours, in order to de-agglomerate the particles, and finally centrifugation and washing steps. In the end, the de-agglomerated particles were suspended in toluene so that a stable ferrofluid could be obtained.

The actual core-shell synthesis takes place through the formation of an organosol by mixing $\text{Ba}(\text{C}_2\text{H}_3\text{O}_2)_2$ with titanium (IV) n-isopropoxide, oleic acid and toluene. This was then mixed with the adequate amount of ferrofluid from the previous step, followed by the addition of anhydrous tetramethylammonium hydroxide (TMAH) while the solution was kept at 90 °C. This agent initiates the gelation and subsequent particle formation, so that the next step only consists of the evaporation of the solvent in order to obtain dried powders. The addition of toluene and TMAH is vital for the formation of the core-shell particles, as an omission of these substances leads to the formation of separate CFO and BTO particles.

After calcination and washing steps, the resulting powders were analyzed by an array of measurement methods, the most important ones of which shall be mentioned here. XRD and SEM were again utilized for a structural characterization, showing no impurities in the CFO and BTO phases, while the overall diameter of the composite particles was found to be 110(18) nm, with a BTO shell thickness of 40-50 nm, determined via TEM.¹²¹ To probe the magnetic properties, Mössbauer spectroscopy was employed, with a spectrum recorded at 4.3 K in an applied magnetic field of 5 T parallel to the γ -ray direction being shown in Fig. 5.1. We can observe magnetically ordered behavior, as shown by sextet subspectra, with no signs of any parasitic phases. In addition to the determination of the standard hyperfine parameters, which showed agreement to literature,¹²¹ we were able to differentiate between the subspectra from the tetrahedral A- and octahedral B-sites, which allows the calculation of the degree of inversion (see

section 3.2). This is done by using the relative spectra area of the A- and B-site subspectra A_A and A_B to calculate the ratio $R_{AB} = A_A/A_B$, which can then be used to determine the inversion parameter S as follows:

$$S = \frac{2 \cdot R_{AB}}{1 + R_{AB}} \quad (5.1)$$

The physical origin of this spectral shape is easier to understand if we look back at Fig. 2.2, and observe how the sublattice magnetizations, depending on their orientation, have the external field added to or subtracted from them, leading to the two subspectra being moved in opposite directions, resulting in the spectra we see in Fig. 5.1.

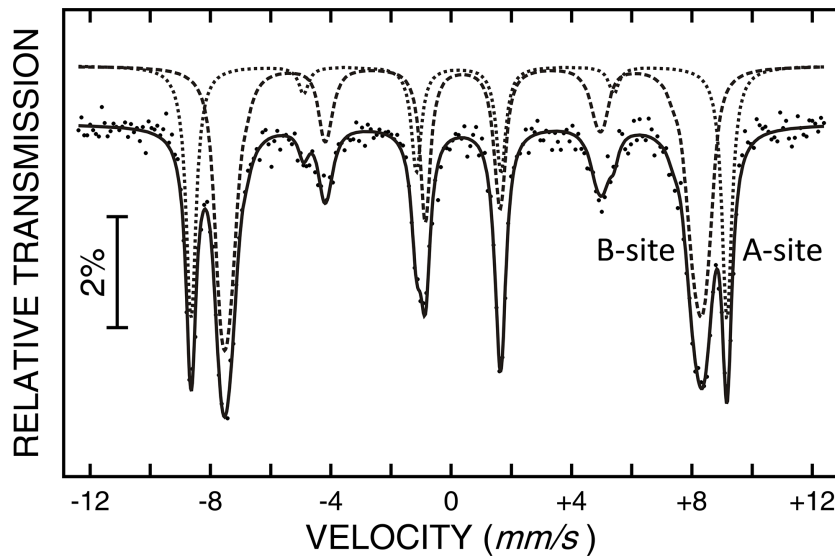


Figure 5.1: Mössbauer spectra of the CFO-BTO core-shell nanoparticles, recorded at 4.3 K in a magnetic field of 5 T applied in parallel to the γ -ray direction. The short-dashed line denotes the tetrahedral A-site while the dashed line represents the octahedral B-site. Adapted from Ref. 121, reprinted with permission.

For this sample, the inversion parameter was determined to be 0.7(2), which is in good agreement with literature values for pure CFO,⁸⁰ as it crystalizes in a predominantly inverse spinel structure (0 would represent a pure spinel and 1 a completely inverse spinel structure). Furthermore, the ratio between lines 2 and 5 relative to the central lines 3 and 4 provides us with the A_{23} ratio, providing information about the spin canting angle, the angle between the applied field and the magnetic moment of the particles. In this case, values of 20° for the A-site and 31° for the B-site were obtained,¹²¹ in excellent agreement with Ref. 167.

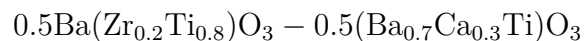
It was thus concluded that the combination of organosol and co-precipitation methods enabled the fabrication of core-shell CFO-BTO nanoparticles with the desired nanostructure, with a particle size of ca. 110 nm and a shell thickness of 40-50 nm. Thanks to the Mössbauer measurement being in agreement with literature values, one can assume that the magnetic properties

of the particles were not disturbed by the synthesis or the presence of the BTO shell. Although the ferroelectricity of the BTO shell was still to be proven at that point in time, it was deemed that these particles were suitable for the preparation of ceramic composite samples with a (0-3) structure. Therefore, all of the CFO-BTO composites discussed in chapter 6.2 were formed from these nanoparticle powder samples. The explanation of the steps necessary to form ceramics is in its own section 5.4, explaining the basics of these methods, as well as their strengths and weaknesses.

5.3 Solid state fabrication route for BCZT-based ceramics

In the later stage of the two groups' publication and cooperation history, after the results from the above described synthesis methods didn't lead to the desired improvements, the decision was made to return to a conventional solid state reaction method, but with different constituents. This is valid for all publications that deal with the BCZT system,^{94,125,126} in which an improvement of the ME effect was sought through the usage of a different ferroelectric material in lieu of pure BTO. It's important to note that this concerns only the formation of the precursor materials, not replacing the pressing and subsequent sintering of the finished magnetoelectric ceramics!

Adhering to the description from Ref. 94, which was the first occasion of this method being used for our ME ceramics, the two-step solid state reaction was performed with reagent grade carbonates CaCO_3 , BaCO_3 , and oxides TiO_2 and ZrO_2 obtained from commercial suppliers. These are then mixed according to the stoichiometry of the final product, in this case:



The reason for this lies in the phase diagram of $(1-x)\text{BZT}-x\text{BCT}$ ^{98,100} as explained in Ref. 94, with the emphasis being placed on the high piezoelectric constant of this composition. The powders were mixed with ethanol, ball-milled for 12 h, then dried at room temperature for 24 h. This was followed by calcination at 1400 °C for 6 h, and ball milling for 10 h using the same parameters as before. The last step consisted of another calcination step, 1500 °C for 6 h, and a last milling step of 10 h with the previously used parameters.

For the BCZT-NFO sample set we will deal with towards the very end of this thesis, this fabrication method is virtually unchanged and doesn't need further explanation. However, during the preparation of the Al^{3+} doped BCZT-CFO, there were some peculiarities during the synthesis that need to be resolved to avoid any ambiguity later on. For this sample set, we again used the mixed oxide route, with the oxides of iron, cobalt and aluminum being mixed in stoichiometric ratios before the established mixing, milling and calcination took place.

Two samples were formed, a regular BCZT-CFO sample with 50-50 weight distribution, and an Al^{3+} doped sample, in which the magnetostrictive phase was made up of $\text{Co}(\text{Fe}_{1.5}\text{Al}_{0.5})\text{O}_4$ rather than CoFe_2O_4 . What's interesting is the striking difference that was observed in the magnetization curves for these precursor powders, shown in Fig. 5.2, which at first seemed to contradict the magnetometry results of the finished ceramics that we will see in Fig. 6.53 in the results section, showing almost equal magnetization at high fields. The sample with the pure CFO phase had a saturation magnetization of $469.3(1)$ kA/m, which is in line with values from literature,¹⁶⁸ while the Al^{3+} doped sample shows only $211.2(1)$ kA/m, significantly lower. Furthermore, the coercive field also displayed a considerable decrease, from $458(1)$ mT at 4.3 K for the undoped sample, down to $28(1)$ mT for the Al^{3+} doped sample. This needs to be addressed before the main data evaluation in section 6.2.6 can be performed.

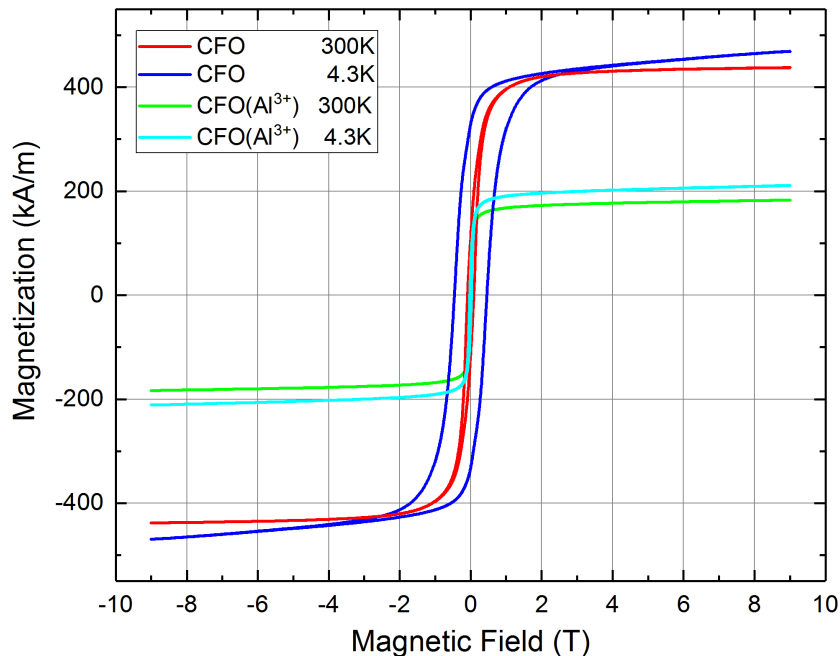


Figure 5.2: $M(H)$ curves of the precursor powders with pure (red, blue) and Al^{3+} doped CFO phase (green, cyan) recorded at 4.3 K and 300 K. Adapted from Ref. 125, reprinted with permission.

Mössbauer spectra have also been recorded on the same samples at a temperature of 4.3 K under an applied magnetic field of 5 T, parallel to the γ -ray direction, with the resulting spectra being shown in Fig. 5.3. The fitting procedure was performed with the established method of using a superposition of a set number of subspectra, based on a free distribution of magnetic hyperfine fields. Both samples show clearly resolved sextets, with the individual subspectra of the tetrahedral A and octahedral B sites being visible. We can conclude that the samples are both in a magnetically ordered phase, with no (super)paramagnetic spectral components or other signs of any parasitic iron-bearing phases being visible.

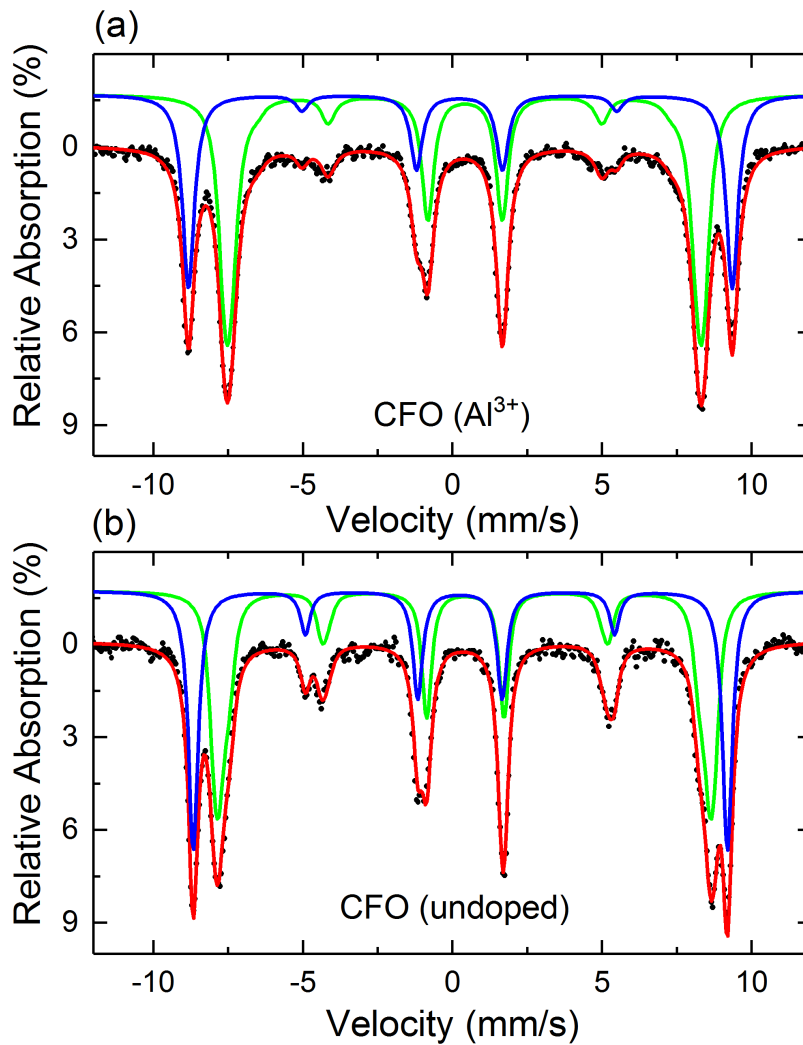


Figure 5.3: Mössbauer spectra of precursor powders with Al³⁺ doped CFO (a) and pure CFO (b), recorded at 4.3 K at an applied magnetic field of $\mu_0 H_{DC} = 5$ T parallel to the γ -ray propagation direction. Adapted from Ref. 125, reprinted with permission.

The A_{23} ratio was used again to obtain information on the alignment of magnetic moments relative to the applied magnetic field. Calculating the mean canting angles for the two Fe-ion sites, we arrive at canting angles of 28° (B-site) and 25° (A-site) for the sample with the pure CFO constituent, while the Al³⁺ sample produced 20° (B-site) and 18° (A-site). Combining these results with XRD characterization that was also performed on these samples, we can further conclude that the Fe ions have a clear preference for the octahedral lattice positions, as both samples show a 60:40 relation between B and A site spectral area, which would point towards an inversion parameter S of 0.8, in good agreement with the value obtained for the CFO-BTO nanoparticles (see Fig. 5.1). With this information, we can begin to explain the sudden drop in magnetization for the Al³⁺ doped sample: From the lower canting angles for the Al³⁺ doped sample obtained by Mössbauer spectroscopy, we can deduce a decrease of magnetic anisotropy, which is directly correlated with the striking decrease of coercive field that could be observed for this sample.

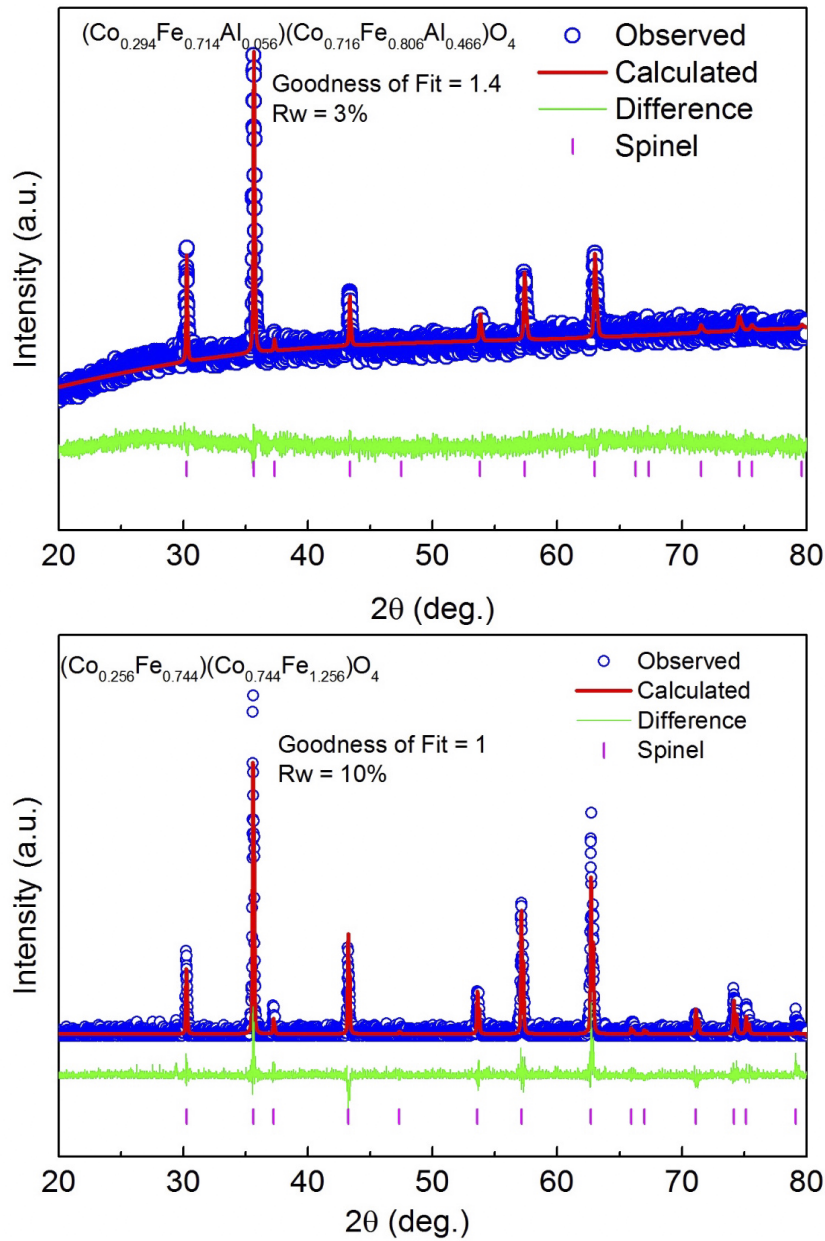


Figure 5.4: X-ray diffractograms of the Al³⁺ doped (top) and pure CFO (bottom) precursor powders, with red line representing the Rietveld refinement. Taken from Ref. 125, reprinted with permission.

This still leaves the saturation magnetization decrease that needs to be explained. For this, we consider the atomic magnetic moments that contribute to the overall magnetization of the sample, namely $5 \mu_B$ for Fe³⁺, $3 \mu_B$ for Co²⁺, with no significant contribution from Al³⁺. For clarity, we refer to the typical structure of sublattice magnetizations in ferrites, previously shown in Fig. 2.2. We can therefore conclude that in the precursor powder we are looking at here, almost all of the Al³⁺ ions ended up on B-sites, which has only negligible contribution to the dominant B-site sublattice magnetization, as we also explained in Ref. 125. This strong preference of the Al³⁺ to occupy the B-site was also shown in literature,¹⁶⁹ and is consistent with the cation distribution that was obtained from XRD spectra, displayed in Fig. 5.4, showing

that 88 % of Al^{3+} is located on the B-site, with no discernible change visible in the distribution of Co^{2+} ions. As a result, the Fe^{3+} ions displaced from the B-site now move to the A-site, increasing the A-site magnetization. As CFO is ferrimagnetic, with the net magnetic moment being the result of the difference value between the two sublattices, we now witness the case of the two sublattice magnetizations being more equalized than in pure, undoped CFO. This is the underlying reason for the striking difference in magnetic properties between pure and Al^{3+} doped CFO, a result we will refer to when dealing with the evaluation of the ceramic sample data in section 6.2.6.

5.4 Fabrication techniques for ceramics

As mentioned in the previous section, the sintering process plays a critical role, influencing the quality of the final sample that will be subject to the main body of measurements in the results section. While the synthesis chapter dealt with the methodology, quality and properties of the precursor materials, this chapter deals with the transition from precursor to final ceramic. Even when we start out with good quality precursor materials, as it was the case at the stage of 2013 publications,¹²² it's the final pressing and sintering process that ultimately decides on the macroscopic magnetoelectric properties.

5.4.1 Conventional sintering procedure

The procedure described here shall be known as the standard or conventional sintering method, mainly to set it apart from the other methods that were attempted during the course of the cooperation. The first step comprises the calcination of the nanoparticle powder obtained from synthesis, performed by heating the powder to 750 °C in a conventional chamber furnace at ambient atmosphere for 15 minutes.¹²³ In order to prevent agglomeration, which was identified as a major quality issue in the final ME ceramics,²¹ repeated ball milling was performed in order to break down any agglomerates that may have formed. After that, the obtained powder was pressed into a pellet with a hydraulic press, applying 2500 MPa of uniaxial pressure. Depending on the size of the used press punch, the samples were usually made with a diameter of 5-6 mm and a thickness of roughly 1 mm, the latter of course being dependent on the amount of sample material, provided that the same pressure is used. In the course of this work, sample thickness ranged from 0.6 mm to 1.4 mm, which has to be taken into account when calculating the effective applied electric field.

The final step, namely the actual sintering process, follows directly after the pressed powder pellets have been formed. They are inserted into a chamber furnace at ambient atmosphere, with the temperature being raised at 6 K/min from room temperature up to 1200 °C, a temperature that was held constant for two hours. Following these steps, the oven was switched off, allowing the sample to cool naturally.

5.4.2 Spark plasma sintering method

This method was used in an attempt to improve the magnetoelectric properties by obtaining dense ceramics with nanometer grain size, which were expected to have a high specific interface area per volume compared to conventionally sintered ceramics. It's generally known that ferroelectric and magnetic properties are strongly size dependent,^{90,170} so it was planned to observe the effect of reduced particle size on the ME coupling coefficient. The main idea is based on the application of a high voltage electric pulse during the usual application of pressure to the

sample powder. Instead of first pressing a powder into a pellet and then sintering it into a ceramic, both steps are combined into one.

The precise methodology is described in section 2 of Ref. 123. In short, the sample powder is inserted into a specialized spark plasma sintering system (FCT HP D5), with steps being taken to insulate it from the sidewalls of the die so that the current only flows through the sample faces between the two press punches. A uniaxial pressure of 35 MPa was applied to the sample, with a pulsed electric current being used to heat it to 1000 °C at a rate of 100 °C per minute. After being held at high temperature for 5 minutes, the sample was cooled to 500 °C, again with 100 °C per minute, and then onwards to room temperature by natural cooling and no temperature control, with the pressure being released during this phase as well.

The motivation for the usage of this method lies in the very high heating rates that can be achieved by the described electric pulse heating. As mentioned in Ref. 123, it's expected for this process to significantly decrease the densification time, to mere minutes compared to the two hours of the conventional method. More importantly, it's supposed to suppress grain growth and reduce diffusion at grain boundaries. One would expect a system with less agglomeration, smaller magnetic clusters in the ferroelectric matrix, and clearly defined grain boundaries, maximizing the interface between the two phases. This method was previously used for the densification of BTO^{171,172} while Ghosh et al. were also successful in the formation of multiferroic nanocomposite CFO-BTO ceramic samples via SPS.¹⁷³

5.4.3 Poling procedure

One crucial step that is often neglected consists of the poling of the samples, which decides between the ability, or lack thereof, to observe magnetoelectric coupling. This was explicitly characterized and tested in Ref. 124 by comparing results for a poled and de-poled sample, which will be explained in detail in 6.2.4. The physical principles behind the procedure have been explained in section 2.2.3, while modeling and simulation of its effectiveness has been performed by Ma et al.¹⁷⁴ The technical procedure¹²³ consists of contacting the sample, akin to how it's done for the ME measurements, placing it into insulating silicon oil and applying a high electric field, in our case 12 kV/cm, while heating the sample to 415 K (see Fig. 3.3). This was followed by passive cooling (without control) to room temperature while the electric field remained switched on. Unless stated otherwise, this procedure was performed on all samples, as it was quite clear from the outset that the ME effect would be severely diminished without it.¹⁷⁵

6 Results

6.1 BFO nanoparticles

We now arrive at the results chapter, starting off with the intrinsic single-phase multiferroic, BFO. After the formation of nanoparticles via the synthesis route described in section 5.1, a number of measurement methods were utilized to obtain a concise picture of their overall properties, enabling a precise and proper evaluation. As previously mentioned, this work contains a very large amount of experimental procedures, making it necessary to prioritize some of them. Because of this, not all of the methods and results from Ref. 119 are shown here. Instead, we mainly concentrate on the ones that are most important to our subsequent evaluation of the Mössbauer data, which is in its separate chapter, while the other measurement results are summarized in the precharacterization chapter below.

6.1.1 Precharacterization

Characterization performed on these samples included SEM measurements (ESEM Quanta 400 FEG), the obtained micrographs being displayed in Fig. 6.2, taken from Ref. 72, with (a) and (b) showing powders calcinated at 500 °C and 600 °C, respectively. The according size distribution from Ref. 119 is shown in Fig. 6.1, with the particles having mean diameters of 54 nm (500 °C) and 150 nm (600 °C), while particles from the citric acid route heated at 825 °C grew to a much larger size of 1-2 μm. These samples shall be referred to by their size from here onward, while the sample with 1-2 μm particles will be referred to as the 1 μm sample due to its bulk-like properties negating the need for a precise size indication.

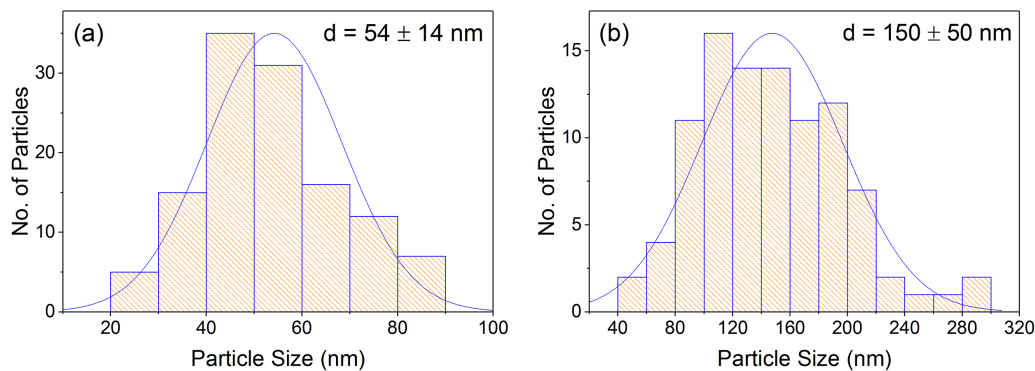


Figure 6.1: Particle size distribution of the 54 nm (a) and 150 nm sample (b), adapted from Ref. 119, reprinted with permission.

Additional analysis was performed via TEM (Philips Tecnai F20): Fig. 6.2 (a) and (c) show micrographs of the 54 nm powder calcinated at 500 °C. HRTEM measurements were performed

to gain deeper insight into the crystal structure, with distinctive line patterns and higher order diffractions in the Fourier transformed image inset in (d) clearly pointing towards a monocrystalline character. Structural characterization was further accomplished via XRD spectra (Siemens D-5000, Cu K- α radiation) recorded at room temperature, the results being shown in Fig. 6.3.

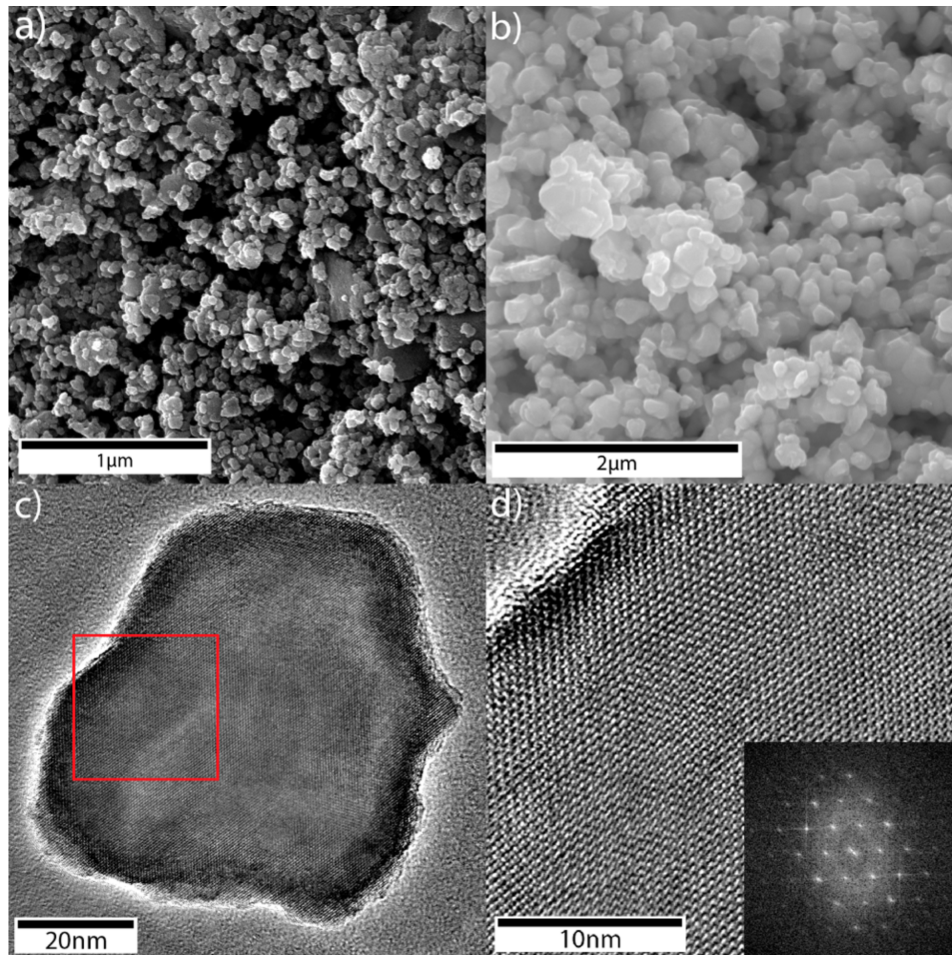


Figure 6.2: SEM images of the 54 nm (a) and 150 nm (b) sample; TEM image of a single particle from the 54 nm sample (c) and a magnification of the marked region (d) with the corresponding fast Fourier transformation (FFT). Taken from Ref. 72, reprinted with permission.

The BFO phase is clearly observable and in good agreement with reference data (PDF 71-2494). The 54 nm sample shows slight line broadening due to the small particle size, while the 1 μm sample contained minor amounts of a parasitic phase $\text{Bi}_{25}\text{FeO}_{40}$. A slight increase of the unit cell volume was also observed, which was deemed as typical behavior for partly covalent oxides, having been determined to take place in other systems below a certain size threshold. For BFO, it was reported by Selbach et al.⁷³ that such an increase only commences at 30 nm and below,⁷³ which deviates slightly from our results. However, there are always small variations in the properties of particles from different synthesis methods, with Selbach et al. having utilized the Pechini method discussed previously in section 5.1.

Following these precharacterization steps, we move towards the field of magnetism and ferroelectricity. As BFO is an antiferromagnet, standard magnetometry is usually not fully suitable to resolve the transition temperatures. Furthermore, in order to measure the Néel temperature with this method, one would have to use a high temperature oven insert in the case of our magnetometer, with the low pressure helium atmosphere and high temperatures promoting the decomposition of BFO, often leading to irreversible changes to the sample during the measurement. As a result of these observations, no high temperature magnetometry data will be shown here.

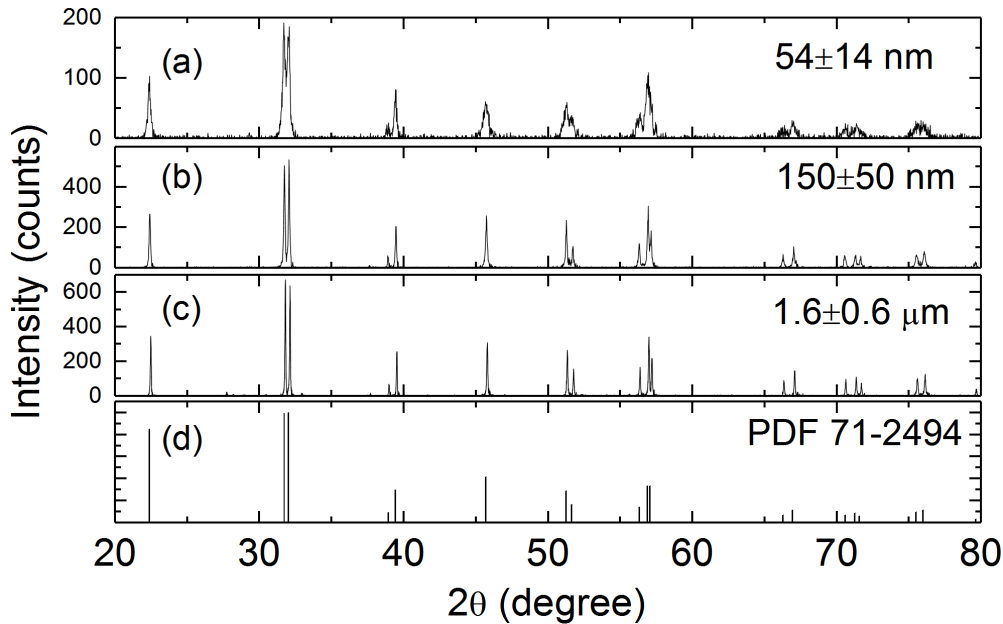


Figure 6.3: X-ray diffractograms for BFO nanopowders with different particle sizes, with the reference data shown in (d). Adapted from Ref. 119, reprinted with permission.

Nevertheless, it was possible to perform regular zero-field-cooled (ZFC) and field-cooled (FC) measurements of the 54 nm and 150 nm particles between 5 K and 300 K in an applied field of 0.1 T. This is carried out by cooling the sample down to 5 K at zero applied field, then ramping the magnetic field to 0.1 T and recording the magnetization while heating the sample to 300 K, representing the ZFC branch of the curve. The FC branch is recorded while cooling the sample down again from 300 K to 5 K in the applied magnetic field. This allows us to analyze the temperature dependent macroscopic properties of the particles via their net magnetization. The results are shown in Fig. 6.4, with the 150 nm sample showing a clear splitting between the ZFC and FC curves at temperatures below 200 K. Although such effects have been observed in thin film¹⁷⁶ and bulk samples⁶³ as reported in Ref. 119, the reason for this behavior is still a matter of debate. Possible explanations could be a spin-reorientation transition,¹⁷⁷ spin-glass transition¹⁷⁶ or surface phase transition.¹⁷⁸ Generally speaking, our studies related to a possible coupling between electric and magnetic properties revolve around the Néel temperature, and as such, the described transitions are not the main focus with regards to the intrinsic properties

of BFO. In contrast, the 54 nm sample shows a clear peak in the ZFC curve at approximately 40 K, a behavior that has also been described by Park et al.,⁶⁴ although the peaks in their work appeared at higher temperatures (95 K) for similar particle sizes (51 nm) while being strongly broadened. As we are well below the Néel temperature, such peaks are usually indicators for the superparamagnetic blocking temperature, with the occurring broadening in the data of Park et al. pointing towards a wider size distribution of their particles.

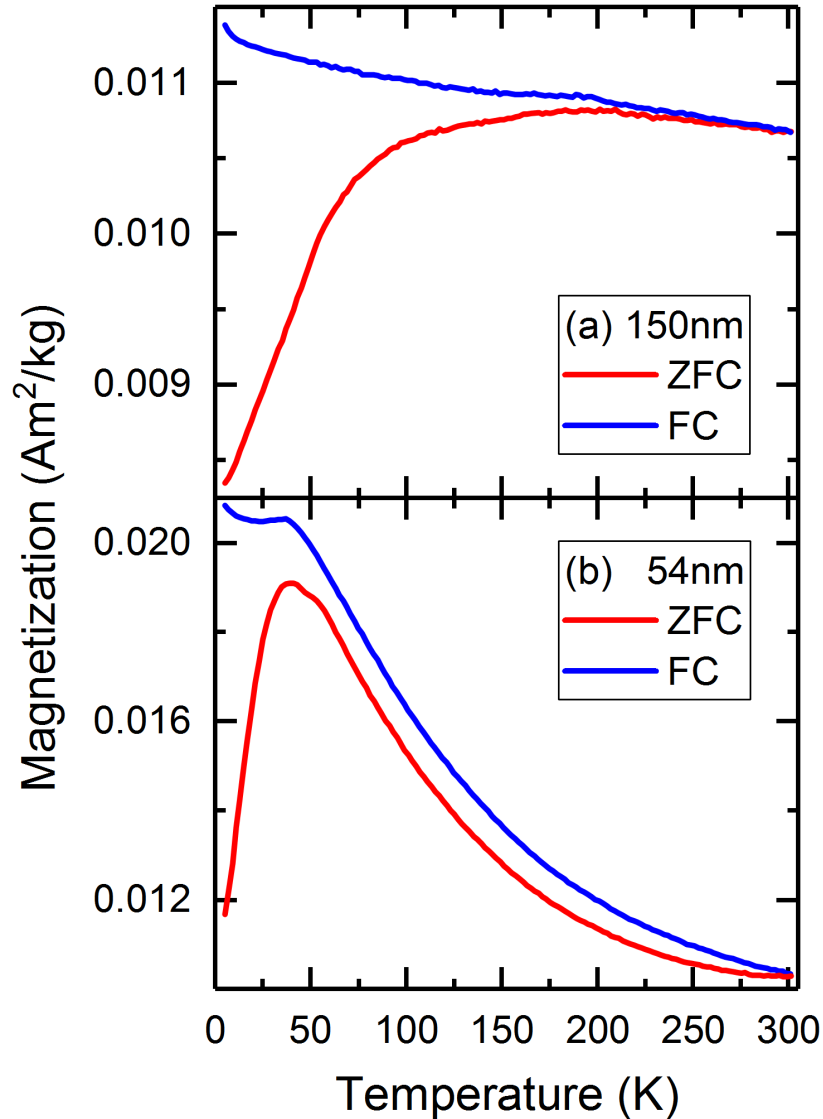


Figure 6.4: Temperature dependence of sample magnetization recorded in zero-field-cooled (red line) and field-cooled mode (blue line) on the 150 nm (a) and 54 nm (b) samples in an applied field of $\mu_0 H = 0.1$ T. Adapted from Ref. 119, reprinted with permission.

Other possible explanations for this feature include magnetic phase transitions, with the intrinsic link of magnetic and electric properties in this multiferroic material also leading to anomalies in dielectric measurements near 50 K, as reported by Redfern et al.¹⁷⁹ Further suggestions include a spin-glass-like freezing temperature,¹⁸⁰ while Park et al.⁶⁴ also proposed a superspin glass state. They claim that the main drive behind the transition into this superspin glass state

lies in the interparticle interactions influenced by finite size effects and the random distribution of anisotropy axes in the nanoparticle assembly, as described in Ref. 119. However, Singh et al.¹⁷⁷ also observed a sharp cusp in ZFC curves of BFO single crystals at 50 K, which would rule out superspin glass states as the underlying cause for this behavior. Instead, the magnetization data was regarded as typical for superparamagnetic blocking behavior, comparable to the cusp of $\gamma - \text{Fe}_2\text{O}_3$ at 72 K.¹⁸¹ The general statement made by Singh et al.¹⁷⁷ referred to this temperature being defined by typical blocking processes of an assembly of superparamagnetic spins, which they qualitatively relate to the presence of small particles, domains or domain walls. We can thus assume that superparamagnetic behavior of the smallest particles in the 54 nm sample is the most likely explanation for the behavior we are seeing here. We can furthermore assume that the particles used in our work, with their narrower size distribution and sharper ZFC peak, offer a more precise overview of the general characteristics of BFO than the particles with broader size distributions from the previous works⁶⁴ mentioned here.

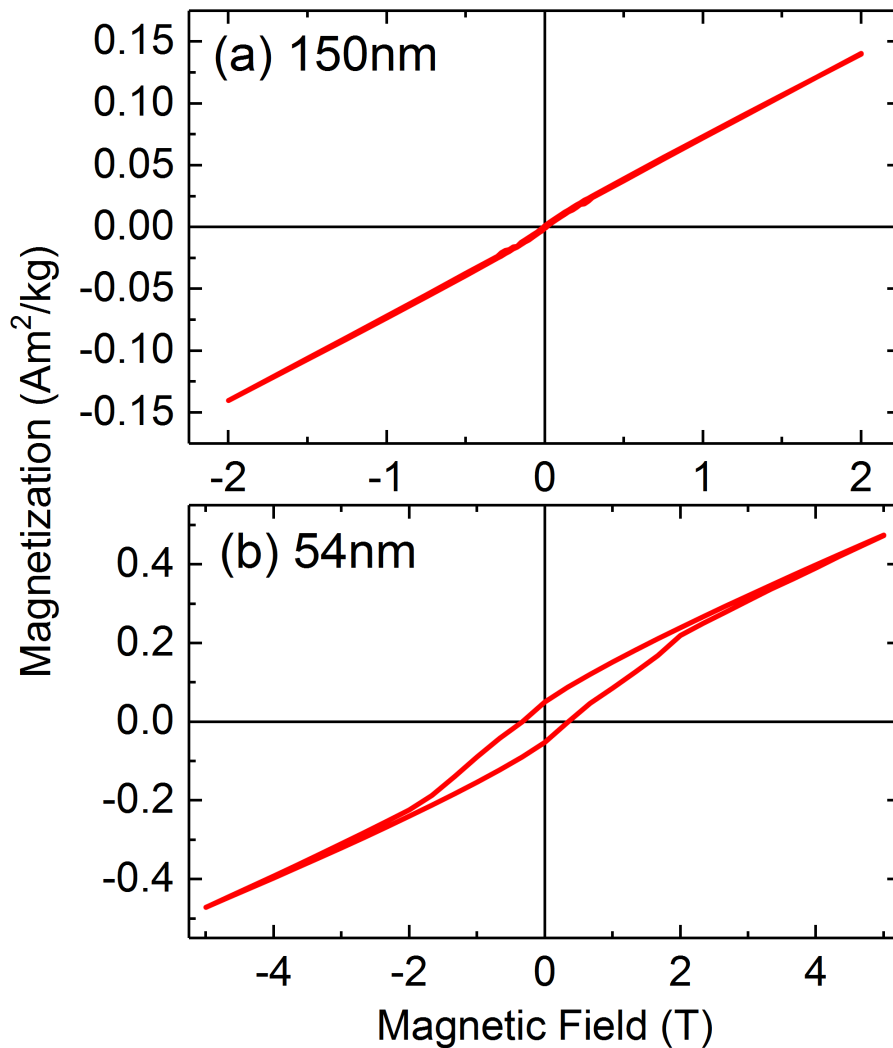


Figure 6.5: Magnetic field dependence of sample magnetization for 154 nm (a) and 50 nm (b) particles, recorded at 300 K. Adapted from Ref. 119, reprinted with permission.

Continuing with field dependent magnetometry measurements performed at room temperature, the results of which are displayed in Fig. 6.5, two main results can be stated. On the one hand, for the 54 nm sample, parameters such as the remanent and maximum (5 T) magnetization values of $0.051 \text{ Am}^2/\text{kg}$ and $0.474 \text{ Am}^2/\text{kg}$ were in agreement with the data reported by Park et al.⁶⁴ On the other hand, a clear difference could be observed between the 54 nm and 150 nm sample. While the larger 150 nm particles showed a completely closed hysteresis loop, consisting of a mostly linear, weak 'paramagnetic' curve typical for antiferromagnetic systems, the smaller 54 nm particles produced a clearly open hysteresis, as visible in Fig. 6.5. This is an important indication, as it shows that sufficiently small BFO nanoparticles have a detectable (macroscopic) net magnetic moment and a magnetic remanence rather than being purely antiferromagnetic, which was previously explained in section 3.1.

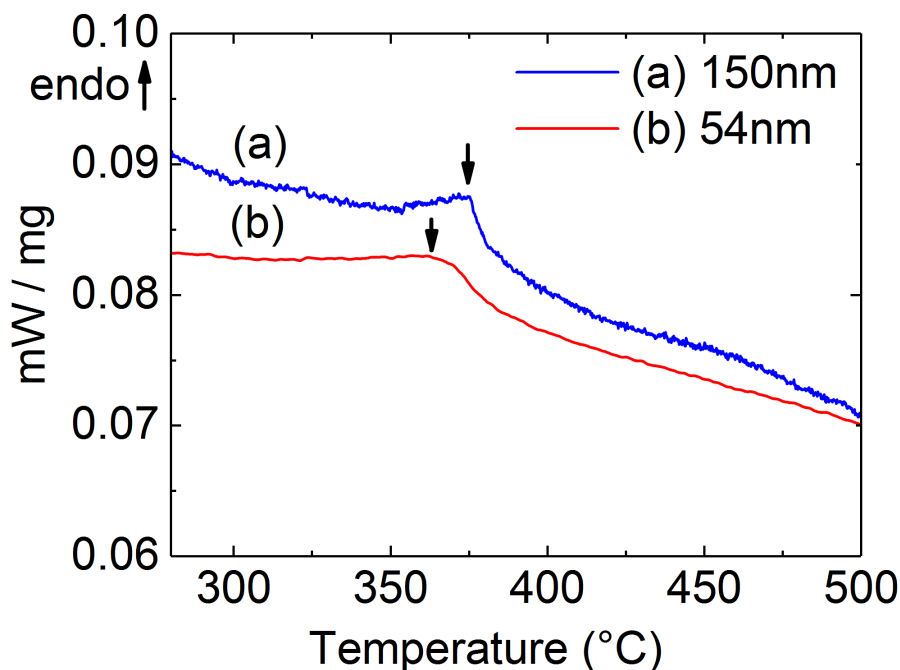


Figure 6.6: Differential scanning calorimetry curves of the 150 nm (a) and 54 nm (b) samples, measured upon heating ($10^\circ\text{C}/\text{min}$), with phase transitions indicated by arrows. Adapted from Ref. 119, reprinted with permission.

As magnetometry was not the most suitable method to determine the Néel temperature for this material, as there is almost negligible net magnetic moment, differential scanning calorimetry (DSC) was utilized for this purpose, with the results for samples with 54 and 154 nm displayed in Fig. 6.6. Both curves feature an endothermic peak, corresponding to the first-order phase transition from the antiferromagnetic (AF) to the paramagnetic (PM) state when crossing the Néel temperature. The transition temperature for the 154 nm particles was determined to be 373°C , only slightly below the bulk Néel temperature of 380°C ,⁶⁵ while the smaller 54 nm particles showed 362°C . In addition to a lower transition temperature, the peak itself was also broadened when compared to the larger sized particles. These are noteworthy observations for the main body of Mössbauer measurements that will be described in detail later on, and can

also be confirmed by reports in literature (see table 6.1). A decrease of the particle size leads to a decrease of the Néel temperature, which can be attributed to finite size effects. Another important factor is the possible relation of the observed decrease in T_N to the behavior of the spontaneous polarization, which shall be analyzed next.

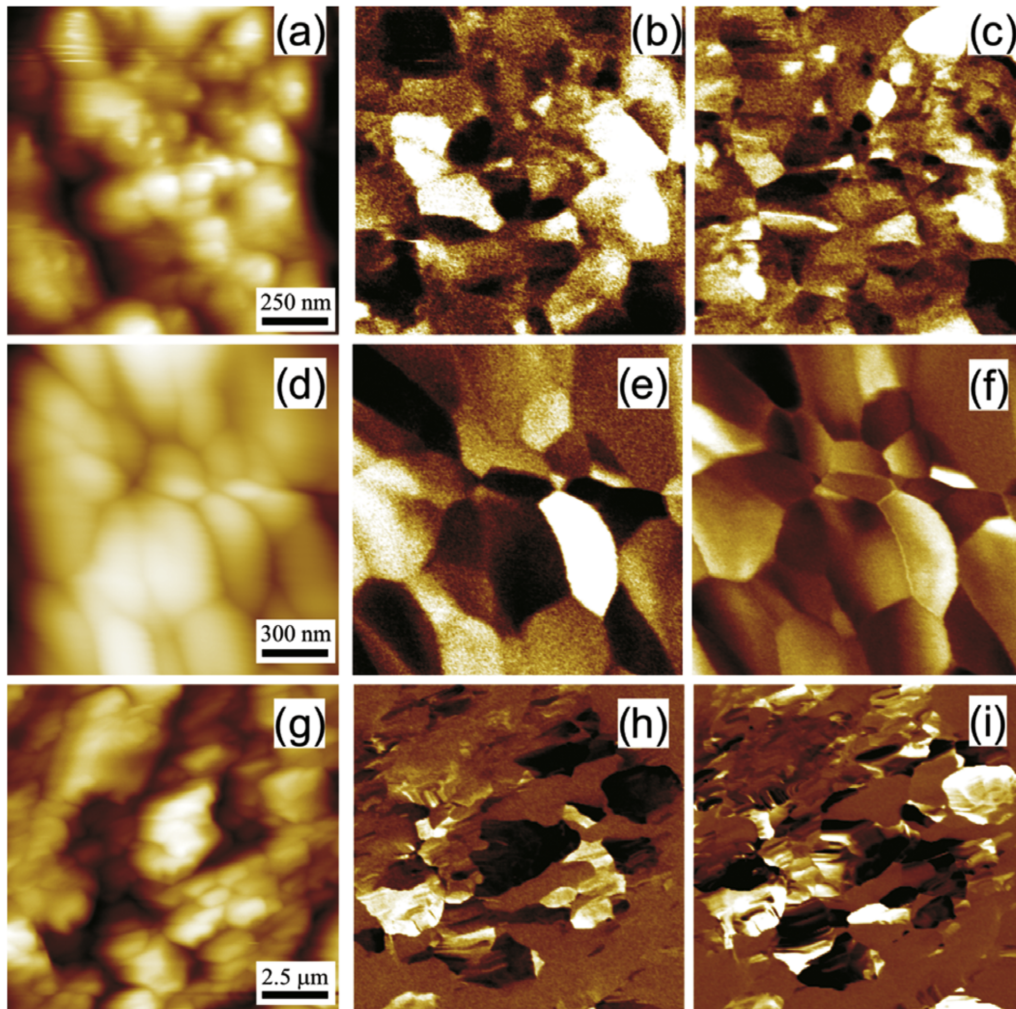


Figure 6.7: Topography (a, d, g), as well as vertical (b, e, h) and lateral (c, f, i) PFM images of BFO samples with mean particle diameters of 54 nm, 150 nm and 1 μm, respectively. Taken from Ref. 119, reprinted with permission.

In order to probe local effects of polarization in dependence of grain size, piezoresponse force microscopy (PFM) was employed, allowing an analysis of both topography and polarization. For this purpose, the particles were embedded in epoxy resin that was finely polished before the measurements. This makes it possible to select specific grains so that their size can be correlated to their piezoresponse, which allows the size dependence of this effect to be analyzed in detail. Fig. 6.7 displays typical PFM results for all three samples, with the left column showing the topography, the middle column the vertical, and the right column the lateral piezoresponse. We can clearly see differences between the latter two columns, with bright and dark areas showing the respective grains that are responsive to the vertical and lateral electric field application,

while the brownish background noise indicates the non-responsive epoxy matrix. It was also observed that a single-domain state becomes favorable below a particle diameter of roughly 80-100 nm and that the larger particles of the 1 μm sample display complex domain patterns, resembling those also found in bulk BFO,¹⁸² which leads to a flattening of the curve towards higher particle sizes (Fig. 6.8).

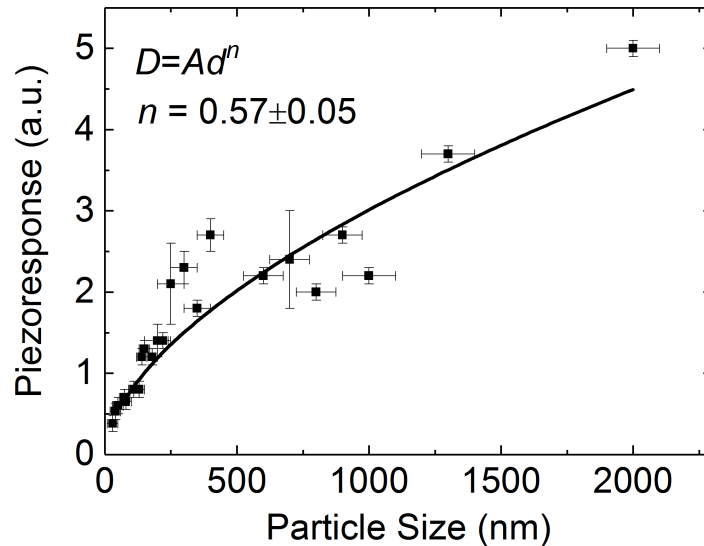


Figure 6.8: Particle size dependence of local piezoresponse (measured inside individual domains), taken from Ref. 119, reprinted with permission.

A problem one runs into during a quantitative analysis is the arbitrary crystallographic orientation of the individual particles, as their random orientation makes it impossible to take all of them into account individually, which would normally only allow an averaged description of the entire sample. Instead, individual particles with large vertical piezoresponse were selected, making sure that a change in piezoresponse depended only on the particle size and not on the orientation. The former could be determined directly by recording the topology of the sample area that is to be used for the PFM measurements. Using this methodology, a number of particles were measured in terms of piezoresponse, the results being displayed in Fig. 6.8. Clearly, there is a dependence of piezoresponse on the particle size, with an increase by one order of magnitude for an increase of particle size from ca. 40 nm to 2 μm . Using a power law approximation $\langle D \rangle \sim S^n$ for this dataset gives us $n = 0.5 - 0.6$, a square root dependence. When we then take into account the proportional relation between the longitudinal piezoelectric coefficient d_{zz} and the spontaneous polarization P_s , we arrive at $d_{zz} \sim \epsilon P_s$ with the factor ϵ being the intrinsic dielectric permittivity. We can deduce that the spontaneous polarization shows a clear size dependence, decreasing when the particle size is reduced.

Again, a comparison was made to Selbach et al.⁷³ and their detailed study of size dependent properties of BFO nanoparticles. In this study, a large number of particles were synthesized at different temperatures and analyzed via XRD for their average size, while DSC was used

to determine the Néel temperatures. As shown in Table 6.1, the clear trend that is visible in Ref. 119 is also observable for our samples: The Néel temperature drops from 378 °C for a bulk reference sample down to 355 °C for a sample with 13 nm particle size. Some differences can be observed, such as the Néel temperature for a 51 nm sample that was determined to be 375 °C, higher than for the particles used here.⁷³ Again, a possible explanation could lie in the different synthesis methods, which is also why the wet chemical method was used for the particles discussed in this thesis, rather than the Pechini route.⁷³

T (°C)	size d (nm)	a_{hex}	c_{hex}	T_N (°C)
410	13.0± 1	5.585(55)	13.83(88)	355± 7
425	13.3± 1	5.587(87)	13.84(17)	360.7± 5.5
450	15.3± 1	5.585(66)	13.84(60)	363.3± 4
500	20.4± 2	5.580(67)	13.852(42)	371.1± 3
550	34.4± 6	5.578(26)	13.859(46)	375.4± 2.5
600	72.1± 18	5.5775(23)	13.863(14)	379.7± 2
bulk		5.5772(04)	13.865(75)	378.0± 2

Table 6.1: Dependence of particle size d , unit cell parameters a_{hex} and c_{hex} as well as Néel temperature T_N on the calcination temperature during synthesis. Data taken from Ref. 73, reprinted with permission.

Furthermore, Selbach et al.⁷³ made a very important suggestion, namely that the polarization might exert an influence on T_N , in addition to finite size effects, steering us onto the path of magnetoelectric phenomena. At first, they purposefully ignored any potential ME influence and concentrated only on size effects, being able to conclude that T_N scales linearly with the inverse volume V^{-1} in the size range where size dependent changes of T_N become observable. It was assumed that this inverse volume dependence of T_N "indicates that the ordering temperature is proportional to the number of antiferromagnetic exchange interactions in a certain size region larger than the magnetic correlation volume".⁷³ However, when observing the correlation between T_N and (s-t), the displacements of Bi^{3+} (s) and Fe^{3+} (t) ions, it can be seen that (s-t) scales linearly with the Néel temperature. Selbach concluded that the AF ordering might not only be influenced by the polarization, but that the former may even be stabilized by it. He proposed that the observed decrease in T_N "could be associated with the decrease in spontaneous polarization quantified by (s-t)"⁷³ in addition to the previously mentioned decrease in the number of antiferromagnetic interactions. This gives an important clue towards the coupling between polarization and antiferromagnetic ordering, which is further substantiated by observations of dielectric¹⁸³ and phonon anomalies near T_N .¹⁸⁴ The latter are rather interesting, as they were determined to be larger by an order of magnitude than on a reference system, EuFeO_3 . This material, while also antiferromagnetic, lacks ferroelectric ordering, again pointing towards an interplay between the two ferroic orders in BFO. It is this intrinsic multiferroic property that we want to deconvolute and observe in detail during our data evaluation.

Our main goal was therefore the characterization of local magnetic properties to uncover the reason for this interplay, and to find a link between magnetic and electric order that was anticipated after the detailed analysis of the Néel temperature's size dependence. The initial expectation was to uncover a way of increasing the weak ferromagnetism found in this material, so that it may become usable with the link to the intrinsic ferroelectric behavior. Clearly, the only way to more closely probe the magnetic properties in detail is by not only using macroscopic measurement methods such as DSC and magnetometry, but to also utilize techniques from nuclear physics, such as Mössbauer spectroscopy. The results of this approach are discussed in depth in the next section, which concludes the precharacterization chapter for this sample system.

6.1.2 Mössbauer spectroscopy results

Before we look at the detailed description of our spectra, it's important to keep in mind that all of the following results have one thing in common: We are dealing with an element specific measurement method, sensitive only to ^{57}Fe , which is contained in naturally occurring Fe with an abundance of about 2.1%.¹³⁴ All of the spectra that have been recorded in the course of this thesis, both for BFO and the upcoming CFO-based samples, are the result of resonant absorption by this small percentage of ^{57}Fe in our samples. There is the possibility of enriching samples with ^{57}Fe in order to significantly increase the rate of resonant absorption, thus reducing measurement time and increasing the signal to noise ratio. This is commonly done for samples with very low iron content, thin film samples with limited thickness, samples with extremely high non-resonant absorption, or due to time constraints when performing measurement at synchrotron radiation facilities. Due to the high price of the ^{57}Fe isotope, this approach is rather costly and not always feasible. In the case of our samples, we are faced with the problem of bismuth being a high-Z element, thus causing a significant amount of non-resonant electronic absorption, strongly increasing the time required to record each spectrum. To improve the quality of our spectra while cutting down on the time needed to record them, an attempt was made to synthesize BFO nanoparticles with a certain amount of natural Fe being replaced by ^{57}Fe . However, due to the fact that the commercial grade Fe-containing precursors such as $\text{Fe}(\text{NO}_3)_3 \cdot 9\text{H}_2\text{O}$ would need to be synthesized separately before the BFO particle synthesis can commence, it would add further steps to the overall process. Most ^{57}Fe is produced as thin metal foil rather than fine powder, leading to additional quality issues. Because of this, the properties of an enriched test sample, such as morphology and particle size distribution, were deemed inferior when compared to the original nanoparticle powders. Therefore, all samples that are discussed in the upcoming chapters remained non-enriched. Because of this, some results, such as the in-field spectra from Fig. 6.9, show a somewhat diminished signal to noise ratio, caused by the comparatively small resonant absorption in combination with technical factors of the measurement geometry that are specific to this cryostat. Due to

the high liquid helium consumption of such measurements, it was not feasible to perform them over an extended period of time, leading to the less than optimal quality of the spectra.

A large number of Mössbauer spectra were recorded on the three samples with 54 and 150 nm as well as 1 μm particle size. The main parameter that was varied apart from the particle size was the temperature at which the measurements took place, ranging from measurements down to Helium temperature (4.3 K) and up to nearly 800 K using the oven setup described in the experimental section 4.3. To find a starting point, we look at the chronology in which the measurements were performed to showcase the development of the theoretical model we use to unravel the magnetic fine structure intrinsic to BFO.

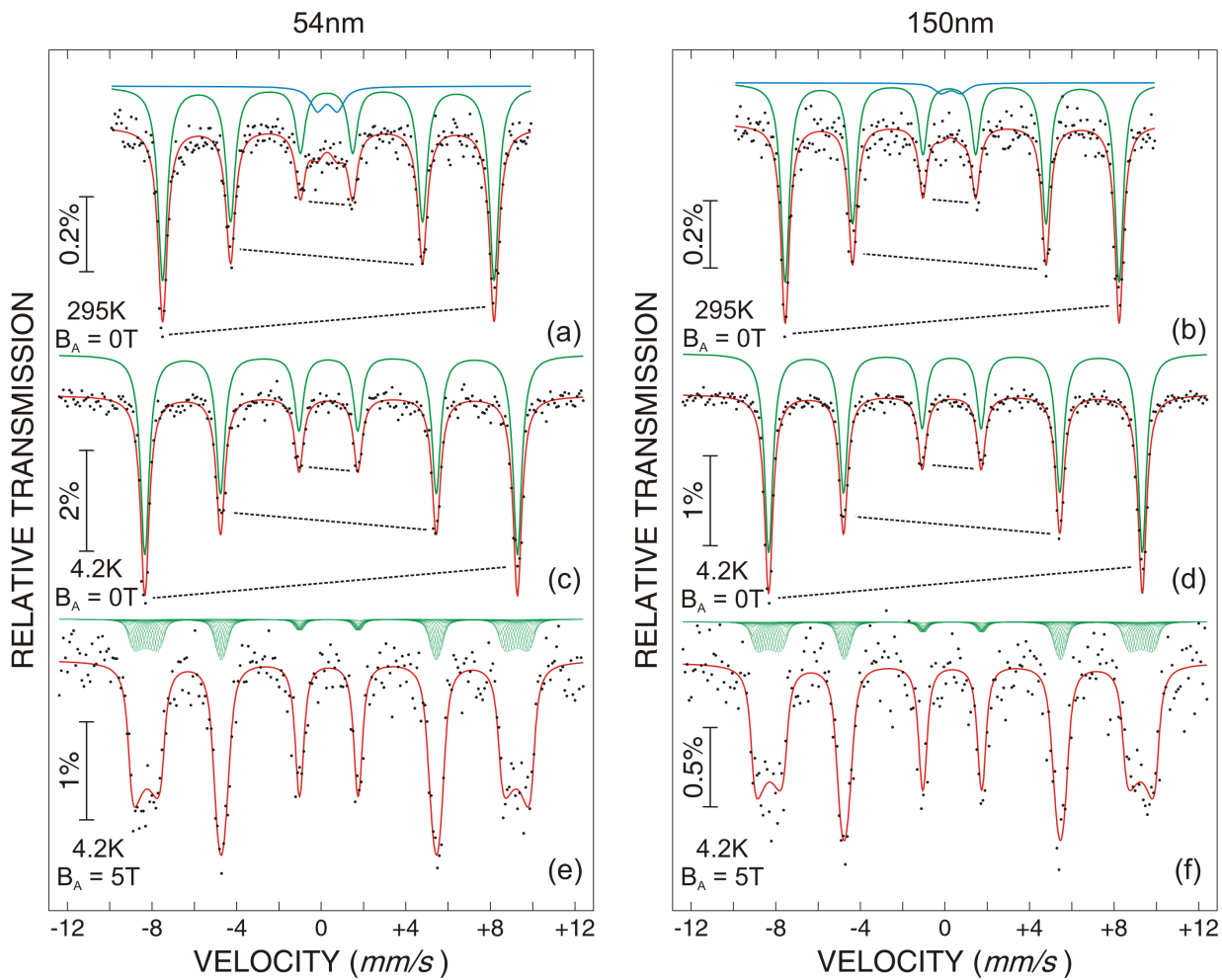


Figure 6.9: Mössbauer spectra of BFO nanoparticles of 54 nm (left) and 150 nm size (right) recorded at room temperature (a,b), 4.2 K (c,d) and 4.2 K in an applied field of 5 T parallel to the γ -ray direction (e,f). The dashed lines are a guide to the eye, representing the asymmetry of spectral lines explained in the text. Taken from Ref. 119, reprinted with permission.

The initial work was performed in the course of the previously mentioned cooperation with Dr. Marianela Escobar Castillo, with further evaluations and Mössbauer measurements being performed during the course of my master thesis. It was after the completion of the latter that

the main topic of this section came to be, namely the development of our modeling approach that would disentangle the cycloidal spin structure.

The first Mössbauer measurements performed on this system, shown in Fig. 6.9 from Ref. 119, consisted of spectra of the 54 nm and 150 nm sized particles, recorded at room temperature, 4.2 K, as well as at 4.2 K in an applied field of 5 T parallel to the γ -ray direction. Using a least-squares data fitting procedure, the individual spectral components could be evaluated by overlaying the experimental data with theoretical subspectra, which are then adjusted by the used software package "Pi"¹⁴⁰ (see section 4.3.1) to minimize the error between the data and the theoretical spectrum. This way, as can be seen for the RT measurements, a sextet subspectrum was utilized, representing the magnetically blocked (ordered) phase, along with a very small doublet contribution, representing a phase that shows (super)paramagnetic behavior. In our case, knowing from XRD spectra that there are no unwanted parasitic phases, we can assume this to be caused by the smallest portion of the particle size distribution, showing superparamagnetic relaxation. This phase disappears upon cooling the sample to 4.3 K, without the appearance of additional magnetically blocked phases. This clearly shows that we are dealing with a size dependent property of BFO rather than a parasitic paramagnetic phase. Still, this is already an indicator for properties of the underlying spin structure, as the 54 nm particles are relatively large to show superparamagnetism. Instead, one could interpret it as a sign of a low magnetic anisotropy constant K_{eff} , indicating a weak coupling between magnetic moments and the crystal lattice⁶⁹ due to the incommensurate spin structure.

In terms of a qualitative evaluation, we can start with the more complex spectra that only play a minor role in this work. These were recorded at 4.3 K in an applied magnetic field of 5 T parallel to the γ -ray direction, in order to observe any change in A_{23} , the ratio between the spectral areas of lines 2 and 3, which would indicate a change in the orientation of magnetic moments relative to the field. A distribution of hyperfine magnetic fields was utilized to account for the deformation of the spectrum by the external field, as shown by the 18 individual, equidistant subspectra in Fig. 6.9 (e) and (f). No significant modification of the A_{23} ratio or was observed, proving that we are dealing with pinned moments that retain their ordering even in high magnetic fields. Furthermore, the external magnetic field didn't lead to any modification of the magnetic hyperfine field that we could obtain from the data fits. This is in excellent agreement with results from Pankhurst and Pollard,¹⁸⁵ who performed Mössbauer spectroscopy on antiferromagnetic polycrystalline samples, evaluating them with a different theoretical model, but obtaining the same typical spectra with deformed lines 1 and 6. This means that the magnetic moments do not align to the field direction, with the superposition of the magnetic hyperfine field B_{hf} with the external field B_{ext} resulting in the broad, characteristic distribution we observe in the spectra. This is consistent with the $M(H)$ results that were shown previously.

Moving on to the evaluation from the fitting of the spectra recorded in zero field, no significant difference was observed in the isomer shift of the two samples, while the magnetic hyperfine fields B_{hf} showed the expected behavior, in terms of the 150 nm sample having a slightly higher value of 54.8(1) T in contrast to the 54.6(1) T of the 54 nm sample, which can be explained by the larger particles suffering much less from size effects that lead to a decrease of magnetization due to e.g. spin canting. An important spectral property, as indicated by the dashed lines, is the asymmetry visible between spectral lines, characteristic of local angular correlation between the directions of the magnetic hyperfine field and the principal axis of the electric field gradient (EFG).^{119,186} It is this feature that we want to evaluate in greater detail. The most important hyperfine parameter for that purpose is the quadrupole shift 2ε seen in the sextet spectrum, which is connected to the quadrupole splitting of the high temperature doublet phase via Eq. 6.1 from Ref. 69. This was introduced as Eq. 4.37 in the Mössbauer theory section, but for clarity, we will show it again here:

$$2\varepsilon = \Delta E_Q \frac{3 \cos^2(\theta - 1)}{2} \quad (6.1)$$

This gives us a relation between 2ε and ΔE_Q through the angle θ between the magnetic hyperfine field and the principal axis of the EFG, which is parallel to the hexagonal [001] direction.

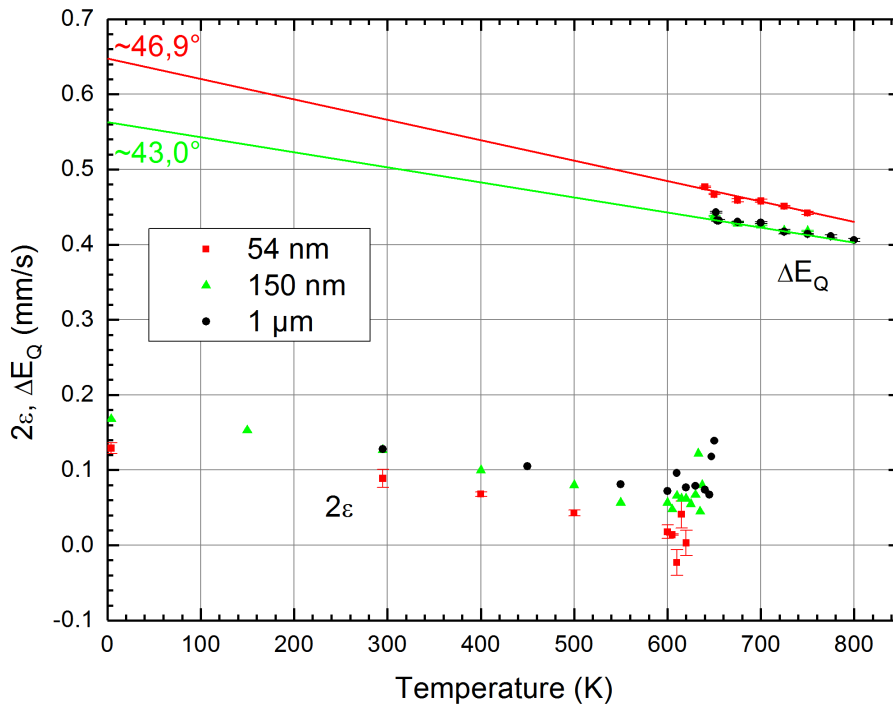


Figure 6.10: Quadrupole splitting 2ε and shift ΔE_Q of the 54 nm, 150 nm and 1 μm particles recorded at 4-800 K, adapted from Ref. 187.

The values of $\theta = 47 - 49^\circ$ in Ref. 119 were extrapolated from low temperature data points, and while already showing a clear difference compared to a random 3D spin orientation (54.7°), they lacked the necessary precision. It was because of this that a large number of spectra were

recorded up to high temperatures, which was performed during the course of my master thesis.¹⁸⁷ The final figure of that work, depicted in Fig. 6.10, shows the extrapolation of ΔE_Q from high to low temperatures (red and green lines). These values, used to represent ΔE_Q at low temperatures, allowed the calculation of θ via Eq. 6.1. The angles determined here, ca. 46.9° for the 54 nm particles and 43.0° for the 150 nm particles clearly showed a large deviation from the 54.7° value that one would expect for completely random 3D orientation.

When my master thesis concluded, this extrapolation of ΔE_Q had provided an important clue on the relationship between electric and magnetic properties of BFO in general, but we had no way of quantifying it in detail. This was pursued through a model that sought to explain what kind of ordering takes place in BFO intrinsically, and how this is influenced by temperature, particle size, and most importantly, whether there any possibilities of harnessing this interaction on our route to possible single phase magnetoelectric materials.

6.1.3 Modeling of the cycloidal spin structure

The model chosen for this task is based on the theoretical groundwork of Zaleskiĭ et al.^{188,189} and Pokatilov et al.,¹⁹⁰ and was originally used to evaluate NMR spectra. It was with this spectroscopy method that the spin structure of BFO was initially discovered, however, the measurements were mostly performed on bulk samples and almost never on nanosized particles. While BFO in its bulk form is completely antiferromagnetic, the small ferromagnetic moment we saw in $M(H)$ measurements (see Fig. 6.5) gave us the motivation to go down this route, in the hope of finding out whether the influence of size effects on the spin structure would perhaps make it possible to harness the multiferroic properties.

It was previously reported^{70,188,189,191} that the long range modulation can be modeled using an anharmonic cycloidal structure of Fe^{3+} magnetic moments, with this structure propagating along the $[110]_{\text{hex}}$ direction. The magnetic moments lie in the two dimensional plane that is defined by this propagation vector and the polarization vector, which agrees well with the angles we had obtained from Fig. 6.10. The superposition of randomly distributed magnetic moments in a 2D plane would result in an average angle of 45° , a value very close to the results we had obtained through 2ε .

With this knowledge at hand, we can begin the detailed theoretical evaluation of the main body of measurements, consisting of the mentioned large number of spectra that were recorded between 4.3 K and 800 K for all three different particle sizes. Typical spectra and their data fits in the vicinity of the phase transition are shown in Fig. 6.11. It is from these spectra that we want to produce our overall evaluations and conclusions that result from the application of our new model. We start by an overview of the spectral contributions in dependence of sample

temperature, measured through the AF-PM phase transition at T_N . Fig. 6.12 shows the relative doublet area, with values near 0% corresponding to almost complete magnetic ordering, while values near 100% indicate a completely paramagnetic sample. The small percentage of doublet contribution at low temperatures, especially in the 54 nm sample, is caused by the small superparamagnetic phase that was discussed in the description of Fig. 6.8. The stability of the samples was monitored while approaching the temperature region above 650 K by XRD measurements before and after high temperature data points to make sure that no decomposition of the samples took place, as it was observed in high temperature $M(T)$ measurements. It was only at temperatures above 750 K that we witnessed the formation of parasitic phases that indicated a decomposition of the material, usually through the loss of oxygen to the vacuum in the oven. XRD results revealed the presence of sphaerobismite (a tetragonal form of Bi_2O_3) while subsequent Mössbauer spectra showed traces of hematite (Fe_2O_3), clearly proving the partial breakup of BFO into the precursors often used during solid state synthesis methods.

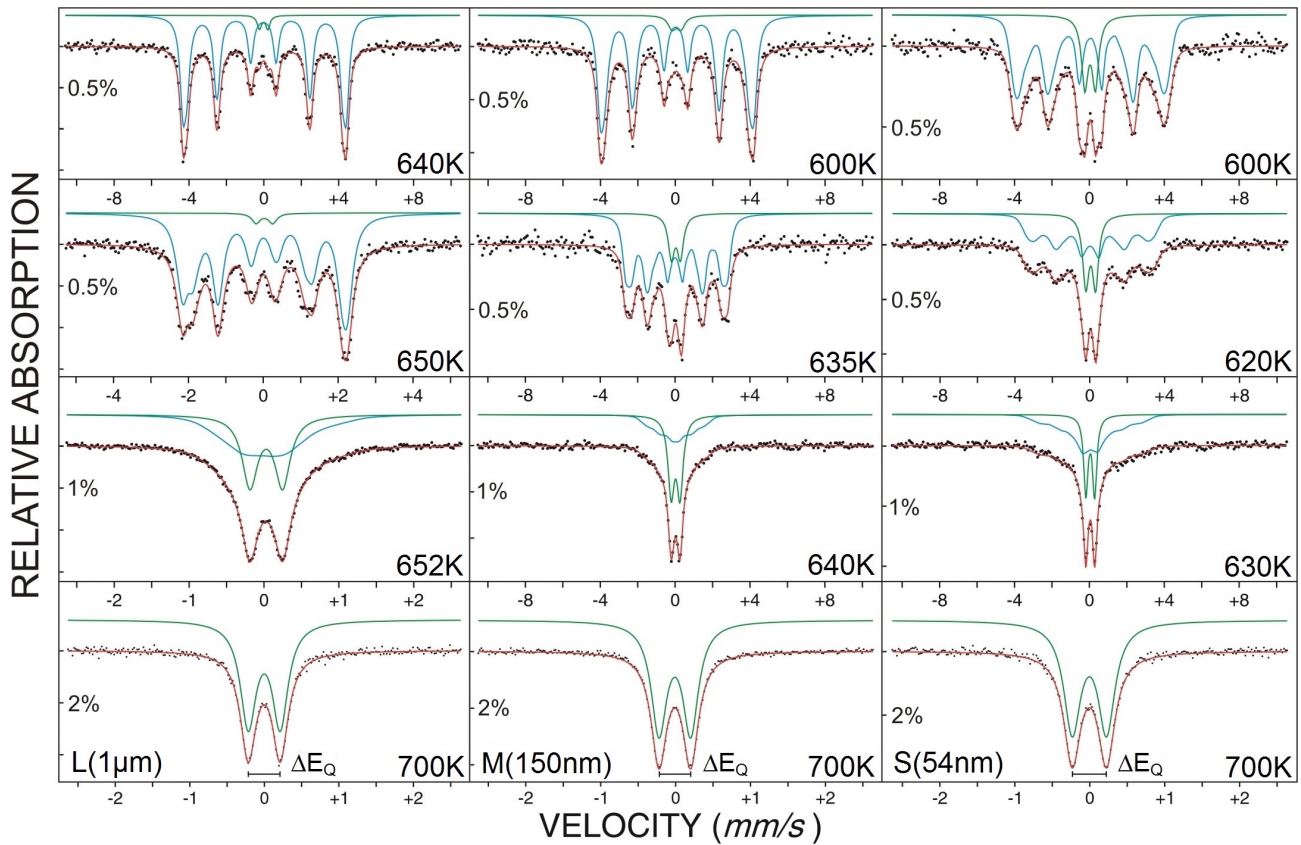


Figure 6.11: Selection of spectra recorded at temperatures above and below the phase transition for the 1 μm (left), 150 nm (middle) and 54 nm sample (right). Taken from Ref. 72, reprinted with permission.

The evaluation of the isomer shift in this temperature range showed a temperature dependent decrease due to the second order Doppler shift, with no deviations being visible from this trend. The magnetic hyperfine fields also showed the expected trend, following the Brillouin function until reaching the Néel temperature. These two parameters have been discussed in detail in

Ref. 187, along with the effects of sample decomposition, so we will only concentrate on the modeling of the anharmonicity parameter here. The most interesting feature visible in Fig. 6.12 is the distinct broadening of the phase transition, which stems from a distribution of Néel temperatures, caused by the size distribution of the nanoparticles we saw in Fig. 6.1. This leads to a distribution of hyperfine fields at each given temperature, for which we can define a width of $\Delta B_{N\acute{e}el}$. The distribution is superimposed onto the spectral fine structure of the spin cycloid that we want to unravel, thus limiting the scope of our study by making certain portions of our dataset unsuitable for evaluation. To estimate up to which point we can apply our model, a maximum temperature T_{max} was defined⁷² so that we were able to use $\Delta B_{N\acute{e}el} < 0.1\Delta B_{hf}$ in order to determine the highest temperature at which our model is still valid. Here, ΔB_{hf} is the width of the hyperfine field distribution $p(B_{hf})$ corresponding to the cycloidal spin structure (ca. 0.6 T). Consequently, as long as $T < T_{max}$ is valid, the hyperfine field distribution remains mostly unaffected by the additional line broadening. Applying this rule allowed us to determine that T_{max} is ca. 200 K for the 54 nm and 150 nm particles and 450 K for the 1 μm particles.

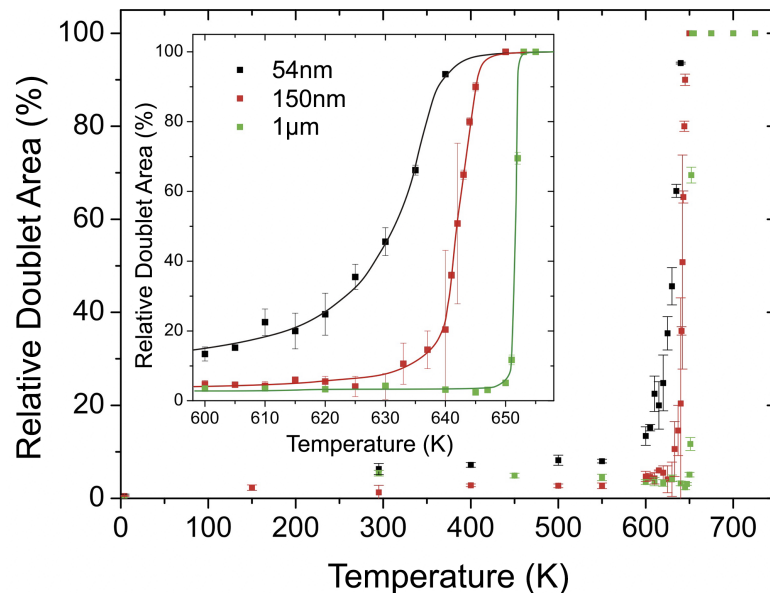


Figure 6.12: Temperature dependence of the relative doublet area, measured for the 54 nm, 150 nm and 1 μm sample, adapted from Ref. 72, reprinted with permission.

With this limitation now clear, we can derive the basis of our evaluation model. Previously, in Ref. 119, we already noted the distinct spectral asymmetry (dashed lines in Fig. 6.9) and the relation between 2ε and ΔE_Q , but were not yet able to quantitatively evaluate this feature. It is at this point that we want to utilize the relation between magnetic and electric properties to fully understand the magnetic ordering in this system: Using the NMR evaluation approach by Zaleskii et al.,¹⁸⁸ we observe that the atomic displacement along the polarization axis \vec{P} (in $[001]_{\text{hex}}$ direction) leads to a correlation of the hyperfine field B_{hf} with the angle θ relative to \vec{P} , which can be described by

$$B_{hf}(\theta) = B_{per} + \Delta B_{hf} \cos^2(\theta) \quad (6.2)$$

with B_{per} representing the hyperfine magnetic fields perpendicular to \vec{P} while ΔB_{hf} gives us the difference value to parallel orientation. The similar dependence, valid for the quadrupole shift 2ε , was shown previously in Eq. 6.1, for which we can assume two extreme cases: As described in Ref. 72, in the case of parallel spin orientation, the quadrupole shift 2ε becomes identical to ΔE_Q , while for perpendicular orientation relative to $[001]_{\text{hex}}$, the relation $2\varepsilon = -0.5\Delta E_Q$ is valid. The spectral asymmetry from Fig. 6.9 can therefore be modeled by a superposition of the quadrupole and the magnetic hyperfine field distributions corresponding to angles θ between 0° and 90° .

Applying this model to our spectra revealed that while the basic calculations are sound, they are still not able to fully describe the experimental data. This was most obvious when comparing different temperatures and particle sizes: At high temperatures around 400 K, the 1 μm particles showed an almost completely harmonic structure, with a linear correlation between the angle θ and the coordinate x along the propagation direction. However, at lower temperatures, a clear anharmonicity was present in the spin structure, which needed to be taken into account. For a clearer understanding, schematic examples of completely harmonic and strongly anharmonic spin structures are shown in Fig. 6.14 (a). At this point, we again utilize calculations that were originally conceived for NMR^{188–190} and arrive at the equation

$$\cos(\theta(x)) = \text{sn} \left(\pm \frac{4K(m)x}{\lambda}, m \right) \quad (6.3)$$

that was successfully used in the past to reproduce not only NMR, but also Mössbauer data for bulk BiFeO_3 samples. In it, x provides the distance we travel along the cycloid propagation direction parallel to $[110]_{\text{hex}}$, $\text{sn}(x)$ is the elliptic Jacobi function, $K(m)$ the elliptic integral of the first kind, λ the period of the cycloidal structure (62 nm) and, most importantly, m is a parameter that represents the degree of cycloidal anharmonicity. It can take on values from $m = 0$ for an almost completely harmonic cycloid and $m \rightarrow 1$ for an anharmonic cycloid that begins to evolve into a domain-like state (see Fig. 6.14 (a) for $m = 0.95$). This would correspond to large fractions of the spins being either parallel or antiparallel relative to the polarization \vec{P} , with the perpendicular fraction diminishing.⁶⁸

To more clearly show the effect of this model on Mössbauer spectra, we used simulated, idealized spectra, foregoing any effects that would cause additional line broadening, as shown in Fig. 6.13. The calculated hyperfine field distributions are shown in the center of the image, for three different values of anharmonicity, the overall shape of the distribution agreeing well with Fig. 1 in Ref. 192. The increasing preference for parallel orientation relative to the $[001]_{\text{hex}}$ polarization axis is clearly evident with increasing anharmonicity. If we then use this model to

simulate theoretical spectra for different values of m , we can clearly show how the hyperfine field distribution causes the typical asymmetry of the sextet, well visible when comparing lines 1 and 6. This model is not only able to generate theoretical spectra, but allows us to apply it in form of an evaluation procedure to obtain values for the anharmonicity and the hyperfine parameter. This was accomplished by a fit routine using 180 subspectra with equidistant spacing along the propagation direction x . For each position along the x -axis, the angle θ from Eq. 6.3 was calculated, followed by the derivation of B_{hf} and 2ε from Eq. 6.2. The fitting procedure, using the least-squares approach, varied the parameters B_{per} , ΔB_{hf} , ΔE_Q and the anharmonicity parameter m until the deviation between experimental and theoretical spectrum was minimized. This is shown exemplarily in Fig. 6.14 using a spectrum of the 150 nm sample measured at 120 K.

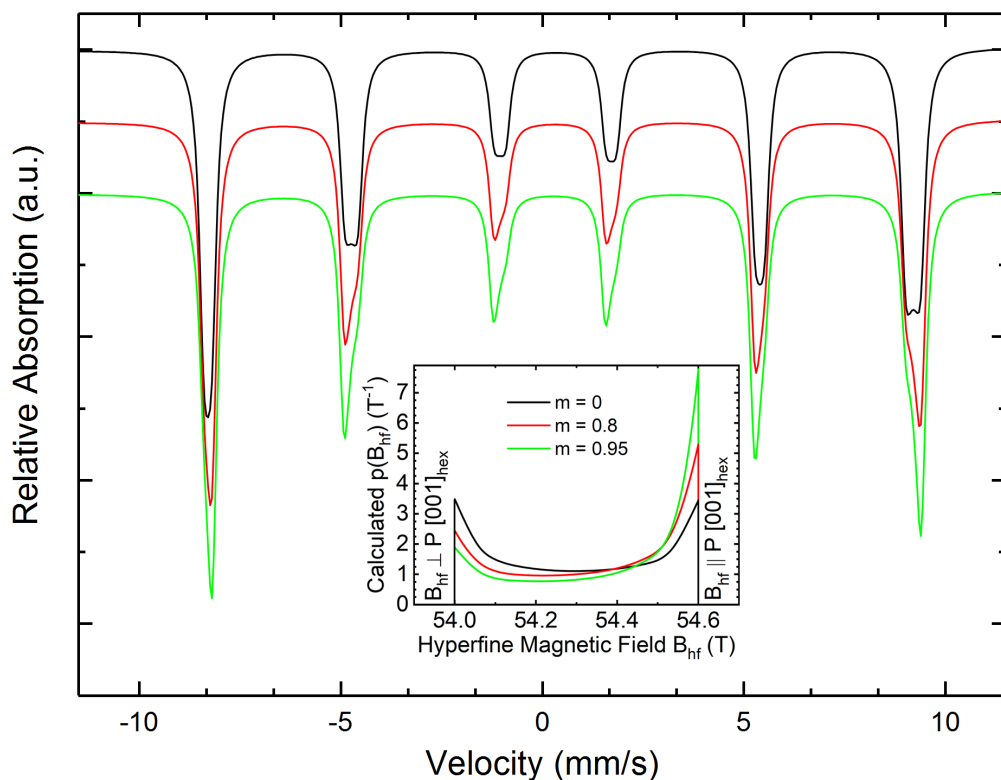


Figure 6.13: Simulated spectra for different anharmonicities, with the corresponding hyperfine field distribution being shown in the center. Spectra are offset on the y-axis for clarity.

We can observe the effects of the parallel and perpendicular spin orientations relative to \vec{P} , aptly showing how the larger hyperfine field $B_{par} = B_{per} + \Delta B_{hf}$ displays increased line intensity, while the intensity of B_{per} is visibly reduced. Due to the manner in which the quadrupole shift influences the spectrum, explained in section 4.2.3, with the inner four lines being moved in opposite direction to the outer two lines, it causes a clearly visible broadening of line 6 while the intensity of line 1 increases. In essence, the coupling of 2ε to B_{hf} causes the asymmetry of the absorption lines relative to each other, while the anharmonicity m is responsible for the

fine structure of the individual lines, leading to non-Lorentzian line shapes. It needs to be mentioned at this point that there is an equally valid method, using the sine instead of the cosine function to achieve the same goal,^{78,193} which results in the inversion of B_{per} and B_{par} values. Both models produce the same hyperfine field distribution, but we chose to use the cosine function as this negates the otherwise necessary addition of a correction term.

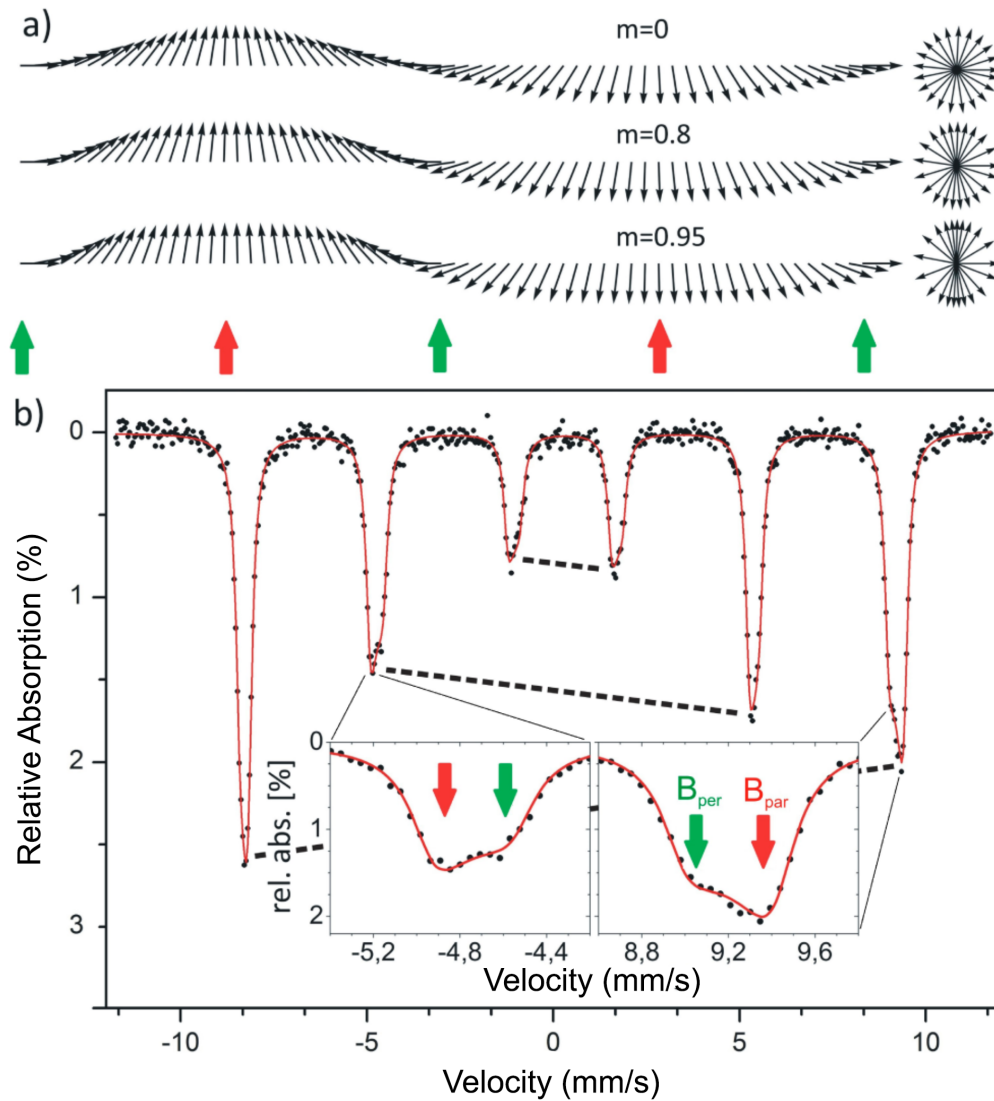


Figure 6.14: Schematic representation of the spin cycloid (a) for different anharmonicities m . The effects of the different orientations of magnetic moments on the spectral shape are shown on an example spectrum of the 154 nm sample at 120 K in (b) with green and red arrows showing perpendicular and parallel orientation, respectively, of the magnetic moments relative to the polarization axis. Adapted from Ref. 72, reprinted with permission.

We felt that this approach was also vindicated by the publication of a comprehensive work by Rusakov et al.¹⁹² very shortly after the publication of our paper. In it, the same model is used on a bulk BFO sample, with a very detailed theoretical circumscription and similar results for the temperature dependence of the anharmonicity.

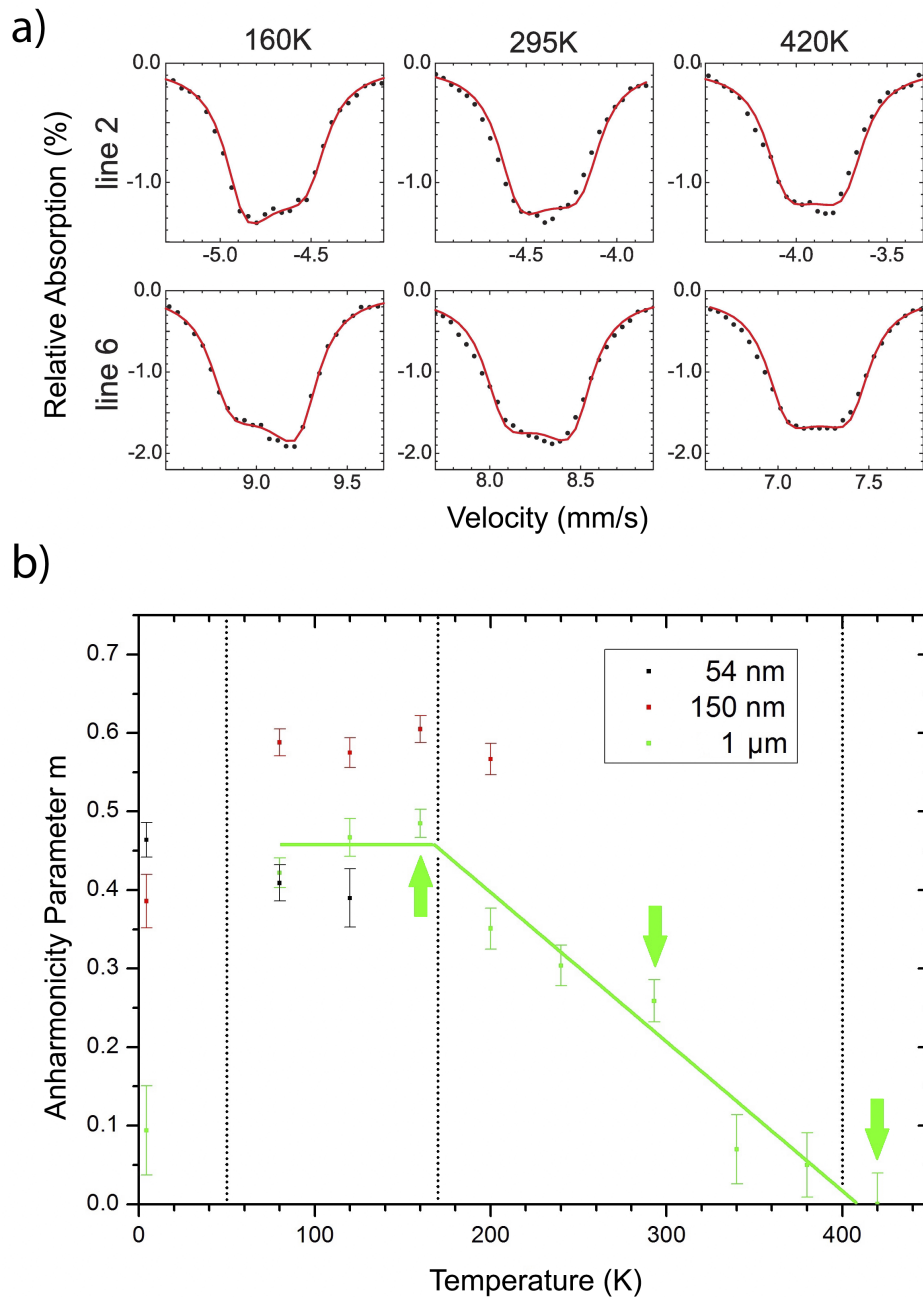


Figure 6.15: Magnification of lines 2 (top) and 6 (bottom) of the Mössbauer spectra of the 1 μm particles at 160 K, 295 K and 420 K (a). The size and temperature dependence of the anharmonicity for all three samples is shown in (b), with the green line being a guide to the eye. Green arrows indicate the temperatures at which the lines in (a) have been obtained. Adapted from Ref. 72, reprinted with permission.

However, only one bulk sample was used, while we apply the theoretical modeling to several nanoparticle samples, which we will now discuss. The most interesting result from our measurement is the change of the anharmonicity parameter m that we obtained from our fitting model, all while taking care to steer clear of areas in which the superimposed hyperfine field distribution, stemming from the particle size distribution, would disturb our evaluation.

The main results are plotted in Fig. 6.15, showing the temperature and particle size dependence of m from the entirety of the recorded data for this sample set (b) in addition to a graphic display of the influence of the change in anharmonicity on the shapes of lines 2 and 6 of the 1 μm sample (a). Starting at low temperatures, we observed rather poor agreement between our experimental and calculated spectra, leading to a stronger variation of m for the different sample sizes. We attribute this to potential spin-glass behavior that has been reported for BFO below 50 K,^{64,176} of which we also saw evidence in the $M(T)$ magnetization curve of the 54 nm sample in Fig. 6.5. Accordingly, we used dotted lines to separate the different sections that show different temperature behavior. Going to higher temperatures, we see rather constant values of anharmonicity, with m ranging between 0.4 and 0.6 with no discernible temperature dependence. The value was higher for the 150 nm sample than for the other two, but due to the overall fluctuations in m , there was no clear trend to be seen that would point towards a clear dependence on the particle size.

Going towards higher temperatures, the limitation imposed by the particle size distribution induced hyperfine field distribution made it impossible to use the results from the 54 and 150 nm sample, but the 1 μm sample continued producing usable results. We observe a continuous decrease of the anharmonicity, until the system reaches the completely harmonic state near 400 K. This is also made evident by the detailed depiction of lines 2 and 6 from the spectra of this sample, recorded at different temperatures, giving us clear indications of the influence from the decreasing anharmonicity and the appropriate increase in the perpendicular fraction of B_{hf} , as was shown in Fig. 6.15 (a). Literature data suggests the onset of spin reorientation processes, which could possibly explain why the decrease of m begins in the region of 150-200 K.^{176,194} Generally speaking, the observed transition from an anharmonic cycloid at low temperatures to a harmonic state towards higher temperatures is in agreement with previous studies on polycrystalline bulk materials¹⁹³ and single crystals,¹⁹⁵ making our study the first ever to observe the anharmonicity in BFO nanoparticles. No clear trend could be observed for the influence of the particle size on the anharmonicity, due to the width of the magnetic hyperfine field distribution stemming from the particle size distribution. This would require particle samples with a narrower size distribution to increase T_{max} , or the use of thin film samples, which is described in the outlook (chapter 8).

6.2 Magnetoelectric ceramics

As the results of the previous section indicate, intrinsic multiferroics are sometimes fraught with significant challenges that are not always easy to overcome. This next section therefore deals with results from magnetoelectric composites that were purposefully engineered to take advantage of so called product properties, combining the piezoelectric and magnetostrictive systems that were described in chapter 3. Before we look at the detailed results, it's important to consider the history of the long running cooperations that are the main subject of this thesis, as they provide the overall framework by which we arrived at the point where we are now. As previously mentioned in the synthesis section, there have been previous attempts at measuring the ME effect in a CFO-BTO ceramic formed by covering commercial CFO nanoparticles with a BTO shell, as described by Shvartsman et al.²¹ in 2011. Using the same setup that was described in section 4.7, a converse magnetoelectric coefficient of 22 ps/m was obtained. However, it was noted that PFM images revealed a strong agglomeration of the initial CFO nanoparticles, leading to a percolation of CFO clusters in the BTO matrix, degrading the overall ME performance by hindering effective poling through increased conductivity. Additionally, the observed agglomeration also negated advantageous size effects such as the higher surface to volume ratio in nanoparticles, providing an higher interface area per volume between the two constituents.

As a logical consequence, attempts were made to rectify this problem by moving away from commercial particles that were subsequently coated and instead employing a synthesis technique, described in section 5.2, that produces core-shell particles. This way, it was hoped that agglomeration effects can be reduced, thus arriving at composites that can be poled more effectively in order to achieve a higher magnetoelectric coefficient. This was the main motivation behind the initial experiments, with the subsequent measurements and publications being a result of further improvements and changes made to the composite, always striving for improved ME effects.

It was decided to describe and analyze the data in the chronology of the publications that resulted from our cooperation, which is a rather didactic approach. However, this way, it's completely logical that the first measurements weren't performed with the same range of parameters as the later ones, as our experience and abilities grew over time. Indeed, while the first few papers usually only contained a smaller section dedicated to the converse ME measurements, the latest publication¹²⁶ has several pages of figures and text dedicated to the results from this method. It therefore made sense to use the chronology of our cooperations as a leitmotif in this work, performing more expansive measurements with each sample set that was collectively worked on, and going into more and more detail with regards to evaluations and comparisons to literature as our knowledge increased. It would of course have been possible to summarize the results in a shorter, more compact way, but that would have required numerous

explanations in between to show the reader why certain sample sets were measured differently. Instead, if we stick to the chronology of the measurements as they have been performed over time, it should be easier to guide the reader through our results in the most logical fashion.

6.2.1 Analysis of measurement data

Before we deal with the detailed analysis of the data obtained from the converse setup described in section 4.7, we will first observe how the data was calculated to begin with. Conveniently, it's only the final $ME(E)$ measurement that requires a purely quantitative evaluation in order to obtain the converse magnetoelectric coupling coefficient. The temperature and field dependent measurements mostly serve to find the optimum temperature and field for the final measurement, while also providing information on general sample characteristics, which means that further unit conversions can be foregone. For the $ME(E)$ data, we start off with the calculation of the electric field that was applied to the sample: The device outputs values in Oersted due to the fact that the measurement setup is built upon the AC susceptibility option, which would normally put out an alternating magnetic field. As described in section 4.6, we use the known calibration of the wide band amplifier that was measured via oscilloscope to determine the applied AC voltage, and then divide it by the thickness of the sample in order to arrive at the electric field via the standard $E = U/d$ capacitor equation. As the real part of the measurement signal is directly output in magnetic units, in this case emu, we can easily convert it to either mass magnetization via weighting the sample, or volume magnetization through determination of the sample volume. For the magnetoelectric measurements, we always used the volume magnetization, as the samples are generally homogeneous, round disks. One can simply calculate the volume from thickness and diameter of the ceramic, which can in turn be measured by high precision calipers or micrometer screws.

With this information at hand, the magnetization can be plotted against the applied electric AC field amplitude. As we are only recording the magnetization that was induced from the alternating electric field, no further deconvolution must take place, as the (comparatively very high) static magnetic moment of the sample is rejected by the lock-in amplifier. Instead, we can immediately utilize a linear fit, and then use the slope to determine the converse coupling coefficient α_C .

In most publications, the unit for the converse coupling coefficient is seconds per meter, which isn't immediately obvious from the plot of A/m against kV/m, with no effort being usually made to explain how the final unit arises. Because of this, we will shortly derive it here.

Starting with the basic definition of α_C

$$\alpha_C = \mu_0 \frac{dM}{dE} \quad (6.4)$$

we can write out the units for the magnetic terms to receive

$$\mu_0 M \left[\frac{Vs}{Am} \cdot \frac{A}{m} \right]. \quad (6.5)$$

Completing the formula with the electric field then yields

$$\alpha_C = \frac{\mu_0 dM}{dE} \left[\frac{Vs}{Am} \cdot \frac{A}{m} \cdot \frac{m}{V} \right], \quad (6.6)$$

which quickly shows how we end up with s/m as the unit for α_C . Now we can continue with the error estimation for this measurement type, to obtain an overview of the quality of the data that can be delivered by the converse ME measurement setup.

6.2.2 Error estimation

An important consideration is the correct estimation of the error for the converse magnetoelectric coefficient α_C . As we can see, for example in Fig. 6.48, the data points have been plotted with the standard deviation error that is output by the SQUID, which uses the difference value between at least two data points to determine this error. In our case, we average four measurements for one data point in order to minimize statistical errors. The linear fitting procedure takes these deviations into account, and in this case, puts out an error that is often less than 0.01% of the total value. However, as we will see, this error is too small and needs to be estimated more conservatively. As it's generally known from magnetometry, the largest error is not introduced by the high precision magnetometers themselves, but by the mass or volume normalization, which uses scales or micrometer screws that introduce a much higher error into our calculation. Because of this, we take into account the error of a standard micrometer screw used to measure the ceramics, in the range of 0.01 mm, and determine the largest deviation it can cause for the final coefficient. Two measurements go into our calculations, the thickness of the ceramic, as well as its diameter, which have influence on both the calculated electric field the sample is subjected to, as well as the volume magnetization. For a conservative estimate, we vary the thickness and diameter in the range of the mentioned error of the micrometer screw and perform the linear fitting procedure for each possible combination. The difference value between the two farthest outlying values is then used as the error margin, which is often one order of magnitude larger than the simple statistical uncertainty of the fitting procedure and the magnetic measurement itself, usually around ± 0.01 ps/m, proving the necessity of this estimation. However, even with this conservative estimation resulting in a higher error, it is usually still well below 1% relative to the final value, proving the high precision of our setup. For fractured or irregularly shaped samples, the proper determination of the overall surface

area becomes tricky. In this case, the ceramic piece can be photographed on millimeter paper, with the software package "Pi"¹⁴⁰ being used to determine the surface area, along with the appropriate error bars.

What now follows is the evaluation of the individual sample sets, which are subdivided by the material system used, as well as the overall publication that was composed from the respective data.

6.2.3 CFO-BTO composites with different connectivity schemes

As with the BFO section, we now arrive at the very core of this work, namely the first ME evaluation of a set of CFO-BTO 50-50 ceramic samples that were characterized cooperatively by the groups of Prof. Lupascu and Prof. Wende. This is actually the second publication of this nature, dealing with the ME effect in ceramics and not only with the properties of the precursor materials. The previous one,¹²² published in 2013, uses the synthesis method that was discussed in detail in section 5.2 in order to obtain core-shell particles that were then sintered into ceramics. With very promising results from SEM that clearly show the CFO clusters within the BTO matrix, PFM and MFM imaging revealed magnetic and electronic response on the local scale, while XRD and magnetometry data revealed that the samples were phase-pure and showed results that were comparable to literature data. The converse ME effect was successfully measured, and determined to be in the range of $\alpha_C = 4.4$ ps/m, which was also in agreement for literature values reported for this composition.

One of the main problems was often the unreliability of the converse ME setup, with the difficulties in obtaining good quality data also being visible in the large error bars and general spread of the data points in Fig. 7 of Ref. 122. This was rectified by a complete rebuilding of the wiring between the wide band amplifier, replacing excessive lengths of simple unshielded electrical connections with coaxial cables, while also modifying certain minor aspects of the circuitry following advice from Dr. Pavel Borisov. The rebuilt setup is in the state as it was described in section 4.6. As we will see in the quality and low noise of the converse ME data, this modification greatly improved performance and reliability of our setup.

Now we can observe and discuss the data collected on the CFO-BTO 50-50 samples. Due to the large number of measurement methods involved, only those that saw repeated use in following publications were discussed in greater detail in section 4. In total, four samples were produced for this series of measurements. A powder sample S1 as a reference, foregoing the sintering step after synthesis of core-shell particles. Sample S2 was a ceramic that was sintered via the SPS method described in 5.4.2 while sample S3 was annealed at 900 °C for 2 h at ambient atmosphere in a regular chamber furnace following the SPS ceramic formation. Meanwhile, sample

S4 was produced from the same initially synthesized core-shell particles, but the ceramic was formed by the conventional sintering method described in section 5.4.1. It is on these four samples that the characterization was performed, while only sample S3 and S4 were characterized with the converse ME setup. S1 is of course a powder and thus not suitable for this type of measurement, while S2 was found to be in a paraelectric phase, as described below. Still, the precharacterization results for the other sample will also be mentioned in the following, as they provide important information on the problems and issues that were encountered following the use of the SPS method.

	S1	S2	S3	S4
Description	powder	SP sintered	SP sintered and annealed	conventionally sintered
Connectivity		(3-0)	(3-0)	(0-3)
BTO structure	cubic	cubic	tetragonal	tetragonal
BTO grain size (nm)	40 (shell) - 120	160±30	650±50	1000-2500
CFO grain size (nm)	40 (core)	70±10	210±25	1000-2500

Table 6.2: Description of samples S1-S4, including morphologies and structural properties. Data taken from Ref. 123, reprinted with permission.

Structural characterization

Crystal structure and phase content were analyzed by XRD (Siemens D5000), with only BTO and CFO phases being detectable, as shown in Fig. 6.16.

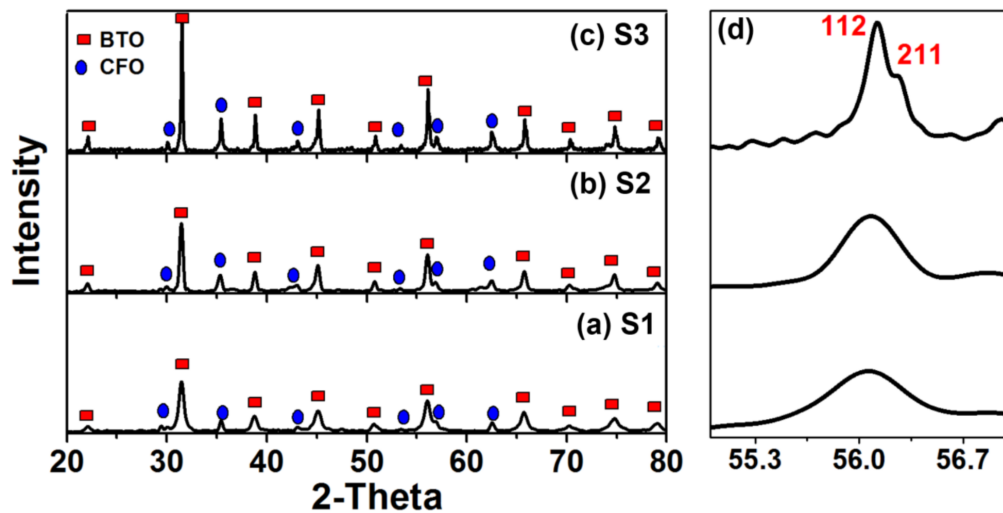


Figure 6.16: X-ray diffractograms for samples S1 (a), S2 (b) and S3 (c), with the righthand panel (d) showing enlarged views of the diffraction peaks corresponding to the (112) and (211) planes of BTO. Taken from Ref. 123, reprinted with permission.

Sample S4 is not included here, as it was fabricated according to the previously used method¹²² that reliably produces phase pure samples. No impurities or traces thereof were observed in any of the samples, with the powder S1 showing broadened Bragg peaks due to the small particle size compared to the sintered samples, as sintering always leads to a growth and partial

agglomeration of crystallites. When looking at the splitting of the Bragg peaks corresponding to the crystallographic planes indicated in the figure, one notices that the powder S1 and the initially produced SPS sample S2 show no splitting, indicating BTO to be in a cubic state. It's only for the annealed SPS sample that a splitting can be observed, indicating that BTO is in its tetragonal phase, thus being ferroelectric.¹⁹⁶ It was further observed that the (112) peak shows higher intensity than the (211) one (see Fig. 6.16), being a sign of texturing in the sample, and thereby also of a preferential c-axis alignment that's perpendicular to the sample surface.¹²³ This is an advantage for us, as it is the only direction in which electric fields can be applied during converse ME measurements, while also being the principal direction of the magnetic field measurement.

Continuing with SEM imaging (Quanta 400 FEG), the morphology of the ceramics was recorded, with the corresponding SEM images for samples S1-S3 being shown in Fig. 6.17, taken from Ref. 123. Going by the data summarized for these measurements in table 6.2, we can see that the initial powder contains core-shell particles with a mean size around 120 nm (including the BTO shell), but also a number of bare 40 nm CFO particles without a shell. The general structure was in agreement with previous works.¹²¹ Upon the formation of a ceramic via SPS, in stark contrast to the conventional sintering method, a reversal of the connectivity was observed, with BTO particles in the range of 150 nm being surrounded by a CFO matrix formed from agglomerated CFO grains, which increased in size from 40 to 70 nm. Further annealing of the sample also lead to a further growth of the BTO grains, now being in the range of 0.6 – 0.7 μm . Obviously, the high temperature and longer time of the annealing process compared to the original SPS method caused this strong additional growth. However, two goals were reached: The BTO was now in the tetragonal ferroelectric phase, while the grains were still a great deal smaller than those from the conventionally sintered sample (not shown here), which showed BTO grain sizes of up to 1 – 2.5 μm .¹²³

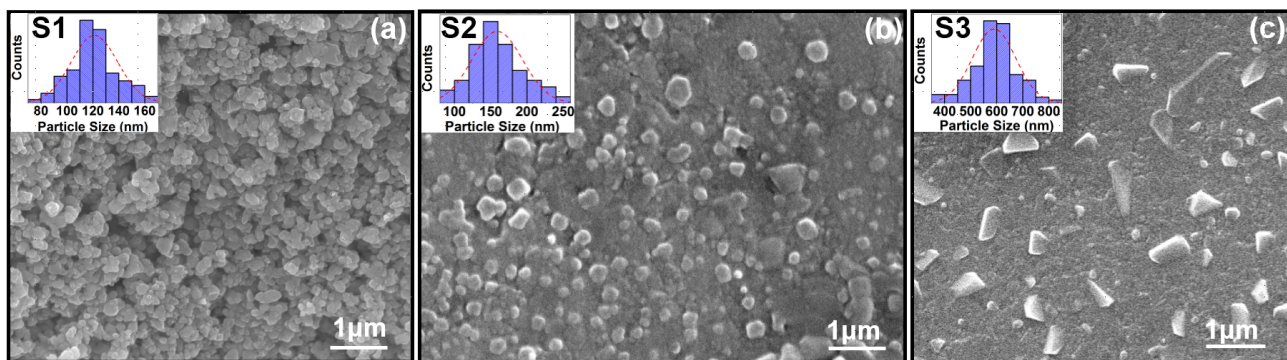


Figure 6.17: SEM micrographs recorded via backscattered electron mode of samples S1 (a), S2 (b) and S3 (c), with the insets showing the BTO particle size distribution. Taken from Ref. 123, reprinted with permission.

Electrical characterization

Although PFM is strictly speaking also a microscopy method, it will be included in this part due to the fact that it mainly observes the piezoresponse of the samples and thus counts as electrical characterization method, more so than as a purely structural one. Performed with an Asylum Research MFP-3D, the recorded images on the polished samples S2-S4 show both topography (Fig. 6.18 top) and PFM response (bottom), being a useful crosscheck for the SEM images discussed previously. It was at this point that the cubic, rather than tetragonal structure of the BTO phase in S2 became an apparent problem: The sample showed no piezoresponse (b), while the annealed sample S3 (d) and conventionally sintered sample S4 (f) displayed clearly visible contrast changes, indicative of piezoactive regions, corresponding to ferroelectric BTO grains. These are apparently distributed in a CFO matrix, as seen in SEM, which would mean that a (3-0) sample was formed, in contrast to the (0-3) sample from conventional sintering (e,f), although some regions appear to be near the (3-3) connectivity type as well (see Fig. 2.12).

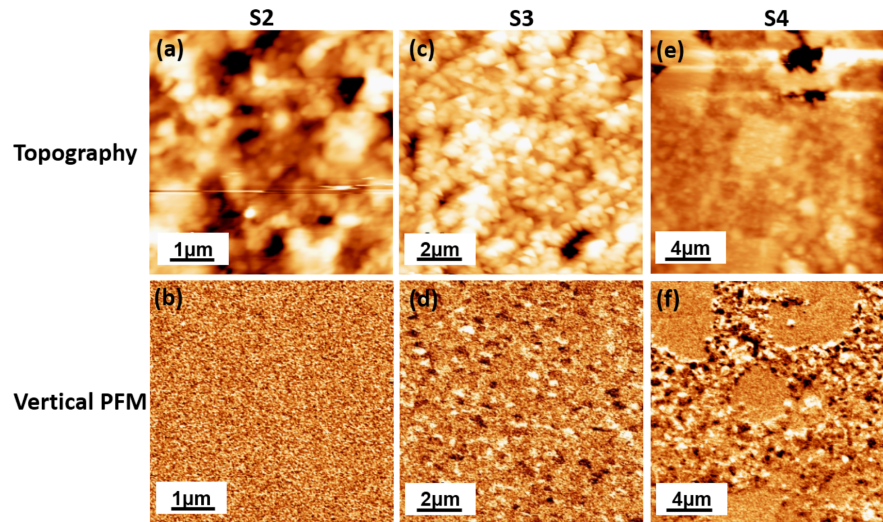


Figure 6.18: PFM micrographs of the CFO-BTO composites, showing topography (top) and vertical PFM response (bottom) for samples S2, S3 and S4. Taken from Ref. 123, reprinted with permission.

The BTO grains were estimated to have sizes around 700 nm, in agreement with SEM data. Microscopically, we therefore have a sample that has potential for ME measurements, namely sample S3 with its piezoactive regions, while sample S4, showing isolated CFO grains in a BTO matrix, is a good model system for regular (0-3) ceramics, as also obtained in previous works.¹²² After elucidating the microscopic properties, we must also take into account the more important parameters of macroscopic measurements. This importance stems from the fact that there have been samples in the past, albeit from a completely different system, that showed promising microscopic ME response, but could not produce any macroscopic effect. Such a sample, while interesting from a physical standpoint, is of course not suitable from an applications point of view, which should always be a goal to strive for when working with magnetoelectrics.

The macroscopic properties were characterized by $P(E)$ loops, recorded with a home-built Sawyer-Tower circuit, using the appropriate method described by Sawyer et al.¹²⁹ Sample S2 not only showed no piezoresponse, but suffered from leakage currents so large that no polarization switching was observed. It was suggested in Ref. 123 that this may be caused by some amount of graphite remaining in the sample after the SPS procedure. This seems to be a logical explanation, as one would expect S3 to have equally high or even higher leakage currents, due to the general growth of the grains and the subsequently larger volume of uninterrupted CFO in the sample providing conductivity. We are thus only left with samples S3 and S4 in order to compare SPS and conventionally sintered samples. An immediately obvious problem, as shown in Fig. 6.19, was a strong leakage effect in S3, caused by the higher conductivity of the CFO matrix, being 4-5 orders of magnitude larger than that of BTO.¹⁹⁷ Additionally, the dielectric characteristics of all ceramic samples S2-S4 were recorded with a Solartron 1260 impedance analyzer, using the dielectric interface 1296. The results for the real part of electric permittivity ϵ' and the dielectric loss tangent $\tan(\delta)$ are also shown in table 6.3. The two SPS samples S2 and S3 display larger values of permittivity than the conventionally sintered sample S4, despite the comparatively small BTO grain size in S2. This was attributed to a significant contribution from AC conductivity from the CFO matrix, which is further supported by the higher dielectric losses that we can also observe for these samples.

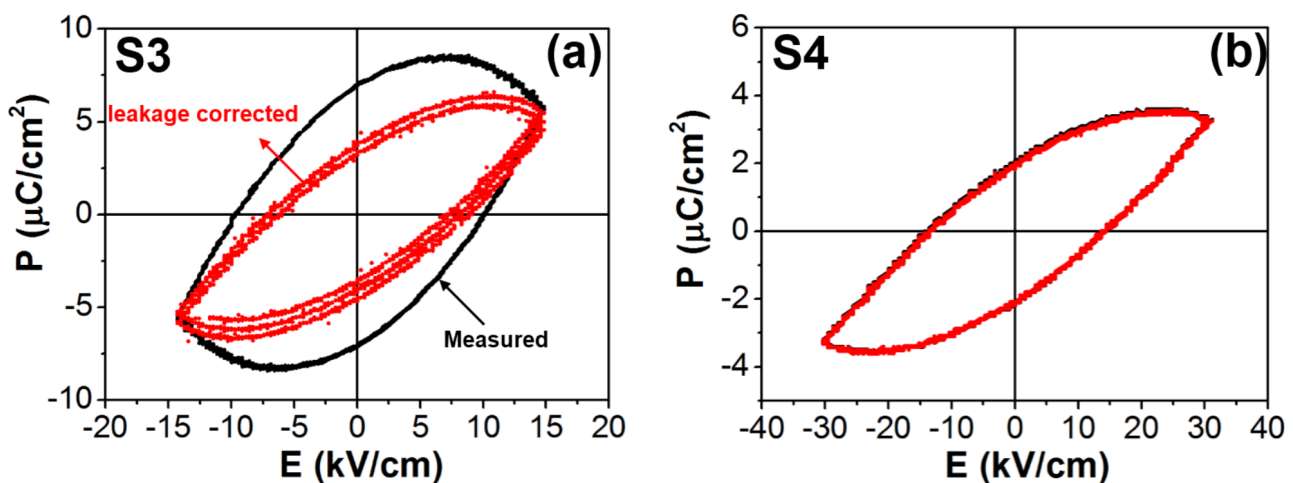


Figure 6.19: $P(E)$ hysteresis loops recorded at room temperature for S3 (a) and S4 (b) at 100 Hz. Curve corrected for static leakage contribution is shown in red. Taken from Ref. 123, reprinted with permission.

Magnetic characterization

The magnetic properties were characterized by SQUID magnetometry (see section 4.4), with the results for powder and ceramic samples being shown in Fig. 6.20, plotted as mass magnetization against the applied magnetic field. All results discussed here are summarized in table 6.3. As described in Ref. 123, it was necessary to secure the powder sample S1 in the sample holder in order to avoid a macroscopic rotation of the particles, which diminished the coercive field

and remanent magnetization. We only discuss the results for the properly secured powder here. If we consider that the atomic mass of a formula unit of BTO and CFO can be calculated to 233.2 g/mol and 234.5 g/mol, respectively, it's prudent to assume them to be equal as an approximation. This means that the 20 Am²/kg for S1 in table 6.3 must be corrected for the mass of the non-ferrimagnetic BTO to obtain the saturation magnetization of the CFO phase. We end up with ca. 40 Am²/kg, significantly lower than the 80 Am²/kg usually given in literature.²³

Sample	ε' at 100 kHz	$\tan \delta$ at 100 kHz	M_S (Am ² /kg)	M_r (Am ² /kg)	$\mu_0 H_c$ (mT)
S1	-	-	20	9	75
S2	175	0.25	32.5	15.5	47
S3	208	0.47	32	15	45
S4	73	0.033	27	10	45

Table 6.3: Dielectric and magnetic properties of samples S1-S4 at room temperature. Data taken from Ref. 123.

When comparing all samples, we see that S2, formed by SPS, shows a reduced coercive field and remanent magnetization compared to the powder S1, while the saturation magnetization increased, presumably due to the larger CFO grains. We therefore have to assume that the untreated nanoparticle sample is affected by size effects such as surface spin canting, leading to a reduction of saturation magnetization. The grain growth taking place during the formation of ceramics partially negates this effect, which explains why samples S2-S4 show a higher overall saturation magnetization. Comparing the untreated S2 with the annealed S3, only a very minor difference is visible, indicating that the annealing procedure did not significantly alter the magnetic properties of the sample.

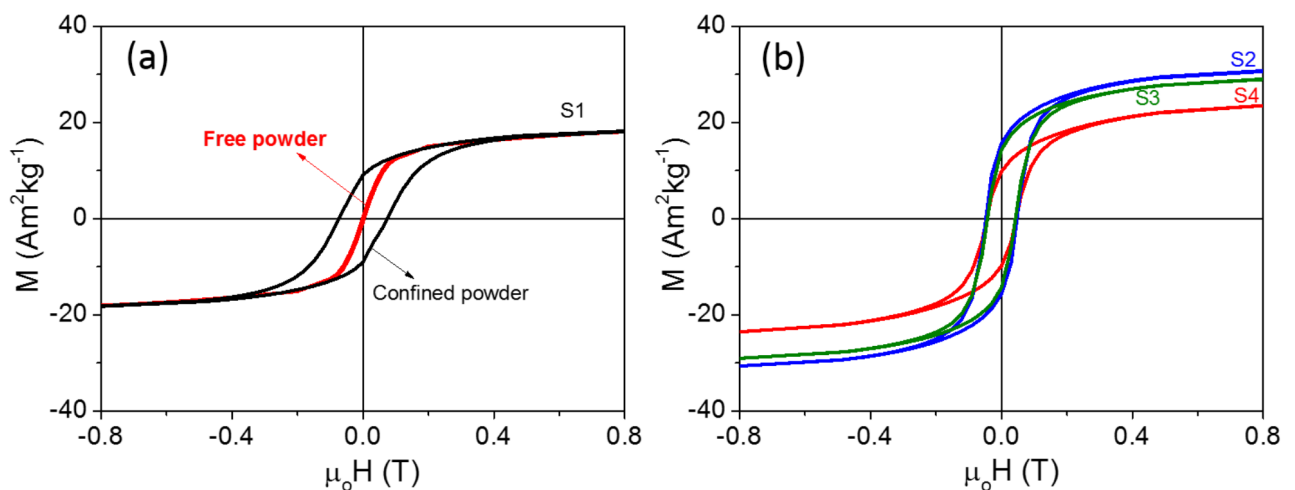


Figure 6.20: $M(H)$ hysteresis loops of all samples, recorded at room temperature, with only the small field region up to 0.8 T being shown. Taken from Ref. 123, reprinted with permission.

Obviously, the grains in S2 are already sufficiently large to avoid any size effects, with further growth in S3 thus not having any additional influence. When looking at the magnetization

curve for S4, there's a clearly visible decrease of the saturation magnetization when compared to the other samples, while remanence and coercivity do not change, as visible in table 6.3. It was suggested in Ref. 123 that the increased density of the SPS samples may be responsible for this effect, but as the $M(H)$ curves are normalized to weight, not volume, this should not be the case. We must therefore assume that the behavior we see here is related not only to grain size^{120,198} but also to possible cationic disorder^{199–201} and anti-phase boundaries.^{199,202} Generally speaking, one would expect a decrease of the saturation magnetization with decreasing particle size¹⁹⁸ due to spin frustration at the surface of the particles. It is generally not adequate to refer to such a decreased high field magnetization as saturation magnetization, despite it being commonly done in literature, as such a decrease is only the result of much higher fields being needed to realign the spins near the particle surfaces. Here, we also refer to the possible reduction of the magnetic permittivity in composites, which was discussed in detail for the next sample set in section 6.2.4 via equations 6.7 and 6.8.

Converse magnetoelectric measurements

With the electrical and magnetic characteristics having been carefully studied, it is now time to analyze the results of the converse magnetoelectric measurements. In a look ahead to the upcoming chapters, it has to be mentioned here that normally, a converse measurement is accompanied by a direct measurement of the ME effect through the application of magnetic fields while simultaneously measuring the induced polarization. This will be performed in detail for the upcoming sample set. However, in this case, due to the strong leakage currents found in S3, this was not possible. We were only able to obtain converse ME data for this sample because the amplifier of our setup (described in section 4.6 in detail) is able to supply sufficient power in order to compensate the Ohmic losses in the sample, thus also being able to apply electric fields high enough in order to obtain a magnetic signal. One must be careful with this approach though, as excessive Joule heating of the sample can occur if the leakage current through the sample is too high, as described in section 4.8.1. The first measurement we performed concerned the temperature dependence of the induced ME magnetization. For the sake of easier understanding, we will start with the conventionally sintered sample S4. As this is the first of several characterization steps, we use parameters that are known from previous measurements¹²² to be in the right range for an induced ME effect, in this case an applied DC magnetic field of $\mu_0 H = 0.15$ T and a frequency of the electric AC field of 3 Hz, as low frequencies between 1 and 10 Hz are usually the least problematic for the setup. Our initial sweep was carried out from 350 K down to 200 K, steering well clear of any regions that might be a problem for the sample holder. The resulting curve, shown in Fig. 6.21, is composed of data points with very small error bars (calculated by the standard deviation of at least two averaged measurements per data point) and overall low scattering of data points relative to each other, proving that the setup is capable of performing reliable and precise measurements.

This is especially true when directly compared to previously performed measurements such as Fig. 6 from Ref. 122, recorded prior to the rebuilding and rewiring of the sample holder, with the data not having received a proper evaluation at that time. From standard $M(T)$ reference measurements, no anomalies were observed that would correspond to the features we see in the $ME(T)$ curve, with the correct prediction having been made that the data is not representing any transformation of magnetic structure. Instead, as we will see, it is caused by the temperature evolution of the piezoelectric response of BTO.

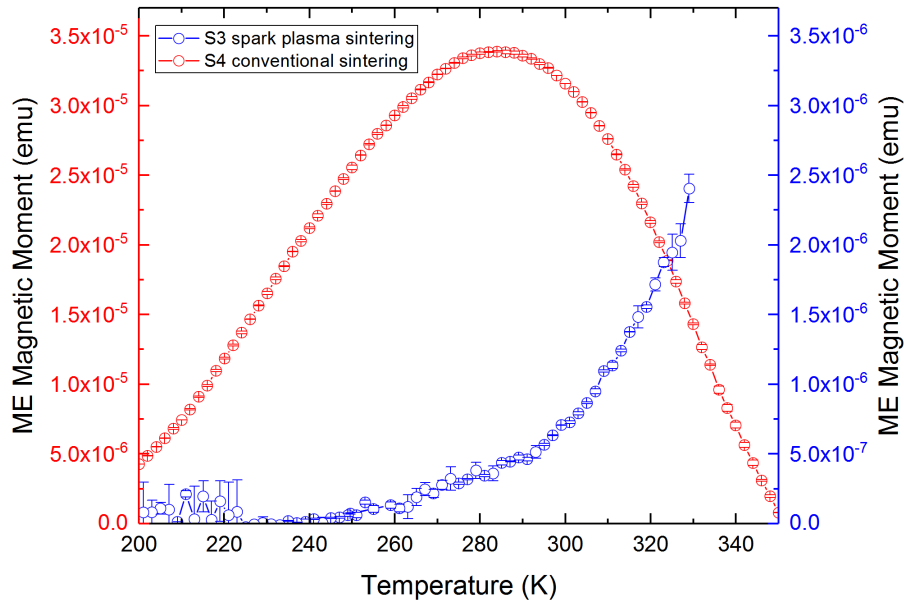


Figure 6.21: Temperature dependence of the induced magnetic moment $ME(T)$ for composite S3 and S4, recorded at $E_{AC} = 3.35 \text{ kV/cm}$, $f_{AC} = 3 \text{ Hz}$, $\mu_0 H_{DC} = 0.15 \text{ T}$.

The location of the maximum for S4 (red curve) at roughly $283 \pm 2 \text{ K}$ agrees very well with the phase transitions known from literature, such as from Merz et al.,²⁰³ who determined the upper limit of the phase transition to 280 K. Furthermore, we see a marked decrease of the effect to both sides of the maximum, with the decrease towards high temperatures indicating that we are dealing with an actual ME effect rather than stray signals from conductivity. We thus used this temperature to perform our other measurements at. While there is much more to the temperature dependence when correlated with the structural phase transitions, we will discuss that in more detail in the next subsection, as more detailed $ME(T)$ curves have also been recorded on upcoming samples. At this early stage, we were mainly interested in obtaining the temperature at which the effect is at its largest. The next sample set will also deal with the temperature dependence of the dielectric permittivity, thus allowing a better insight into the temperature dependence of the induced ME magnetization. However, we are already able to conclude that it's possible to obtain very high quality data with the rebuilt setup, allowing a much clearer display of temperature dependent effects than in preceding publications.

Moving on to the SPS sample S3 (blue curve), we see the obvious problem that no clear peak is visible that would correspond to any of the phase transitions in BTO. Instead, the signal just shows a very strong increase towards higher temperatures, while the overall amplitude of the signal is significantly lower than for the conventionally sintered sample S4. We are therefore dealing with a signal that is mostly caused by conductivity effects and not by magnetoelectric strain coupling alone, as it was explained in the pitfalls section 4.8.1. This measurement is therefore not suitable to determine a maximum in temperature dependence, and generally speaking, results from this sample need to be viewed with a great deal of caution as far as their evaluation goes. Fortunately, the strong increase only commences above 280 K, which means that the number of available charge carriers is sufficiently low to allow the partial observation of magnetoelectric coupling in the sample that is not strongly superimposed by apparent signals from conductivity. The measurement was not continued to higher temperatures as the increase in conductivity often bears the danger of excessive Joule heating, also explained in section 4.8.1.

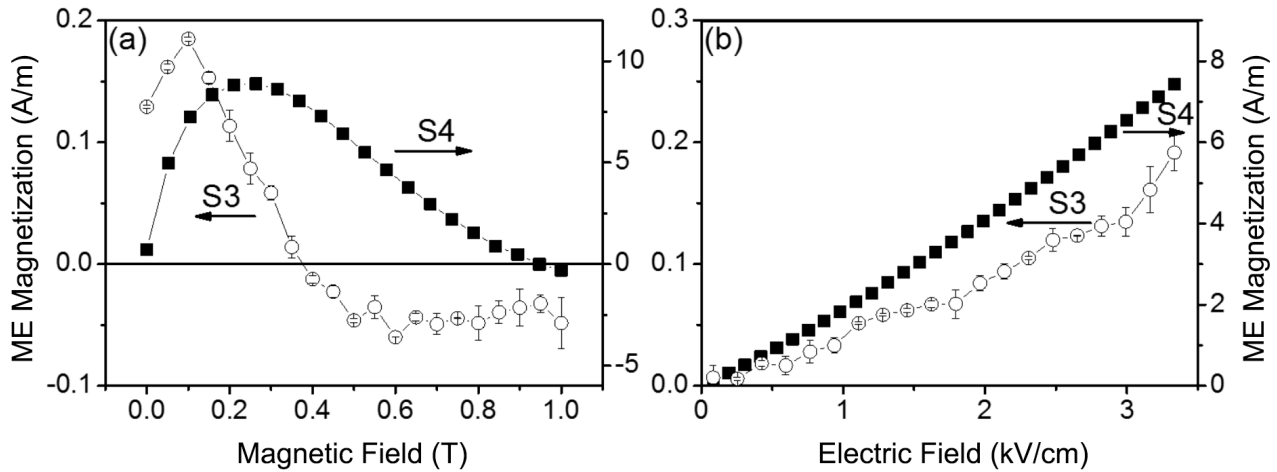


Figure 6.22: Magnetic field dependence (a) of the induced magnetization $ME(H)$ for composite S3 and S4, measured at $T = 285$ K, $E_{AC} = 3.35$ kV/cm, $f_{AC} = 3$ Hz. Electric field dependence (b) of the induced magnetization $ME(E)$ measured at $T = 285$ K, $f_{AC} = 3$ Hz, $\mu_0 H_{DC} = 0.15$ T. Adapted from Ref. 123, reprinted with permission.

The next parameter that was checked for maxima is the applied DC magnetic field. While it was measured over a wide field range in future measurements to obtain a greater understanding of the relation to magnetostriction, we only used a small range from zero to 1 T here. Even from this small section, a clear trend is visible in the results of S4, as shown in Fig. 6.22: A broad peak is reached after a strong signal increase in the low field range, followed by a decrease towards zero when going to higher fields. This measurement was only performed for increasing fields, as this was the first sample set that was evaluated, so no discussion of hysteretic behavior takes place yet. This will be dealt with during the evaluation of the next sample set. In order to explain the shape of such $ME(H)$ curves, we have to look at the behavior of the magnetic phase, as it's only on this that the applied DC magnetic field will exert a noticeable

influence. One work dealing with the magnetoelastic properties of CFO is Ref. 204, in which the dependence of these properties on the processing parameters is elucidated. In Fig. 6 of this work, CFO ceramic samples with different processing parameters are characterized by strain gauges, to directly measure the effect of magnetostriction vs. applied magnetic field. Just like in our experiments, the magnetic field was applied perpendicular to the sample surface, with the magnetostriction being measured parallel to this direction. As we are looking for a general explanation rather than detailed numerical results, a schematic representation, based on this figure, was created, as shown in Fig. 6.23.

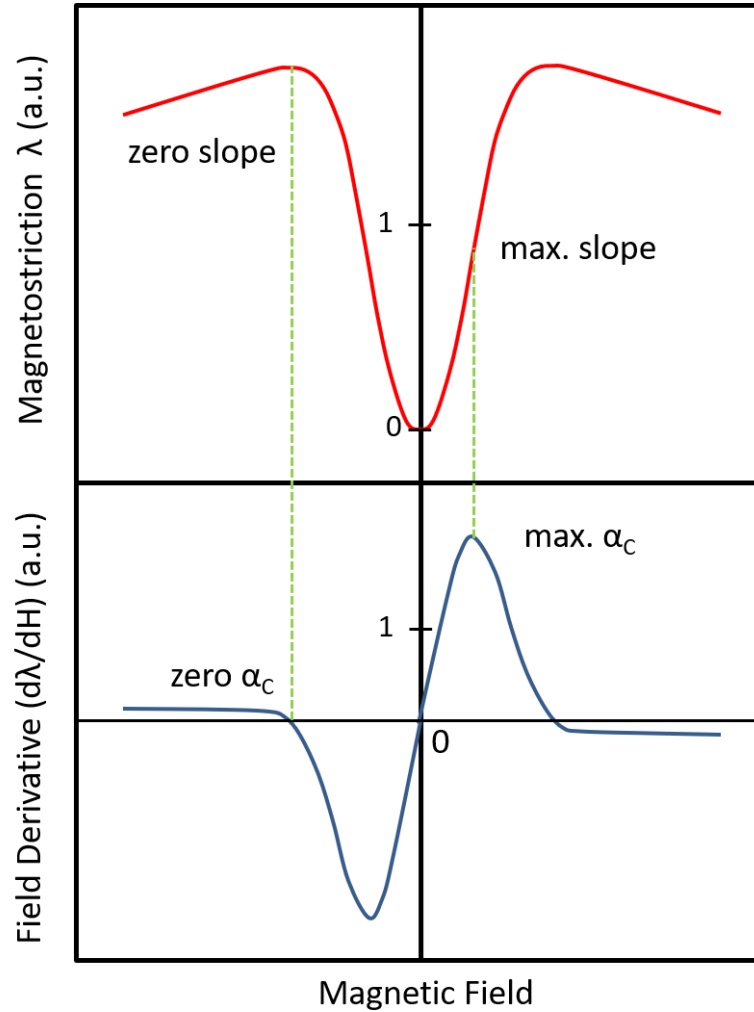


Figure 6.23: Schematic representation of the relation between the magnetic field dependent magnetostriction λ (a) and its field derivative $d\lambda/dH$ (b) representing the typical shape of a $ME(H)$ curve, adapted from Ref. 204.

First of all, the magnetostriction value can be both positive and negative, which can be explained by the fact that a negative magnetostriction value is indicative of contraction (compressive stress), while positive magnetostriction represents an elongation of the material (expansive stress), with the former being quite typical for ferrite systems.²⁰⁵ As far as the correlation between magnetostriction and induced ME magnetization is concerned, we can look at certain

segments of the curves in detail in order to explain the origin of the shape of our ME magnetization curve. Starting off at zero magnetic field, the magnetostriction is effectively nonexistent, while our measurements show a small ME magnetization. This can be explained in part by the high field superconducting solenoid of the SQUID magnetometer not having been degaussed prior to this measurement, with the magnetic field from a small amount of trapped flux causing a signal that is larger than zero. However, the remanent magnetization of the sample is assumed to contribute the largest part to the nonzero ME magnetization at zero applied field, which was clearly seen in the results obtained by Agarwal et al.²⁰⁶ using similar composites. Moving on, the magnetostriction curve shows a very steep increase, corresponding directly to the maximum of our magnetization curve. In this sense, the induced magnetization can be regarded to be tracking the derivative of the magnetostriction curve $d\lambda/dH$, with the maximum of the induced ME effect being located at the maximum slope of the magnetostriction. Moving further along the curve, $\lambda(H)$ reaches its maximum, with the slope decreasing to zero, corresponding to the derivative, and thus also the ME magnetization signal dropping to zero. For this first sample set, we thus had a satisfactory explanation as far as the source of the ME magnetization curve shape goes. Following these measurements, the question was raised about possible hysteresis effects and minor loops having an influence on the results, with such low-field measurements potentially not being properly representative of the sample properties. Because of this, a more detailed characterization of the magnetic field dependence of the ME effect will be performed in the next section. As mentioned, it was decided early on during the writing of this thesis that the ME results are to be shown chronologically, as otherwise, such measurements with seemingly incomplete parameters wouldn't make sense when evaluated alongside our more elaborate results. This chapter is therefore a proof of concept for our general approach to these measurements, which will be further refined in the following.

The final set of measurements for this sample set consists of the determination of the magnetoelectric coupling coefficient, performed by recording the induced ME signal in dependence of the applied electric AC field. For the publication that was composed from this data,¹²³ a direct comparison was planned between the SPS sample S3 and the conventionally annealed sample S4. However, due to the excessive conductivity, and resulting low poling state, the SPS sample was generally not suitable for the determination of the optimum temperature, and showed a very low field value of 0.1 T for its maximum. To offer a more direct comparison, the identical parameters were to be used for this final measurement, which resulted in an applied DC magnetic field of 0.15 T, located just between the two maxima of the respective samples, while the temperature could only be based on the successful measurement on sample S3, namely 285 K, agreeing well with the BTO phase transition between its tetragonal and orthorhombic phase (see Fig. 3.3). The resulting measurement is also displayed in Fig. 6.22, with the conventionally sintered sample showing a linear response with very low noise and no visible scattering of the data points, while the SPS sample produces a much lower signal amplitude and somewhat

erratic behavior. Linear fitting of the respective curves produced a converse magnetoelectric coefficient α_C of only around 1 ps/m, which was within the error bar of ± 1 ps/m (see section 6.2.2), while the conventionally sintered sample gave 25 ps/m.

Summary

From this first sample set that was characterized by the converse ME setup, we could draw a number of basic, but important conclusions. First of all, the setup, especially after the wiring was rebuilt, showed its ability to produce data of very high quality compared to previous measurements,¹²² especially in terms of determining the temperature and magnetic field dependence. This capability will thus be expanded for the next sample set, so that a much greater range of temperatures and magnetic fields, as well as different sample orientations can be utilized.

In terms of physical phenomena, we were able to observe, measure and quantitatively evaluate the converse magnetoelectric effect in a composite sample produced from core-shell particles that were synthesized for this purpose. Unfortunately, one of the main objectives, namely the usage of the SPS method to suppress grain growth and potentially give us a higher ME effect, was not met. To the contrary, the SPS method produced a sample that was only usable after additional annealing, which induced further grain growth, as the initially produced, untreated sample was not usable due to BTO crystallizing in a cubic phase and thus not being in its ferroelectric state. The annealed SPS sample showed high conductivity, making poling and polarization measurements difficult and almost impossible, while the temperature dependence of the induced ME magnetization indicated only effects from conductivity, rather than ME coupling. Nevertheless, thanks to the converse ME setup, it was still possible to record the magnetic and electric field dependence, but both showed very low and noisy signals, with the overall converse ME coefficient being in the range of the error bar. We must therefore conclude that the SPS method, as utilized here, is not suitable to produce ceramics with higher ME effect. Meanwhile, the conventionally sintered sample provided good quality data in all ME measurements, with the recorded effect of 25 ps/m being slightly higher than the 22 ps/m given in Ref. 21, which was the overall goal. However, this increase is rather small, which is why the next section will deal with the further optimization of the effect through the modification of the sample composition, while retaining the well-proven conventional sintering method.

6.2.4 Direct and converse effect in CFO-BTO (0-3) composites

Following the experience gained from the previous set of measurements, it was decided to return to the conventional sintering method in order to produce (0-3) ceramics using the same CFO-BTO system, and also using the same synthesis procedure for the core-shell particles. However, in this work, the ratio of CFO and BTO was altered systematically, in order to determine which composition gave the highest ME coupling coefficient. Additionally, as the conventional sintering method does not suffer from excessive conductivity that results from a (3-0) connectivity, it was also possible to perform measurements of the direct ME coefficient rather than only the converse one. Furthermore, a number of additional steps were taken that significantly increased our knowledge on this multiferroic system: It was mentioned in the experimental section 2.2.3 that the electrical poling of the ceramics after sintering is an important step that strongly increases the recorded ME effect. In this study, a direct comparison was made between poled and depoled samples to quantify the effect of this process. Furthermore, in order to observe the equivalence^{47,48} of the direct and the converse magnetoelectric coefficient, the results of both methods will be directly compared for this sample set, while the measurement of the dielectric permittivity was linked to the ME results. Latter were also obtained for two different sample orientations, with the magnetic field being perpendicular (longitudinal ME effect) and parallel (transverse ME effect) to the sample surface. These results therefore represent our most comprehensive series of measurements and subsequent analysis of precharacterization and ME data at the time.

The synthesis procedure was identical to the one of the previous sample set, as also described in section 5.2. The only important difference lay in the modification of the amounts of CFO and BTO precursor solutions in order to achieve the desired weight ratios between the two phases. The subsequent milling, calcination, pressing and sintering steps were also identical to the previous sample set. In total, four samples were produced, with the wt% composition $(1 - x)\text{CoFe}_2\text{O}_4 - x\text{BaTiO}_3$ and $x = 0.5, 0.6, 0.7$ and 0.8 .

Structural characterization

Phase content and composition of the samples were analyzed by XRD (Siemens D-5000), with the corresponding diffractograms (Fig. 6.24) showing only peaks from the CFO and BTO phase; no other phases could be detected. In contrast to the SPS sample from the previous set, all of the samples produced here display a splitting of some BTO diffraction peaks, such as the (112/211) peaks that were also displayed separately in Fig. 6.16. This indicates the presence of a tetragonal cell, so that we can expect BTO to be in its ferroelectric phase. As such, XRD provides evidence that all samples are usable for ME measurements as far as the basic electric properties of the piezoelectric constituent are concerned.

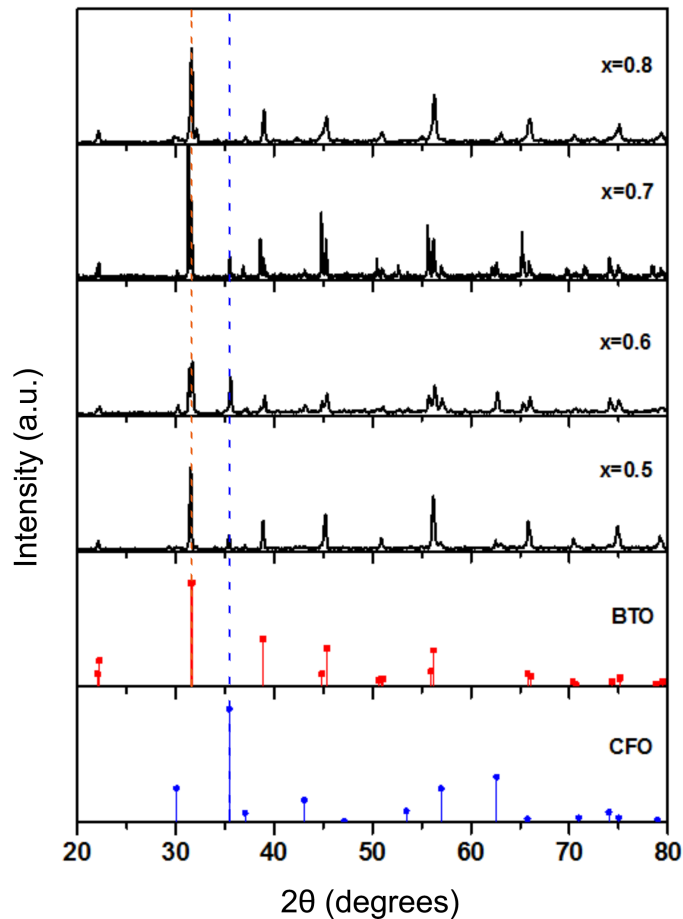


Figure 6.24: X-ray diffractograms of the $(1-x)\text{CFO}-x\text{BTO}$ composite samples, with the two bottom panels showing the spectra of the respective pure constituents (JCPDS database), with the main peak positions superimposed onto the diffractograms by dashed lines. Adapted from Ref. 124, reprinted with permission.

SEM measurements (Quanta 400 FEG) were performed after polishing and etching the sample surfaces, with the results shown in Fig. 6.25 providing a great insight into the intricate structures of the different samples, with all of them showing the desired (0-3) connectivity, containing CFO grains embedded in a BTO matrix. As detailed in Ref. 124, the grains are clearly separated and homogeneously distributed, with a clear interface between CFO and BTO, devoid of any cracks or faults, providing good contact between the two constituents, promising good mechanical coupling and thus a high magnetoelectric coefficient.²⁰⁷ Only sample $x = 0.5$ deviates slightly from this trend, with white regions in the interface area pointing towards defects and undesirable crystal growth. In terms of size, the grains have grown to diameters of about $1\text{-}2\ \mu\text{m}$, being comparable to the conventionally sintered (0-3) sample from the previous sample set.¹²³ For $x = 0.8$, a small area of the sample surface (Fig. 6.26 (a)) is shown in magnification (b), giving us a very clear view of a CFO grain and the well-defined interface, showing no defects or signs of interdiffusion.

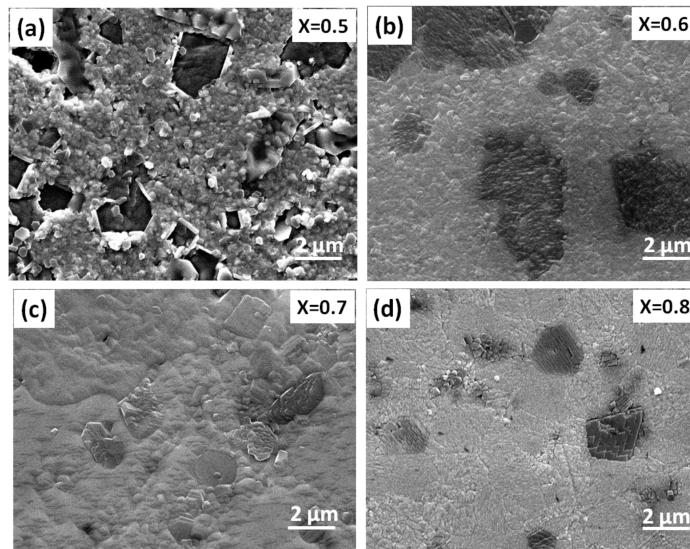


Figure 6.25: SEM micrographs of the polished surfaces of the (1-x)CFO-xBTO composite samples. Taken from Ref. 124, reprinted with permission.

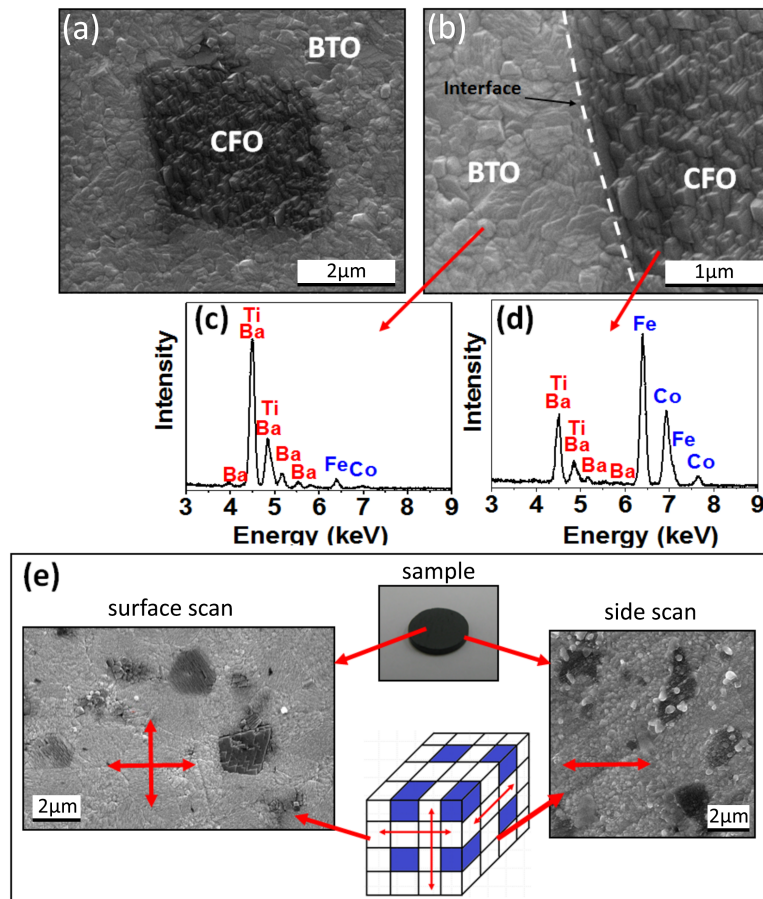


Figure 6.26: SEM micrograph of sample $x = 0.8$ showing a magnified view of a CFO grain within the BTO matrix (a), as well as the interface between them (b), with corresponding EDX spectra for the CFO (c) and BTO (d) region. Further SEM images are shown in (e) to compare the connectivity on the sample surface and side. Adapted from Ref. 124, reprinted with permission.

Going into detail even further, the top and side surfaces of sample $x=0.8$ were analyzed separately (Fig. 6.26 (e)), in order to check for homogeneous distribution of the CFO grains. It's clearly visible that the grains are well separated in both locations, not forming percolating clusters. This means that there should be no issues regarding excessive conductivity that caused trouble during the ME measurement of the SPS sample. For these samples, no visible interconnected grains exist that might provide paths for the current to flow through the sample at lower resistance than that offered by the BTO matrix. We can therefore assume that 1.) these samples can be properly poled for a high ME effect and 2.) that not only the converse but also the direct effect should be measurable. Furthermore, energy dispersive X-ray spectroscopy (EDX) was performed on different local areas of the sample, with spectra being shown in Fig. 6.26 (c) and (d) of a BTO and CFO-rich section, respectively. The clear shifts in line intensity further underlined the clear separation of the two phases. The small BTO peaks in (d) can be attributed to the electron beam hitting not only the grain but also some of the surrounding matrix, while (c) shows almost no contribution from CFO, owing to the greater ease of targeting only the surrounding matrix without hitting any of the grains.

Electrical characterization

Here, the microscopic characterization was foregone and instead, the macroscopic electrical properties were evaluated right away. First shown is the temperature dependence of dielectric permittivity, measured at different frequencies, summarized in Fig. 6.27.

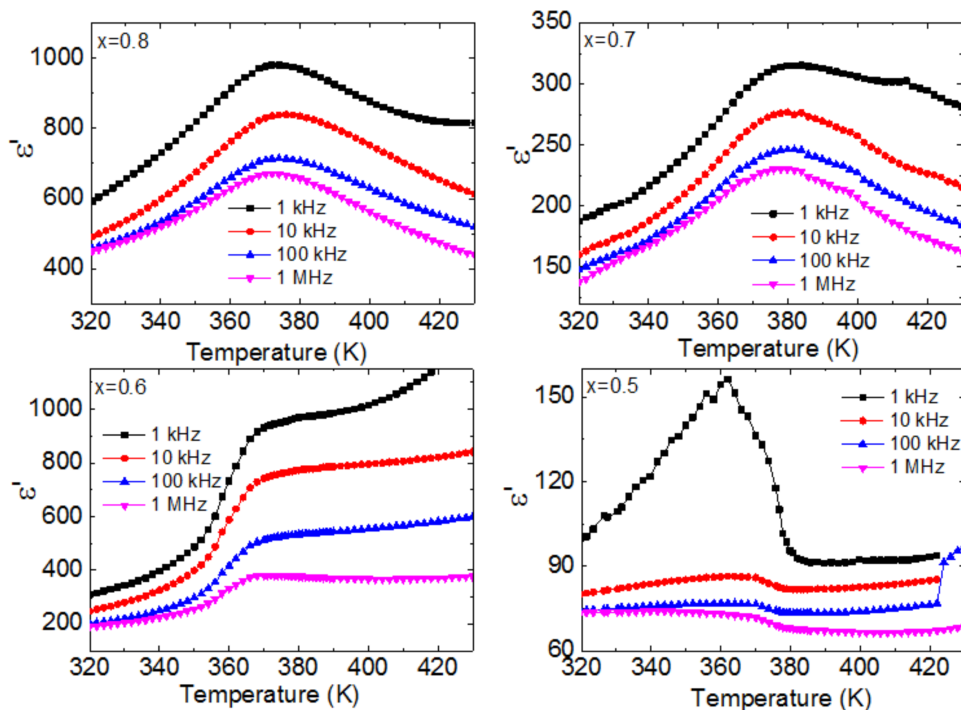


Figure 6.27: Temperature dependence of the real part ϵ' of dielectric permittivity of the $(1-x)\text{CFO}-x\text{BTO}$ composite samples, taken from Ref. 124, reprinted with permission.

The ferroelectric Curie temperature is visible as a peak between 370 and 380 K, which is slightly below the literature value for bulk BTO,²⁰⁷ with samples $x = 0.6 - 0.8$ showing substantial broadening of these transition peaks. One would normally associate the latter with size effects due to the small grain size, but as this is an effect of the ferroelectric phase, namely the BTO matrix, that probably doesn't apply here. Apart from the potential incorporation of Fe or Co in the BTO phase during the high temperature processing, one valid explanation may very well be the strain exerted on the BTO matrix by the CFO grains. Another important aspect is a decrease of the dielectric permittivity, associated with an increase of dielectric losses, upon increasing CFO content. It was discussed before that samples with a high percentage of CFO tend to have increased conductance and leakage currents as a result. This is visible here for samples $x = 0.5 - 0.6$, the samples with the highest CFO content, showing stronger frequency dispersion towards decreasing frequencies, with it being noted in Ref. 124 that Maxwell-Wagner relaxation¹⁵² became substantial at this point. As explained in section 4.8.4, this effect occurs in dielectrics that are not homogeneous, such as grained composites²⁰⁸ and layer systems, leading to a strongly frequency dependent charge buildup at the interfaces between constituents of different permittivity and conductivity. In our case, this would of course be the BTO and CFO phases. The strong frequency dispersion at low frequencies is usually associated with dielectric losses stemming from conductivity.

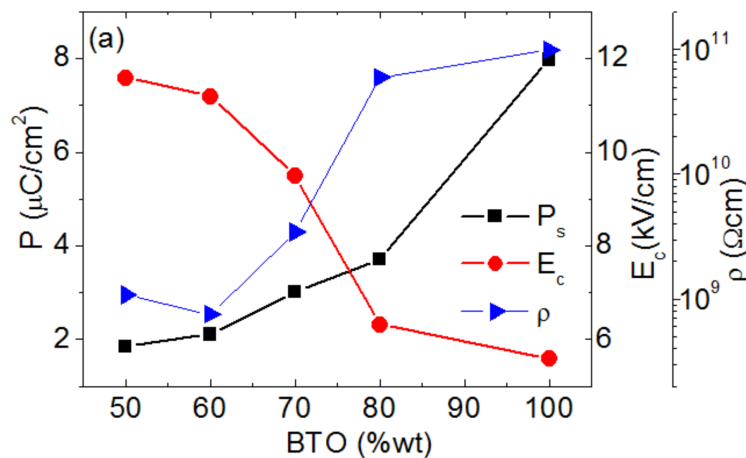


Figure 6.28: Summarized results from $P(E)$ loops recorded on the $(1-x)\text{CFO}-x\text{BTO}$ composite samples, showing spontaneous polarization P_s (black), coercive field E_C (red) and resistance ρ (blue). Taken from Ref. 124, reprinted with permission.

$P(E)$ loops were recorded at room temperature at 250 Hz using a home-built Sawyer-Tower circuit, with the obtained results such as coercive field and spontaneous polarization being displayed in Fig. 6.28 along with the resistivity of each sample. Plotted against the BTO content, we can see striking characteristic changes that we should keep in mind not just for these samples but also for the other studies that will be described in the following. The resistivity clearly increases with higher BTO content, which is logical when keeping in mind that CFO

has much higher conductivity (as mentioned in section 6.2.4 and Ref. 197.). The spontaneous polarization P_s shows a similar increase, going along with the finding of SPS samples not being suitable for poling due to their excessive conductivity and leakage currents. We can therefore assume that samples with high BTO content have good prerequisites for high ME coefficients, as far as the electrical properties are concerned. When looking at the coercive field, a decrease can be observed upon increasing BTO content. This was explained in Ref. 124 by conductive CFO grains impeding polarization switching in BTO through screening effects by free charge carriers, lowering the effective electric field that is acting on the BTO phase. We can thus keep in mind: For advantageous electrical properties, high BTO content seems to be the favorable route to take.

Magnetic characterization

Similarly to the electrical characterization, the magnetic properties were checked by measuring $M(H)$ hysteresis loops up to 2 T at room temperature, in order to record saturation magnetization and coercive field for all samples. The low field region of these measurements, up to 0.4 T, is shown in Fig. 6.29. A pure CFO ceramic was used as a reference, showing a saturation magnetization of 84.4(5) Am²/kg, which is in agreement with literature values of bulk CFO²³ that is usually around 80 Am²/kg. The composite samples show a significant decrease in saturation magnetization due to the lower mass fraction of CFO, while coercivity also decreases from 25(2) mT for the pure CFO sample down to 5(1) mT for the composites. These observations are in excellent agreement with a similar study conducted by Agarwal et al.,²⁰⁶ who used bulk powders for their samples, observing a saturation magnetization of 80 Am²/kg while obtaining 36.2 Am²/kg for $x = 0.5$ and 11.8 Am²/kg for $x = 0.8$, comparable to our results of 30.0(4) Am²/kg for $x = 0.5$ and 14.9(6) Am²/kg for $x = 0.8$. These findings have been summarized in Fig. 6.30 (red circles), plotted against the weight percentage of CFO instead of the x -notation used for most of the figures, to more clearly show the dependence on the ferrite content.

Furthermore, we can see that the decrease in magnetization does not take place completely linearly with the change in composition, as the magnetization for $x = 0.5$ drops by more than 50 %, from 85 Am²/kg down to 28 Am²/kg instead of the expected value of ca. 33 Am²/kg. This effect becomes clearer when we correct the magnetization values by disregarding the mass of the non-magnetic BTO, shown in Fig. 6.30 (blue squares). The magnetization of the composites is consistently lower than of the pure CFO sample, even after mass correction. This phenomenon was observed in some preceding works, such as Fig. 5 in Ref. 122, while also being described in several other publications,^{206,209} usually attributed to size effects in nanoscale materials, such as surface spin canting in small crystallites. As we saw in the SEM images, the CFO grains in our composites grew substantially, but the complex nature of such sintered composites still allows for some smaller grains to be present, as seen in Fig. 6.26 (e). Additionally, in case of such high

temperature sintered materials that show considerable growth of the magnetostrictive grains, additional influence may arise from a change of inversion,¹²¹ as well as a cation redistribution in the spinel lattice. Furthermore, the decreasing ratio of the ferrimagnetic constituent leads to a decrease of the effective permeability of the composite,²¹⁰ which in turn contributes to the decrease of magnetization.

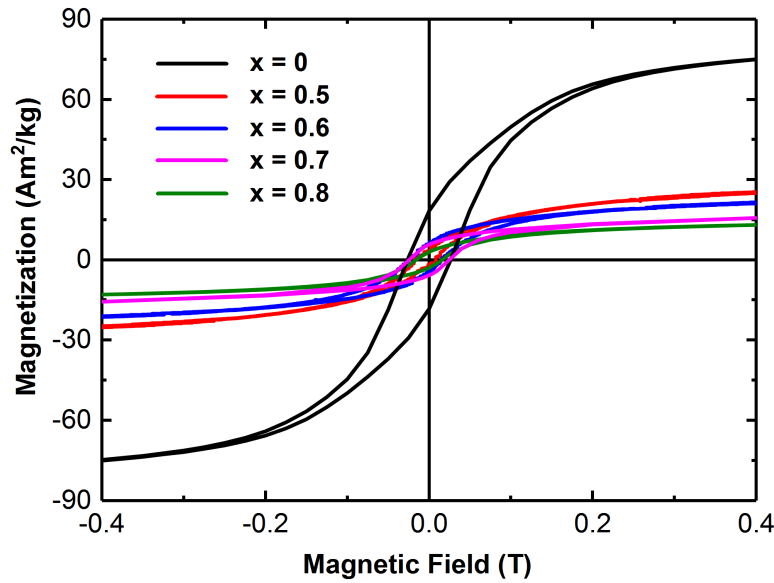


Figure 6.29: Field dependent magnetization $M(H)$ curves for the $(1-x)\text{CFO}-x\text{BTO}$ composite samples recorded at room temperature up to $\mu_0 H = 2\text{ T}$, with only the small field region being shown. Adapted from Ref. 124, reprinted with permission.

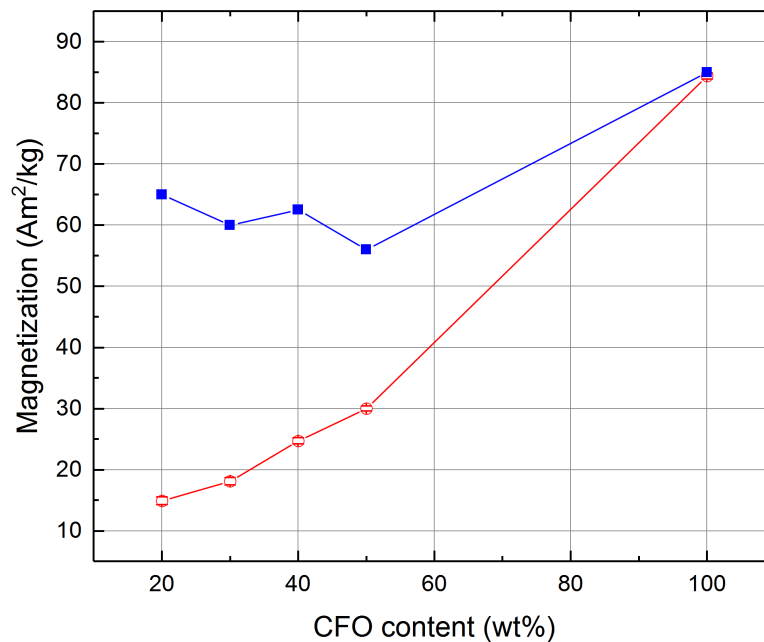


Figure 6.30: Total magnetization for the $(1-x)\text{CFO}-x\text{BTO}$ composites (red) and the CFO magnetization (blue), corrected for the non-magnetic mass content of the samples.

This can be described by an effective medium approximation,²¹¹ for example Bruggeman's model, as described by Qi et al.²¹² When dealing with a composite formed of two individual components with the respective magnetic permeabilities given by μ_1 and μ_2 , and under the assumption of a uniform distribution of the constituent elements, the following equation can be utilized to describe the relation of the two permeabilities relative to each other:

$$\frac{3(1-f)}{2 + \frac{\mu_2}{\mu_{eff}}} + \frac{3f}{2 + \frac{\mu_1}{\mu_{eff}}} = 1 \quad (6.7)$$

Here, f is the volume fraction, which is given by the respective composition of the sample at hand, while μ_{eff} represents the effective permeability of the composites.²¹³ In our case, we will define μ_1 and μ_2 to represent the permeability of BTO and CFO, respectively. Due to the fact that BTO can be considered as non-magnetic, its permeability will be approximated by unity, so that the equation is simplified to

$$\frac{3(1-f)}{2 + \frac{\mu_2}{\mu_{eff}}} + \frac{3f}{2} = 1. \quad (6.8)$$

From this, we can qualitatively deduce that the increase of the BTO phase, and the associated change in the volume ratio f , also leads to a decrease of the effective permeability μ_{eff} of the composite. This in turn contributes to the decrease of the magnetization that we have observed for our samples. As mentioned in the previous section, referring to the 2 T magnetization for these samples as saturation magnetization is technically not fully adequate, although it is being done throughout the literature. We previously discussed how spin frustration simply leads to higher applied fields being necessary to bring the sample to saturation. Similarly, following Bruggeman's model explained above, the effect of the lower permeability would be much less noticeable if higher magnetic fields would be utilized, so the lower magnetization for these samples is also caused by the comparatively low 2 T maximum field.

Converse magnetoelectric measurements

Now we again arrive at the main topic of this thesis, the macroscopic measurement of the converse ME effect. Unlike in the first sample set, some additional measurement steps have been included here, which makes this sample set the most comprehensively characterized one until now. The temperature dependence of the ME effect, recorded as in the previous section, was now performed in a much larger temperature range, from 330 K all the way down to 5 K, in order to observe the general trend in the signal, and to see whether additional phase transitions of BTO would be visible.

It needs to be considered that one such measurement needs a substantial amount of time to be completed, with the temperature dependence shown here alone requiring over 24 hours, due to the extensive noise reduction and nulling procedures performed at each data point. It is for this

reason that our initial sweep in Fig. 6.21 was only performed in a much narrower temperature range around the most important phase transition. For the same reason, only one of the samples from the current set was subjected to this extended temperature range, which is also the same sample that was used for a similarly extensive DC magnetic field survey. This sample, with the composition $x = 0.6$, will serve as our model system for the other samples used in this study.

In anticipation for the $ME(H)$ measurement, with which we intended to check both the longitudinal and transverse coefficient, this sample was measured in two ways. The first one was the regular geometry with electric field and magnetic field both being applied out of plane, perpendicular to the sample surface. The second one saw the sample rotated by 90° so that the magnetic field was parallel to the sample surface, while the electric field orientation relative to the sample surface remained unchanged, as shown in Fig. 6.31.

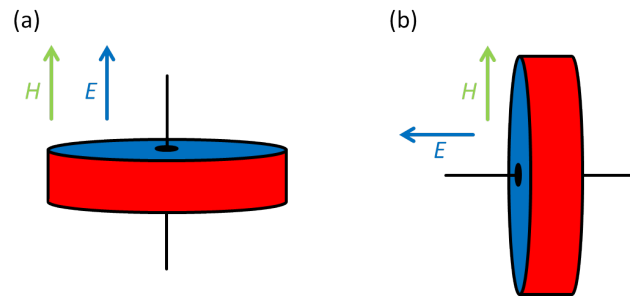


Figure 6.31: Schematic representation of the different sample orientations used here, with the sample displayed in red and the electrode in blue. (a) shows the normally used longitudinal geometry in which H and E are out of plane while (b) shows the transverse geometry with H in plane and E out of plane.

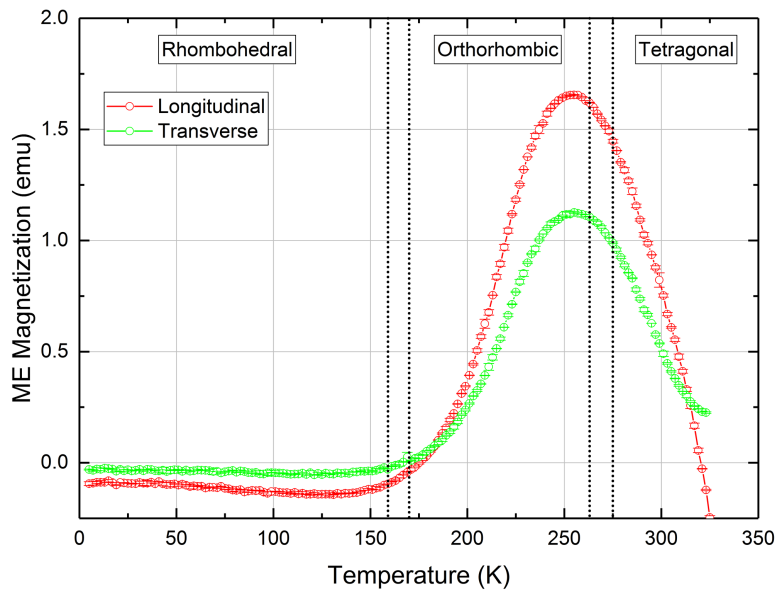


Figure 6.32: Temperature dependence of the induced ME magnetization for sample $x = 0.6$ in longitudinal and transverse geometry, recorded at $E_{AC} = 3.3$ kV/cm, $f_{AC} = 3$ Hz, $\mu_0 H_{DC} = 0.15$ T. The transverse curve was inverted for easier comparison.

This was achieved by adding a small additional section of straw to the construction previously introduced in Fig. 4.21, which held the sample in place vertically. This caused an inversion of the signal for the rotated sample, which will be explained when we observe the $ME(H)$ results. Here, for ease of comparison, both curves were given a positive prefix at the main peak position when shown in Fig. 6.32. For both orientations, we observe a similar behavior, albeit with a strongly reduced effect for the rotated sample. Again, we can see that the data is very clear and devoid of any excessive noise or other artifacts that would indicate problems with the validity of the data, with no jumps or sudden changes in the phase shift being detected. A broad but clear peak is observed at 254 ± 2 K for both orientations, with the signal dropping to both sides of it. Going towards lower temperatures, the signals also becomes negative near 175 K, coinciding with the orthorhombic to rhombohedral phase transition, with its absolute value further decreasing at even lower temperatures. There is a rather broad plateau around 123 K at which the absolute value for the negative signal becomes the highest. Towards high temperatures, the curve for the rotated samples shows signs of leveling off, while the sample in regular geometry continues its strong decline, becoming negative at 320 K.

When we insert the temperature regions of the phase transitions, taken from Fig. 1 of Ref. 203 and our Fig. 3.3 adapted from Ref. 93, we can see that there is a noticeable difference between the position of the maximum near 254 K and the lower edge of the phase transition from the tetragonal to the orthorhombic phase, which is reported to be at 263 K.⁹³ When regarding the original data from the two references, it was shown that the phase transition has a certain width, reported to be around 12 K in Ref. 203, depending strongly on the direction in which the measurement is performed, which is also well visible in Fig. 3.3. In our case, we also performed the measurement going from high to low temperatures, and should thus be located on the low end of transition temperatures, but this difference is still not sufficient to explain the peak shift visible in the data. At the time, no clear evaluation was performed for this deviation from expected literature values. However, after performing some of our later experiments, a more detailed observation showed that the temperature dependence does not come solely from the phase transitions of the ferroelectric phase. This shall be elucidated in detail in section 6.2.6 when we discuss effects from the magnetomechanical and electromechanical coupling, as well as the elastic compliance that results from the stiffness of the sample.

With the temperature dependence having been reviewed, the magnetic field dependence was characterized, using the same modified sample holder. This allowed us to record the sample response in both regular geometry and with the sample rotated by 90° , so that the magnetic field was applied parallel to the sample surface. Using otherwise standard settings, the magnetic field was now ramped in both directions, up to a maximum field of ± 2 T, so that hysteresis effects could also be observed. The result of this approach is shown in Fig. 6.33, which contains the signal from both sample orientations, as presented in Fig. 6.31. It becomes immediately

obvious that the signal for the rotated sample is inverted, reduced by roughly 50%, and that the maximum of the ME effect occurs at a much lower magnetic field of 0.02 T in contrast to the 0.15 T of the regular geometry. Two obvious conclusions would be that the regular geometry is more suitable if one wants to achieve a high ME effect, and that the most optimal field for this would be around 0.15 T. However, with the more detailed data at hand compared to Fig. 6.22, we also need to determine the underlying cause for the overall shape of the curve. Three characteristics must thus be elucidated: The lower amplitude, the sign change, and the lower magnetic field at which the maximum of the $ME(H)$ signal occurs. While the overall shape is already known from the relation to magnetostriction (see Fig. 6.23), we now want to relate our results to more detailed studies found in the literature. For this, we will now use the nomenclature from Ref. 206 to account for the magnetic and electric field directions, namely α_{33} for regular and α_{31} for our rotated geometry (see Fig. 6.31).

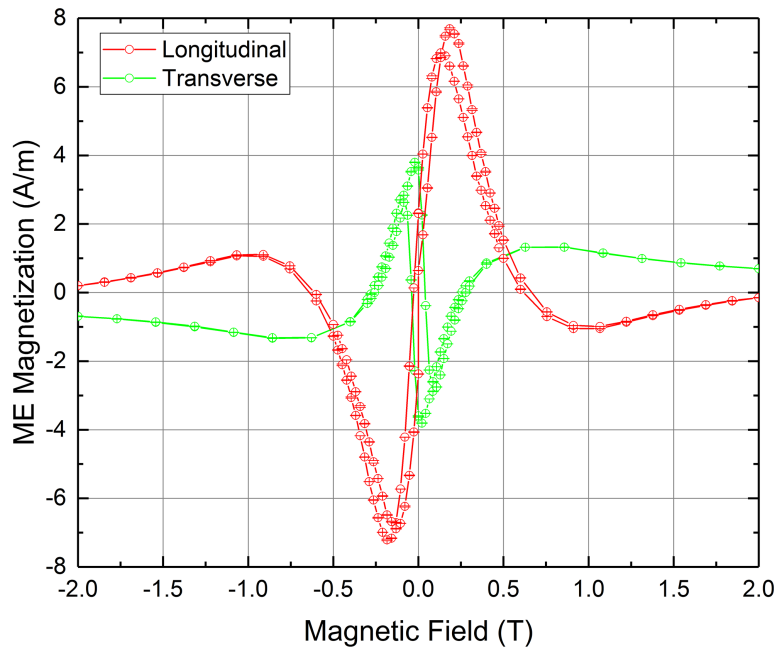


Figure 6.33: Magnetic field dependence of the induced ME magnetization for sample $x = 0.6$ in longitudinal and transverse geometry, recorded at $E_{AC} = 3.3 \text{ kV/cm}$, $f_{AC} = 3 \text{ Hz}$, $\mu_0 H_{DC} = 0.15 \text{ T}$ and 285 K .

To account for the change in the position of the field dependent maximum in parallel and perpendicular orientation, the demagnetizing factor comes into play. A similar study was performed on a CFO-BTO composite by Duong et al.,²¹⁴ who developed a magnetic pulse field method to determine the ME effect, which is in essence a method to measure the direct ME effect, which will also be done on our samples (Fig. 6.38). The main difference is the ability of Duong's setup to use pulsed magnetic fields, thus being able to observe dynamic properties as well, in addition to the quasi-static ones. They also performed a regular $M(H)$ sweep on the sample using both orientations, which we have also completed, as is shown in Fig. 6.34, showing very good correspondence with results from Duong et al., enabling us to

attempt a direct comparison between the two datasets. One characteristic we can see with the naked eye, also important for the rest of the evaluation, is the somewhat quicker saturation of the rotated sample compared to the sample in regular geometry, while the coercive field of 650(4) Oe is comparable for both. Just like in our sample set, Duong observed a higher effect for α_{33} , which occurred at higher fields than for α_{31} , in the very same field range as for our samples, between 1 kOe and 2 kOe, shown clearly in Fig. 4 of their work.²¹⁴ An explanation that was offered for this circumstance is the demagnetizing field, which leads to a decrease of the magnetic field within the sample, thus shifting the field dependent position of maximum ME effect in the $ME(H)$ curves. If we refer to this field as the effective field, then CFO grains within the longitudinal sample are subjected to a lower magnetic field amplitude and thus require a higher applied field to reach their maximum of induced ME magnetization. It has to be mentioned that there is also the electric counterpart, the depolarizing field. However, as the electric field application cannot be changed due to the sample contacting, we will only regard the demagnetizing field here.

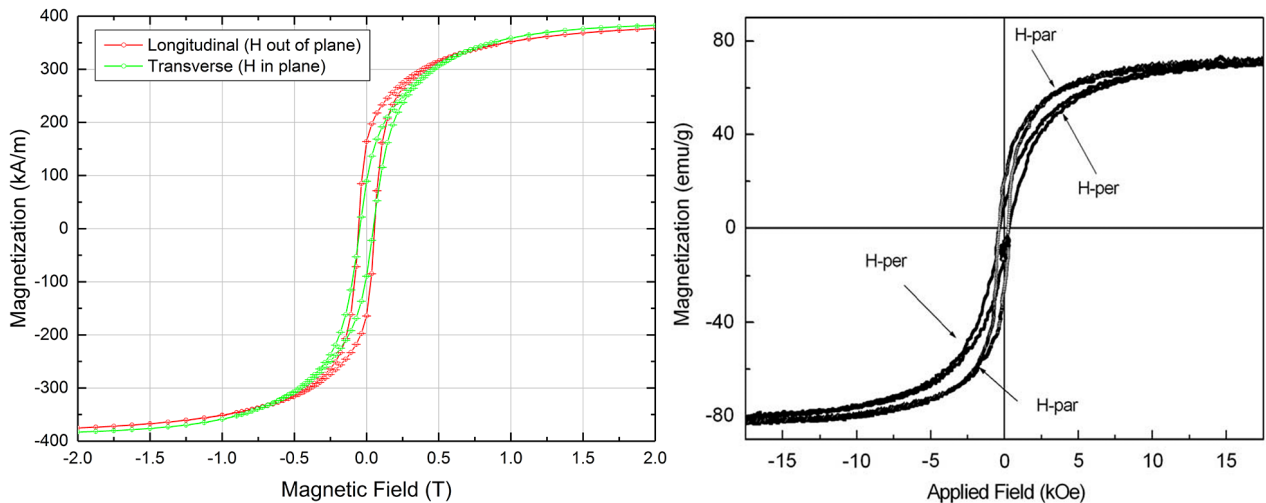


Figure 6.34: $M(H)$ curves of sample $x = 0.6$ recorded at 255 K (left) directly compared to $M(H)$ curves of a CFO-BTO 50-50 composite (right) recorded by Duong et al. (Ref. 214) at room temperature, reprinted with permission.

Going into more detail, we refer to the work of Chen et al.,²¹⁵ who have performed a comprehensive survey on demagnetization factors for cylinders by magnetometry techniques. It's a convenient coincidence that our sample is also cylindrical, allowing a direct relation to the data from Chen. When observing the effect of the demagnetizing field $H_{mid,vol}$, they utilized the equation

$$H_{mid,vol} = H_a + H_{d,mid,vol} = H_a - N_{f,m} M_{mid,vol} \quad (6.9)$$

with the applied field H_a , assumed to be uniform, with the calculation averaged over the entire midplane (mid) and volume (vol) of the sample. Eq. 6.9 thus gives us the proportionality

between the demagnetizing field H_d and the magnetization M . The demagnetizing factor $N_{f,m}$ for both fluxmetry (f) and magnetometry (m) applications, which is given as

$$N_{f,m} = -\frac{H_{d,mid,vol}}{M_{mid,vol}} \quad (6.10)$$

in Ref. 215. Furthermore, the aspect ratio of the cylindrical sample plays a major role, defined as the relation between length $2l$ and radius a , given as

$$\gamma = \frac{l}{a} \quad (6.11)$$

in order to account for the shape of the sample material that the magnetic field has to penetrate. In all cases, we assume a material of homogeneous susceptibility, which seems valid, considering the microscopy measurement that were described earlier. However, as the tables in Ref. 215 do not take composite samples into account, we used a pure Co cylinder as a rough approximation, in order to obtain an overall idea of the scale of the demagnetizing factor. Similarly, the inversion of the aspect ratio for transverse orientation does not fully take into account the shape of the sample, so these results can only be regarded as qualitative. In the end, it was determined that the applied magnetic field of the sample in longitudinal geometry must be corrected by a factor of 0.2, while the transverse sample needed a field correction by a factor of 0.9. This would clearly shift the maximum of the transversely oriented sample closer to the longitudinally oriented one, almost completely negating the different field positions of the maxima.

We are thus able to conclude that the shift of the maxima is caused by the change of the demagnetizing factor, which is strongly dependent on the sample's aspect ratio. This begs the question whether it needs to be evaluated in detail for any further measurements that have been performed from this point onwards. However, this is not necessarily the case. While each sample may be different in terms of dimensions, usually through slight variations in thickness, it is sufficient to keep this in mind when evaluating the magnetic field dependence of the induced ME magnetization. From an application point of view, we want to know which magnetic field we need to apply to our sample in order to maximize the ME effect, rather than what field we actually find within the sample. The demagnetizing factor is thus of higher importance when deciding on the shape of the sample for a certain purpose. In our measurements, the disk shaped samples in longitudinal geometry lead to very low aspect ratios γ , which in turn causes rather high demagnetizing factors. As a result, in order to reach the optimum field for the highest ME coupling, higher magnetic fields need to be applied. This is presumably the main deciding factor on the field position of the $ME(H)$ maximum we characterize in our samples. It is thus safe to assume the peak positions of the two sample orientations would be very close to each other if we'd disregard the demagnetizing field and regard only the electric and magnetic field applications relative to each other. One thought that occurred to us during the experiments was that of using a sample with equal symmetry in both directions, which in

this case would be a cube. This can be rotated without changing the aspect ratio, and it would be logical to assume, save for poling directions or any preferred direction of crystalline growth, that the effect and the $ME(H)$ maximum would not change upon rotation.

With the reason for the shift of the maxima now being clear, we need to look at the overall shape of the curves, which was not explained in detail in our previous work¹²³ described in section 6.2.3. In fact, the hysteretic behavior of the ME effect in composites like ours is rarely discussed in literature, with one of the first publications to go into detail about this topic being a review of CFO-BTO bulk composites by Agarwal et al.²⁰⁶ In this work, the field-dependent ME effect in a series of CFO-BTO bulk composites with different constituent ratios was observed in detail, also in transverse and longitudinal configuration, just like for our samples. The results of their work are shown here for comparison in Fig. 6.35 as well as table 6.4.

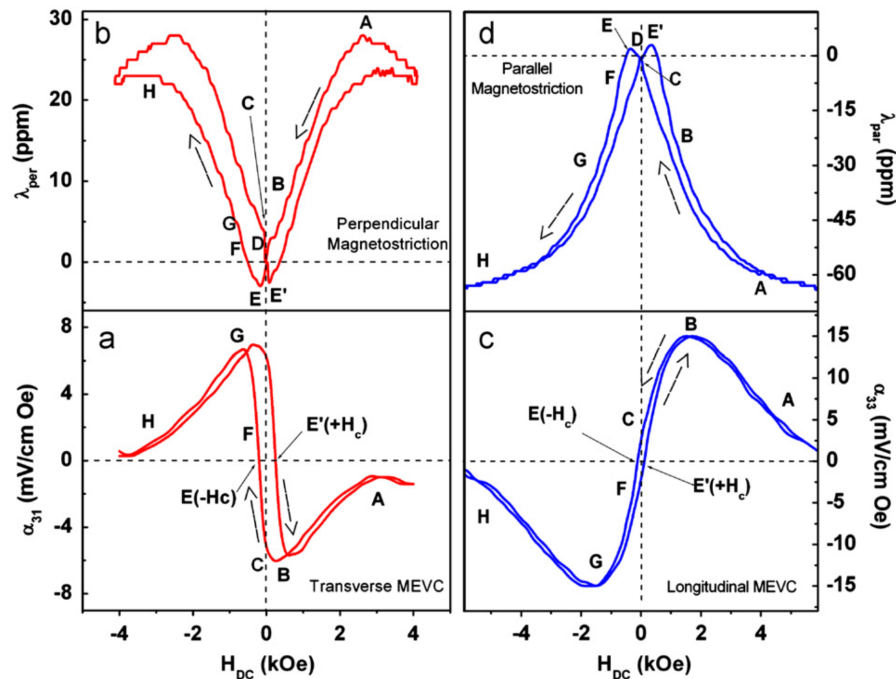


Figure 6.35: Comparison of the magnetic field dependence of the magnetolectric coupling coefficient of a CFO-BTO 60-40 sample done by Agarwal et al. in transverse (a) and longitudinal geometry (c), along with the corresponding magnetostriction curves (b) and (d), respectively. Taken from Ref. 206 using data from Ref. 216, reprinted with permission.

It was found that the sign of the curve, as was mentioned before, is determined by the way in which magnetostriction acts in the composite, a positive sign of the magnetostriction indicating compressive stress while a negative sign represents tensile stress. Just as in our samples, Agarwal et al. obtained a positive ME magnetization for the longitudinal and a negative magnetization for the transverse sample orientation, with the differences in amplitude of roughly 50 % showing an excellent match with our results in Fig. 6.33. Delving deeper into the pecu-

liarities of the magnetostriction curves and its relation to the field dependence of the ME effect, we regard the representative curves in Fig. 6.35 to observe the finer details of the magnetic field dependence, with data taken from the works of Hrib and Caltun²¹⁶ as reported by Agarwal et al.²⁰⁶ Comparing these curves of λ plotted against the applied magnetic field H , we can correlate the individual sections of characteristic shape from the magnetostriction curve directly to the induced ME magnetization curves. This way of representing the data was taken from Fig. 4 in Ref. 206, with the contents of their table 2 being summarized in our table 6.4, describing in detail how the converse coupling coefficient α_C follows the magnetic field derivative of the magnetostriction, $\alpha_C \propto d\lambda/dH$, including hysteresis effects.

Region	$ \lambda $	$d\lambda/dH$	α
A	high	very small	small
A-B	moderate	increasing	increasing
B	optimum	high	maximum
B-C	decreasing	high	decreasing
C	finite/low	decreasing	low (remanent)
C-E	very low	decreasing	low
E	low	zero	zero (phase reversal)
E-G	increasing	increasing	increasing
G	optimum	high	maximum
G-H	moderate	decreasing	decreasing
H	high	very small	very small

Table 6.4: Description of the correlation between magnetostriction and magnetoelectric coupling in a CFO-BTO 60-40 sample as done by Agarwal et al. Data taken from Ref. 216 as shown in Ref. 206, reprinted with permission.

The two peaks of the falling and rising field sweep are located at the zero transitions in the $\lambda(H)$ curve, which seem to correspond to the coercive fields from Fig. 6.34, where a 180° phase reversal occurs in both α_{33} and α_{31} . Interestingly, this phase reversal can also be observed in the raw data of our measurements, when, instead of using the normally utilized real part of the induced magnetization, one uses the phase difference between the amplitude of the induced magnetization and the original AC electric field signal. Generally speaking, we can observe excellent agreement between our results, shown in Fig. 6.33, with the data and its description from Agarwal et al.²⁰⁶ displayed in Fig. 6.35, clearly underlining the validity of our data and its interpretation. Even peculiarities like the two peaks of the $ME(H)$ curve (Fig. 6.35 (a)), depending on the prior field exposure history of the sample, is reproduced in their data as well. Finally, Agarwal et al.²⁰⁶ noted that the higher overall value of the signal in longitudinal orientation clearly indicates an increased stress level, which means that it's harder to magnetize the composite in this direction (see also the $M(H)$ curves in Fig. 6.34), while also leading to a higher induced ME magnetization. We can therefore keep in mind that the longitudinal orientation, while requiring higher applied fields to account for the demagnetizing field due to the sample's shape, still offers the highest effective ME magnetization. Because of this, all future measurements will only be performed in longitudinal geometry.

Comparison between direct and converse ME measurements

Thanks to these samples not suffering from excessive conductivity as the SPS sample, we had the opportunity to also use the direct ME setup described in section 4.1.5. The plan was to perform some of the same types of measurements, in order to obtain a direct comparison between the two methods.

There are of course some limitations to these comparisons, as the direct ME setup is not based on a cryostat system and can therefore only operate at room temperature. First, we can observe the magnetic field dependence of the direct ME effect, measured at 300 K at an applied AC magnetic field of 1.8 mT to induce the signal, while a DC magnetic field was ramped from zero to 0.4 T just like in the converse $ME(H)$ measurements. We can observe good agreement between this type of measurement and the converse one in relation to the peak position and overall shape (see Fig. 6.33), while the two samples of different compositions show different signal strengths, as one would expect.

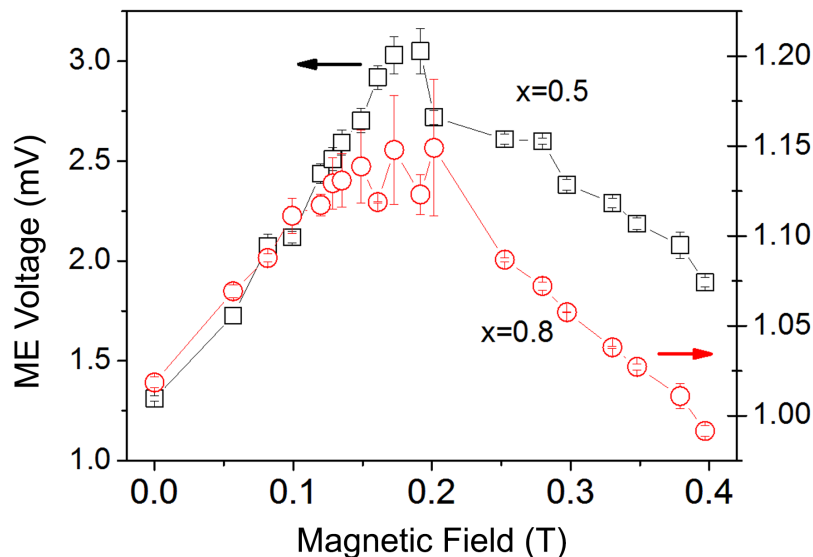


Figure 6.36: Magnetic field dependent ME induced voltage measured on samples $x=0.5$ and $x=0.8$ with the direct ME setup at $\mu_0 H_{AC} = 1.8$ mT with $f_{AC} = 3$ Hz at $T = 300$ K. Adapted from Ref. 123, reprinted with permission.

After completing the magnetic field dependence survey, it is time for the final measurements, in order to record the converse and direct magnetoelectric coefficient, namely the linear electric field sweep. During the course of these, an additional test was performed, to gain some understanding on the effect of the poling process, which is considered a standard procedure that needs to be performed before undertaking ME measurements, as described in section 2.2.3. To observe the effects that a lack of poling would have, one CFO-BTO 50-50 sample was purposefully de-poled, by keeping it heated to 140 °C for 30 minutes with it being short circuited, while the other samples were cooled down to room temperature in an electric field of 15 kV/cm. The

resulting two $ME(E)$ curves are displayed in Fig. 6.37, taken from Ref. 124. As made obvious, the depoled sample has a very low signal amplitude and higher amount of noise, not being suitable for evaluation. We have thus shown that the poling process is of utmost importance when wanting to obtain meaningful ME results, as samples that were not poled show strongly diminished signals, which was explained in section 2.2.3.

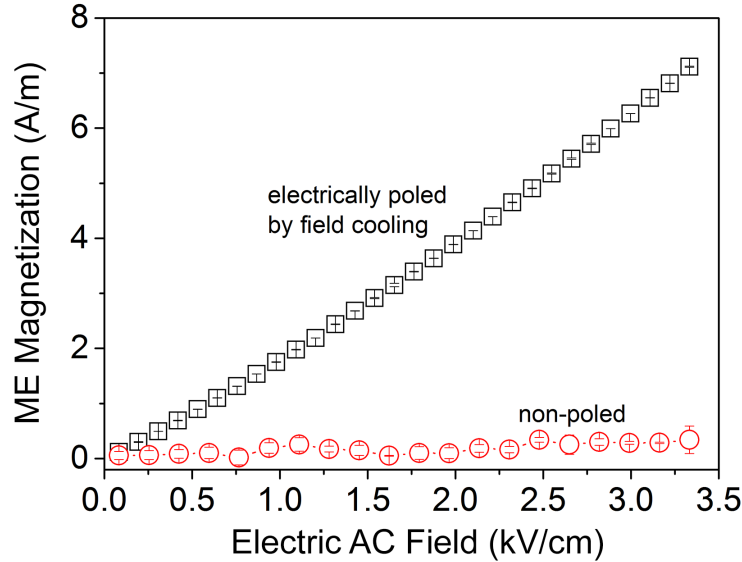


Figure 6.37: Electric field dependent ME magnetization measured on sample $x=0.5$ in poled and depoled state at $f_{AC} = 3$ Hz, $\mu_0 H_{DC} = 0.15$ T and $T = 285$ K. Adapted from Ref. 123, reprinted with permission.

The last order of business was the calculation of the converse ME coefficient from a linear fit of the $ME(E)$ sweeps. In this case, a direct comparison could be made to the direct ME results. In order to achieve a somewhat closer match in parameters, $ME(E)$ sweeps with the converse setup were performed at a somewhat higher temperature of 285 K in order to account for the fact that the direct ME setup operates only at room temperature. Exemplary results are shown in Fig. 6.38, taken from Ref. 124, using two samples with different composition as representatives of the overall sample set.

We can see that both setups are able to reproduce the linear behavior, with the differences in magnitude between the two samples also being well visible. Summarizing the coefficients calculated from both methods for all sample compositions, we arrive at the final result for this section and this sample set, shown in Fig. 6.39, also from Ref. 124, depicting the direct and converse magnetolectric coefficients plotted against the sample composition. In order to check whether the coefficients show a drop at a higher CFO content than 50 %, an additional sample $x = 0.3$ (70 % CFO) was produced and added to this dataset after successful ME measurements. We can also observe that the qualitative equivalence of the converse and direct ME coupling

coefficients described in section 2.3 holds true, with both measurement methods reproducing the same magnetic field dependence (Fig. 6.36), electric field dependence (Fig. 6.38), and finally also composition dependence (Fig. 6.39).

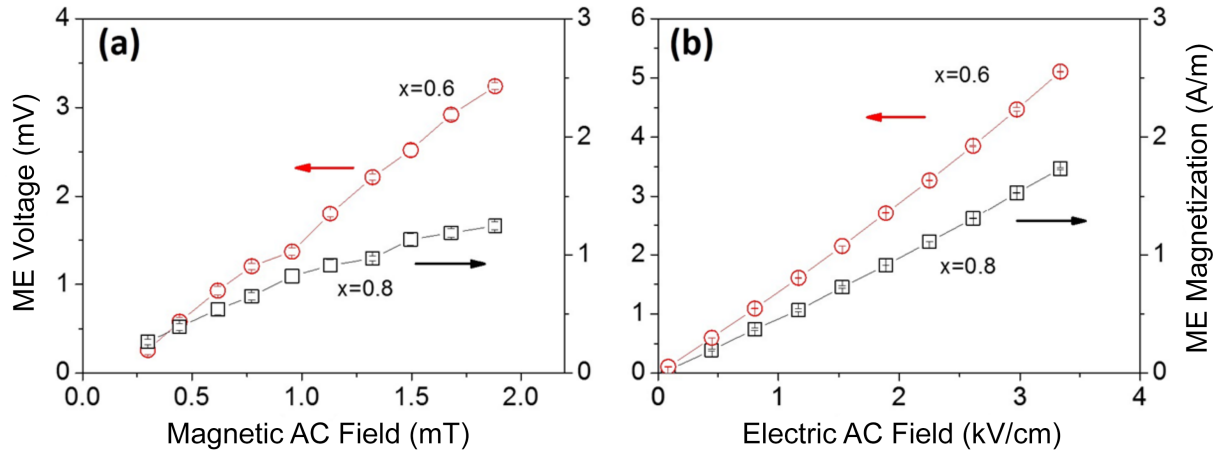


Figure 6.38: Direct comparison between magnetic field induced direct ME effect (a) measured at $f_{AC} = 3$ Hz, $H_{DC} = 0.15$ T and room temperature, and the electric field induced converse ME effect (b) measured at $f_{AC} = 3$ Hz, $\mu_0 H_{DC} = 0.15$ T and $T = 285$ K on samples $x = 0.6$ and $x = 0.8$. Adapted from Ref. 123, reprinted with permission

Our results show that, using the same geometry, similar temperatures and the same applied magnetic field and measurement frequency for all samples, leaving only the composition as a varying parameter, the sample with a 50-50 ratio of CFO-BTO gives us the highest ME effect. Some peculiarities can also be observed, such as the overall higher effect of the 50-50 sample relative to the neighboring compositions in the converse measurement, which of course begs the question of which results one should trust more. Generally speaking, and looking at the raw data, the points of the converse measurements show a much smaller deviation from the linear trend, have smaller error bars, and furthermore offer the added benefit of a freely selectable sample temperature.

It's thus highly likely that the direct ME measurements suffer from a reduction of the recorded effect due to the sample being at room temperature, somewhat away from its optimum temperature, especially when latter is shifted towards lower temperatures, as seen in Fig. 6.32. Still, we can also see that the two measurement methods were able to reproduce the same behavior in terms of showing changes to the ME coefficients α_C and α_D for varying sample composition. This is in line with the discussion from section 2.3, clearly showing that the two coefficients can be regarded as equivalent. In this case, as both measurements were performed at the same frequency, there is a constant factor of roughly 10 between α_C and α_D , caused partially by the permittivity ε at 3 Hz in Eq. 2.63, as well as the temperature difference between the two measurements.

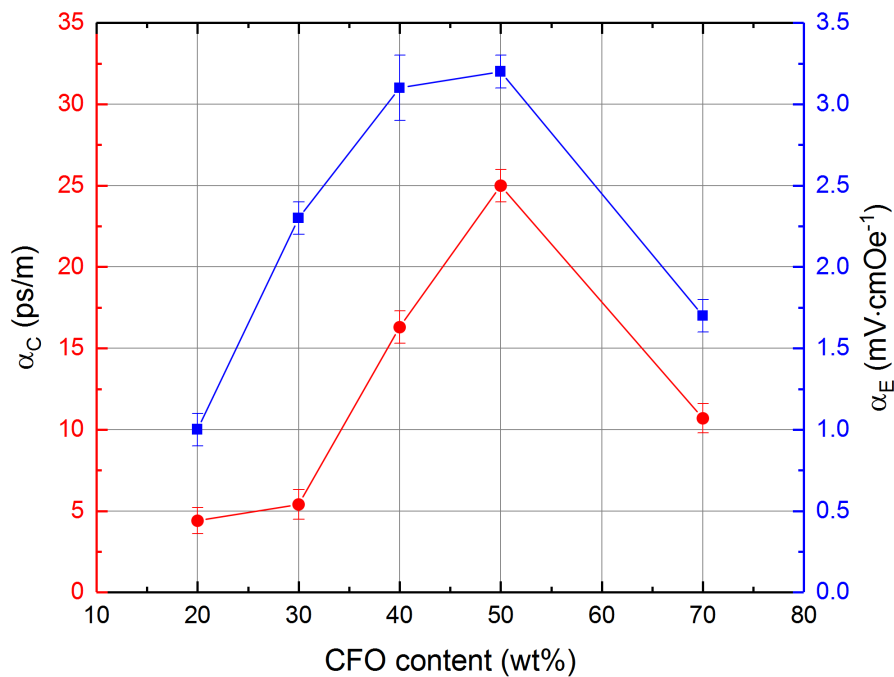


Figure 6.39: Direct comparison between the direct (blue) and converse (red) magnetolectric coupling coefficients. Data taken from Ref. 123, reprinted with permission

Summary

Arriving at the end of this study, there are a number of conclusions we can draw. The most obvious one being of course that we were able to obtain the highest converse ME coupling coefficient of 25 ps/m, which is equal to the result from the preceding section. However, we have now shown that the effect has a clear dependence on sample composition, as the sample with a CFO-BTO ratio of 50-50 had the highest α_C of this set. We also gained valuable insights into the peculiarities of this sample system: We were able to show how the samples react to applied magnetic fields in different orientations, with the demagnetizing field playing a major role as far as the sample geometry is concerned. The overall shape of the $ME(H)$ curves was explained by comparison to measurements of the magnetostriction in CFO (Fig. 6.35), while the temperature dependence has been shown to depend mainly on the structural phase transitions of the piezoelectric BTO. Finally, the importance of the poling procedure prior to the measurements was clearly demonstrated by a direct comparison between a poled and depoled sample. When considering the overall value of the converse ME coupling coefficient, one may have noticed that we were not able to achieve a higher value, despite using the most optimal sintering technique, as determined in the previous section 6.2.3, and despite optimizing the sample composition. This was due to the fact that, by chance, the sample of the previous section already had the composition that we have now determined to be optimal for high ME effects. The decision was therefore made to move away from the CFO-BTO system and to replace the piezoelectric, and later on the magnetostrictive constituent. This will be the basis of the upcoming sections.

6.2.5 BCZT-CFO composites

After completion of the previous, rather comprehensive study on CFO-BTO composites, it appeared as if no further optimization was possible through modification of the composition. The conventional sintering method had been established as the most suitable one to obtain the most advantageous (0-3) connectivity, while a constituent ratio near 50-50 was determined as the one that gives the highest ME effect. The focus therefore turned to the objective of achieving higher effects by the usage of different materials to take the place of both CFO and BTO. In the progress of our cooperation, both constituents were eventually replaced entirely, but we will first concentrate on the piezoelectric phase and its replacement. As discussed in Ref. 94, it was decided to replace the BTO constituent with BCZT, in order to utilize its superior piezoelectric coefficient⁹⁷ of 600 pC/N, which is threefold higher than that of BTO.¹⁰⁵ The detailed description of the physical properties and phase transitions that make this material suitable for our purpose can be found in section 3.5, while the two-step solid state synthesis route of the precursors was explained in section 5.3, with the conventional sintering method from 5.4.1 being used for the formation of ceramic samples. For this first study of the new piezoelectric constituent, only one sample produced usable results, with the mass composition BCZT-CFO 85-15. It is on this sample that all the precharacterization and ME measurements were performed, the results of which shall be summarized in the following.

Structural characterization

As with the previously used system, a structural characterization via XRD (Siemens D5000) was performed first, in order to check for phase purity of the precursor powders of CFO and

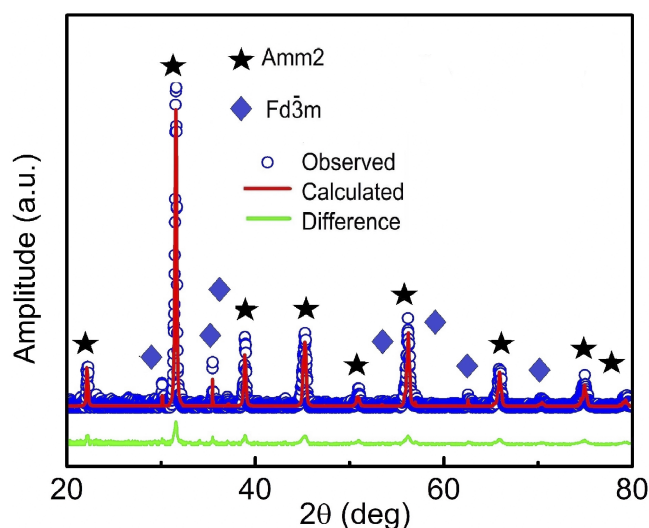


Figure 6.40: X-ray diffractogram of the BCZT-CFO 85-15 composite sample recorded at room temperature, with the peaks representing the Amm2 space group of BCTZ (black stars), the Fd-3m space group of CFO (blue diamonds), with a fit function calculated by Rietveld refinement (red line) and the resulting difference function (green line). Adapted from Ref. 94, reprinted with permission

BCZT, as well as for the final ceramic sample, latter being shown in Fig. 6.40. In addition to the raw data, a superimposed Rietveld analysis is shown in red, with the difference function between data and theoretical calculation shown in green. The peaks do not show any noticeable broadening, prompting the assumption that the grains of either constituent are probably not smaller than a few hundred nanometers, thus not suffering from size effects. Diffraction peaks can be assigned to individual constituents, namely the Amm2 space group of BCZT (black stars) and the Fd-3m space group for CFO (blue diamonds). When regarding the difference function (green line), no additional peaks of unwanted parasitic phases can be observed, clearly showing that this sample is phase pure. Analysis of the Rietveld refinement (red line) gives us the lattice parameters for BCZT of $a = 4.002 \text{ \AA}$, $b = 5.676 \text{ \AA}$ and $c = 5.656 \text{ \AA}$, while a lattice parameter of $a = 8.400 \text{ \AA}$ for CFO was obtained, agreeing well with literature values.¹⁰²

Electrical characterization

AFM and PFM images (MFP-3D, Asylum Research) were recorded on a polished sample, displayed in Fig. 6.41, using the same area for both measurements to make sure that any interference of topography on the PFM results can be ruled out.

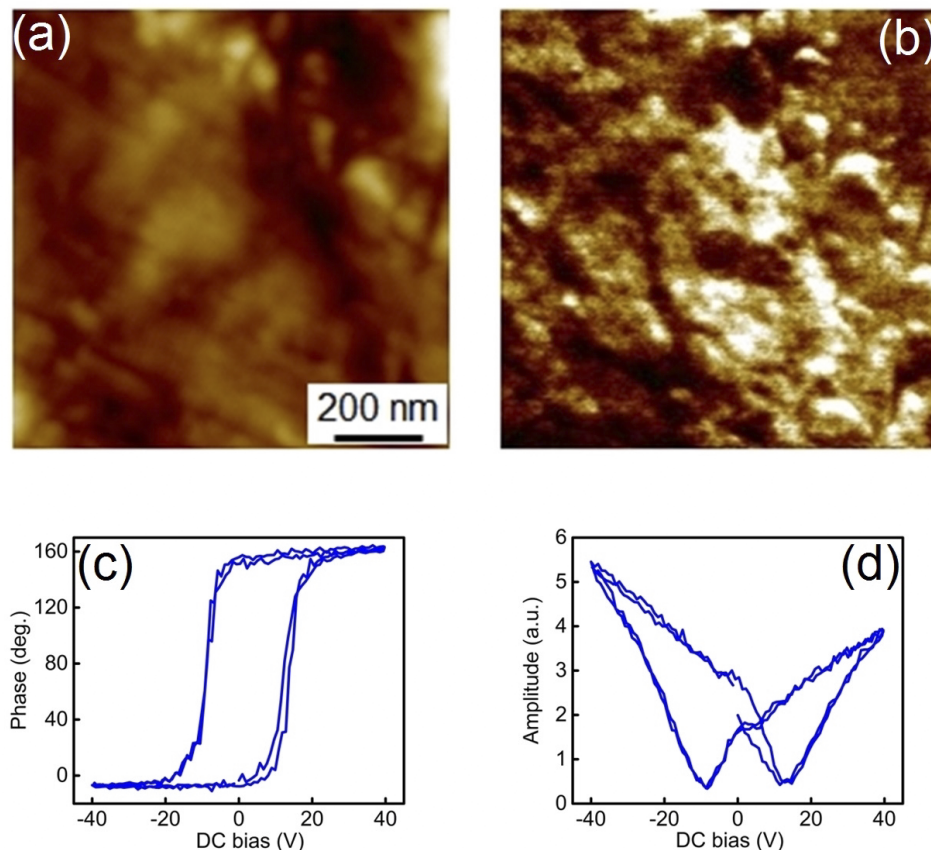


Figure 6.41: Topography (a) and lateral PFM response (b) of BCZT-CFO 85-15 composite sample, recorded at room temperature, as well as local piezoresponse force microscopy phase loop (c) and amplitude hysteresis loop (d) recorded inside a piezoactive region. Taken from Ref. 94, reprinted with permission

The contrast between the light and dark areas is indicative of piezoactive regions, in this case the BCZT phase. In order to actively manipulate the piezoresponse, a DC bias voltage has been applied to the sample during measurement, with Fig. 6.41 (c) showing typical switching behavior, revealing that the piezoresponse can be directly influenced by an external voltage. This proves that at least microscopically, we have a ferroelectric and therefore piezoresponsive sample. We then move to macroscopic measurements, as done for the previous BTO-based systems, such as $P(E)$ hysteresis loops recorded at 300 K using a home-built Sawyer-Tower circuit at an applied electrical frequency of 100 Hz, showing a typical ferroelectric-like behavior (Fig. 6.42).

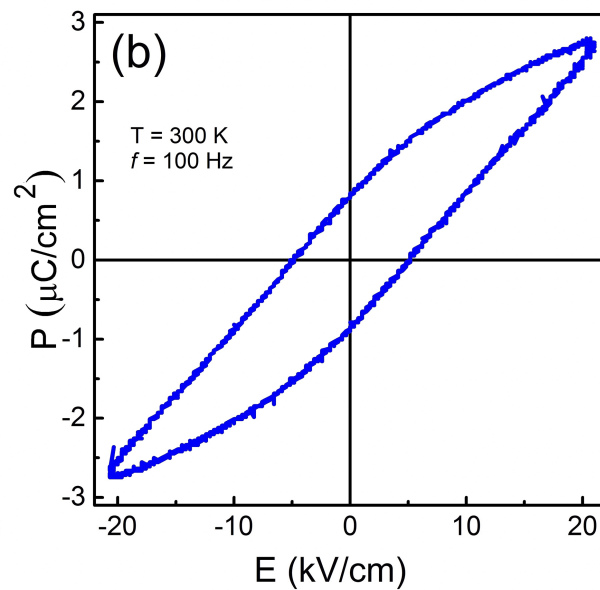


Figure 6.42: $P(E)$ hysteresis loop of BCZT-CFO 85-15 composite recorded at room temperature, taken from Ref. 94, reprinted with permission

For this first sample of the new composition, a more detailed macroscopic electrical characterization was performed, which was foregone for the remaining sample sets due to the BCZT phase not being modified any further. The real part of electric permittivity, ε' , was recorded in dependence of temperature and frequency, for the ceramic sample itself, as well as for ceramics that were formed of the pure constituents BCZT and CFO, respectively, to elucidate the contributions to the electric properties from each individual constituent. All results of these measurements are summarized in Fig. 6.43. The pure BCZT shows a maximum at ca. 370 K, matching the ferroelectric-paraelectric phase transition, while an additional anomaly is visible at 320 K, presumed to be caused by the polymorphic phase transition between the (ferroelectric) orthorhombic and the tetragonal phase,^{102,217} which were described in the phase diagram in section 3.5. We can also see a frequency dispersion, with the amplitude of the peak in ε' decreasing with increasing frequency, a behavior considered typical for a ferroelectric with a diffuse phase transition, as is presumably the case for such sintered composites. Meanwhile,

the $\varepsilon'(T)$ curves of pure CFO show no sharp peaks, while the amplitude of the permittivity is strongly frequency dependent, being rather low at higher frequencies. Despite the majority of the sample in terms of weight being composed of BCZT, the results are very strongly influenced by the CFO phase, which has a lower electric permittivity at high frequencies.

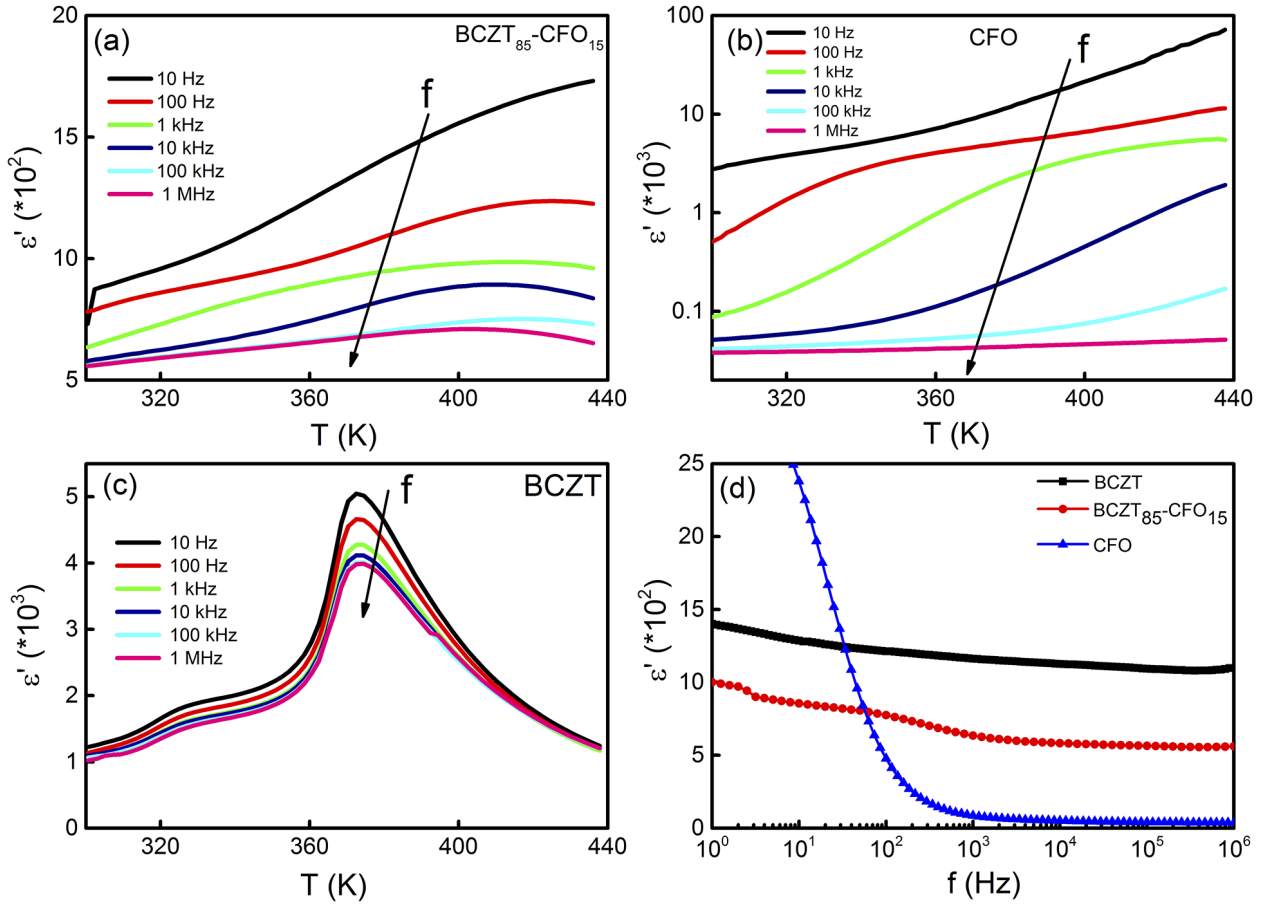


Figure 6.43: Temperature dependence of the real part of the electric permittivity ε' of the BCZT-CFO 85-15 composite measured at different frequencies (a), temperature dependence of ε' for pure CFO (b) and pure BCZT (c), frequency dependence of ε' for all three samples (d) recorded at room temperature. Taken from Ref. 94, reprinted with permission

The same behavior could also be observed in the imaginary part ε'' , shown in Fig. 6.44, displaying a strong increase of the measurement signal at low frequencies, with no sharp or discernible peaks being visible. This overall behavior has been observed throughout literature for other multiferroic composites^{218–220} and could thus be considered as a typical result. The strong influence from CFO, affecting both ε' and ε'' , has an impact on the overall properties of the composite through two mechanisms. One is the higher conductivity of the ferrite phase, which explains the increased signal at higher temperatures, and is also something we're familiar with from our discussion of the pitfalls of the converse ME setup, explained in section 4.8.1.

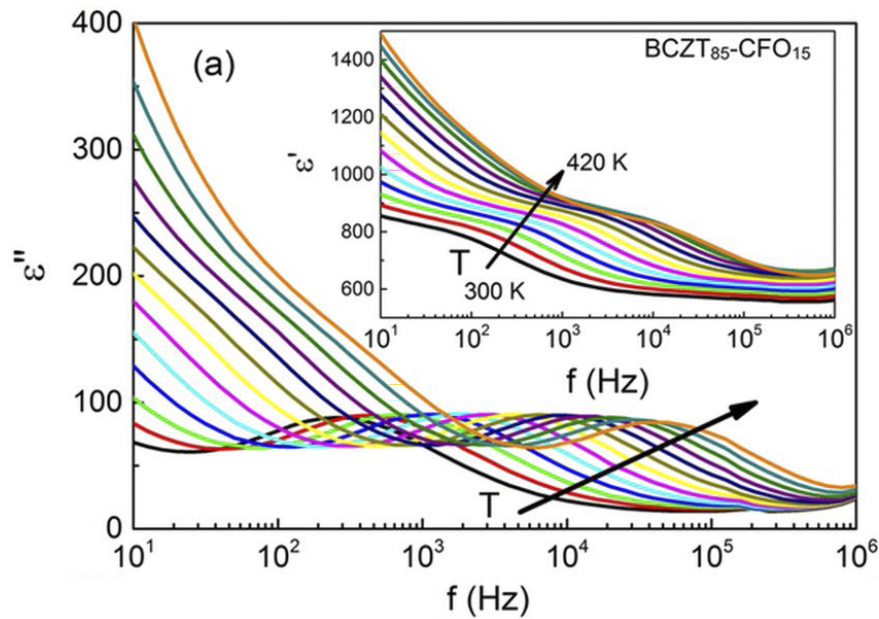


Figure 6.44: Temperature dependence of the imaginary part of the electric permittivity ϵ'' of the BCZT-CFO 85-15 composite measured at different frequencies and temperatures, taken from Ref. 94, reprinted with permission

The other mechanism is caused by the interface between CFO and the much less conductive BCZT, leading to Maxwell-Wagner relaxation,¹⁵² which has been mentioned previously for similar results of CFO-BTO composites in section 6.2.4. This type of relaxation is often seen in grained ceramics²⁰⁸ due to inhomogeneities at the interfaces, and has also been proposed for other systems than ours, such as $\text{BaTiO}_3 - \text{Ni}_{0.5}\text{Zn}_{0.5}\text{Fe}_2\text{O}_4$, the functional properties of which have been discussed in the literature.^{208,221} What we need to keep in mind here is that polarization can become strongly inhomogeneous in the vicinity of interfaces, with the arising uncompensated surface/interface giving rise to inner fields, which can potentially lead to large dielectric losses, especially at low frequencies.²⁰⁸ It is this effect that will play a major role in explaining an outlier in the last BCZT-based sample set discussed in section 6.2.7, where the effects of a low measurement frequency and higher measurement temperatures lead to a strong, undesired increase of the measurement signal.

Magnetic characterization

The magnetic properties were recorded in conjunction with the magnetoelectric measurements described in the next section, which is the reason for 280 K being used during the recording of the $M(H)$ curve in Fig. 6.45. We obtain a saturation magnetization of 43.3(1) A/m and a remanence of 8.3(2) kA/m. As these samples were normalized according to their volume, we need to calculate the magnetization stemming from the CFO phase. As the molecular weight of CFO (234.5 g/mol) and BCZT (222.8 g/mol) are rather similar, we use a rough approximation by multiplying the magnetization by the factor one would need to obtain a 100% CFO sample from the 15% one we have here, which gives us roughly 290 kA/m. This is lower than the

424 kA/m we would expect for pure CFO when determining the volume magnetization from the well-known²³ mass magnetization of $80 \text{ Am}^2/\text{kg}$ using a density of 5.3 g/cm^3 . There are several possible explanation for this behavior, which is also observable in the other two BCZT-based sample sets. As the magnetization is normalized to volume in the case of the composite samples, a certain amount of porosity could lead to a lowering of the calculated value. One also needs to consider the possible formation of a barium orthoferrate (BaFeO_{3-x}) phase during the high temperature sintering. This phase, described in detail in Ref. 222 and 223, can appear in a tetragonal unit cell, therefore being indistinguishable from BCZT due to the very similar lattice parameters.²²⁴ The magnetic properties of BaFeO_{3-x} can vary quite widely depending on oxygen content, with the tetragonal phase that may be present in our samples having been characterized as paramagnetic.²²⁵ We can therefore assume that the reduction in magnetization is partially being caused by the presence of this parasitic phase. We can also presume that no size effects known from nanoparticles play a role here, as bulk precursors were utilized for the solid state synthesis. As previously discussed for the CFO-BTO sample sets, a decrease in magnetic permeability can occur in composite systems, which would lead to a lowering of the magnetization.^{210,212} Furthermore, the overall slim hysteresis loop with a remanent magnetization of $8.3(2) \text{ kA/m}$ and coercive field of $0.04(2) \text{ T}$ can be considered as typical for a ferrimagnetic sample, comparable to the previously discussed pure CFO reference sample S1 (see Table 6.3).

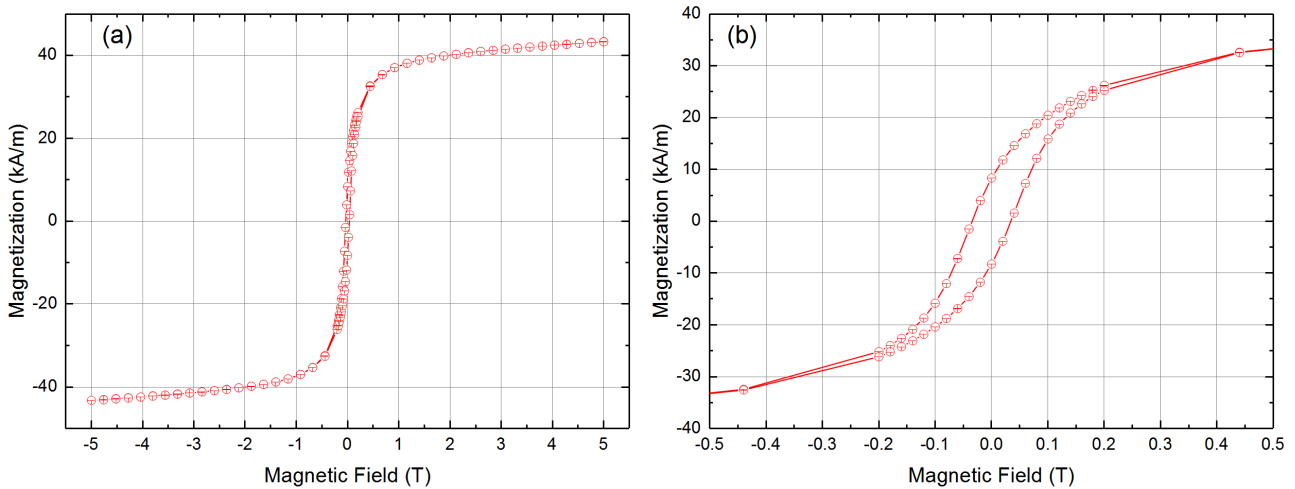


Figure 6.45: $M(H)$ curve of BCZT-CFO 85-15 recorded at 280 K showing the full 5 T field (a) and low field region (b).

Converse magnetoelectric measurements

As this is the first time that we observe the behavior of this new sample system using our converse ME setup, we will look at the results in more detail, including some data that was not shown in the respective publication,⁹⁴ to also get a better understanding of the characteristics of the setup itself. The first step, as described in section 4.7.1, is always the test of the temperature dependence of the induced ME magnetization. In order to avoid possible effects

from frequency doubling, a unipolar signal was used, through the application of a 100 V DC offset, superimposed onto the 100 V AC signal, as explained in section 4.8.1. Regarding Fig. 6.46 (a), we obtained a clear magnetization signal with low statistical error. The striking decrease towards higher temperatures is a strong indicator for a signal that is the result of ME coupling from the piezoelectric phase, enabling us to assume that we do not see any visible effects from conductivity and leakage currents. The highest signal was recorded near 280 K, so this temperature was used in all subsequent measurements on this sample. It's in good agreement with the known properties of the parent phase BTO. It was also observed that the signal showed some artefacts when approaching low temperatures, which were not seen in the previous sample sets that used pure BTO as their piezoelectric constituent. The question was whether this is some kind of problem stemming from the setup itself, or whether it may be related to a sample property, namely one of the low temperature phase transitions. In the end, it was determined that this effect is caused by the low signal causing an instability, due to the device being unable to fit the raw signal at the correct phase position. We can see this by plotting the phase difference between the real signal, which we generally display as the induced ME magnetization, and the original input signal used to generate the electric field.

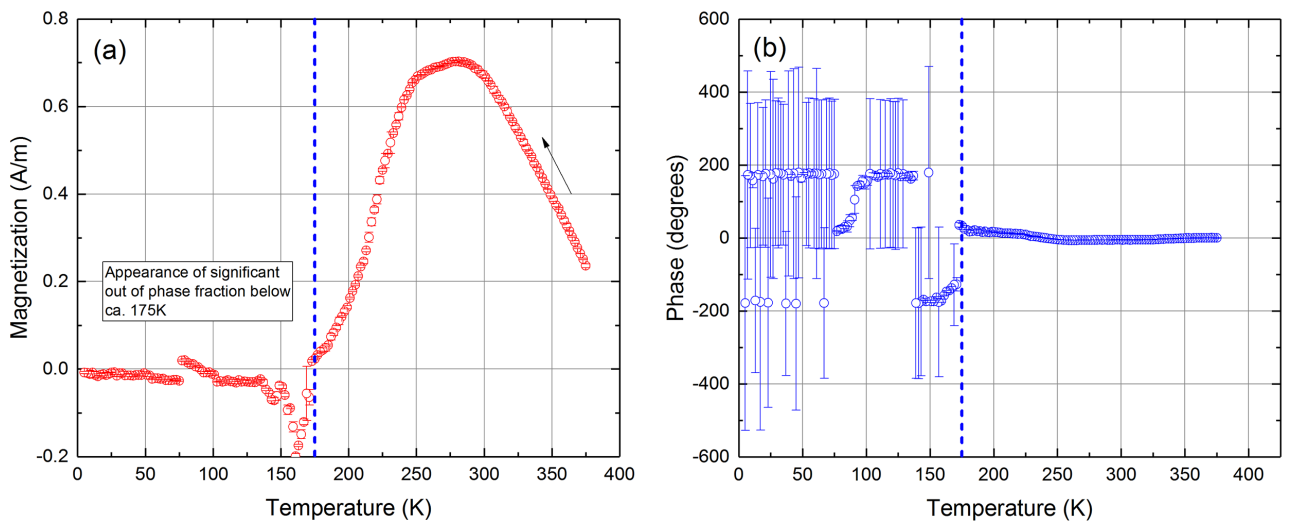


Figure 6.46: Temperature dependent ME magnetization (a) recorded at $U_{AC} = 100$ V, $U_{DC} = 100$ V, $f_{AC} = 11$ Hz and $\mu_0 H_{DC} = 0.16$ T, with the accompanying phase shift (b) of the real part of the measurement signal relative to U_{AC} . The 'safe' region for measurements is to the right of the blue dashed line.

For clarity, the phase shift is shown here in Fig. 6.46 (b). In the region of high signal strength, from 375 K down to 175 K, the phase shift is very small, showing no significant deviation from the original signal. It then takes on an erratic nature, switching between $\pm 180^\circ$ and 0° as the measurement progresses down to 5 K. It's easy to imagine how the fitting procedure may cause such errors, when the signal becomes so weak that the algorithm jumps to the left or right when it attempts to superimpose the sinusoidal fit function onto the raw measurement data. We can therefore disregard the data below 175 K, which, thankfully, is outside of the important region

around 280 K that we want to observe in detail. It's interesting to note that 175 K is also the location of the orthorhombic to rhombohedral phase transition, at which other samples showed a signal that went through zero, also accompanied by phase reversal. We can thus conclude that the effect we see here is caused by an intrinsic property, namely the phase transition of the BCZT-phase, while the erratic behavior is also based on the instability of the small signal, with the device being unable to correctly identify the phase shift. Towards the later part of this thesis, namely during the characterization of the upcoming two BCZT-based sample sets, it was also decided to forego the sweep to low temperatures, due to this often seen instability of the data, the lack of its usefulness, as well as to protect the sample holder against damage in case of small leaks, as mentioned in section 4.6.

With no problematic differences visible in the temperature dependence, we can move on to the magnetic field dependence and check for any deviation compared to the previous studies. At this point in our studies, we stopped using only the low field region and performed not just the $M(H)$ but also the $ME(H)$ sweeps up to the maximum field of 5 T. Furthermore only the longitudinal configuration was used, as the rotation of the sample may have been useful for a better understanding of underlying phenomena, but not for the achievement of the highest possible ME effect of an individual sample. The result is displayed in Fig. 6.47 (a), including a closeup of the small field region (b).

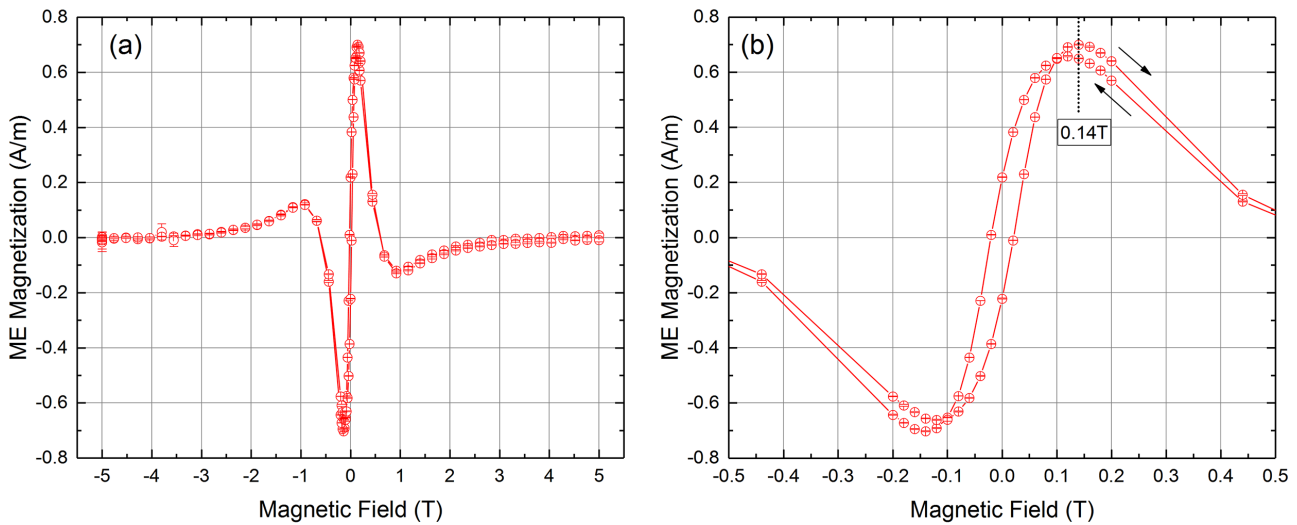


Figure 6.47: Magnetic field dependent ME magnetization (a) recorded at $U_{AC} = 100$ V, $U_{DC} = 100$ V, $f_{AC} = 11$ Hz, $T = 280$ K, with a closeup of the small field region (b).

The same hysteretic behavior and overall shape were observed, just as for the previous constituents, which is to be expected, as the magnetic phase should have remained identical (see Fig. 6.23 and 6.35). The main peak was slightly lower than for our last CFO-BTO composites, at 0.14 T rather than 0.15 T, which such minute differences being attributable to the demagnetizing factor varying with the sample dimensions, as any variation in thickness or radius of the

disk shaped pellet will alter the aspect ratio γ . We can therefore conclude that the usage of a modified piezoelectric constituent didn't have any negative impact on our magnetistrictive phase, with the overall properties in terms of magnetic field response having been preserved as we knew them. No clear correlation was visible between the coercive field of 35 mT seen in magnetometry, compared to the position of zero ME effect located at 20 mT for this sample. Since this measurement represents the first time we ramped the field to its maximum value of 5 T, we can also observe that there is no discernible ME contribution at these high fields, with the signal tending to zero. Looking back at Fig. 2.1.4 from the theory chapter, we can assume that effects from forced magnetostriction do not play a significant role in these samples.

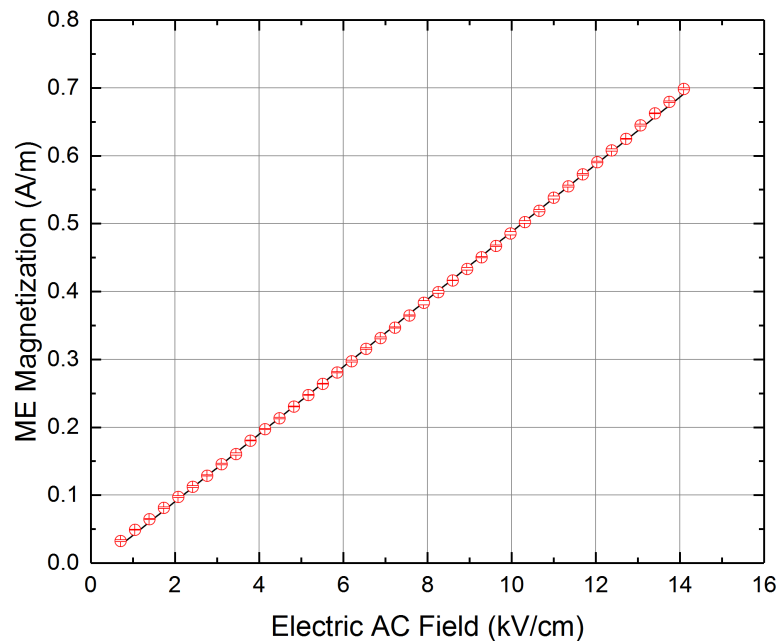


Figure 6.48: Electric field dependent ME magnetization recorded at $U_{AC} = 100$ V, $U_{DC} = 100$ V, $f_{AC} = 11$ Hz, $\mu_0 H_{DC} = 0.14$ T and $T = 280$ K, with the black line representing a linear data fit.

The last step was, as always, the determination of α_C via the linear fitting of the electric field response. As this joint work didn't contain any direct ME measurement that needed to match temperature or frequency, we were free to choose our parameters based on the optimum value from the previous two measurements, using 0.14 T and 280 K. The resulting data, again showing good quality with minuscule error bars, was fitted by a linear function, with the slope providing a value of 6.03(1) ps/m, as depicted in Fig. 6.48. We can also see a very slight curvature of the data points relative to the linear fit, indicative of higher order coupling effects, as discussed during the theoretical derivation of the converse coupling coefficient in section 2.3. If we compare this to our previous work, it's of course a somewhat underwhelming result. However, we have to keep in mind that this first sample, serving more as a proof of concept, does not have the optimum composition, which may result in the less than optimum effect. If we make a comparison to previous joint works using a sample with equally low CFO content of 20 wt%,

we arrive at a value of 4.4 ps/m from Ref. 122, which would mean that our new BCZT-based sample has a converse ME effect that is 37% higher. There were attempts of improving the effect, as with the previous system, by varying the BCZT to CFO ratio, but these attempts were not successful at the time. Due to this, a new goal was the improvement of the ME properties by doping of the magnetostrictive phase, and later on the complete replacement of this phase, as will be elaborated on in the upcoming two sections. In these, we will also find out why we may not have been able to initially improve the ME coupling by modifying the BCZT-CFO ratio.

Summary

Our first attempts of creating and measuring a new composite, utilizing BCZT instead of BTO, have proven successful for the composition used here, serving as a proof of concept that this is a feasible route to achieve greater ME coefficients. When directly compared to a sample of the same composition but using the parent compound BTO, we were able to increase α_C by 37%, underlining the feasibility of the route taken. At this point in time, the formation of samples with other BCZT-CFO ratios was not successful due to high conductance hindering measurements. It was for this reason that we first sought to improve the properties by a modification of the CFO phase, which is the topic of the next section. In the end, we were also successful in the formation of composites with different constituent ratios for our last sample set, described in section 6.2.7, with the TOF-SIMS results aptly showing that the rod-like growth of the NFO phase within the BCZT matrix is presumably what gave rise to excessive conductivity in these types of samples, leading to the problems we faced in our early efforts.

6.2.6 Al-modification of BCZT-CFO composites

After the proof of concept for the BCZT-CFO system, the main goal became the enhancement of the ME coupling coefficient. We already know from section 6.2.3 that the SPS method for ceramic formation is not suitable due to excessive conductivity. As a result, we kept using the conventional sintering method and opted for a modification of the magnetostrictive phase through doping with Al-ions, while retaining the piezoelectric BCZT with its extremely high longitudinal piezoelectric coefficient of 600 pC/N. The overall composition for the two samples was BCZT-CFO 50-50, with ceramics formation being achieved by the previously described solid state synthesis route from section 5.3 followed by the conventional sintering procedure from section 5.4.1. Of the two samples, one retained the pure CFO phase for its magnetostrictive constituent, while the other one was composed of $\text{Co}(\text{Fe}_{1.5}\text{Al}_{0.5})\text{O}_4$, henceforth referred to as BCZT-CFO(Al).

Structural characterization

The standard XRD analysis (Siemens D5000) performed on both samples (Fig. 6.49) showed clear peaks for the tetragonal perovskite structure of BCZT (P) as well as the cubic spinel structure of the CFO phase (S).

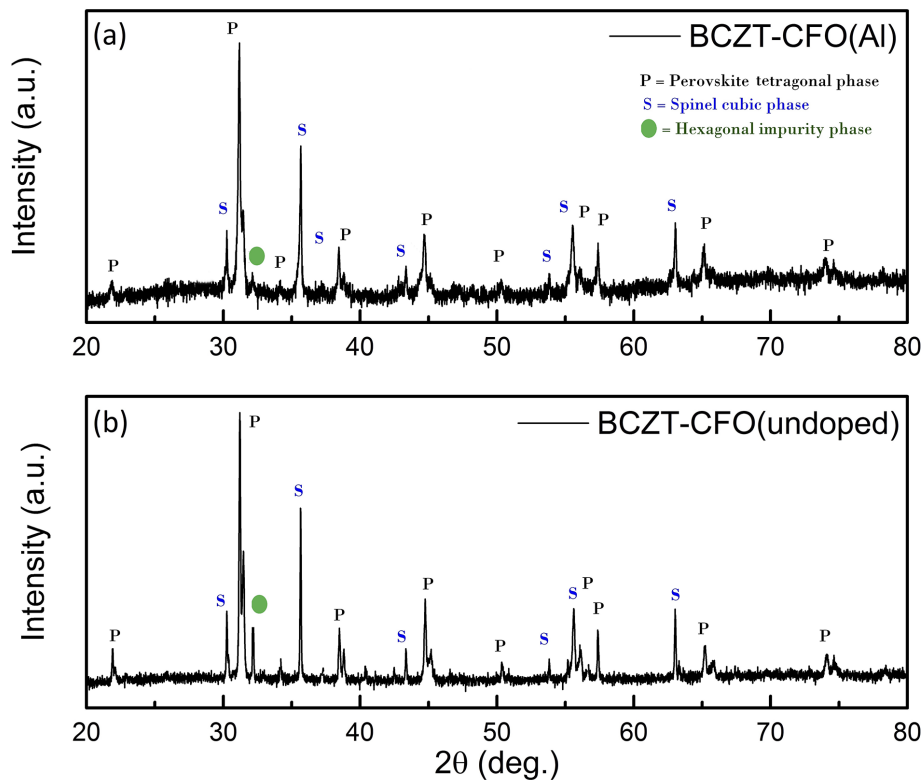


Figure 6.49: X-ray diffractograms for BCZT-CFO(Al) (a) and BCZT-CFO (b), recorded at room temperature, with indicated peak positions for different phases. Taken from Ref. 125, reprinted with permission.

However, there is one anomaly that will play a role for the magnetic characteristics: In both samples, a peak of a parasitic phase (green dot) is visible, identified as a hexagonal $\text{Ba}(\text{TiCo})_x\text{Fe}_{12-x}\text{O}_{19}$ phase, which was described in detail by Li et al. in Ref. 226. As we can see by the intensity of the peak, the undoped sample contains a higher amount of this parasitic phase, which we need to keep in mind for the magnetometry evaluation.

SEM images (Quanta FEG) were recorded on the polished surface of the ceramic samples (Fig. 6.50), providing us with an important piece of information: With the bright regions corresponding to BCZT and the dark ones to CFO, we can see a complete intermixing of the constituents. In contrast to the previous studies in which the most useful connectivity scheme turned out to be the (0-3) one, here, we seem to have produced a (3-3) connectivity, with both phases showing distributions in all spatial directions. This also provides us with an important explanation with regards to the previously studied sample: Potentially, the lack of improvement of the ME effect by a higher CFO content was caused by excessive conductivity due to the (3-3) connectivity present in these samples, which makes sense, as we no longer use a core-shell nanoparticle approach that would induce a clear separation of the more highly conductive CFO phase into clusters that are not interconnected. Here, the effect of conductivity through the interconnected 3D structures may again play a role, so we will have to be on the lookout for any effects of this nature when performing our $ME(T)$ sweeps.

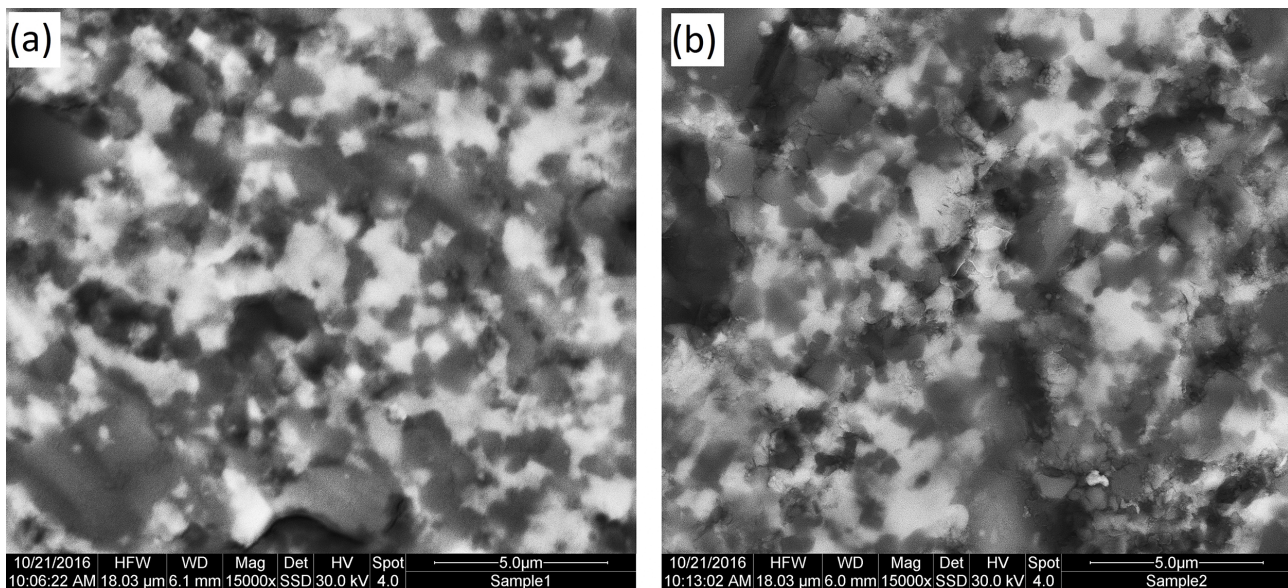


Figure 6.50: SEM micrographs for BCZT-CFO(Al) (a) and BCZT-CFO (b), taken from Ref. 125, reprinted with permission.

Electrical characterization

The recording of $P(E)$ loops was attempted for these two samples (Fig. 6.51), however, no saturation could be obtained, which again points towards conductivity effects preventing full polarization of the samples, which is a commonly known issue in the literature.^{212,227,228}

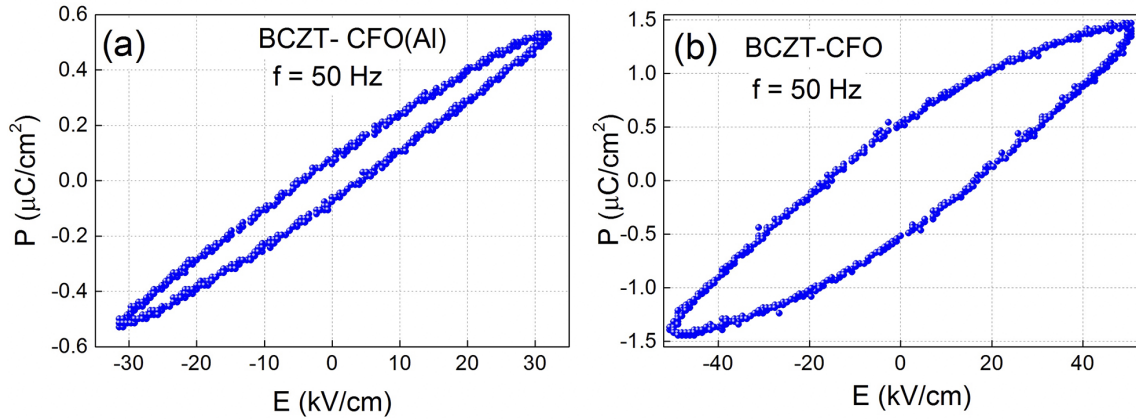


Figure 6.51: $P(E)$ hysteresis loops for BCZT-CFO(Al) (a) and BCZT-CFO (b), taken from Ref. 125, reprinted with permission.

The macroscopic measurement was followed by the recording of PFM micrographs under applied magnetic fields. To be certain that no interference from any structural features is present, the topography was also recorded (not shown here). Following this check, the measurements were performed at zero magnetic field, followed by the application of an in-plane 50 mT field, the reduction of this field to zero, and the application of the same field strength in opposite direction relative to the previous application. With this, not only the piezoelectric response to the magnetic field, but also possible hysteretic effects were to be investigated, the results being displayed in Fig. 6.52.

Indeed, upon the first 50 mT field application, we were able to see the occurrence of bright regions in the PFM image that were not visible previously, indicative of magnetic field induced polarization. These regions were concentrated at certain specific locations, which must correspond to the location of areas with high BCZT concentration that were exposed by the polishing procedure. Upon ramping the field to zero, the areas still retained some of their brightness, showing that they didn't return to their previous state completely. This makes complete sense, as we will see by the magnetic characterization in the next section, showing typical hysteresis loops in the $M(H)$ measurements. We cannot directly compare the magnitude of these two measurements as the small 50 mT field doesn't saturate the samples in the same manner as the high 5 T field of the SQUID. Still, in qualitative terms, the behavior we see here corresponds to our expectations. During application of -50 mT, the bright regions increase in size once again, being in line with the standard $ME(H)$ response.

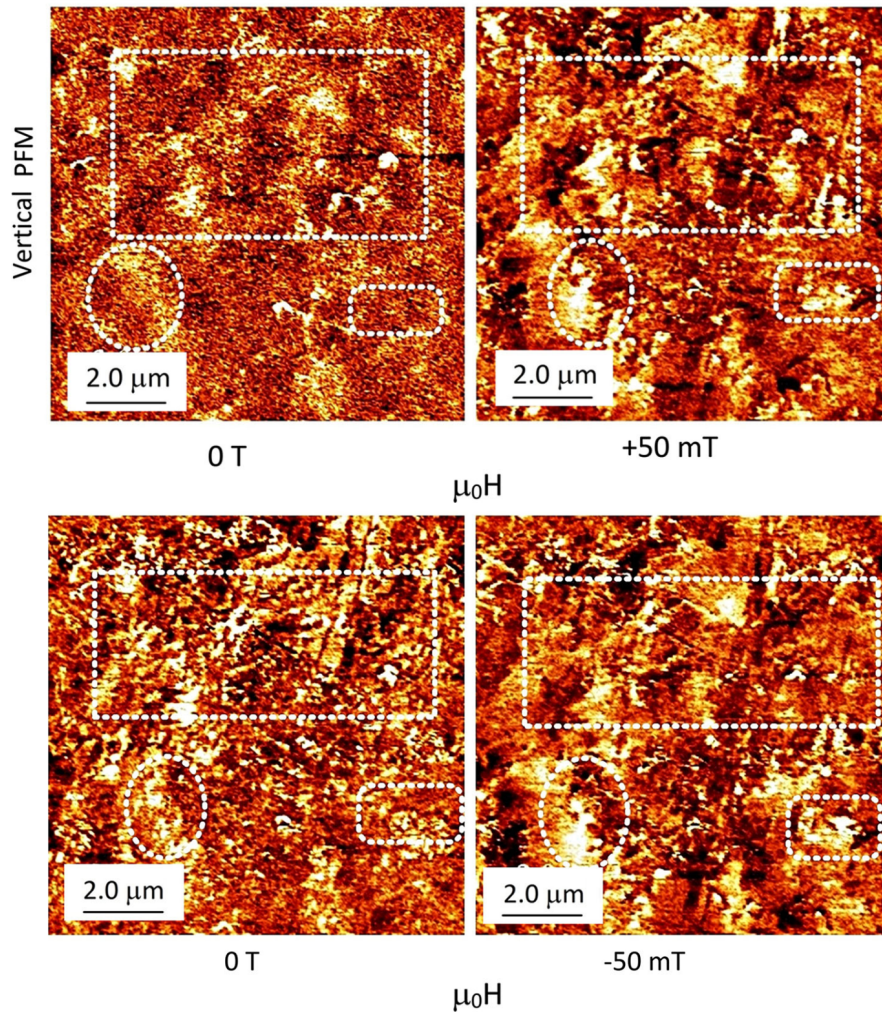


Figure 6.52: Vertical PFM images of BCZT-CFO(Al) showing a variation of piezoresponse with different in-plane magnetic field biases, adapted from Ref. 125, reprinted with permission.

Magnetic characterization

After witnessing the change in the PFM micrographs in response to applied magnetic fields, it was already clear that, at least on a microscopic scale, ME coupling was visible. It was thus necessary to characterize the magnetic properties in detail, which was especially important for this sample set, as we are directly influencing the properties of the magnetostrictive component by the Al^{3+} doping. Due to the higher complexity of performing Mössbauer spectroscopy on ceramic samples, which would require either CEMS or backscattering modes, we instead opted for only conventional magnetometry in order to probe the magnetic properties before moving on to the ME experiments. Here, we refer to the interesting data we have obtained during precharacterization in the synthesis section 5.3, which showed a strongly decreased saturation magnetization and coercive field for the Al^{3+} doped sample. After the formation of ceramics through regular sintering, we again recorded $M(H)$ loops near room temperature for both the pure CFO-based sample, as well as the Al^{3+} doped one.

The overall reduction in saturation magnetization of the pure CFO based ceramics is chiefly caused by the inclusion of about 50 vol% of BCZT, which is not ferrimagnetic. However, if we correct the magnetization values by this factor, we see that they are still well below the expected value for CFO,²³ which would be in the range of 400 kA/m, with the corrected value for the two composites only reaching half of that. This means that the high temperature sintering process must have further influence on this material system, which was previously evident in the results for the first BCZT-CFO 85-25 sample. In fact, if we go back all the way to our first sample sets (see Fig. 6.20), we were able to observe that the spark plasma sintered (SPS) samples showed a higher net magnetization when compared to the conventionally sintered sample. While it was determined that SPS samples were not suitable for ME measurements due to their excessive conductivity, this comparison would indicate that the conventional high temperature sintering method is potentially not the most advantageous route when it comes to the preservation of magnetic properties. However, as far as the magnetoelectric properties go, it still provided us with the highest coupling coefficients for the samples discussed here.

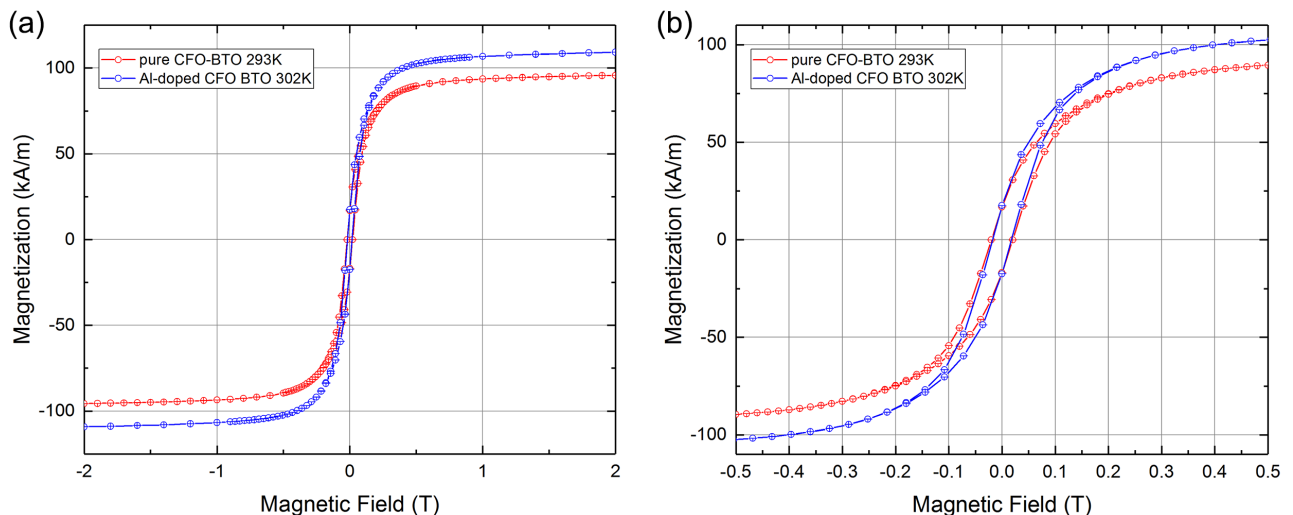


Figure 6.53: $M(H)$ curves of ceramic samples shown in high (a) and low field range (b) with pure (red) and Al^{3+} doped CFO phase (blue) recorded near room temperature. The slightly different temperature points are due to these measurements being done in conjunction with the $ME(H)$ sweeps, which were performed at the respective optimum temperatures seen in $ME(T)$ results.

Another feature of the magnetization curves was the slightly higher saturation magnetization for the Al^{3+} doped sample of 113.1(1) kA/m compared to 95.7(1) kA/m for the pure CFO sample, while both show similar coercive fields of roughly 20(1) mT. Obviously, the striking difference that was visible in the precursor powders has disappeared completely, which means that the sintering process must have led to a redistribution of the Al^{3+} ions, negating the strong 50% drop in magnetization that was observed for the Al^{3+} doped precursor sample. The minor difference that remains in the magnetization of the ceramics can be explained by the formation of an impurity phase during the sintering process, which is marked in the X-ray diffractograms

with a green dot, identified as having a hexagonal structure. As shown by literature data, this phase was found to be ferrimagnetic as well as magnetically hard, with a much lower saturation magnetization than CFO.²²⁹ Due to the slightly larger peak in the X-ray diffractogram of the undoped sample, we can assume that the slightly lower saturation magnetization is being caused by a slightly higher amount of the impurity phase in this sample. Furthermore, it is possible that the sample contains traces of the perovskite BaFeO_{3-x} , as observed in Ref. 222, with this phase having a tetragonal unit cell that cannot be distinguished from BCZT due to having very similar lattice parameters,^{223,224} as was elucidated in Ref. 125. Trace amounts of this paramagnetic phase²²⁵ can thus also contribute to the overall lowering of the magnetization.

Magnetoelectric measurements

As before, we begin with the recording of $ME(T)$ curves in order to find the temperature at which the maximum of the ME coupling occurs, with the measurements for the two respective samples being shown in Fig. 6.54. The peaks are rather broad compared to previous measurement, which is probably also due to the (3-3) connectivity when compared to previous sample sets. The pure CFO sample has its maximum at 290 K, slightly elevated compared to the previous sample set, while the Al^{3+} doped sample reaches its maximum at an even higher 302 K. It has to be noted at this point that, due to the nature of this initial test measurement, the two $ME(T)$ curves were recorded with different parameters, especially in terms of applied magnetic field $\mu_0 H_{\text{DC}}$.

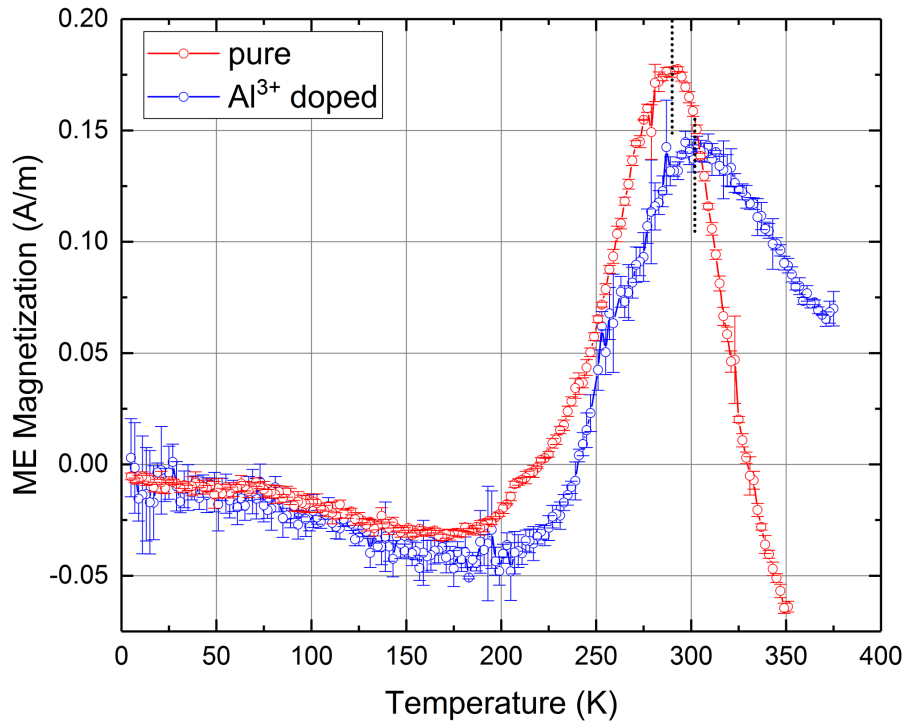


Figure 6.54: Temperature dependent ME magnetization recorded for the sample with pure CFO phase (red) at $E_{\text{AC}} = 0.95 \text{ kV/cm}$, $f_{\text{AC}} = 1.5 \text{ Hz}$, $\mu_0 H_{\text{DC}} = 0.10 \text{ T}$ and the Al^{3+} doped sample (blue) at $E_{\text{AC}} = 0.31 \text{ kV/cm}$, $f_{\text{AC}} = 11.0 \text{ Hz}$, $\mu_0 H_{\text{DC}} = 0.14 \text{ T}$.

It is this difference that causes the curve for the non-doped sample to reach a higher amplitude. By no means should this be interpreted in terms of the strength of the magnetoelectric coupling, as this will be tested with optimized consistent parameters for both samples at the end of this section. However, it is evident that the transition temperatures are shifted relative to the expected phase transition of pure BTO near 280 K, while also being shifted relative to each other. With previous sample sets, no clear evaluation was performed at the time, due to intrinsic problems that made it impossible to record temperature dependent curves, as with the SPS sample, or due to the extended $ME(T)$ measurement only being performed on one sample, as was the case for the second CFO-BTO sample set, or the previous BCZT-CFO sample, as only one composition proved suitable for measurements. The shift of the orthorhombic-tetragonal phase transition towards slightly elevated temperatures as such is not a problem, as it has been previously reported for Zr-doped BTO.²³⁰

In this case though, we have two samples with identical composition, which only differ in the doping of their magnetostrictive constituent. Normally, one would assume the temperature dependence to be caused solely by the structural phase transitions of the ferroelectric phase. In fact, this was touted as one of the great advantages of composite systems, as they allow the parameters of the two constituents to be tuned independently of each other. This sample set seems to disprove this, showing a shift of the optimum temperature between the two samples. We must therefore find a way to explain this behavior before we can continue. During the description of the BCZT system, we have already brought forward the publication of Cordero et al.¹⁰⁹ that deals with the elastic response of BCZT composites, fortunately also containing results on a 0.5BZT-0.5BCT sample. This matches the composition of the BCZT used by us, thereby allowing a direct comparison to our experimental results. As previously shown in Fig. 3.6, the elastic compliance for this sample composition had been measured and characterized, showing the characteristic temperature dependence we also see in our $ME(T)$ curves. The elastic compliance, the complex reciprocal of the elastic (Young's) modulus, provides us with the mechanical analogue of the dielectric susceptibility, without the direct coupling to polarization, thus providing direct access to property changes brought about by structural phase transitions. It is generally known that the stiffness and thus elasticity of materials shows some dependence on temperature, which probably contributes to the shift in the optimum transition temperature we see here. Indeed, in order to gain a full understanding of the temperature dependence, we must also look at temperature dependent effects from the magnetostrictive phase, which were not considered at the time.

To derive our explanation, we start off with Eq. 2.65 from the end of the theory section, which we shorten to

$$\alpha_{ij}^M(H) = \frac{\mu_0 dM_i(H)}{dE_j} = q_{imn} \cdot c_{mnkl}^* \cdot d_{jkl}. \quad (6.12)$$

To reiterate, we can see that the (in this case magnetic field dependent) coupling coefficient depends on the piezomagnetic tensor q_{imn} , the piezoelectric tensor d_{jkl} , as well as the stiffness c_{mnkl}^* . The temperature dependence of the piezoelectric tensor is already known from the phase transitions of the piezoelectric phase, while the magnetic field dependence of the magnetostriction has also been discussed before. However, the temperature dependence of the effective piezomagnetic tensor and the stiffness have not yet been regarded.

To gain some understanding of this connection, we look at a publication by Brockman et al.²⁰⁵ who observed the change of the coupling coefficient in the temperature window between 0 °C and 20 °C in magnetostrictive ferrites, which happens to be the temperature window in which the peaks in our $ME(T)$ curves occur. They introduce the coupling coefficient k for magnetostrictive materials, which in essence, provides a measure of the conversion of magnetic to mechanical energy, which is also conversely valid. In the literature,²³¹ this is defined as the square root of the ratio between converted stored energy and the input stored energy, using an idealized case with no losses. As written in Ref. 205, the coupling coefficient k is written in dependence of the anisotropy energies present in ferrites:

$$k^2 = \frac{\lambda_S^2 E_S}{|K_1| + |\sigma_i \lambda_S| + K_{internal-shape}} \quad (6.13)$$

Here, λ_S is the saturation magnetostriction, E_S is Young's modulus at saturation magnetization, K_1 is the first order magnetocrystalline anisotropy constant, $K_{internal-shape}$ the internal shape anisotropy and σ_i the average internal stress. In our case, we are not fully saturating the magnetostriction, as that would cause the ME effect to tend to zero. However, we should still be able to use this equation as an approximation while we elucidate the temperature dependence of our parameters.

Eq. 6.13 aptly shows that the electromechanical coupling coefficient, as defined in Ref. 205, can be maximized by minimizing the sum of these anisotropy energies. In case of ceramic samples, the internal stress anisotropy, as well as the internal shape anisotropy, are dependent on the processing parameters such as pressure and temperature during sintering, which has strong influence on the density of the finished samples. The internal shape anisotropy for example can be minimized by low porosity, while internal stress can be minimized by a slow sintering cycle with low temperature ramping rates. In our case, both samples were prepared with identical sintering procedures, so we can assume that this is not the main culprit for the different temperature dependent behavior.

Looking at the magnetocrystalline anisotropy energy K_1 , we do have a dependence on both temperature and chemical composition. In this case, CFO is a special case, having a K_1 value that is positive and roughly 100 times larger than that of other ferrites (see section 3.2). While

the chemical composition received a slight alteration, it's clear that we are mainly interested in the temperature dependence. Looking at other works from literature, we can also utilize a tensor equation for the coupling coefficient k and write it as

$$k_{ij} = \frac{d_{ij}}{\sqrt{\varepsilon_{ii}S_{jj}}} \quad (6.14)$$

with the component of dielectric permittivity ε and the elastic compliance S . It is the latter that we are interested in, as it's the value that was measured by Cordero,¹⁰⁹ as shown in Fig. 3.6. We therefore know that k has a degree of temperature dependence due to the strong temperature dependence of the elastic compliance S , and a minor temperature dependence of the magnetocrystalline anisotropy energy, meaning that we don't just see a purely electrical, but a general material property that is the result of a change of the elastic stiffness. Because of this, a shift of the maximum of the ME effect at the orthorhombic to tetragonal phase transition can occur, as visible in our experimental results. Due to the number of factors that play a role in the mechanical coupling factor, it is not easy to purposefully tune the parameters in order to influence the phase transition. As we will see in the result of the next sample set, a certain variation of the transition temperature must be taken into account.

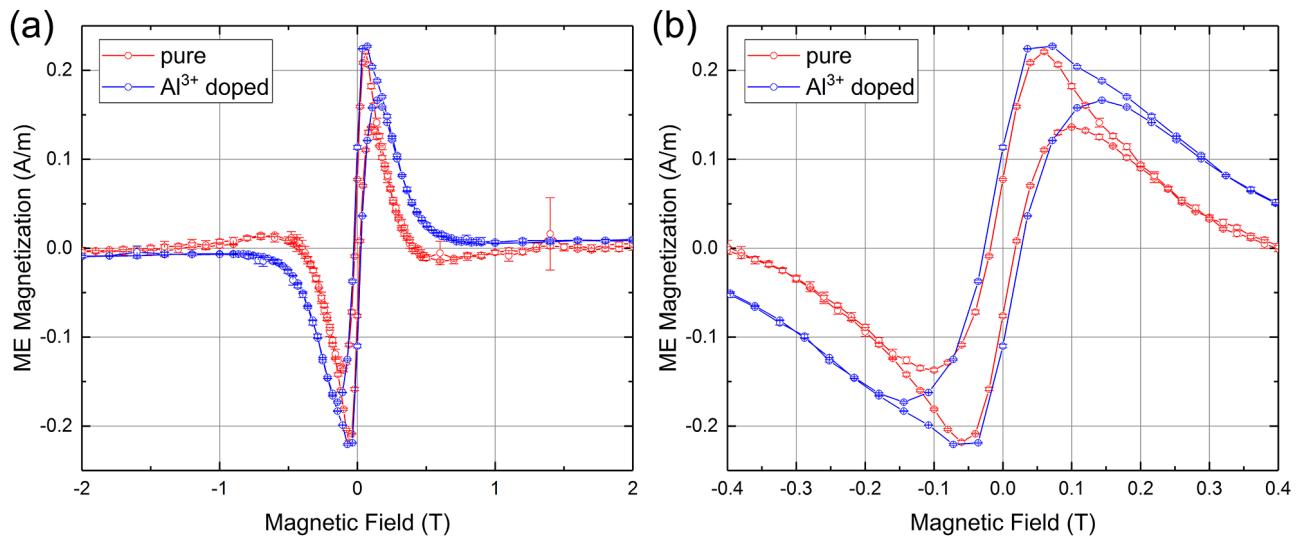


Figure 6.55: Magnetic field dependent ME magnetization shown in high (a) and low field region (b) recorded at $E_{AC} = 0.95$ kV/cm, $\mu_0 H_{DC} = 0.06$ T, $T = 293$ K and $f_{AC} = 1.5$ Hz for the pure (red) and $E_{AC} = 0.31$ kV/cm, $\mu_0 H_{DC} = 0.072$ T, $T = 300$ K and $f_{AC} = 2.3$ Hz for the Al^{3+} doped (blue) sample.

With the temperature dependence now being clear, we observe the magnetic field dependence, which is of high importance due to our modification of the ferrimagnetic phase. We can see that the overall shape and character of the curve corresponds to our previous measurements of $ME(H)$ in longitudinal geometry (see Fig. 6.23 and 6.35). Two peaks are visible in Fig. 6.47, depending on the direction in which the field was ramped before reaching that point, which was previously explained by comparisons to hysteresis effects in magnetostriction curves. One

minor difference between the two curves that we noticed was that the signal for the Al^{3+} -modified sample simply tended towards zero at higher applied fields, while the unmodified sample showed a change of sign around 0.4 T before tending to zero. However, this effect is very small compared to previous sample sets, for which it was not discussed at the time the results were published.

Generally speaking, the overall shape of the $ME(H)$ curve tracks the field derivative of the magnetostriction λ/dH , as it was explained previously. If we regard Eq. 2.8, we can further establish that the overall behavior of the magnetostriction is the result of superimposed contributions from different crystal planes, given by λ_{100} and λ_{111} , the latter being the dominant fraction during the initial curve that contains the first maximum. From this, we can gather that the changes in the magnetic field dependent magnetoelectric effect are caused by the modification of the magnetostriction. The Al^{3+} doping leads to an enhancement, as well as a slight modification of the field dependent behavior of λ , indicated by the change of sign that is not present in the unmodified sample. The maxima were located at fields of ca. 0.06 T for the undoped sample and 0.072 T for the Al^{3+} doped one, showing only small deviations, with these values being used in the subsequent $ME(E)$ measurements.

It is also sometimes noted that even at zero applied field, some ME coupling is still observable, with the curves not going through zero. This is possibly due to a self-biasing effect, known from literature,^{232,233} but is probably also caused at least partially by trapped flux in the high field superconducting solenoid of the SQUID, leading to a residual field at the theoretical 0 T position. The major part is assumed to be caused by the remanent magnetization of the sample itself,²⁰⁶ as it was discussed previously in section 6.2.3.

After confirming the optimum magnetic field and temperature for both samples, the final sweep for the applied electric field was performed, with the results shown in Fig. 6.56. The difference between the doped and undoped sample is immediately obvious, with the former reaching higher magnetization values at lower electric fields. From the linear extrapolation, a converse magnetoelectric coefficient of 10.9(1) ps/m was determined for the Al^{3+} doped sample, while the undoped sample reached a value of 2.9(1) ps/m. In total, the doped sample produced an effect 3 times larger than the undoped one. From this, we can conclude that the doping of the magnetic CFO phase lead to a large increase of the ME coupling coefficient, which must therefore be due to an increased sensitivity to magnetic fields, and thus a higher degree of magnetostriction in this sample. We assume this effect to stem mainly from a modification of the spin-orbit coupling by the Al^{3+} doping, which was described in section 2.1.4 as the basis of the phenomenon of magnetostriction, causing an increased sensitivity of the magnetostriction to external fields. As explained in Ref. 125, it has been suggested in the literature²³ that the field derivative of magnetostriction $d\lambda/dH$ shows a strong dependence on the magnetic anisotropy,

which is in turn influenced by the Al^{3+} doping. The magnetic anisotropy originates from the magnetic exchange interaction, $\varepsilon_{\text{exchange}} = -J_{AB} \langle S_A \cdot S_B \rangle$ given by the spins of nearest neighbor ions S_A , S_B and the Heisenberg exchange integral for two nearest neighbors J_{AB} . For our AB_2O_4 spinel system, we were able to see in the Mössbauer and XRD measurements in section 5.3 that the preference of Al^{3+} to occupy B-sites leads to a displacement of Fe^{3+} . This causes the remaining Fe^{3+} ions on the B-sites to be coupled to fewer A-site Fe^{3+} ions via super-exchange interaction, with this decrease in interaction also contributing to the decrease in magnetic anisotropy.

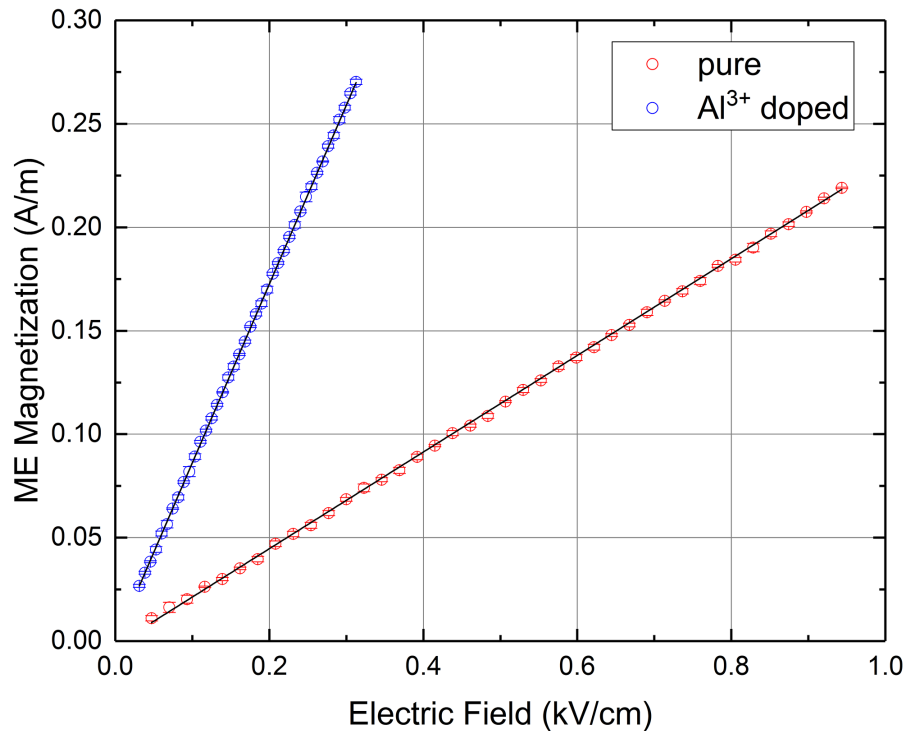


Figure 6.56: Electric field dependent ME magnetization recorded at $f_{\text{AC}} = 1.5$ Hz, $\mu_0 H_{\text{DC}} = 0.06$ T and $T = 293$ K for the pure (red) and $f_{\text{AC}} = 2.3$ Hz, $\mu_0 H_{\text{DC}} = 0.072$ T and $T = 300$ K for the Al^{3+} doped (blue) sample, with the black lines representing linear data fits.

It's also interesting to compare this sample set to the previous one: The BCZT-CFO 85-15 sample produced around 6 ps/m, which would mean that our undoped 50-50 sample, which has a higher CFO content relative to the one from the previous chapter, produced a lower ME coupling coefficient. We attribute this to the increased conductivity of the CFO phase, which shows that the compositional dependence of the ME effect is always a balance between the ME effect itself, and opposing effects through conductivity, which reduce the efficiency of the performed poling procedure. In the same way as the temperature dependence that was discussed above, this relation is not dependent on a singular effect, but is a superposition of ME coupling on the one hand and undesired conductivity effects on the other.

Summary

This sample set aptly shows us one of the great advantages of multiferroic composites, namely the ability to separately tune one of the components without modifying the other. We were able to significantly improve the converse magnetoelectric coupling coefficient from 2.9 ps/m to 10.9 ps/m through Al^{3+} doping, with no detrimental effects on the composite being observable. While the precursor suffered from a stark reduction in high field magnetization, this effect, caused by the preference of Al^{3+} to occupy A-sites, was rectified by the sintering procedure during ceramic formation. Nevertheless, the effect of Al^{3+} -doping was still observable through higher magnetoelectric coupling, presumably caused by the decrease in magnetic anisotropy leading to a higher sensitivity of magnetostriction to external magnetic fields. However, the long discussion of results also reveals that such sintered systems are highly complex. This is especially true for the elucidation of the temperature dependent properties, depending not only on the phase transition of the BCZT phase, but also on the elastic compliance resulting from the stiffness, as well as the magnetomechanical coupling factor, with their respective dependences on the sample temperature. The complex nature of such samples will be further reviewed in the context of the last sample set in the next section.

6.2.7 BCZT-NFO composites

We arrive at the final chapter of the results section, which contains the most detailed representation of experimental data from our converse ME setup. It should be noted that the importance of these ME results grew steadily with each of our joint publications. While it often consisted of just one or two figures at the early phase of this long running cooperation, it has now grown to considerable size as far as the space it takes up in the respective paper (Ref. 126) is concerned. We think that this is a testament to the reliability and practicality of our measurement setup, enabling routine processing of samples with a large variation in temperature and magnetic field. This represents a wide parameter space of temperature, magnetic field, electric field, frequency and sample composition and morphology that allows us to form a very comprehensive picture about the properties of our sample.

With the latest composite discussed in the following, our goal became the combination of the improved piezoelectric coupling of the BCZT constituent, which was shown in the previous two sections to give a superior converse coupling coefficient when compared to CFO-BTO composites of the same composition, to a new magnetostrictive constituent. While the doping of the CFO phase with Al^{3+} ions did prove to be successful in increasing the magnetostriction, it also led to significant modifications of the magnetic phase due to the preference of Al^{3+} to occupy B-sites, and although this was later partly rectified by the sintering procedure, it points towards a process that is difficult to control. One of the materials initially proposed to replace CFO was Terfenol-D, an alloy that was originally developed for the Naval Ordnance Laboratory in the USA, with the composition $\text{Tb}_{0.3}\text{Dy}_{1.7}\text{Fe}_2$. This material has the highest magnetostriction of any alloy, up to 2000 ppm at room temperature at saturation,²³⁴ but is based on high cost materials such as Tb and Dy. Coupled with poor mechanical properties, it was decided to use a different material instead. However, there is a reason for Terfenol-D to be mentioned here, as experiments with this material have commenced while this thesis was being written. More on this can be found in section 8.2 in the outlook at the very end of this work.

Returning to the system at hand, it was ultimately decided to utilize nickel ferrite, NiFe_2O_4 (NFO) as a magnetostrictive constituent in the last sample set we will discuss, due to the fact that it was reported⁹¹ to have a large magnetostriction derivative $d\lambda/dH$ and a high magnetomechanical coupling factor, with the other general properties having been described in section 3.3. As we saw in the discussion of the previous section, the coupling factors turned out to be an important parameter when it comes to the selection of the optimum field and temperature for the ME measurements. Four samples with different BCZT-NFO ratios have been fabricated using the solid state reaction method described in section 5.3 to form the precursor powders and the conventional sintering method from section 5.4.1 to produce the ceramics that were used for the ME measurements. These will henceforth be referred to by their NFO

content, with NFO20 corresponding to sample BCZT-NFO 80-20 and so forth. In total, four samples were produced, with NFO contents of 20, 30, 40 and 50 wt%. In contrast to previous attempts at modifying the ratio of the constituents with BCZT-CFO, we were now successful in modifying the ME effect by this method without running into dire problems resulting from conductivity, which is probably based on the morphology and connectivity, as we will see in the upcoming evaluation.

Structural characterization

XRD spectra (Philips PW1730) were recorded on all samples, with Rietveld refinement being performed with respect to the two expected phases, the tetragonal perovskite (BCZT) and cubic spinel (NFO), just like in the previous section, with the results being displayed in Fig. 6.57.

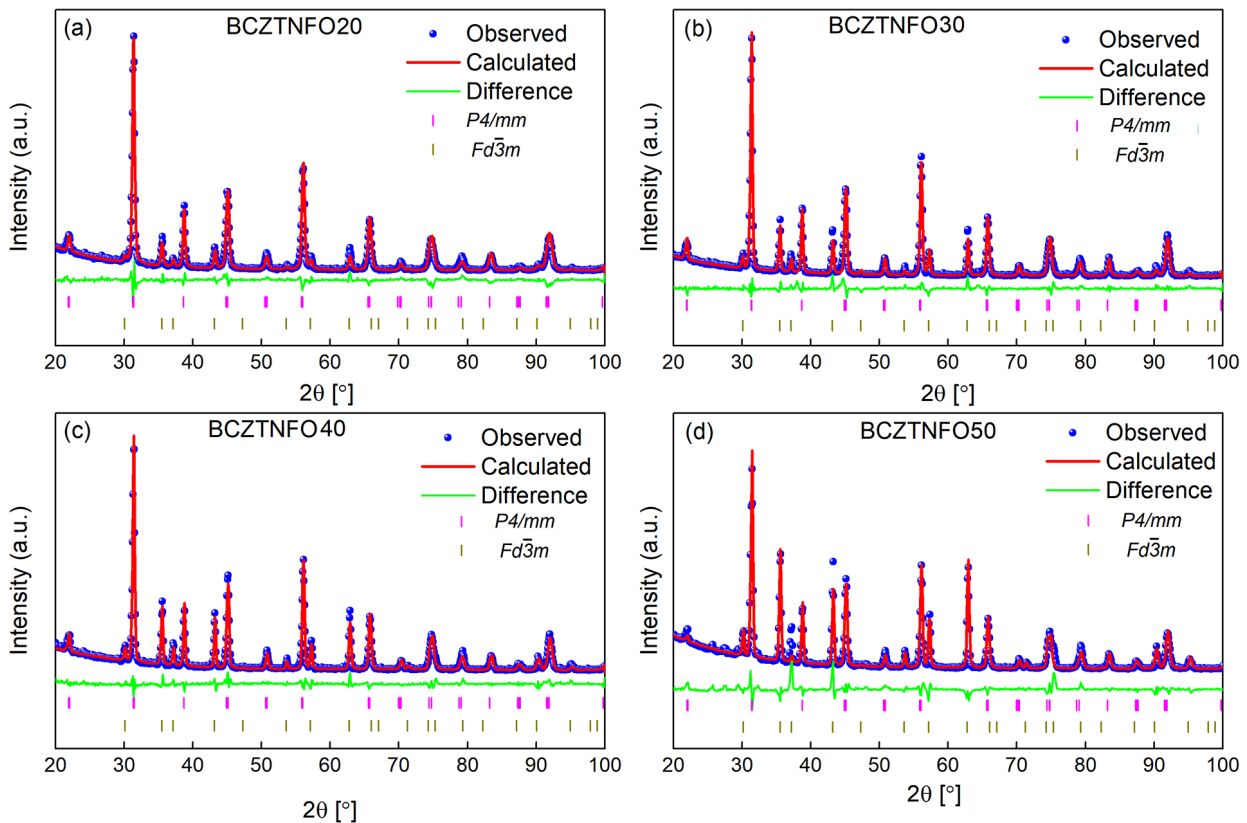


Figure 6.57: X-ray diffractograms for for samples NFO20-NFO50 recorded at room temperature, with Rietveld refinements, taken from Ref. 126, reprinted with permission.

In contrast to the Al-doped sample set, no parasitic phase was detected here, indicating phase pure samples. Also, the intensities of the peaks from the tetragonal phase decrease with increasing NFO content, while the opposite is true for the spinel peaks. The results thus show the coexistence of these two phases without intermixing, representing the desired chemical makeup of our samples.

It is at this point that we use TOF-SIMS for the first time, with this method having been described in section 4.1.4. The decision to include this method, despite its singular use, was based on the value of the results obtained through it, which provide us with an intricate 3D structure of our samples, enabling us to see the development of the connectivity in great detail.

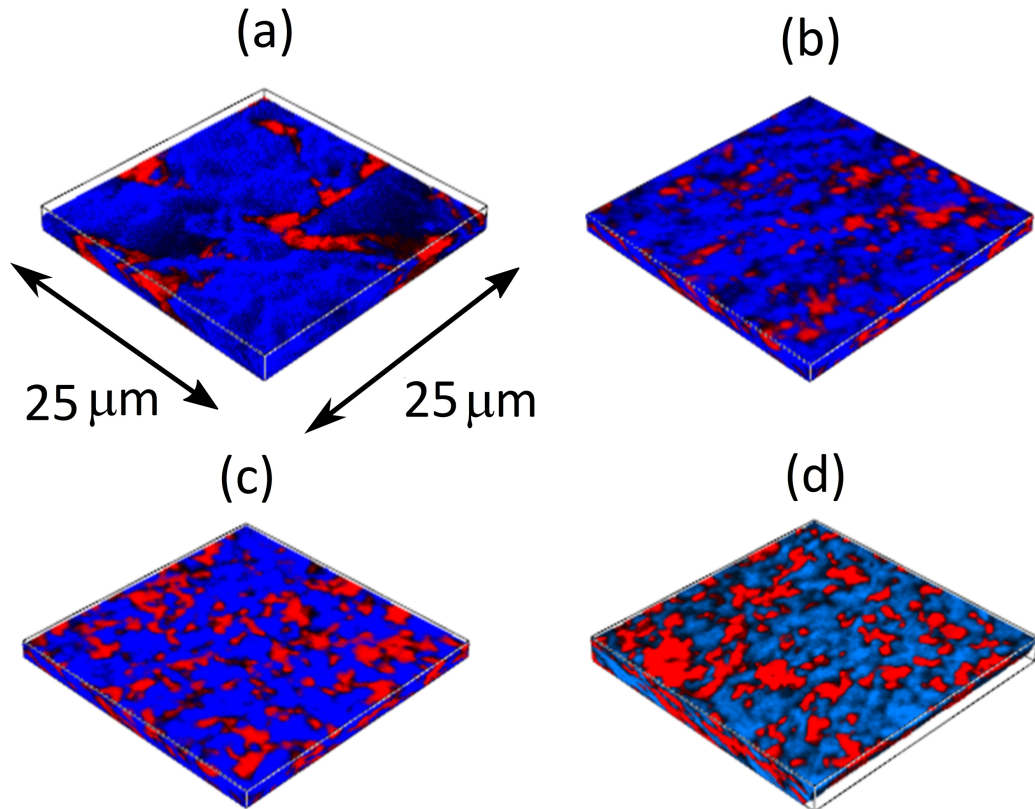


Figure 6.58: TOF-SIMS 3D maps of samples NFO20 (a), NFO30 (b), NFO40 (c), NFO50 (d). The blue color represents Ba ions, while red shows the presence of Fe ions. Taken from Ref. 126, reprinted with permission.

Displayed in Fig. 6.58 taken from Ref. 126, the 3D reconstruction is shown for all four samples, which were profiled to a depth of 200 nm beneath the surface. Due to the mass selective nature of this measurement method, it's possible to differentiate between phases rich in Fe and Ba ions, representing the NFO and BCZT phase, respectively. Starting off with the sample of lowest NFO concentration in Fig. 6.58 (a), we observe the distribution of NFO inclusions in a BCZT matrix, which would be akin to the (0-3) connectivity of the CFO-BTO ceramics synthesized from core-shell nanoparticles. However, we don't observe any clusters or grains, but elongated NFO regions of several μm length, which could be described as stripes or irregular rod shapes, pointing at least partially towards a (1-3) structure. Upon increasing NFO content, it's clear that these stripes form a more and more closely knit network, with the interconnections giv-

ing rise to a transition from the initial (0-3)/(1-3) to a (3-3) connectivity. We can offer two conclusions for this: On the one hand, we have successfully measured the similar composite BCZT-CFO with a (3-3) connectivity, so in principle, an ME effect should be observable. However, we now have a valid explanation for our inability to increase the ME coupling in our initial BCZT-CFO study in section 6.2.5, and the low effect in BCZT-CFO 50-50 compared to the 85-15 sample. It's safe to assume that the increase of the CFO content also leads to the formation of these networks of higher conductivity, thus negating any increase of the ME effect through a decrease of the ability to properly pole the sample.

In any case, this result is of high importance in terms of relating the effect of the morphology and connectivity to the magnetoelectric qualities of a sample, and despite being a destructive method, it's highly recommended for future measurements on magnetoelectric composites. As only about 200 nm of material depth is removed from the sample, it shouldn't disturb the macroscopic properties of the ceramic piece, which can be refinished by polishing.

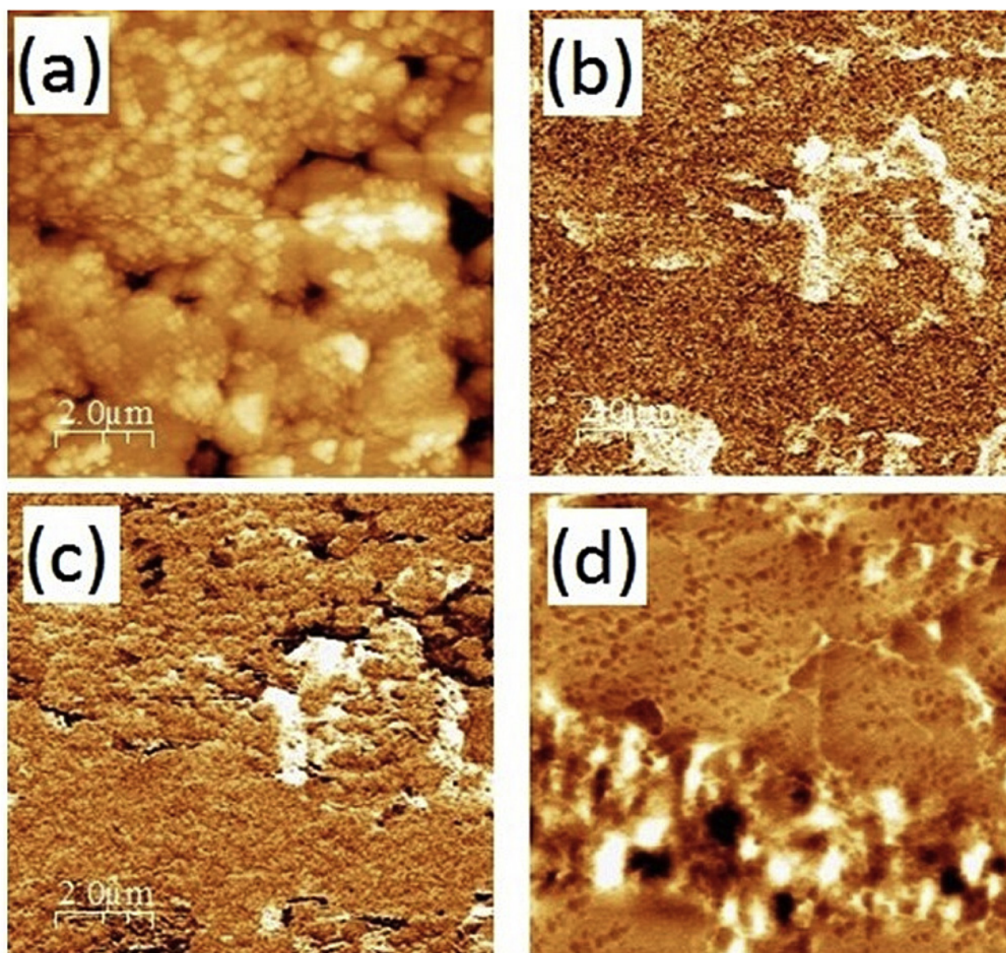


Figure 6.59: PFM micrographs of sample NFO30, with the topography (a) as well as vertical (b) and lateral (c) piezoresponse, while part (d) shows the MFM response. Taken from Ref. 126, reprinted with permission.

Electrical characterization

For this sample set, no macroscopic $P(E)$ curves were recorded, as the previous set revealed an inability to fully polarize such samples, with the effects of ferroelectricity thus having to be probed on a local level using microscopy techniques. PFM and MFM micrographs were recorded on all samples, which of course mixes not only the structural characterization with the electrical, but now also with the magnetic properties. However, we elected to keep the title consistent with the previous sets of data. Due to the large number of micrographs that were recorded, only one is shown here in Fig. 6.59 as representative of the sample set, with the others being included in the respective publication¹²⁶ in the appendix. As before, the topography (a) was also recorded as a reference, to ensure that no effects stem from surface irregularities and the likes. The piezoresponse was measured in vertical (b) and lateral (c) mode, while the overall MFM response (d) was also recorded. We can clearly observe areas of strong light/dark contrast, representing the respective areas of piezoactive and magnetostrictive grains. Furthermore, we can see that the areas of high PFM contrast are always separated from those of high MFM contrast, showing local coexistence of ferroelectrically and magnetostrictively active grains. When regarding the entirety of the dataset (not shown here), an increase of the relative area occupied by magnetic grains can also be observed, which matches the increasing NFO content. We can summarize that the multiferroic properties of the samples could be clearly witnessed in PFM and MFM micrographs, pointing towards the presence of a macroscopic ME effect that will be measured later on. Additionally, it can clearly be seen that the contrasts are not caused by the topography itself, as all micrographs were recorded in the same local area, allowing direct comparisons.

Magnetic characterization

A standard $M(H)$ characterization of all samples was performed, with the results being shown in Fig. 6.60. The differing temperatures are due to the fact that these measurements were run in conjunction with the $ME(H)$ sweeps, which were performed at their respective optimum temperatures. However, being sufficiently close to room temperature, the results are still comparable, since the high Curie temperature of 858 K⁸³ for NiFe_2O_4 negates any significance of the temperature dependence of saturation magnetization between 270 K and 335 K.²³⁵ All samples show similar behavior, quickly reaching their saturation, indicative of magnetic ordering in the form of ferrimagnetism, while the hysteresis loops were very slim, with low coercive fields of ca. 10 mT, indicative of soft magnetism from the NFO phase. The saturation magnetization shows large variations through the sample set, which are caused by the differing amounts of magnetically active NFO. As expected, the sample with the lowest fraction of NFO also has the lowest corresponding saturation magnetization. We therefore know that the magnetic properties are in line with our expectations for this material system, with the present magnetic ordering pointing towards the suitability of this yet untested material for magnetoelectric ceramics. One potential problem becomes visible when we observe that the saturation mag-

netization values are not equidistant, even though the composition was always varied by the same amount of 10%. Due to the fact that the final ME results show some peculiarities for this sample set, a closer look shall be taken at the saturation magnetization data. For this purpose, the 5 T magnetization values from Fig. 6.60 were plotted against the NFO content and displayed in Fig. 6.61. Already, we can see that while the magnetization (red circles and line) rises linearly with the increasing amount of NFO contained in the composites, NFO30 shows a slight deviation to higher values.

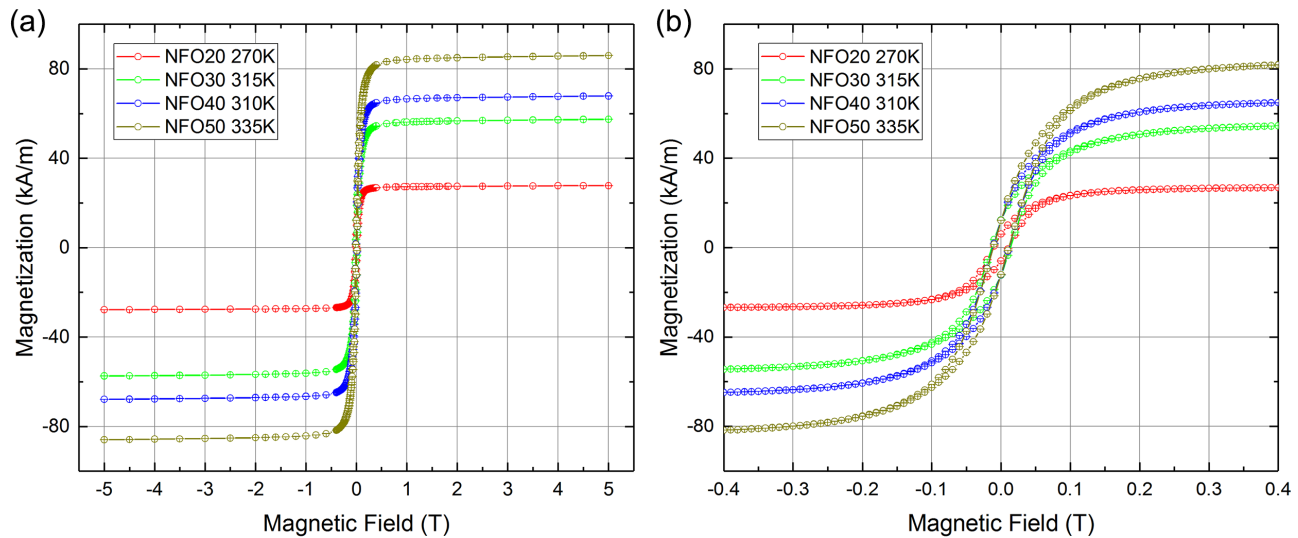


Figure 6.60: $M(H)$ curves for samples NFO20-NFO50 in full 5 T (a) and low field range (b) with the temperature at which the measurements were performed being denoted in the legend.

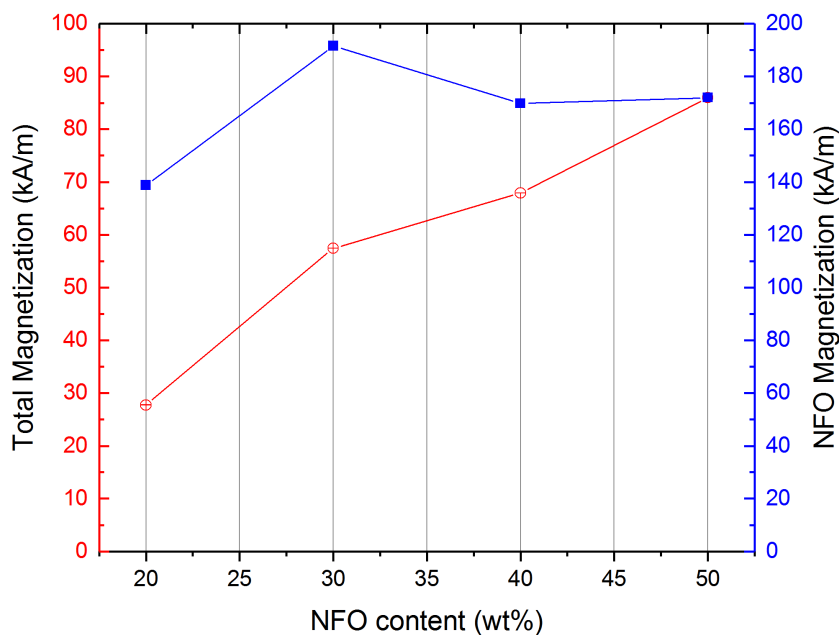


Figure 6.61: 5 T magnetization values obtained from Fig. 6.60 (red) corrected for the non-magnetic mass content of the samples (blue). Lines are guides to the eye.

If we apply a rough correction to these values by calculating the magnetization one would have measured for a sample made up of 100 % NFO, we end up with the points shown by the blue squares and lines. Two main deductions can be made from this data: The first, as for the previous sample sets, concerns a lowering of the saturation magnetization below what one would expect for bulk polycrystalline NFO, just under 300 kA/m.²³⁶ We assume that the same mechanisms are at play, such as the formation of parasitic tetragonal phases that are not visible in XRD, potential interdiffusion, effects from lower density, as well as reduced permittivity. However, this drop is not as dramatic as for the BCZT-CFO sample sets, pointing towards an improvement of the preservation of magnetic properties during sintering for NFO-based samples. Furthermore, we can clearly see that NFO30 has a higher saturation magnetization than the neighboring compositions, which will become important when discussing the results of the final converse ME measurements.

Magnetoelectric measurements

After observing the presence of microscopic coupling effects via PFM and MFM, the standard repertoire of ME measurements were performed. The first one was the $ME(T)$ temperature sweep, performed only in the range from 150 K up to 350 K, where the phase transitions of pure BTO are known to occur. We were interested not only in the usual check for possible stray signals from conductivity, but also in potential shifts of the temperature of maximum magnetoelectric coupling caused by the Ca and Zr doping of the ferroelectric phase. All of the resulting $ME(T)$ curves are displayed in Fig. 6.62, with this sample set showing some differences between the different compositions. As a general trend, the maximum shifts towards slightly lower temperatures from ca. 337 K in the sample with the highest content of 50 % NFO down to around 270 K for the sample with the lowest content of 20 % NFO. At this point, due to having such a large sample set compared to previous studies, an attempt was made to explain this shift by a direct comparison to the magnetic field dependence $ME(H)$ of the induced magnetic moment.

When we look at the $ME(H)$ data, summarized for all samples in Fig. 6.63, we can see the by now well-known behavior^{237,238} of distinct peaks at low fields, in this case at 30 - 50 mT, with a small hysteresis behavior, based on the field dependence of magnetostriction (see Fig. 6.23 and 6.35). The magnetic field positions of maximum values (shown in the legend) are incommensurate with the trend visible in saturation magnetization values, while the field positions of ca. 10 mT at which the ME effect goes through zero agree well with the coercive field from $M(H)$. The overall higher effect seen in NFO50 in this case is not indicative of a higher ME coupling per se, as all samples were measured using the same AC voltage. The effective electric field is therefore only dependent on the sample thickness, with thinner samples being subjected to higher fields and thus giving a higher overall effect. For a direct comparison, only the final $ME(E)$ curve in Fig. 6.65 should be used, as it's the only one that is normalized to the applied electric field.

It must be mentioned at this point that the measurements for NFO50 have been performed at 1.7 Hz instead of the 8 Hz used for the rest of the sample set, due to the fact that we had problems with the signal stability for this sample.

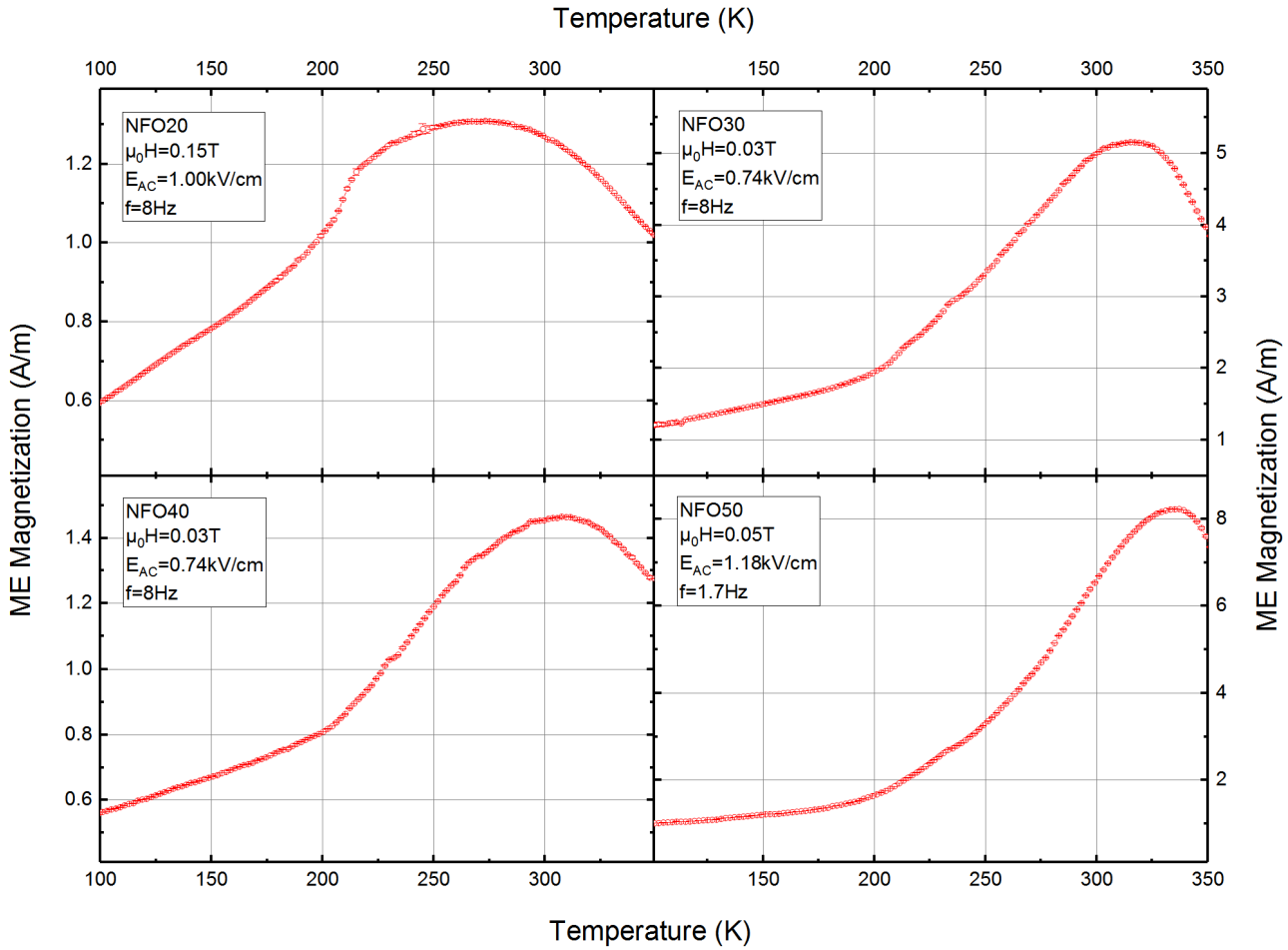


Figure 6.62: Temperature dependence of induced ME magnetization for samples NFO20 - NFO50 with the measurement parameters being denoted in the legends.

This comparatively small change in frequency turned out to be fatal for the final evaluation, which will be elucidated later on in this section. As we discussed earlier, the $ME(H)$ signal is tracking the field derivative of the magnetostriction $d\lambda/dH$, with the peaks representing the sections of highest slope in λ caused by magnetic domain switching, and the small hysteresis also being directly caused by the hysteresis found in the field dependence of λ .²³⁷ Conversely, the induced $ME(H)$ moment goes to zero when the magnetostriction reaches a maximum or minimum, as its slope of course becomes zero at these points (see Fig. 6.23 and 6.35). This often takes place when the coercive field is reached, which agrees well with our results, with $ME(H)$ going through zero at roughly the same field at which the static $M(H)$ magnetization reaches its coercive field. This has been established with the previous sample sets, and as we can see, also holds true for this NFO-based composite. We can further observe a shift of the main peak from 30 mT for the lowest NFO contents to around 50 mT for the NFO50 sample.

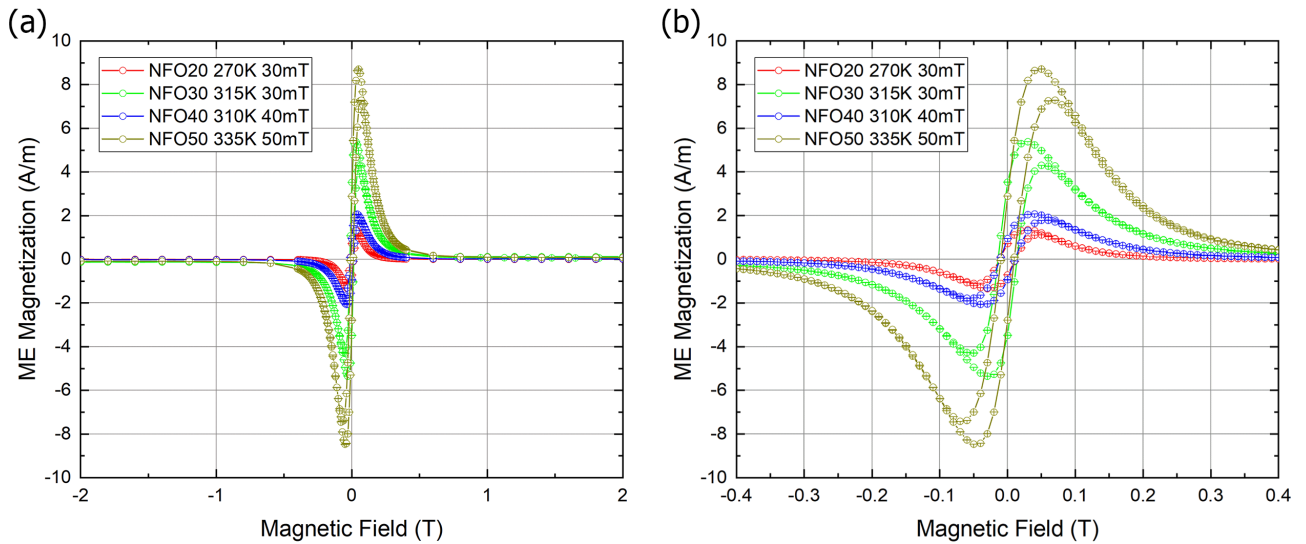


Figure 6.63: Magnetic field dependence of induced ME magnetization in high (a) and low field range (b) for samples NFO20-NFO50, with the temperature, as well as the field position of the maximum signal being denoted in the legend.

What we are now interested in is the interplay between the temperature dependence and magnetic field dependence. Previously, we mainly observed the temperature dependence in terms of phase transitions of the ferroelectric phase, and as a crosscheck to avoid any stray signals from conductivity. To more clearly explain the peak form and the associated shifts, we have performed the magnetic field dependent $ME(H)$ measurements for one of the samples at different temperatures. Basically, we used different points along the $ME(T)$ curve to measure $ME(H)$ and to observe whether it still holds true that the temperature and magnetic field dependent maxima are at the location we had previously determined. Performed exemplarily for the NFO50 sample, the results are depicted in Fig. 6.64 with the individual $ME(H)$ curves shown at the respective temperature they were recorded at. The field dependent maximum of each individual curve has been marked, with the resulting projection onto the temperature axis (dashed grey lines) corresponding well to the original $ME(T)$ curve that was recorded for this sample, with the $ME(H)$ curve of the highest maximum having been recorded at 335 K. For this direct comparison, only the amplitude of the $ME(T)$ curve was normalized to the maximum of the $ME(H)$ curve at 335 K, with the difference between the two stemming from the different measurement frequencies (1.7 Hz for $ME(T)$ and 8 Hz for $ME(H)$). This caused an unwanted signal increase of the original $ME(T)$ curve, with this effect having been discussed in section 4.8.1. Overall, we see excellent agreement between the position of the maxima and the $ME(T)$ curve. The deviations in the high field range of the 200 K measurement were caused by erratic phase shifts of the signal, which were more prevalent in this sample than in the others. This will be discussed in more detail towards the end of this section.

We can thus conclude that no shift of the magnetic field dependent maximum takes place while moving away from the temperature dependent maximum. Early assumptions were made,

claiming that the drop in signal towards low temperatures is caused by the shift of the coercive field, as it takes on higher field values at lower temperatures. It was thus assumed that the maximum of the $ME(H)$ curve would simply shift to higher field values, which would in turn mean that the $ME(H)$ curves recorded at lower temperatures would have to display a shift of the peak.

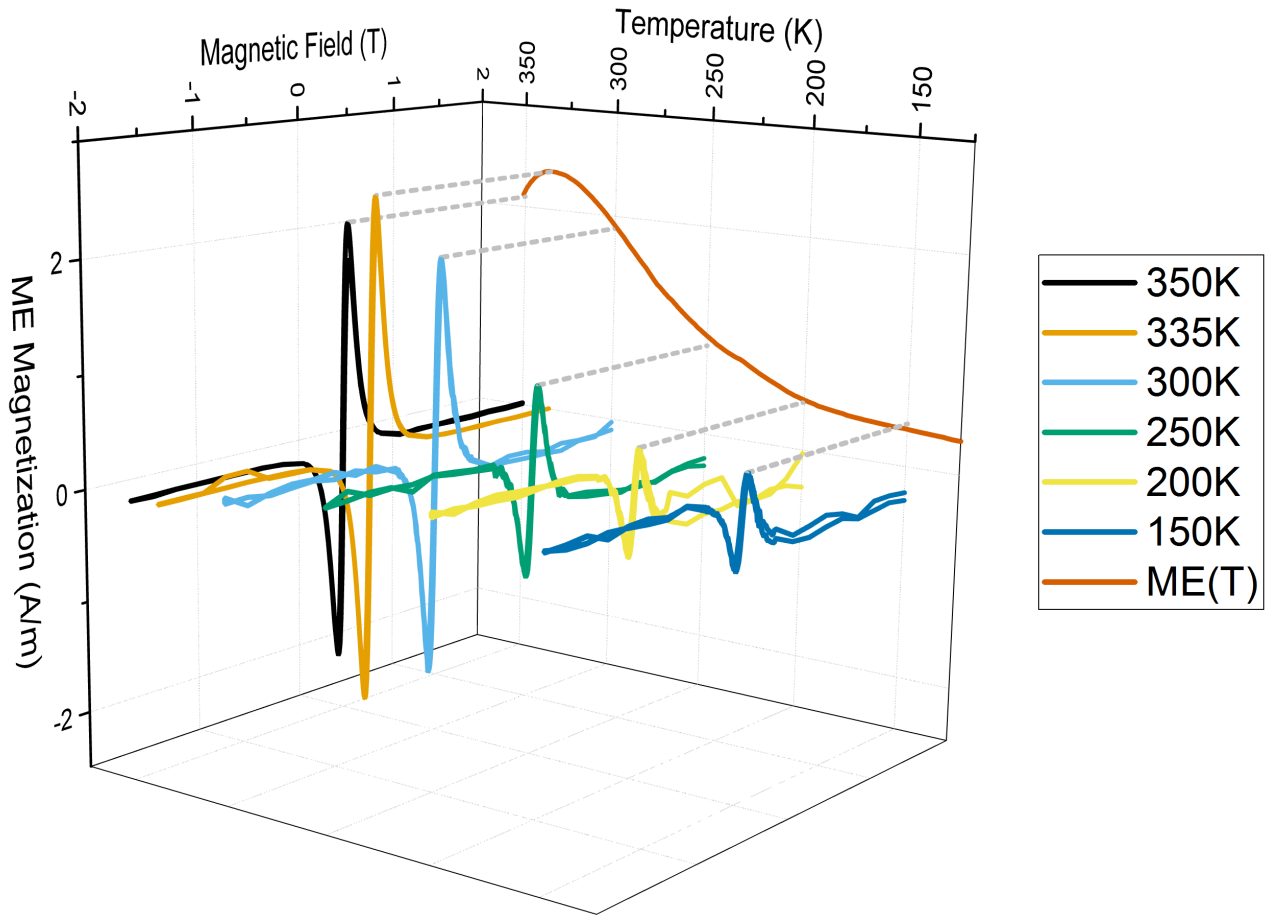


Figure 6.64: Magnetic field dependent ME magnetization curves for sample NFO50 recorded at different temperatures between 350 K and 150 K, shown in comparison (grey dashed lines) to the renormalized $ME(T)$ curve recorded at $\mu_0 H_{DC} = 50$ mT for the same sample from Fig. 6.62 (shown projected onto the $\mu_0 H_{DC} = 2$ T plane for clarity).

However, the data in Fig. 6.64 clearly shows that no shift of the field dependent peaks takes place, it's only the signal amplitude that decreases, with the position of the maximum remaining unchanged. Furthermore, this assumption would not explain the drop of the signal at higher temperatures. Clearly, the main dependence on the temperature stems from the ferroelectric phase and the associated phase transitions that are known from pure BTO. The properties of the magnetic phase are not significantly altered, as we can see in the $M(H)$ and $ME(H)$ curves, so we can assume, like for the previous sample, that a modification of the elastic compliance (see Fig. 3.6) and the strength of the coupling within the two phases (as given by Eq. 2.65)

leads to a modification of the temperature dependent maximum of the ME magnetization, as these properties would not directly influence the static magnetization. The shift is therefore caused by the temperature dependence of the electro- and magnetomechanical coupling factors, which themselves are of course modified by the different composition and the modification of the connectivity as the ratio between BCZT and NFO changes. When looking at literature values,²³⁹ we can see that the real part of the magnetomechanical coupling factor of pure NFO shows a nearly linear temperature dependence, which would mean that this rise would be superimposed onto the peak caused by structural phase transitions in BCZT, leading to a shift of the maximum, with the magnitude of the shift depending on the slope of the coupling factor's temperature dependence. It's also evident that this temperature behavior is highly sensitive to the phase purity of NFO, so the question remains whether any minute interdiffusion or similar effects might alter the NFO fraction near phase boundaries and thus increase the temperature sensitivity of magnetomechanical coupling. When regarding electromechanical coupling, we know from Fig. 3.6 and Eq. 6.14 that it's very closely intertwined with the elastic compliance, which is the main temperature dependent factor. Regarding the literature data such as Ref. 109, it makes sense to assume that the shift of the temperature dependent peaks is the result of an interplay between magnetomechanical and electromechanical coupling factors, with the latter showing a strong temperature dependence through the elastic compliance.

At this point, we also need to consider effects of the demagnetizing field again, which we last discussed for the CFO-BTO sample that was measured in two different orientations.¹²⁴ In that case, it was mostly the macroscopic shape of the sample and its orientation relative to the magnetic field that was considered, as this significantly changes the aspect ratio on which the demagnetization field strongly depends. We saw that for a sample that was oriented so that the magnetic field is applied in plane, the ME effect is strongly reduced, due to the reduction of the effective magnetic field acting on the magnetic grains within the sample because of the increased demagnetization field. Now though, we also want to take into account local effects that act on the magnetic regions in our samples, as they were all measured in the same geometry and only show marginal differences in thickness (0.9-1.3 mm) with identical diameters (6 mm). We can therefore assume that any major change in the demagnetization field will be brought about by the microstructure and connectivity. A very useful study to discuss this topic is a publication by Mattei and Le Floch,²⁴⁰ who analyzed the demagnetizing effects in disordered heterostructures with regards to percolation. If we think back to the initial experiments on which our approach is based,²¹ it becomes obvious that we are dealing with the same problem of percolation of the magnetic grains, which not only leads to an increase of conductivity by providing current paths through the sample, but also has an influence on the shape of the magnetostrictive regions and thus on the demagnetizing field. In this study, the authors of Ref. 21 discovered that there is a specific concentration of the magnetic load C , which, when undershot, causes a cut-off of the magnetic flux paths in the composite medium. The material

thus switches from showing both macroscopic and microscopic demagnetization effects to only local, microscopic ones. It is generally understood that non-uniform internal fields, as they will occur in complex systems like ours, will lead to a broadening of certain parameters due to a wider distribution of size and shape dependent properties.

These authors²¹ start off with the general statement that the shape of a body determines its shape tensor as well as the demagnetizing tensor, with the shape dependence of the latter being easily obtainable through classical electromagnetism for finite bodies such as ellipsoids, elongated cylinders and thin films.²⁴⁰ In the simplest example of an ideal ellipsoid, the demagnetizing field inside the particle is uniform, with the shape tensor \hat{A} being used to describe this shape anisotropy. They further state that magnetic poles form on the surface of a body when it's magnetized, with the magnetostatic self-energy being defined as the interaction of the magnetization with the demagnetizing field, latter being formed by the mentioned poles. If we use the difference between applied and internal field as our definition for the demagnetizing field, we can use the relation

$$E_m = \frac{\mu_0}{2} \int_V M \cdot H_d dv \quad (6.15)$$

to describe the magnetostatic self-energy through the magnetization M and the demagnetizing field H_d , with integration being performed over the volume of the body in question.

If the magnetic ellipsoid has a permeability μ_i and is described by the shape tensor \hat{A} , expressed as a diagonal tensor of the components A_α with $\alpha = x, y, z$, surrounded by a matrix with permeability μ , the decrease of the external field H_0 through the magnetization M can be given by the demagnetization tensor \hat{N} . This leads to the expression for the internal field H_i :

$$H_i = H_0 - \hat{N} \cdot M. \quad (6.16)$$

If we use only the diagonal components of the demagnetization factor \hat{N} , namely N_α , we can define it as

$$N_\alpha = \frac{\mu_i - \mu}{\mu(\mu_i + 1)} A_\alpha, \quad (6.17)$$

which links the shape of the body described by A_α , its magnetic properties as given by μ_i , and the magnetic properties of the surrounding matrix given by μ . Several simplifications can be performed, such as setting $\mu = 1$ for particles in an empty space, leading to $N_\alpha = A_\alpha$, or $N_\alpha < A_\alpha$ for $\mu > 1$. It's intuitive that the term disappears when the magnetic properties of the particles and the matrix match. Continuing with the elucidation from Mattei and Floc'h,²⁴⁰ we return to the magnetic concentration load C that was mentioned earlier. For this purpose, an experiment was performed using cylindrical rods composed of ferromagnetic particles dispersed in an epoxy matrix. It was observed that no demagnetization was observable until a

certain threshold was passed, after which the demagnetizing field rose rapidly until reaching a saturation value that corresponds to the theoretical value for a bulk cylinder.

From this, we can learn that the demagnetizing factor does play an important role with respect to the percolation we can witness in such samples. Indeed, this validates the claim of preceding works²¹ that identified the percolation of the magnetic phase to be a major problem that needs to be overcome for the formation of effective ME ceramics. In short, if the particle concentration is kept below a certain threshold, demagnetization effects can be avoided almost completely. So in essence, our temperature and field dependent measurements represent a competition between the most optimal composition for ME coupling itself, for magnetomechanical and electromechanical coupling within the constituents, with influence from stiffness and thus elastic compliance, as well as effects from percolation such as the increase of the demagnetizing field and an increase of conductivity, latter leading to a reduction in poling and an increase of stray signals from current flows through the sample. It's clear that we have some difficulties to adequately describe our results in this case, as this last sample set clearly shows the multitude of effects that play a role in the characterization of multiferroic ceramics.

To add the final piece to the puzzle, the optimized parameters obtained from $ME(T)$ and $ME(H)$ measurements were combined into the final electric field dependent $ME(E)$ measurements, summarized in Fig. 6.65. As before, the different maximum electric fields are the result of using the identical voltages on all samples, composed of a 100 V AC superimposed onto 100 V DC, with the different values in kV/cm arising from the different sample thicknesses, since the two outer members of the composition were somewhat thinner than the two inner ones. The final result, summarized in Fig. 6.66, is not immediately clear for this sample set, with NFO20 giving 16.9(6) ps/m, which rises to 90.1(6) ps/m for NFO30, dropping to 34.9(2) ps/m for NFO40 and rising again to 86.2(6) ps/m for NFO50. The direct conclusion we can draw is of course that NFO30 shows the highest ME effect, which is also supported by the highest 5 T magnetization (Fig. 6.60), closely followed by NFO50, while the other two samples show a much lower effect. This is an interesting result, as one would usually expect to see one composition dependent peak, with the effect decreasing continuously in both directions in which the composition can be altered. That would be in line with previous results on CFO-BTO as shown in Fig. 6.39, where the decrease towards higher ferrite content was presumably caused by lower poling through higher conductance. In this regard, the result for NFO50 is quite surprising, as the experience from previous experiments shows that a high ferrite content usually translates to problems stemming from conductivity. Indeed, we saw a fall of the sample resistance from 30 G Ω for NFO20 down to under 1 G Ω for NFO50 in this sample set. Additionally, as it was just discussed, this sample with its (3-3) connectivity is most susceptible to high demagnetization fields. We therefore need to determine the cause for this peculiar behavior.

As we discussed previously, the distribution of magnetic grains and their shape and structure have a greater effect than expected on the results of this sample set. The longer derivation regarding the percolation of magnetic grains starting on page 202 aptly shows how the morphology and connectivity may play a role in the magnitude of the ME effect expressed through α_C , but the TOF-SIMS results do not provide a clear insight as to why NFO40 has a lower effect than NFO50, even though latter clearly has (3-3) connectivity due to the increased NFO concentration. One possible partial explanation for the surprisingly high effect in NFO50 is the ability of our converse ME setup to compensate dielectric losses due to the high power output of the amplifier, which was also what enabled the measurement of the rather leaky SPS sample (see Fig 6.22). In this case, the behavior of the sample also depends on the orientation of the magnetic grains of higher conductivity, as the TOF-SIMS images clearly showed their rod-like growth. Depending on how they are oriented relative to the piezoelectric surrounding, the electric field that is felt by the matrix can be enhanced or reduced, which directly influences the ME response. It can thus be possible that this unwanted enhancement through certain orientations of the magnetic regions, coupled with the ability of the amplifier to compensate for electric losses, allows NFO50 to have a higher effect than NFO30. We would therefore regard NFO50 as an outlier. This is further supported by the fact that the $ME(T)$ measurement could only be performed up to 350 K, and although the values clearly show a drop above 335 K, it could be possible that an underlying increase of the $ME(T)$ curve would have been visible at higher temperatures, which would have pointed towards sufficient conductivity to cause an apparent ME signal. This superposition of actual and apparent ME signals could not be fully deconvoluted in this case, as higher temperatures were not used, to avoid a deterioration of the sample holder.

Additionally, due to problems with the reliability of the measurement signal, a lower frequency of 1.7 Hz was utilized for this sample in order to achieve a stable output. As we saw in Fig. 4.26 in section 4.8.1, low frequencies can lead to an undesired rise of the measurement signal, which also necessitated a renormalization of the $ME(T)$ curve measured at 1.7 Hz when we compared it to the $ME(H)$ curves that were recorded at a later point in time at 8 Hz. The stability problems can be seen in Fig. 6.64 for the measurement performed at 200 K, showing somewhat erratic behavior at higher fields. We need to conclude that the results of NFO50 are artificially enhanced by a combination of conductivity and the inconsistency in terms of the measurement frequency, the choice of which, caused by an unstable signal, was potentially also provoked by the underlying leaky nature of this sample. The low frequency regime is often fraught with problems, as aptly shown by Fig. 4.26, recorded for NFO40. In the case of NFO50, the additional ferrite content causes a strong increase of frequency dependence, presumably through Maxwell-Wagner relaxation,^{152,208} due to the different permittivities of the two constituents. This was further increased by the higher temperature of the magnetic field dependent maximum. So basically, the strongest effects of conductivity through low frequencies and higher temperatures played a major role for the unusually high apparent coupling for this sample.

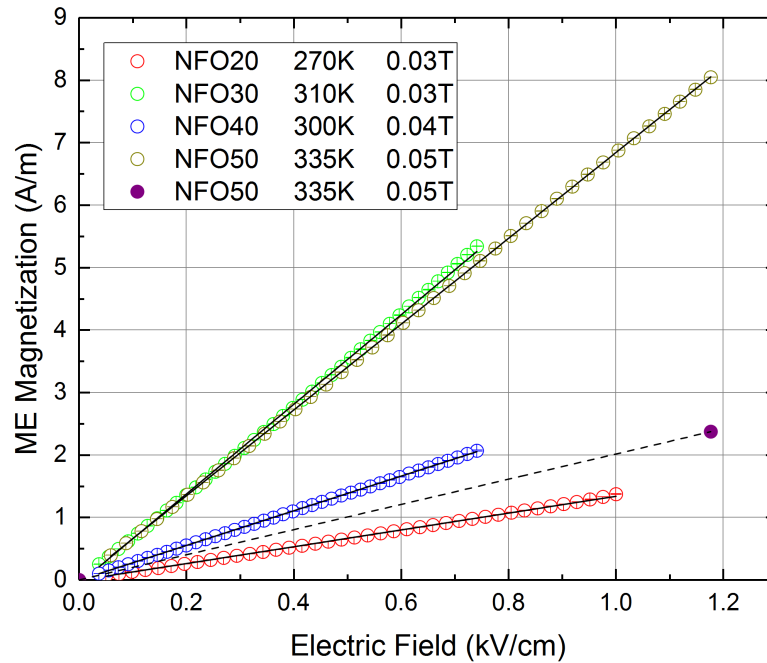


Figure 6.65: Electric field dependence of induced ME magnetization for NFO20-NFO50, with the temperature and applied bias field $\mu_0 H_{DC}$ being denoted in the legend. The single purple dot represents the magnetization value obtained from the extrapolation using the maximum of the 335 K $ME(H)$ curve from Fig. 6.64.

While the temperature and magnetic field results are usable for a comparison to the rest of the sample set, the converse coupling coefficient α_C for this sample should be disregarded. To obtain a more realistic estimation of α_C , we utilized the measurements shown in Fig. 6.64, which were performed at a frequency of 8 Hz due to the fact that this data was recorded separately from the rest of the sample set. With the strong effect from the low frequency negated we can use the maximum magnetization value of the curve measured at 335 K. This point was recorded at the optimum field (50 mT), optimum temperature (335 V), using the highest electric field that had also been used in the previous recording of the $ME(E)$ data (1.18 kV/cm). We can thus make a crude approximation by using this point and the point of origin, since we saw that all linear fits of $ME(E)$ data go approximately through zero. Using these two points, shown in purple in Fig. 6.65, and calculating the slope of the connecting line, we can obtain an estimate of 25.4 ps/m for the converse coupling coefficient of NFO50, shown without error bars in Fig. 6.66. Considering the quality and consistency of the data in Fig. 6.64, we feel that this somewhat simple extrapolation is valid in this case, just to obtain a general idea about the magnitude of the correct coefficient for this sample.

Summary

In summary, this last sample set provides two important conclusions. On the one hand, it represents the samples with the highest ME effect that we have ever recorded, with a value as high as the 90 ps/m for sample NFO30 never having been reached in our prior publications. In fact,

the BCZT-NFO system as such has not received as much attention as the CFO-BTO system until now, with some publications only characterizing the ME coupling indirectly²⁴¹ through $P(E)$ loops after magnetic poling. Others recorded only the direct ME effect in particulate²⁴² and thin film samples,²⁴³ with all of them using rather high frequencies (1-380 kHz), which leads to a strong change in the factor given by ε between α_C and α_D , as defined by Eq. 2.63. As a result, not direct comparison to literature could be made at this point. Nevertheless, this sample set represents the peak of our endeavors of obtaining the highest magnetolectric coupling coefficients through the variation of piezoelectric and magnetostrictive constituents and their connectivity. The last two BCZT-based sets also introduced the importance of the electro- and magnetomechanical coupling factors as well as the elastic compliance, which had not been considered in our early measurements. However, and this brings us to our second point, it also showed that the complexity of these sintered ceramics is still a problem, not just due to the inability to use simple model calculations, but also due to the fact that the morphology and connectivity are factors that, on the one hand, have a strong influence on the quality of ME coupling, but on the other hand, are difficult to control. The same is also true for the magnetic properties, with pronounced drops in saturation magnetization being visible in all sample sets. The highest effect of NFO30 is therefore supported by a somewhat higher saturation magnetization that was observed for this sample. We are thus faced with the previously known problem that sintered ceramics are robust materials in terms of measurements and mechanical stability, but allow for a variation of certain parameters that are difficult to control compared to layered biphasic composites.

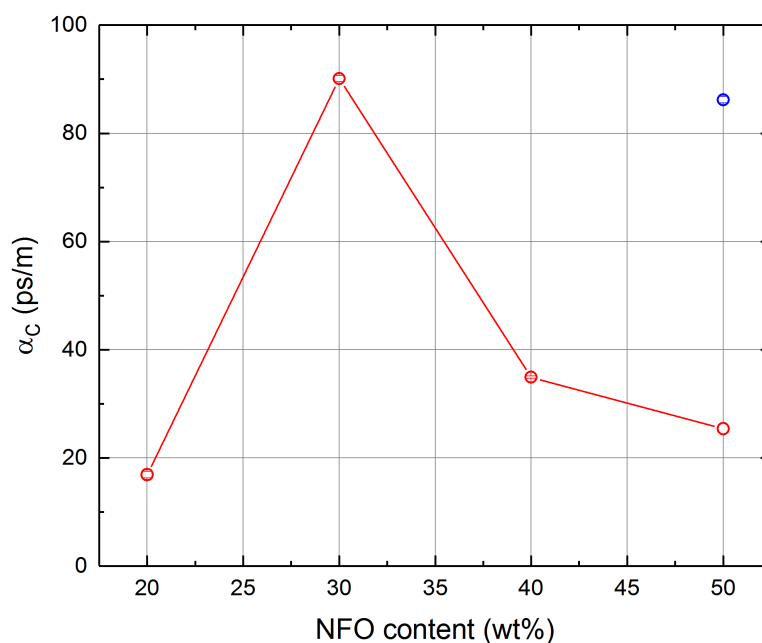


Figure 6.66: Converse ME coupling coefficient α_C plotted against NFO content. The outlier of sample NFO50 is shown in blue, while the approximate value is shown without error bars. Line is a guide to the eye.

7 Conclusion

It's always difficult to sum up such a large amount of experimental data in a short and concise fashion, as certain details and clues always go missing. Because of this, we will regard our two data sets for single-phase BFO and our composite ceramics separately.

7.1 BFO nanoparticles

Thanks to our experiments performed on the single-phase multiferroic BFO, we were able to deconvolute and precisely model the behavior of the inherent anharmonic spin cycloid in this material. With this, we were the first, and until now, the only ones who have performed this detailed evaluation on nanoparticle samples in a wide temperature range. Other publications, even those published very shortly¹⁹² after ours, usually deal only with bulk samples, while at the same time proving the validity of our theoretical model, which was derived from NMR methods. The model was useful for both theoretical simulations of spectra to observe the effects of anharmonicity on the cycloid and thereby on our spectral features, while we were also able to directly utilize our approach for the fitting of experimental spectra. Clear trends in the temperature dependence of the anharmonicity were discovered, showing a distinct decrease to zero between 170 K and 400 K, which was in line with previous studies on bulk¹⁹³ and single crystal¹⁹⁵ BFO. As it was mentioned in Ref. 1, one of the great weaknesses that lead to a decline in the research of multiferroics was the limited understanding of the microscopic sources of their behavior. With our characterization being performed down to local properties, it's clear that this work provided significant information to the community regarding the microscopic effects of ME coupling in BFO.

However, if we're critical, the most interesting open question could not be answered, namely whether the particle size, which has been shown via magnetometry (Fig. 6.5) to cause weak ferromagnetic behavior, is an adequate instrument to actively alter the spin structure. As our calculations are based on the inherent coupling between ferroelectric and antiferromagnetic ordering in this material system, our hope was to potentially crack the cycloid and thereby unlock a new single-phase material with inherent ME coupling, which is often described as the 'holy grail' of multiferroics.⁶⁸ However, it has to be said that we were not able to move forward in that direction, as the particle size distribution, something that nanoparticle samples are always burdened with, didn't allow for an investigation of the anharmonicity of the smallest and therefore most interesting particles from our sample set. However, all was not in vain, as we have acquired important knowledge on this material that can be used for further evaluations on other samples. This is especially true for the model we have developed, which can be applied to either particles with a narrower size distribution, or to thin film samples, allowing universal

access not only to the regular hyperfine parameters, but also to the degree of anharmonicity. Thin films also have the added benefit of well-defined parameters, and thereby the ease of mathematical modeling, as well as the possibility of using strain to further influence the cycloid. A more comprehensive description of our plans for this material system can be found in the outlook. Due to the overall difficulties that single-phase materials are faced with, and as our data revealed that the cycloid would not be cracked by small particle sizes, a change to composite systems seemed like the logical next step. This brings us to the two other systems we have characterized, CFO-BTO as well as BCZT-based composites.

7.2 CFO-BTO ceramic composites

Looking first at the initial CFO-BTO sample systems, we clearly showed that, even though promising from its description, the spark plasma sintering (SPS) method is not suitable for the formation of magnetoelectric ceramics, due to the resulting (3-0) connectivity causing excessive conductance, lack of polarization and thus poling, as well as stray signals from current flow through the sample. Instead, the conventional sintering route was found to provide samples with advantageous properties, while a 50-50 fraction of CFO to BTO gave the highest converse ME effect α_C of all samples studied. Furthermore, we clearly demonstrated the importance of poling, which is often hardly described or mentioned in literature, but is vital for the measurement of the ME effect in ceramics, as clearly shown in Fig. 6.37. In contrast to previous works,²¹ we not only characterized the temperature dependence with regards to structural phase transitions, but also performed a detailed analysis of the dependence of the ME effect on applied magnetic fields. A clear correlation with the field derivative of magnetostriction was found, while our results for linear and transverse sample orientations were directly comparable to works found in literature, providing vital information on the effect of the demagnetizing field, which is often not taken into consideration, even though it can significantly reduce the effective magnetic field acting on the magnetostrictive constituent.

If we again look at our results critically, we can see that despite performing the synthesis of core-shell particles in order to obtain a clear (0-3) connectivity with well-defined phase separation, our results were only slightly superior to those of a directly preceding work,²¹ in which it was estimated that higher effects were attainable when percolation and thus unwanted conductivity effects are limited. However, even though the core-shell particles, once sintered into ceramics, provided clearly separated CFO grains in a BTO matrix, the overall effect was not as high as we had hoped. Clearly, such ceramic systems are extremely complex and sensitive to parameters used during their formation when regarding grain growth and density, so it's quite possible that further optimization is required. Still, our coupling coefficients are among the highest found in literature, and were recorded with great care and attention to detail, providing a broad knowledge base on which further experiments can be planned.

7.3 BCZT-based ceramic composites

After seeing only little improvement through the optimizations of the CFO-BTO system, BCZT was utilized as a ferroelectric constituent to attain a higher converse ME coupling coefficient. Measurements were successfully performed on BCZT-CFO 85-15 and showed reliable data. The converse ME coupling coefficient of 6 ps/m was smaller than the maximum attained for CFO-BTO 50-50, but, when compared to literature values of CFO-BTO with a 85-15 composition, showed a clear improvement of 37%. However, it was not possible to obtain satisfactory results on compositions with higher CFO fraction due to excessive conductivity, as it was not possible to directly influence the connectivity in the composite, with these samples having been prepared by a standard solid state reaction, rather than from core-shell particles. Due to the complexity of attempting to synthesize nanoparticles with BCZT, this approach was not used here. Instead, a modification of the magnetostrictive phase was attempted.

The resulting Al^{3+} doping of the CFO phase was successfully carried out, as was the formation of a suitable BCZT-CFO 50-50 sample without doping as a reference. The precursor materials were also precharacterized via Mössbauer spectroscopy and magnetometry, showing striking differences in saturation magnetization, with the doped sample displaying a saturation magnetization that is more than 50% lower than that of the undoped sample, while Mössbauer spectra revealed lower canting angles for the doped sample, indicative of a decreased magnetic anisotropy. From these results, we were able to determine that Al^{3+} has a strong preference to occupy the octahedral B-sites, with the displacement of the Fe^{3+} ions from these sites leading to an overall decrease in net magnetization, as the difference between the two sublattice magnetizations is being reduced. This effect was then mostly negated by the sintering procedure, with the high temperatures leading to a more equal distribution of the ions across the sites. Any residual small differences in terms of saturation magnetization were found to be caused by an impurity phase that formed during the final sintering step. However, the effect of Al^{3+} -doping was still very much observable in our main results, as described below:

Magnetolectric measurements were successfully performed, showing no significant deviations in magnetic field dependence that may have been caused by the Al^{3+} doping, while the magnitude of the converse ME coefficient from the linear effect showed a significant improvement for the doped sample, increasing the value from 3 ps/m up to 11 ps/m. The two main conclusions we can draw is that Al^{3+} doping is able to significantly improve the ME coupling by an increase of magnetostriction, as only the magnetostrictive phase was modified, with this improvement being caused by a decrease in magnetic anisotropy, leading to higher magnetostrictive strain. The unmodified 50-50 sample showed a rather low effect overall, pointing towards persisting problems regarding the sample quality. The most likely culprit is again the conductivity, which always becomes a more significant issue when the fraction of the magnetostrictive component

is increased. Indeed, we see that the goal of obtaining the optimum composition for the highest ME effect is often hindered by problems stemming from increased conductivity. Furthermore, a shift of the temperature dependent maximum was discussed in detail, uncovering that effects from elastic compliance and also from electro- and magnetomechanical coupling factors must be taken into account, as they are able to shift the temperature of maximum ME coupling. This effect had not yet been discussed in detail before, and can thus also explain the shift of the peak to lower temperatures in our second CFO-BTO sample set.¹²⁴

The last sample set that was characterized represents the peak of our efforts to obtain a higher converse ME effect, using NFO instead of CFO as the magnetostrictive phase. Thanks to the use of TOF-SIMS, it was possible to probe the 3D structure of these samples down to a certain depth, giving us a clear view of the connectivity and the distribution of magnetostrictive regions in the ferroelectric matrix. The growth of rod like structures was visible, in addition to a gradual change of the connectivity from (0-3)/(1-3) to (3-3), which added additional influences on the ME coupling apart from the composition itself. Very high ME coupling coefficients of up to 90 ps/m were obtained, which are the highest that we have ever measured up to that point, nearly four times as large as the coefficients of our CFO-BTO sample sets. Questions arose regarding the shift of the temperature dependent maximum in $ME(T)$ as well as the lack of a defined composition dependent peak due to the high effect of the NFO50 sample. A very detailed discussion provided the framework to interpret these results, with the morphology of the sample itself playing a greater role than expected, in addition to effects known from the previous set, including the elastic compliance and magnetomechanical coupling factor, having an influence on the temperature dependence. The high effect seen in NFO50 was determined to be caused by a number of factors, chief among which were the conductivity, resulting from the high ferrite content and (3-3) connectivity, as well as the low measurement frequency. Latter was chosen due to problems with signal stability in this sample, which was assumed to be a side effect of the high conductivity. Using one of a series of field dependent measurements at different temperatures, a more realistic estimate for the coupling coefficient was obtained for this sample, so that the optimum composition for this sample set was determined to be BCZT-NFO 70-30 (wt%).

7.4 Converse ME measurement setup

From our numerous experiments performed on magnetoelectric ceramics with different connectivity schemes and different magnetic and electric constituents, we can also make a somewhat technical conclusion, which should not be overlooked in the light of the actual physical phenomena: We have shown that the converse ME measurement setup, using a modified SQUID AC susceptometer, offers one of the most robust and reliable methods of determining the presence and character of ME coupling. The setup for direct ME measurements is limited by conductance effects that make it impossible to measure samples with a certain amount of leakage, but which would otherwise still show actual ME coupling. Thanks to the power provided by our wide band amplifier, we were able to perform a basic characterization even of samples that showed excessive conductance. Furthermore, the measurements in the direct setup can only be performed at room temperature, while the converse setup offers a full range of temperature, applied magnetic DC field and electric AC field values. Latter could even be increased by use of a more powerful amplifier, in case of very thick samples requiring higher electric fields. It is also important to measure the macroscopic and not just the microscopic effects, as there are samples that show one, but not the other. With the Al^{3+} doped samples, we saw that there was only moderate response from PFM, which doesn't give a clear, quantifiable result, while the converse ME setup can do just that, in dependence of external parameters like temperature and field. Furthermore, microscopic methods are strongly dependent on the connectivity, having trouble if no clearly defined grains or domain structures are present, while the converse setup has no such limits. In short, especially after the rewiring that was performed early on, we clearly have a highly capable, precise and adjustable setup, which was used to its fullest potential by making use of the entire temperature, magnetic field and even frequency range. Thanks to the fact that the automated functions of the SQUID remain fully usable despite the modifications, a large amount of data can be recorded with manageable experimental effort, with the only price to pay being the significant amount of time these measurements need. While other methods exist, such as X-ray absorption spectroscopy and other synchrotron based techniques, also offering possibilities to determine ME coupling, as discussed in Ref. 123, they of course do not possess the utility of a laboratory setup that is always available for measurements.

During the course of our experiments, we also obtained knowledge on how to deal with issues such as excessive conductivity in leaky samples leading to apparent ME effects, unwanted frequency doubling, as well as the frequency dependence of measurement results, allowing us to monitor and avoid any interference, which will prove fruitful for future measurements on composite systems. Especially the deviations we saw in the results of NFO50 clearly shows that the effects of measurement frequency need to be more closely monitored. From now on, we will perform a frequency dependent measurement for every prospective new sample so that any unwanted modifications of the measurement signal can be ruled out.

7.5 Summary

In short, we have characterized a very large number of sample sets in detail, being able to observe the effect of different compositions, different constituents, different sintering methods, connectivities and even chemical doping on the overall strength of the converse ME effect. Not only were we successful in our search for progressively higher converse ME coefficients, reaching its peak with the BCZT-NFO system, but we learned valuable lessons regarding the various pitfalls of our ME setup, especially with regards to problems stemming from conductivity, which needs to be carefully considered when researching new systems for potential applications. We were also able to make accurate comparisons to literature, thanks to our very detailed temperature and magnetic field dependent studies, with our final paper in this series probably containing one of the most comprehensive converse ME datasets in a single publication.

One general statement that we have to make regarding the validity of our experiments on different compositions of the same material, and our efforts to find the most suitable composition for a high ME effect, is the following: It needs to be assumed that we are always seeing the interplay of two main effects. One is of course the magnetoelectric coupling itself, its dependence on the quality and number of the interfaces, which are highly sensitive to sample preparation and subsequent heating and calcination steps. As we found out in our later experiments, additional dependences in the form of elastic compliance and magnetomechanical coupling provide further ways in which the ME effect can be influenced, with such effects being very hard to control.

The other factor is the conductivity, which is always a foe one needs to be aware of. Not only is it responsible for parasitic signals that the noise reduction routine of the SQUID is unable to reject due to the identical frequency, but it also hinders poling and thus reduces the overall effectiveness of our ME measurements. The main problem lies in the higher conductivity of the magnetostrictive phase, and even if the ME effect would indeed increase when using a composition with a higher fraction of magnetic material, the effect can be offset by the additional conductivity. So if we look at composition dependent depictions of the ME coupling, as was done for the second CFO-BTO sample set in section 6.2.3, we need to be aware that the decrease of the coupling coefficient at higher CFO fractions is most likely caused by conductivity effects, not just by lower ME coupling. This problem was discovered early on in preceding works,²¹ with the only solution being the isolation of the conductive phases, as was initially attempted through core-shell particle precursors.¹²³ However, this is not as easy as it sounds, as we saw in the SEM micrographs in Fig. 6.26. These samples are complex systems, with no direct way of controlling grain sizes while leaving other parameters untouched. The sol-gel synthesis route for core-shell particles is also burdened by the complex methodology and a difficulty to obtain reproducible results, with the routine production of a larger amount of sample material not being feasible.

The most optimal sample connectivity (0-3) of magnetostrictive grains in a ferroelectric matrix was not easy to attain, and the use of core-shell particle synthesis always sacrifices some of the ease with which ceramic samples can be produced compared to other nanostructured systems. However, despite some disadvantages, it seems that well-defined samples are the key not just to higher ME coupling as such, but also to a more comprehensive understanding of the ME effect and for the possibility of theoretical modeling, for which our composite samples are often too complex and not sufficiently well-defined. We therefore have to decide what we want: Mechanically robust samples that are easy and quick to manufacture, but which may not always have the most optimal connectivity to suppress conductivity effects and grain growth, or samples that are perhaps not optimal in their mechanical properties, are difficult to produce, but allow excellent control of their parameters such as interfaces, layer thicknesses and so forth. In this work, we obviously chose the first route, and performed a large number of successful experiments. But in the future, it is obvious that we will also need to branch out into other sample formation methods, as shall be outlined in the outlook.

As a final statement, the ME effect measurements always represent a superposition of a large number of factors that influence the field and temperature dependencies, which are not always easy to deconvolute. Our measurements and the interpretation of the results represent an important step in the understanding of such systems, as we didn't just optimize the ME coupling but also went into detail about why certain parameters showed certain changes. This competition between a large number of properties will always be a problem, with the potential of straightforward modeling and the possibility of predictions being sacrificed for the ease of sample formation.

8 Outlook

This section is normally reserved for overly optimistic promises regarding improvements or changes to either the material system or the measurement method in order to create the impression that the course of research didn't abruptly end when the thesis was handed in. In our case, several follow-up projects have already commenced, picking up where the ones described in this work have finished. As we will see, many of these current and future projects deal with the return to certain systems that we initially moved away from, which, more than anything, shows us that one should never discard systems that, at first, didn't provide the most promising results.

8.1 Magnetoelectric ceramics via industrial route

A large number of successful ME measurements have been performed using the well-known CFO-BTO system, synthesized by a different route than before, promising higher effects than their predecessors. Due to the difficulty in obtaining reproducible results through the complex sol-gel precursor synthesis, a new route has been taken, with the preparation being performed by Dipl.-Phys. Ahmadshah Nazrabi of the Lupascu group. These new samples were formed by conventional sintering as used for other samples, with different sized particles (such as 50 nm and 1 μm) being utilized for the precursor materials. The goal is to obtain a higher density by the smaller particles filling the voids between the larger ones, which is hoped to lead to a higher mechanical stiffness of the resulting samples. The main motivation is the usage for mechanical measurements under load, which often lead to a fracturing of the samples. While this is not directly aimed at ME measurements, we saw that the elastic compliance has a temperature dependent influence on the $ME(T)$ peak, so it may very well be possible that an influence of the added stiffness will be observed. A more straightforward reason is also the ability to produce a larger amount of samples with this method while keeping results reproducible, hence the designation 'industrial route'.

8.2 Magnetoelectric ceramics with Terfenol-D

After having replaced both electric and magnetic phases in our composites, it seems like a logical step to perform further attempts at this route, with new samples having been synthesized that utilize Terfenol-D ($\text{Tb}_{0.3}\text{Dy}_{1.7}\text{Fe}_2$) instead of CFO as the magnetostrictive constituent. This material exhibits a microstrain of up to 2000 ppm compared to 60 ppm for Co,^{234,244} thus being an obvious candidate for future samples, although also burdened with the high price of rare earth metals. Our main goal is therefore the experimental proof of this route being viable, rather than large scale applications, so that we can gain more experience on the enhancement

of ME properties. These samples are being prepared by M.Sc. Samira Webers with help from the Lupascu group, with our first attempts of converse ME measurements having been thwarted by the high conductivity Terfenol-D, leading to excessive Joule heating and the destruction of the samples. We are faced with the same problems as with our early CFO-BTO samples, needing to find a way to isolate the magnetostrictive from the piezoelectric phase, in order to eliminate any routes the current can take through a widespread 3D network of interconnected regions. We therefore need to perform a detailed analysis, perhaps again using TOF-SIMS, to obtain a clearer view of the 3D structure in this material. Due to the fact that the formation of core-shell particles via wet chemical synthesis methods is not readily possible, we will need to look at the necessity of increasing the BTO fraction, thereby isolating the Terfenol-D grains as best as we can. This is comparable to the BCZT-NFO samples with the lowest NFO content, as a higher content gradually lead to a (0-3)/(1-3) connectivity to turn into a (3-3) one, which we assume degrades the ME qualities through increased conductivity. While this thesis was being composed, we successfully measured one Terfenol-D - BTO 40-60 sample with our converse ME setup, and while seeing a clear signal, the lack of response to magnetic fields and an almost exponential signal increase towards higher temperatures clearly pointed towards the usual pitfall caused by a leaky sample (see Fig. 4.24). Obviously, more effort is needed before we will be able to perform our first successful measurements on this new system.

8.3 Thin film ME samples via PLD

As we saw in the BFO section, it was not directly possible to draw conclusions regarding the influence of particle size on the anharmonic spin cycloid, or rather, whether there is an obvious mechanism that would disturb or crack the cycloid in a way that would induce a sufficiently high magnetic moment for application purposes. This would entail the often cited 'holy grail', a single-phase room temperature multiferroic, which was always something scientists strived for with BFO. Just as in our multiferroic composites, nanoparticles always have some amount of complexity and ill-defined parameters such as their shape and size distribution, which are not easily controlled.

A different and promising route would be the formation of thin film samples, which have also been shown in literature to influence the anharmonic spin cycloid, not just through size but also through strain effects.⁷⁸ One highly regarded work that was cited before is a publication in Nature Communications by Schmitz-Antoniak et al.⁶⁰ in which pulsed laser deposition (PLD) was utilized to form a CFO-BTO composite sample. Using a premade target with the appropriate composition of the constituents, the effect of self-organization was used in order to obtain a sample of CFO pillars within a BTO matrix. While such samples suffer from the effect of substrate clamping, they still show the possibilities that are available by thin film preparation. Generally speaking, thin film samples often have inferior mechanical properties compared to

the more robust ceramics, and are often more complex to produce. However, their big advantage lies in their clearly defined dimensions and structures, which opens up new possibilities for theoretical modeling. Latter has not been utilized in this thesis due to the generally complex nature of sintered ceramics lacking clear definitions in terms of the distribution of phase boundaries, as we clearly saw in the TOF-SIMS images.

Although it was used to produce the sample used in Ref. 60, the current PLD system suffers from a number of technical limitations and issues. Explaining all of them in detail would go beyond the scope of this outlook, but they all have an effect on sample quality, and with PLD being extremely sensitive to external parameters, we sought to find new ways of sample preparation. In a long process that took over two years, we were able to acquire a highly advanced UHV PLD chamber from the University of Ulm, thanks to P. D. Ulf Wiedwald and Dr. Franziska Scheibel from the group of Prof. Michael Farle. After a lot of work, we were able to perform our first ablation in the first half of 2018. This opens up new possibilities for sample preparation, as the new chamber, with its computer controlled target selection stage, is able to freely switch back and forth between up to four targets during sample preparation. This negates the use of precomposed targets and thus allows a free choice of e.g. CFO to BTO ratios, offering greater flexibility. The resulting use of pure constituent targets also avoids some of the typical problems, such as the inability to account for different ablation rates for different materials, and the resulting deterioration of precomposed targets.

With this new setup, we not only plan to grow epitaxial thin film BFO samples that can then be characterized by conversion electron Mössbauer spectroscopy (CEMS), but we have already successfully prepared CFO-BTO thin film samples, starting with simple bi-layer and multilayer systems, since laminated structures exhibit high ME voltage coefficients and minimal leakage problems as the phases are well separated. However, their mechanical strength is poor²⁰⁶ compared to composites, which has to be taken into consideration. A more difficult, but therefore also highly interesting goal, is the synthesis of other self-organized CFO-BTO samples,⁶⁰ attempting to reduce substrate clamping via overall thicker layers. Last but not least, the promising Terfenol-D system can also be realized in thin film form²⁴⁵ in order to avoid the problems we have faced due to the higher conductivity of this material.

Additionally, a new cooperation with Dr. Andreas Herklotz (Martin-Luther-University Halle-Wittenberg) has recently commenced, utilizing He-implantation in BFO films to achieve different states of strain in these. We therefore plan to perform CEMS measurements on these samples in order to observe any potential changes to the asymmetry, line shape, and thus to the anharmonicity parameter, so that any modification of the spin structure through strain can be uncovered. We hope to achieve a greater theoretical understanding of our systems through this route, thanks to the the well-defined thicknesses of thin film samples. Similar efforts of

possibly modeling the anharmonicity and characterizing the Néel temperature in thin film BFO samples are also underway in cooperation with Dr. Juliana Schell (CERN). Generally speaking, thin film layers of BFO have become promising candidates for spintronic applications,⁷⁸ which adds further motivation to characterize this system in greater depth.

Our experimental efforts can therefore be summarized by several returns to systems that were previously considered to be fully characterized from our point of view. Treading a full loop like the current in a SQUID, we started with BFO nanoparticles, went to CFO-BTO solid state samples, then to nanoparticles, back to solid state samples but with different constituents, and with the PLD, we might indeed be returning to our starting point BFO. The most amateurish conclusion we can draw from our work is that one shouldn't discard a certain system completely just because the first results weren't promising, although our measurements on a large number of systems did lead to a greater understanding of the overall topic, while aptly showing the capabilities of our custom built converse ME setup. One thing is for certain: Many converse ME measurements will be performed in the future, always in the hopes of optimizing and further understanding different composite systems.

Bibliography

- ¹ M. Fiebig, “Revival of the magnetoelectric effect,” Journal of Physics D: Applied Physics, vol. 38, no. 8, pp. R123–R152, 2005.
- ² N. A. Spaldin and M. Fiebig, “Materials Science: The Renaissance of Magnetoelectric Multiferroics,” Science, vol. 309, no. 5733, pp. 391–392, 2005.
- ³ P. Curie, “Sur la symétrie dans les phénomènes physiques, symétrie dun champ électrique et dun champ magnétique,” Journal de Physique Théorique et Appliquée, vol. 3, no. 1, pp. 393–415, 1894.
- ⁴ W. C. Röntgen, “Ueber die durch Bewegung eines im homogenen electrischen Felde befindlichen Dielectricums hervorgerufene electro-dynamische Kraft,” Annalen der Physik und Chemie, vol. 271, no. 10, pp. 264–270, 1888.
- ⁵ P. Debye, “Bemerkung zu einigen neuen Versuchen über einen magneto-elektrischen Richteffekt,” Zeitschrift für Physik, vol. 36, no. 4, pp. 300–301, 1926.
- ⁶ J. H. van Vleck, “The Theory of Electric and Magnetic Susceptibilities,” The Mathematical Gazette, vol. 18, no. 231, p. 328, 1934.
- ⁷ I. E. Dzyaloshinskii, “On the magneto-electrical effects in antiferromagnets,” Soviet Physics - Journal of Theoretical and Experimental Physics, vol. 10, pp. 628–629, 1960.
- ⁸ D. N. Astrov, “The magnetoelectric effect in antiferromagnetics,” Soviet Physics - Journal of Experimental and Theoretical Physics, vol. 11, no. 3, pp. 708–709, 1960.
- ⁹ D. N. Astrov, “Magnetoelectric effect in chromium oxide,” Soviet Physics - Journal of Experimental and Theoretical Physics, vol. 13, no. 4, pp. 729–733, 1961.
- ¹⁰ P. Borisov, A. Hochstrat, V. V. Shvartsman, and W. Kleemann, “Superconducting quantum interference device setup for magnetoelectric measurements,” Review of Scientific Instruments, vol. 78, no. 10, p. 106105, 2007.
- ¹¹ G. T. Rado and V. J. Folen, “Observation of the magnetically induced magnetoelectric effect and evidence for antiferromagnetic domains,” Physical Review Letters, vol. 7, no. 8, p. 310, 1961.
- ¹² V. J. Folen, G. T. Rado, and E. W. Stalder, “Anisotropy of the magnetoelectric effect in Cr_2O_3 ,” Physical Review Letters, vol. 6, no. 11, p. 607, 1961.
- ¹³ R. Hornreich and S. Shtrikman, “Statistical Mechanics and Origin of the Magnetoelectric Effect in Cr_2O_3 ,” Physical Review, vol. 161, no. 2, pp. 506–512, 1967.

- ¹⁴ G. A. Gehring, “On the microscopic theory of the magnetoelectric effect,” Ferroelectrics, vol. 161, no. 1, pp. 275–285, 1994.
- ¹⁵ B. D. H. Tellegen, “The gyrator, a new electric network element,” Philips Research Reports, vol. 3, pp. 81–101, 1948.
- ¹⁶ J. van den Boomgaard and R. A. J. Born, “A sintered magnetoelectric composite material BaTiO₃-Ni(Co,Mn)Fe₂O₄,” Journal of Materials Science, vol. 13, no. 7, pp. 1538–1548, 1978.
- ¹⁷ J. van Suchtelen, “Product Properties: A new Application of Composite Materials,” Philips Research Reports, vol. 27, pp. 28–37, 1972.
- ¹⁸ J. van den Boomgaard, D. R. Terrell, R. A. J. Born, and H. F. J. I. Giller, “An in situ grown eutectic magnetoelectric composite material,” Journal of Materials Science, vol. 9, no. 10, pp. 1705–1709, 1974.
- ¹⁹ A. M. J. G. van Run, D. R. Terrell, and J. H. Scholing, “An in situ grown eutectic magnetoelectric composite material,” Journal of Materials Science, vol. 9, no. 10, pp. 1710–1714, 1974.
- ²⁰ J. van den Boomgaard, A. M. J. G. van Run, and J. van Suchtelen, “Magnetoelectricity in piezoelectric-magnetostrictive composites,” Ferroelectrics, vol. 10, no. 1, pp. 295–298, 1976.
- ²¹ V. V. Shvartsman, F. Alawneh, P. Borisov, D. Kozodaev, and D. C. Lupascu, “Converse magnetoelectric effect in CoFe₂O₄-BaTiO₃ composites with a core-shell structure,” Smart Materials and Structures, vol. 20, no. 7, p. 075006, 2011.
- ²² R. M. Bozorth, Ferromagnetism. IEEE, 1993.
- ²³ G. Cullity, Introduction to Magnetic Materials. John Wiley & Sons, 2008.
- ²⁴ M. L. Néel, “Influence des fluctuations du champ moléculaire sur les propriétés magnétiques des corps,” Annales de Physique, vol. 10, no. 18, pp. 5–105, 1932.
- ²⁵ M. L. Néel, “Propriétés magnétiques des ferrites ferrimagnétisme et antiferromagnétisme,” Annales de Physique, vol. 12, no. 3, pp. 137–198, 1948.
- ²⁶ J. S. Smart, “The Néel Theory of Ferrimagnetism,” American Journal of Physics, vol. 23, no. 6, pp. 356–370, 1955.
- ²⁷ J. P. Joule, “On the effects of magnetism upon the dimensions of iron and steel bars,” The London, Edinburgh, and Dublin Philosophical Magazine and Journal of Science, vol. 30, no. 201, pp. 225–241, 1847.
- ²⁸ B. Lorenz and C. Graham, “Magnetostriction Versus Magnetization of Hiperco 50 From 20°C to 700°C,” IEEE Transactions on Magnetics, vol. 42, no. 12, pp. 3886–3888, 2006.

- ²⁹ L. W. McKeehan, “Magnetostriction,” Journal of the Franklin Institute, vol. 202, no. 6, pp. 737–773, 1926.
- ³⁰ H. B. Callen and N. Goldberg, “Magnetostriction of Polycrystalline Aggregates,” Journal of Applied Physics, vol. 36, no. 3, pp. 976–977, 1965.
- ³¹ A. K. Bain and P. Chand, Ferroelectrics: Principles and Applications. Wiley-VCH Verlag GmbH & Co. KGaA, 2017.
- ³² V. Wadhawan, Introduction to Ferroic Materials. CRC Press, 2000.
- ³³ C. Kittel, Introduction to Solid State Physics. John Wiley and Sons Ltd, 2004.
- ³⁴ W. Eerenstein, N. D. Mathur, and J. F. Scott, “Multiferroic and magnetoelectric materials,” Nature, vol. 442, no. 7104, pp. 759–765, 2006.
- ³⁵ H. Schmid, “Introduction to the proceedings of the 2nd international conference on magnetoelectric interaction phenomena in crystals, MEIPIC-2,” Ferroelectrics, vol. 161, no. 1, pp. 1–28, 1994.
- ³⁶ J.-P. Rivera, “On definitions, units, measurements, tensor forms of the linear magnetoelectric effect and on a new dynamic method applied to Cr-Cl boracite,” Ferroelectrics, vol. 161, no. 1, pp. 165–180, 1994.
- ³⁷ M. E. Lines and A. M. Glass, “Applications of Ferroelectrics,” in Principles and Applications of Ferroelectrics and Related Materials, pp. 559–607, Oxford University Press, 2001.
- ³⁸ T. Lottermoser, T. Lonkai, U. Amann, D. Hohlwein, J. Ihringer, and M. Fiebig, “Magnetic phase control by an electric field,” Nature, vol. 430, no. 6999, pp. 541–544, 2004.
- ³⁹ W. F. Brown, R. M. Hornreich, and S. Shtrikman, “Upper Bound on the Magnetoelectric Susceptibility,” Physical Review, vol. 168, no. 2, pp. 574–577, 1968.
- ⁴⁰ S. L. Hou and N. Bloembergen, “Paramagnetoelectric Effects in $\text{NiSO}_4 \cdot 6\text{H}_2\text{O}$,” Physical Review, vol. 138, no. 4A, pp. A1218–A1226, 1965.
- ⁴¹ H. Grimmer, “The piezomagnetoelectric effect,” Acta Crystallographica Section A: Foundations of Crystallography, vol. 48, no. 3, pp. 266–271, 1992.
- ⁴² P. Sciau, M. Clin, J.-P. Rivera, and H. Schmid, “Magnetoelectric measurements on BaMnF_4 ,” Ferroelectrics, vol. 105, no. 1, pp. 201–206, 1990.
- ⁴³ M. Dawber, K. M. Rabe, and J. F. Scott, “Physics of thin-film ferroelectric oxides,” Reviews of Modern Physics, vol. 77, no. 4, pp. 1083–1130, 2005.

- ⁴⁴ G. Catalan, “Magnetocapacitance without magnetoelectric coupling,” Applied Physics Letters, vol. 88, no. 10, p. 102902, 2006.
- ⁴⁵ D. C. Lupascu, H. Wende, M. Etier, A. Nazrabi, I. Anusca, H. Trivedi, V. V. Shvartsman, J. Landers, S. Salamon, and C. Schmitz-Antoniak, “Measuring the magnetoelectric effect across scales,” GAMM-Mitteilungen, vol. 38, no. 1, pp. 25–74, 2015.
- ⁴⁶ P. Paufler, “J. F. Nye. Physical Properties of Crystals. Clarendon Press — Oxford. First published in paperback with corrections and new material 1985. XVII 329 p. £ 15.00. ISBN 0-19-851165-5,” Crystal Research and Technology, vol. 21, no. 12, pp. 1508–1508, 1986.
- ⁴⁷ J. Lou, G. N. Pellegrini, M. Liu, N. D. Mathur, and N. X. Sun, “Equivalence of direct and converse magnetoelectric coefficients in strain-coupled two-phase systems,” Applied Physics Letters, vol. 100, no. 10, p. 102907, 2012.
- ⁴⁸ G. Liu and S. Dong, “Uniformity of direct and converse magnetoelectric effects in magnetostrictive–piezoelectric composites,” Applied Physics Letters, vol. 105, no. 12, p. 122903, 2014.
- ⁴⁹ P. Record, C. Popov, J. Fletcher, E. Abraham, Z. Huang, H. Chang., and R. Whatmore, “Direct and converse magnetoelectric effect in laminate bonded Terfenol-D–PZT composites,” Sensors and Actuators B: Chemical, vol. 126, no. 1, pp. 344–349, 2007.
- ⁵⁰ C. Popov, H. Chang, P. M. Record, E. Abraham, R. W. Whatmore, and Z. Huang, “Direct and converse magnetoelectric effect at resonant frequency in laminar piezoelectric-magnetostrictive composite,” Journal of Electroceramics, vol. 20, no. 1, pp. 53–58, 2007.
- ⁵¹ Y. Zhou, Y. X. Ye, S. H. Zhou, Z. J. Feng, S. J. Yu, M. G. Chen, and J. C. Zhang, “Frequency and field dependence of magnetoelectric coupling in multiferroic particulate composites,” The European Physical Journal Applied Physics, vol. 56, no. 3, p. 30201, 2011.
- ⁵² T. Wu, C.-M. Chang, T.-K. Chung, and G. Carman, “Comparison of Effective Direct and Converse Magnetoelectric Effects in Laminate Composites,” IEEE Transactions on Magnetics, vol. 45, no. 10, pp. 4333–4336, 2009.
- ⁵³ J. Lee, J. G. Boyd, and D. C. Lagoudas, “Effective properties of three-phase electro-magneto-elastic composites,” International Journal of Engineering Science, vol. 43, no. 10, pp. 790–825, 2005.
- ⁵⁴ C. Miehe, D. Rosato, and B. Kiefer, “Variational principles in dissipative electro-magneto-mechanics: A framework for the macro-modeling of functional materials,” International Journal for Numerical Methods in Engineering, vol. 86, no. 10, pp. 1225–1276, 2011.

- ⁵⁵ A. Ricoeur, A. Avakian, and Z. Wang, “Modeling of ferroelectric-ferromagnetic composites to improve magnetoelectric coupling and durability,” in Behavior and Mechanics of Multifunctional Materials and Composites 2014 (N. C. Goulbourne and H. E. Naguib, eds.), SPIE, 2014.
- ⁵⁶ J. Schröder, M.-A. Keip, M. Labusch, and D. C. Lupascu, “Strain induced product properties of magneto-electric composites,” in Research and Applications in Structural Engineering, Mechanics and Computation, pp. 393–398, CRC Press, aug 2013.
- ⁵⁷ M. Labusch, M. Etier, D. C. Lupascu, J. Schröder, and M.-A. Keip, “Product properties of a two-phase magneto-electric composite: Synthesis and numerical modeling,” Computational Mechanics, vol. 54, no. 1, pp. 71–83, 2014.
- ⁵⁸ G. Srinivasan, E. T. Rasmussen, and R. Hayes, “Magnetoelectric effects in ferrite-lead zirconate titanate layered composites: The influence of zinc substitution in ferrites,” Physical Review B, vol. 67, no. 1, 2003.
- ⁵⁹ R. E. Newnham, D. P. Skinner, and L. E. Cross, “Connectivity and piezoelectric-pyroelectric composites,” Materials Research Bulletin, vol. 13, no. 5, pp. 525–536, 1978.
- ⁶⁰ C. Schmitz-Antoniak, D. Schmitz, P. Borisov, F. M. F. de Groot, S. Stienen, A. Warland, B. Krumme, R. Feyerherm, E. Dudzik, W. Kleemann, and H. Wende, “Electric in-plane polarization in multiferroic $\text{CoFe}_2\text{O}_4/\text{BaTiO}_3$ nanocomposite tuned by magnetic fields,” Nature Communications, vol. 4, no. 1, 2013.
- ⁶¹ G. A. Smolenskii and I. E. Chupis, “Ferroelectromagnets,” Soviet Physics Uspekhi, vol. 25, no. 7, pp. 475–493, 1982.
- ⁶² V. M. Petrov and V. V. Gagulin, “Microwave Absorbing Materials,” Inorganic Materials, vol. 37, no. 2, pp. 93–98, 2001.
- ⁶³ G. Catalan and J. F. Scott, “Physics and Applications of Bismuth Ferrite,” Advanced Materials, vol. 21, no. 24, pp. 2463–2485, 2009.
- ⁶⁴ T.-J. Park, G. C. Papaefthymiou, A. J. Viescas, A. R. Moodenbaugh, and S. S. Wong, “Size-Dependent Magnetic Properties of Single-Crystalline Multiferroic BiFeO_3 Nanoparticles,” Nano Letters, vol. 7, no. 3, pp. 766–772, 2007.
- ⁶⁵ S. V. Kiselev, R. P. Ozerov, and G. S. Zhdanov, “Detection of Magnetic Order in Ferroelectric BiFeO_3 by Neutron Diffraction,” Soviet Physics Doklady, vol. 7, p. 742, 1963.
- ⁶⁶ J. W. Lin, J. S. Gardner, C.-W. Wang, G. Deng, C. M. Wu, V. K. Peterson, and J. G. Lin, “Local bonds anomalies and dynamics in bismuth ferrite,” AIP Advances, vol. 7, no. 5, p. 055836, 2017.

- ⁶⁷ N. A. Spaldin, S.-W. Cheong, and R. Ramesh, “Multiferroics: Past, present, and future,” Physics Today, vol. 63, no. 10, pp. 38–43, 2010.
- ⁶⁸ A. M. Kadomtseva, Y. F. Popov, A. P. Pyatakov, G. P. Vorob’ev, A. K. Zvezdin, and D. Viehland, “Phase transitions in multiferroic BiFeO₃ crystals, thin-layers, and ceramics: enduring potential for a single phase, room-temperature magnetoelectric ‘holy grail’,” Phase Transitions, vol. 79, no. 12, pp. 1019–1042, 2006.
- ⁶⁹ C. Blaauw and F. van der Woude, “Magnetic and structural properties of BiFeO₃,” Journal of Physics C: Solid State Physics, vol. 6, no. 8, pp. 1422–1431, 1973.
- ⁷⁰ I. Sosnowska, T. P. Neumaier, and E. Steichele, “Spiral magnetic ordering in bismuth ferrite,” Journal of Physics C: Solid State Physics, vol. 15, no. 23, pp. 4835–4846, 1982.
- ⁷¹ I. Sosnowska and A. Zvezdin, “Origin of the long period magnetic ordering in BiFeO₃,” Journal of Magnetism and Magnetic Materials, vol. 140-144, pp. 167–168, 1995.
- ⁷² J. Landers, S. Salamon, M. Escobar Castillo, D. C. Lupascu, and H. Wende, “Mössbauer Study of Temperature-Dependent Cycloidal Ordering in BiFeO₃ Nanoparticles,” Nano Letters, vol. 14, no. 11, pp. 6061–6065, 2014.
- ⁷³ S. M. Selbach, T. Tybell, M.-A. Einarsrud, and T. Grande, “Size-Dependent Properties of Multiferroic BiFeO₃ Nanoparticles,” Chemistry of Materials, vol. 19, no. 26, pp. 6478–6484, 2007.
- ⁷⁴ S. Goswami, D. Bhattacharya, and P. Choudhury, “Particle size dependence of magnetization and noncentrosymmetry in nanoscale BiFeO₃,” Journal of Applied Physics, vol. 109, no. 7, p. 07D737, 2011.
- ⁷⁵ Y. Wang, Y. Lin, and C.-W. Nan, “Thickness dependent size effect of BiFeO₃ films grown on LaNiO₃-buffered Si substrates,” Journal of Applied Physics, vol. 104, no. 12, p. 123912, 2008.
- ⁷⁶ S. Ryu, J.-Y. Kim, Y.-H. Shin, B.-G. Park, J. Y. Son, and H. M. Jang, “Enhanced Magnetization and Modulated Orbital Hybridization in Epitaxially Constrained BiFeO₃ Thin Films with Rhombohedral Symmetry,” Chemistry of Materials, vol. 21, no. 21, pp. 5050–5057, 2009.
- ⁷⁷ J. Wang, J. B. Neaton, H. Zheng, V. Nagarajan, S. B. Ogale, B. Liu, D. Viehland, V. Vaithyanathan, D. G. Schlom, U. V. Waghmare, N. A. Spaldin, K. M. Rabe, M. Wuttig, and R. Ramesh, “Epitaxial BiFeO₃ Multiferroic Thin Film Heterostructures,” Science, vol. 299, no. 5613, pp. 1719–1722, 2003.

- ⁷⁸ D. Sando, A. Agbelele, D. Rahmedov, J. Liu, P. Rovillain, C. Toulouse, I. C. Infante, A. P. Pyatakov, S. Fusil, E. Jacquet, C. Carrétéro, C. Deranlot, S. Lisenkov, D. Wang, J.-M. L. Breton, M. Cazayous, A. Sacuto, J. Juraszek, A. K. Zvezdin, L. Bellaiche, B. Dkhil, A. Barthélémy, and M. Bibes, “Crafting the magnonic and spintronic response of BiFeO₃ films by epitaxial strain,” Nature Materials, vol. 12, no. 7, pp. 641–646, 2013.
- ⁷⁹ R. Mazumder, P. S. Devi, D. Bhattacharya, P. Choudhury, A. Sen, and M. Raja, “Ferromagnetism in nanoscale BiFeO₃,” Applied Physics Letters, vol. 91, no. 6, p. 062510, 2007.
- ⁸⁰ G. Concas, G. Spano, C. Cannas, A. Musinu, D. Peddis, and G. Piccaluga, “Inversion degree and saturation magnetization of different nanocrystalline cobalt ferrites,” Journal of Magnetism and Magnetic Materials, vol. 321, no. 12, pp. 1893–1897, 2009.
- ⁸¹ S. E. Shirsath, X. Liu, Y. Yasukawa, S. Li, and A. Morisako, “Switching of magnetic easy-axis using crystal orientation for large perpendicular coercivity in CoFe₂O₄ thin film,” Scientific Reports, vol. 6, no. 1, 2016.
- ⁸² S. J. Kim, S. W. Lee, and C. S. Kim, “Mössbauer Studies on Exchange Interactions in CoFe₂O₄,” Japanese Journal of Applied Physics, vol. 40, no. Part 1, No. 8, pp. 4897–4902, 2001.
- ⁸³ É. du Trémolet de Lacheisserie, D. Gignoux, and M. Schlenker, eds., Magnetism. Springer New York, 2005.
- ⁸⁴ Y. Cedeño-Mattei and O. Perales-Pérez, “Synthesis of high-coercivity cobalt ferrite nanocrystals,” Microelectronics Journal, vol. 40, no. 4-5, pp. 673–676, 2009.
- ⁸⁵ G. A. Sawatzky, F. van der Woude, and A. H. Morrish, “Mössbauer Study of Several Ferromagnetic Spinel,” Physical Review, vol. 187, no. 2, pp. 747–757, 1969.
- ⁸⁶ C. M. Srivastava, G. Srinivasan, and N. G. Nanadikar, “Exchange constants in spinel ferrites,” Physical Review B, vol. 19, no. 1, pp. 499–508, 1979.
- ⁸⁷ R. M. Bozorth, E. F. Tilden, and A. J. Williams, “Anisotropy and Magnetostriction of Some Ferrites,” Physical Review, vol. 99, no. 6, pp. 1788–1798, 1955.
- ⁸⁸ M. El-Okr, M. Salem, M. Salim, R. El-Okr, M. Ashoush, and H. Talaat, “Synthesis of cobalt ferrite nano-particles and their magnetic characterization,” Journal of Magnetism and Magnetic Materials, vol. 323, no. 7, pp. 920–926, 2011.
- ⁸⁹ A. López-Ortega, E. Lottini, C. J. Fernández, and C. Sangregorio, “Exploring the Magnetic Properties of Cobalt-Ferrite Nanoparticles for the Development of a Rare-Earth-Free Permanent Magnet,” Chemistry of Materials, vol. 27, no. 11, pp. 4048–4056, 2015.

- ⁹⁰ K. Maaz, A. Mumtaz, S. K. Hasanain, and A. Ceylan, “Synthesis and magnetic properties of cobalt ferrite (CoFe_2O_4) nanoparticles prepared by wet chemical route,” Journal of Magnetism and Magnetic Materials, vol. 308, no. 2, pp. 289–295, 2007.
- ⁹¹ O. E. Mattiat, ed., Ultrasonic Transducer Materials. Springer US, 1971.
- ⁹² N. Domracheva, M. Caporali, and E. Rentschler, eds., Novel Magnetic Nanostructures. Elsevier Science & Technology, 2018.
- ⁹³ H. F. Kay and P. Vousden, “XCV. Symmetry changes in barium titanate at low temperatures and their relation to its ferroelectric properties,” The London, Edinburgh, and Dublin Philosophical Magazine and Journal of Science, vol. 40, no. 309, pp. 1019–1040, 1949.
- ⁹⁴ M. Naveed-Ul-Haq, V. V. Shvartsman, S. Salamon, H. Wende, H. Trivedi, A. Mumtaz, and D. C. Lupascu, “A new $(\text{Ba,Ca})(\text{Ti,Zr})\text{O}_3$ based multiferroic composite with large magnetoelectric effect,” Scientific Reports, vol. 6, no. 1, p. 32164, 2016.
- ⁹⁵ R. A. Islam and S. Priya, “Effect of piezoelectric grain size on magnetoelectric coefficient of $\text{Pb}(\text{Zr}_{0.52}\text{Ti}_{0.48})\text{O}_3\text{-Ni}_{0.8}\text{Zn}_{0.2}\text{Fe}_2\text{O}_4$ particulate composites,” Journal of Materials Science, vol. 43, no. 10, pp. 3560–3568, 2008.
- ⁹⁶ J. Ryu, S. Priya, K. Uchino, and H.-E. Kim, “Magnetoelectric Effect in Composites of Magnetostrictive and Piezoelectric Materials,” Journal of Electroceramics, vol. 8, no. 2, pp. 107–119, 2002.
- ⁹⁷ W. Liu and X. Ren, “Large Piezoelectric Effect in Pb-Free Ceramics,” Physical Review Letters, vol. 103, no. 25, 2009.
- ⁹⁸ W. Wang, L. D. Wang, W. L. Li, D. Xu, Y. F. Hou, W. P. Cao, Y. Feng, and W. D. Fei, “Piezoelectric properties of $\text{BaTiO}_3\text{-CaTiO}_3\text{-BaZrO}_3$ ceramics with compositions near the morphotropic phase boundary,” Ceramics International, vol. 40, no. 9, pp. 14907–14912, 2014.
- ⁹⁹ M. Zakhovzheva, L. A. Schmitt, M. Acosta, W. Jo, J. Rödel, and H.-J. Kleebe, “In situ electric field induced domain evolution in $\text{Ba}(\text{Zr}_{0.2}\text{Ti}_{0.8})\text{O}_3\text{-}0.3(\text{Ba}_{0.7}\text{Ca}_{0.3})\text{TiO}_3$ ferroelectrics,” Applied Physics Letters, vol. 105, no. 11, p. 112904, 2014.
- ¹⁰⁰ Z. Feng, J. Luo, W. Zhang, X. Tang, Z. Cheng, D. Shi, and S. Dou, “Enhanced piezoelectric properties of solution-modified $\text{Ba}(\text{Zr}_{0.2}\text{Ti}_{0.8})\text{O}_3\text{-(Ba}_{0.7}\text{Ca}_{0.3})\text{TiO}_3$ thick films,” Journal of Alloys and Compounds, vol. 632, pp. 651–654, 2015.
- ¹⁰¹ D. R. J. Brandt, M. Acosta, J. Koruza, and K. G. Webber, “Mechanical constitutive behavior and exceptional blocking force of lead-free BZT-xBCT piezoceramics,” Journal of Applied Physics, vol. 115, no. 20, p. 204107, 2014.

- ¹⁰² M. Acosta, N. Novak, W. Jo, and J. Rödel, “Relationship between electromechanical properties and phase diagram in the $\text{Ba}(\text{Zr}_{0.2}\text{Ti}_{0.8})\text{O}_3 - x(\text{Ba}_{0.7}\text{Ca}_{0.3})\text{TiO}_3$ lead-free piezoceramic,” *Acta Materialia*, vol. 80, pp. 48–55, 2014.
- ¹⁰³ J. Ravez, C. Broustera, and A. Simon, “Lead-free ferroelectric relaxor ceramics in the $\text{BaTiO}_3\text{-BaZrO}_3\text{-CaTiO}_3$ system,” *Journal of Materials Chemistry*, vol. 9, no. 7, pp. 1609–1613, 1999.
- ¹⁰⁴ D. Damjanovic, A. Biancoli, L. A. Vahabzadeh, and J. Trodahl, “Elastic, dielectric, and piezoelectric anomalies and raman spectroscopy of $0.5\text{Ba}(\text{Ti}_{0.8}\text{Zr}_{0.2})\text{O}_3\text{-}0.5(\text{Ba}_{0.7}\text{Ca}_{0.3})\text{TiO}_3$,” *Applied Physics Letters*, vol. 100, no. 19, p. 192907, 2012.
- ¹⁰⁵ D. Berlincourt and H. Jaffe, “Elastic and Piezoelectric Coefficients of Single-Crystal Barium Titanate,” *Physical Review*, vol. 111, no. 1, pp. 143–148, 1958.
- ¹⁰⁶ J. Gao, D. Xue, W. Liu, C. Zhou, and X. Ren, “Recent progress on BaTiO_3 -based piezoelectric ceramics for actuator applications,” *Actuators*, vol. 6, no. 3, p. 24, 2017.
- ¹⁰⁷ Y. K. Choi, T. Hoshina, H. Takeda, and T. Tsurumi, “Effects of Ca and Zr additions and stoichiometry on the electrical properties of barium titanate-based ceramics,” *Journal of the Ceramic Society of Japan*, vol. 118, no. 1382, pp. 881–886, 2010.
- ¹⁰⁸ V. M. Goldschmidt, “Die Gesetze der Krystallochemie,” *Die Naturwissenschaften*, vol. 14, no. 21, pp. 477–485, 1926.
- ¹⁰⁹ F. Cordero, F. Craciun, M. Dinescu, N. Scarisoreanu, C. Galassi, W. Schranz, and V. Soprunyuk, “Elastic response of $(1-x)\text{Ba}(\text{Ti}_{0.8}\text{Zr}_{0.2})\text{O}_3\text{-}x(\text{Ba}_{0.7}\text{Ca}_{0.3})\text{TiO}_3$ ($x=0.45\text{-}0.55$) and the role of the intermediate orthorhombic phase in enhancing the piezoelectric coupling,” *Applied Physics Letters*, vol. 105, no. 23, p. 232904, 2014.
- ¹¹⁰ K. Fujita and Y. Ishibashi, “Phase Diagrams in Successive Phase Transitions in Ferroelectrics with Perovskite-type Structure: Cases of the First Order Transitions from the Cubic Phase,” *Japanese Journal of Applied Physics*, vol. 36, no. Part 1, No. 8, pp. 5214–5218, 1997.
- ¹¹¹ G. A. Rossetti, A. G. Khachatryan, G. Akcay, and Y. Ni, “Ferroelectric solid solutions with morphotropic boundaries: Vanishing polarization anisotropy, adaptive, polar glass, and two-phase states,” *Journal of Applied Physics*, vol. 103, no. 11, p. 114113, 2008.
- ¹¹² B. Noheda, D. E. Cox, G. Shirane, R. Guo, B. Jones, and L. E. Cross, “Stability of the monoclinic phase in the ferroelectric perovskite $\text{PbZr}_{1-x}\text{Ti}_x\text{O}_3$,” *Physical Review B*, vol. 63, no. 1, 2000.
- ¹¹³ M. Ahart, M. Somayazulu, R. E. Cohen, P. Ganesh, P. Dera, H.-K. Mao, R. J. Hemley, Y. Ren, P. Liermann, and Z. Wu, “Origin of morphotropic phase boundaries in ferroelectrics,” *Nature*, vol. 451, no. 7178, pp. 545–548, 2008.

- ¹¹⁴ F. Cordero, F. Craciun, and C. Galassi, “Low-Temperature Phase Transformations of $\text{PbZr}_{1-x}\text{Ti}_x\text{O}_3$ in the Morphotropic Phase-Boundary Region,” Physical Review Letters, vol. 98, no. 25, 2007.
- ¹¹⁵ F. Cordero, F. Trequattrini, F. Craciun, and C. Galassi, “Octahedral tilting, monoclinic phase and the phase diagram of PZT,” Journal of Physics: Condensed Matter, vol. 23, no. 41, p. 415901, 2011.
- ¹¹⁶ Y. M. Jin, Y. U. Wang, A. G. Khachatryan, J. F. Li, and D. Viehland, “Conformal Miniaturization of Domains with Low Domain-Wall Energy: Monoclinic Ferroelectric States near the Morphotropic Phase Boundaries,” Physical Review Letters, vol. 91, no. 19, 2003.
- ¹¹⁷ A. B. Haugen, J. S. Forrester, D. Damjanovic, B. Li, K. J. Bowman, and J. L. Jones, “Structure and phase transitions in $0.5(\text{Ba}_{0.7}\text{Ca}_{0.3}\text{TiO}_3)$ - $0.5(\text{BaZr}_{0.2}\text{Ti}_{0.8}\text{O}_3)$ from -100°C to 150°C ,” Journal of Applied Physics, vol. 113, no. 1, p. 014103, 2013.
- ¹¹⁸ D. Xue, Y. Zhou, J. Gao, X. Ding, and X. Ren, “A comparison between tetragonal-rhombohedral and tetragonal-orthorhombic phase boundaries on piezoelectricity enhancement,” EPL (Europhysics Letters), vol. 100, no. 1, p. 17010, 2012.
- ¹¹⁹ M. Escobar Castillo, V. V. Shvartsman, D. Gobeljic, Y. Gao, J. Landers, H. Wende, and D. C. Lupascu, “Effect of particle size on ferroelectric and magnetic properties of BiFeO_3 nanopowders,” Nanotechnology, vol. 24, no. 35, p. 355701, 2013.
- ¹²⁰ M. F. Etier, V. V. Shvartsman, F. Stromberg, J. Landers, H. Wende, and D. C. Lupascu, “Synthesis and Magnetic Properties of Cobalt Ferrite Nanoparticles,” MRS Proceedings, vol. 1398, 2012.
- ¹²¹ M. Etier, Y. Gao, V. V. Shvartsman, A. Elsukova, J. Landers, H. Wende, and D. C. Lupascu, “Cobalt Ferrite/Barium Titanate Core/Shell Nanoparticles,” Ferroelectrics, vol. 438, no. 1, pp. 115–122, 2012.
- ¹²² M. Etier, V. V. Shvartsman, Y. Gao, J. Landers, H. Wende, and D. C. Lupascu, “Magnetoelectric Effect in (0–3) CoFe_2O_4 - BaTiO_3 (20/80) Composite Ceramics Prepared by the Organosol Route,” Ferroelectrics, vol. 448, no. 1, pp. 77–85, 2013.
- ¹²³ M. Etier, C. Schmitz-Antoniak, S. Salamon, H. Trivedi, Y. Gao, A. Nazrabi, J. Landers, D. Gautam, M. Winterer, D. Schmitz, H. Wende, V. V. Shvartsman, and D. C. Lupascu, “Magnetoelectric coupling on multiferroic cobalt ferrite–barium titanate ceramic composites with different connectivity schemes,” Acta Materialia, vol. 90, pp. 1–9, 2015.
- ¹²⁴ M. Etier, V. V. Shvartsman, S. Salamon, Y. Gao, H. Wende, and D. C. Lupascu, “The Direct and the Converse Magnetoelectric Effect in Multiferroic Cobalt Ferrite-Barium Titanate

- Ceramic Composites,” Journal of the American Ceramic Society, vol. 99, no. 11, pp. 3623–3631, 2016.
- ¹²⁵ M. Naveed-Ul-Haq, V. V. Shvartsman, G. Constantinescu, H. Trivedi, S. Salamon, J. Landers, H. Wende, and D. C. Lupascu, “Effect of Al³⁺ modification on cobalt ferrite and its impact on the magnetoelectric effect in BCZT–CFO multiferroic composites,” Journal of Materials Science, vol. 52, no. 23, pp. 13402–13413, 2017.
- ¹²⁶ M. Naveed-Ul-Haq, V. V. Shvartsman, H. Trivedi, S. Salamon, S. Webers, H. Wende, U. Hagemann, J. Schröder, and D. C. Lupascu, “Strong converse magnetoelectric effect in (Ba,Ca)(Zr,Ti)O₃ - NiFe₂O₄ multiferroics: A relationship between phase-connectivity and interface coupling,” Acta Materialia, vol. 144, pp. 305–313, 2018.
- ¹²⁷ L. Abelmann, S. Porthun, M. Haast, C. Lodder, A. Moser, M. E. Best, P. J. A. van Schendel, B. Stiefel, H. J. Hug, G. P. Heydon, A. Farley, S. R. Hoon, T. Pfaffelhuber, R. Proksch, and K. Babcock, “Comparing the resolution of magnetic force microscopes using the CAMST reference samples,” Journal of Magnetism and Magnetic Materials, vol. 190, no. 1-2, pp. 135–147, 1998.
- ¹²⁸ L. Belliard, A. Thiaville, S. Lemerle, A. Lagrange, J. Ferré, and J. Miltat, “Investigation of the domain contrast in magnetic force microscopy,” Journal of Applied Physics, vol. 81, no. 8, pp. 3849–3851, 1997.
- ¹²⁹ C. B. Sawyer and C. H. Tower, “Rochelle Salt as a Dielectric,” Physical Review, vol. 35, no. 3, pp. 269–273, 1930.
- ¹³⁰ T. K. Song, Y. W. So, D. J. Kim, J. Y. Jo, and T. W. Noh, “Ferroelectric Switching Dynamics and Pulse-Switching Polarization Measurements,” Integrated Ferroelectrics, vol. 78, no. 1, pp. 191–197, 2006.
- ¹³¹ V. M. Petrov, M. I. Bichurina, and G. Srinivasanb, “Maxwell-Wagner relaxation in magnetoelectric composites,” Technical Physics Letters, vol. 30, no. 4, pp. 341–344, 2004.
- ¹³² S. Hofmann, “Sputter-depth profiling for thin-film analysis,” Philosophical Transactions of the Royal Society A: Mathematical, Physical and Engineering Sciences, vol. 362, no. 1814, pp. 55–75, 2004.
- ¹³³ R. L. Mössbauer, “Kernresonanzfluoreszenz von Gammastrahlung in Ir191,” Zeitschrift für Physik, vol. 151, no. 2, pp. 124–143, 1958.
- ¹³⁴ P. Gütllich, E. Bill, and A. X. Trautwein, Mössbauer Spectroscopy and Transition Metal Chemistry. Springer-Verlag GmbH, 2011.
- ¹³⁵ D. Barb, Grundlagen und Anwendungen der Mössbauerspektroskopie. Akademie-Verlag Berlin und Editura Academiei Bucuresti, 1980.

- ¹³⁶ D. A. Shirley, "Application and Interpretation of Isomer Shifts," Reviews of Modern Physics, vol. 36, no. 1, pp. 339–351, 1964.
- ¹³⁷ T. Petrenko, S. D. George, N. Aliaga-Alcalde, E. Bill, B. Mienert, Y. Xiao, Y. Guo, W. Sturhahn, S. P. Cramer, K. Wieghardt, and F. Neese, "Characterization of a Genuine Iron(V)-Nitrido Species by Nuclear Resonant Vibrational Spectroscopy Coupled to Density Functional Calculations," Journal of the American Chemical Society, vol. 129, no. 36, pp. 11053–11060, 2007.
- ¹³⁸ <http://www.wissel-instruments.de/> (accessed July 2018).
- ¹³⁹ A. Thompson, D. Atwood, E. Gullikson, M. Howells, K.-J. Kim, J. Kirz, J. Kortright, I. Lindau, Y. Liu, P. Pianetta, A. Robinson, J. Scofield, J. Underwood, G. Williams, and H. Winick, eds., X-Ray Data Booklet. Center for X-Ray Optics and Advanced Light Source, 2009.
- ¹⁴⁰ <https://www.uni-due.de/~hm236ap/hoersten/home.html> (accessed July 2018).
- ¹⁴¹ G. Bendt, R. Schiwon, S. Salamon, J. Landers, U. Hagemann, C. Limberg, H. Wende, and S. Schulz, "Molecular Design for Tailoring a Single-Source Precursor for Bismuth Ferrite," Inorganic Chemistry, vol. 55, no. 15, pp. 7542–7549, 2016.
- ¹⁴² R. Doll and M. N bauer, "Experimental Proof of Magnetic Flux Quantization in a Superconducting Ring," Physical Review Letters, vol. 7, no. 2, pp. 51–52, 1961.
- ¹⁴³ J. Bowles, "SQUID Attack!," The IRM Quarterly, vol. 19, no. 1, pp. 1–13, 2009.
- ¹⁴⁴ B. W. Petley, "The ubiquitous SQUID," Contemporary Physics, vol. 21, no. 6, pp. 607–630, 1980.
- ¹⁴⁵ J. Clarke and A. I. Braginski, eds., The SQUID Handbook. Wiley-VCH Verlag GmbH & Co. KGaA, 2004.
- ¹⁴⁶ H. Weinstock, ed., SQUID Sensors: Fundamentals, Fabrication and Applications. Springer Netherlands, 1996.
- ¹⁴⁷ Quantum Design, Magnetic Property Measurement System Hardware Reference Manual, 1999.
- ¹⁴⁸ Quantum Design, Magnetic Property Measurement System AC Option User's Manual, 1999.
- ¹⁴⁹ M. Klo , L. Frentzel-Beyme, S. Salamon, J. Landers, H. Wende, and S. Henke, "Cobalt and zinc imidazolate glasses from low-melting zeolitic imidazolate framework solid solutions," Journal of Materials Chemistry A, (submitted June 2018).

- ¹⁵⁰ J. Landers, L. Roeder, S. Salamon, A. M. Schmidt, and H. Wende, "Particle–Matrix Interaction in Cross-Linked PAAm-Hydrogels Analyzed by Mössbauer Spectroscopy," The Journal of Physical Chemistry C, vol. 119, no. 35, pp. 20642–20648, 2015.
- ¹⁵¹ J. Landers, S. Salamon, H. Remmer, F. Ludwig, and H. Wende, "Simultaneous Study of Brownian and Néel Relaxation Phenomena in Ferrofluids by Mössbauer Spectroscopy," Nano Letters, vol. 16, no. 2, pp. 1150–1155, 2016.
- ¹⁵² M. Iwamoto, "Maxwell–Wagner Effect," in Encyclopedia of Nanotechnology, Springer Netherlands, 2015.
- ¹⁵³ H. Han, J. H. Lee, and H. M. Jang, "Low-Temperature Solid-State Synthesis of High-Purity BiFeO₃ Ceramic for Ferroic Thin-Film Deposition," Inorganic Chemistry, vol. 56, no. 19, pp. 11911–11916, 2017.
- ¹⁵⁴ Y. P. Wang, L. Zhou, M. F. Zhang, X. Y. Chen, J.-M. Liu, and Z. G. Liu, "Room-temperature saturated ferroelectric polarization in BiFeO₃ ceramics synthesized by rapid liquid phase sintering," Applied Physics Letters, vol. 84, no. 10, pp. 1731–1733, 2004.
- ¹⁵⁵ V. Kothai and R. Ranjan, "Synthesis of BiFeO₃ by carbonate precipitation," Bulletin of Materials Science, vol. 35, no. 2, pp. 157–161, 2012.
- ¹⁵⁶ M. Tomczyk, D. G. Stroppa, I. M. Reaney, and P. M. Vilarinho, "Growth of BiFeO₃ thin films by chemical solution deposition: the role of electrodes," Physical Chemistry Chemical Physics, vol. 19, no. 22, pp. 14337–14344, 2017.
- ¹⁵⁷ V. F. Freitas, H. L. C. Grande, S. N. de Medeiros, I. A. Santos, L. F. Cótica, and A. A. Coelho, "Structural, microstructural and magnetic investigations in high-energy ball milled BiFeO₃ and Bi_{0.95}Eu_{0.05}FeO₃ powders," Journal of Alloys and Compounds, vol. 461, no. 1-2, pp. 48–52, 2008.
- ¹⁵⁸ C. L. Fu, M. Huo, W. Cai, and X. L. Deng, "Bismuth Ferrite Nanopowders Prepared by Sol-Gel," Advanced Materials Research, vol. 412, pp. 142–145, 2011.
- ¹⁵⁹ T. P. Comyn, D. F. Kanguwe, J. He, and A. P. Brown, "Synthesis of bismuth ferrite lead titanate nano-powders and ceramics using chemical co-precipitation," Journal of the European Ceramic Society, vol. 28, no. 11, pp. 2233–2238, 2008.
- ¹⁶⁰ K. Jiang, J. J. Zhu, J. D. Wu, J. Sun, Z. G. Hu, and J. H. Chu, "Influences of Oxygen Pressure on Optical Properties and Interband Electronic Transitions in Multiferroic Bismuth Ferrite Nanocrystalline Films Grown by Pulsed Laser Deposition," ACS Applied Materials & Interfaces, vol. 3, no. 12, pp. 4844–4852, 2011.

- ¹⁶¹ K. Ahadi, S. M. Mahdavi, A. Nemati, and M. Kianinia, “Photoconductivity and diode effect in Bi rich multiferroic BiFeO₃ thin films grown by pulsed-laser deposition,” Journal of Materials Science: Materials in Electronics, vol. 22, no. 7, pp. 815–820, 2010.
- ¹⁶² M. P. Pechini, “Method of Preparing Lead and Alkaline Earth Titanates and Niobates and Coating Method Using the Same to Form a Capacitor,” 1963. U.S. Patent No. US3330697A.
- ¹⁶³ S. Ghosh, S. Dasgupta, A. Sen, and H. S. Maiti, “Low-Temperature Synthesis of Nanosized Bismuth Ferrite by Soft Chemical Route,” Journal of the American Ceramic Society, vol. 88, pp. 1349–1352, may 2005.
- ¹⁶⁴ E. A. V. Ferri, I. A. Santos, E. Radovanovic, R. Bonzanini, and E. M. Giroto, “Chemical characterization of BiFeO₃ obtained by Pechini method,” Journal of the Brazilian Chemical Society, vol. 19, no. 6, pp. 1153–1157, 2008.
- ¹⁶⁵ Y. Zhang, Z. Yang, D. Yin, Y. Liu, C. L. Fei, R. Xiong, J. Shi, and G. L. Yan, “Composition and magnetic properties of cobalt ferrite nano-particles prepared by the co-precipitation method,” Journal of Magnetism and Magnetic Materials, vol. 322, no. 21, pp. 3470–3475, 2010.
- ¹⁶⁶ C. Vázquez-Vázquez, M. A. López-Quintela, M. C. Buján-Núñez, and J. Rivas, “Finite size and surface effects on the magnetic properties of cobalt ferrite nanoparticles,” Journal of Nanoparticle Research, vol. 13, no. 4, pp. 1663–1676, 2010.
- ¹⁶⁷ P. Didukh, J. M. Greneche, A. Ślawska-Waniewska, P. C. Fannin, and L. Casas, “Surface effects in CoFe₂O₄ magnetic fluids studied by Mössbauer spectrometry,” Journal of Magnetism and Magnetic Materials, vol. 242-245, pp. 613–616, 2002.
- ¹⁶⁸ F. Li, J. Liu, D. G. Evans, and X. Duan, “Stoichiometric Synthesis of Pure MFe₂O₄ (M = Mg, Co, and Ni) Spinel Ferrites from Tailored Layered Double Hydroxide (Hydrotalcite-Like) Precursors,” Chemistry of Materials, vol. 16, no. 8, pp. 1597–1602, 2004.
- ¹⁶⁹ P. N. Anantharamaiah and P. A. Joy, “Magnetic and magnetostrictive properties of aluminium substituted cobalt ferrite synthesized by citrate-gel method,” Journal of Materials Science, vol. 50, no. 19, pp. 6510–6517, 2015.
- ¹⁷⁰ M. H. Frey and D. A. Payne, “Grain-size effect on structure and phase transformations for barium titanate,” Physical Review B, vol. 54, no. 5, pp. 3158–3168, 1996.
- ¹⁷¹ M. T. Buscaglia, V. Buscaglia, M. Viviani, J. Petzelt, M. Savinov, L. Mitoseriu, A. Testino, P. Nanni, C. Harnagea, Z. Zhao, and M. Nygren, “Ferroelectric properties of dense nanocrystalline BaTiO₃ ceramics,” Nanotechnology, vol. 15, no. 9, pp. 1113–1117, 2004.

- ¹⁷² X. Deng, X. Wang, H. Wen, L. Chen, L. Chen, and L. Li, “Ferroelectric properties of nanocrystalline barium titanate ceramics,” Applied Physics Letters, vol. 88, no. 25, p. 252905, 2006.
- ¹⁷³ D. Ghosh, H. Han, J. C. Nino, G. Subhash, and J. L. Jones, “Synthesis of BaTiO₃-20wt%CoFe₂O₄ Nanocomposites via Spark Plasma Sintering,” Journal of the American Ceramic Society, vol. 95, no. 8, pp. 2504–2509, 2012.
- ¹⁷⁴ F. D. Ma, Y. M. Jin, Y. U. Wang, S. L. Kampe, and S. Dong, “Phase field modeling and simulation of particulate magnetoelectric composites: Effects of connectivity, conductivity, poling and bias field,” Acta Materialia, vol. 70, pp. 45–55, 2014.
- ¹⁷⁵ A. Hanumaiah, T. Bhimasankaram, S. V. Suryanarayana, and G. S. Kumar, “Dielectric behaviour and magnetoelectric effect in cobalt ferrite-barium titanate composites,” Bulletin of Materials Science, vol. 17, no. 4, pp. 405–409, 1994.
- ¹⁷⁶ M. K. Singh, R. S. Katiyar, W. P., and J. F. Scott, “The Almeida–Thouless line in BiFeO₃: is bismuth ferrite a mean field spin glass?,” Journal of Physics: Condensed Matter, vol. 21, no. 4, p. 042202, 2008.
- ¹⁷⁷ M. K. Singh, W. Prellier, M. P. Singh, R. S. Katiyar, and J. F. Scott, “Spin-glass transition in single-crystal BiFeO₃,” Physical Review B, vol. 77, no. 14, 2008.
- ¹⁷⁸ R. Jarrier, X. Marti, J. Herrero-Albillos, P. Ferrer, R. Haumont, P. Gemeiner, G. Geneste, P. Berthet, T. Schüllli, P. Cevc, R. Blinc, S. S. Wong, T.-J. Park, M. Alexe, M. A. Carpenter, J. F. Scott, G. Catalan, and B. Dkhil, “Surface phase transitions in BiFeO₃ below room temperature,” Physical Review B, vol. 85, no. 18, 2012.
- ¹⁷⁹ S. A. T. Redfern, C. Wang, J. W. Hong, G. Catalan, and J. F. Scott, “Elastic and electrical anomalies at low-temperature phase transitions in BiFeO₃,” Journal of Physics: Condensed Matter, vol. 20, no. 45, p. 452205, 2008.
- ¹⁸⁰ S. Bedanta and W. Kleemann, “Supermagnetism,” Journal of Physics D: Applied Physics, vol. 42, no. 1, p. 013001, 2008.
- ¹⁸¹ B. Martínez, X. Obradors, L. Balcells, A. Rouanet, and C. Monty, “Low Temperature Surface Spin-Glass Transition in γ -Fe₂O₃ Nanoparticles,” Physical Review Letters, vol. 80, no. 1, pp. 181–184, 1998.
- ¹⁸² V. V. Shvartsman, W. Kleemann, R. Haumont, and J. Kreisel, “Large bulk polarization and regular domain structure in ceramic BiFeO₃,” Applied Physics Letters, vol. 90, no. 17, p. 172115, 2007.

- ¹⁸³ V. R. Palkar, J. John, and R. Pinto, "Observation of saturated polarization and dielectric anomaly in magnetoelectric BiFeO₃ thin films," Applied Physics Letters, vol. 80, no. 9, pp. 1628–1630, 2002.
- ¹⁸⁴ R. Haumont, J. Kreisel, P. Bouvier, and F. Hippert, "Phonon anomalies and the ferroelectric phase transition in multiferroic BiFeO₃," Physical Review B, vol. 73, no. 13, 2006.
- ¹⁸⁵ Q. A. Pankhurst and R. J. Pollard, "Mössbauer spectra of antiferromagnetic powders in applied fields," Journal of Physics: Condensed Matter, vol. 2, no. 35, pp. 7329–7337, 1990.
- ¹⁸⁶ L. Billard and A. Chamberod, "On the dissymmetry of Mössbauer spectra in iron-nickel alloys," Solid State Communications, vol. 17, no. 2, pp. 113–118, 1975.
- ¹⁸⁷ S. Salamon, "Mössbauerspektroskopie an multiferroischen BiFeO₃ Nanopartikeln," Master's thesis, Universität Duisburg-Essen, 2013.
- ¹⁸⁸ A. V. Zalesskiĭ, A. K. Zvezdin, A. A. Frolov, and A. A. Bush, "⁵⁷Fe NMR study of a spatially modulated magnetic structure in BiFeO₃," Journal of Experimental and Theoretical Physics Letters, vol. 71, no. 11, pp. 465–468, 2000.
- ¹⁸⁹ A. V. Zalesskiĭ, A. A. Frolov, T. A. Khimich, A. A. Bush, V. S. Pokatilov, and A. K. Zvezdin, "⁵⁷Fe NMR study of spin-modulated magnetic structure in BiFeO₃," Europhysics Letters, vol. 50, no. 4, pp. 547–551, 2000.
- ¹⁹⁰ V. S. Pokatilov, A. S. Sigov, and A. O. Konovalova, "NMR and Mössbauer study of multiferroic BiFeO₃," Bulletin of the Russian Academy of Sciences: Physics, vol. 74, no. 3, pp. 347–351, 2010.
- ¹⁹¹ A. A. Bush, A. A. Gippius, A. V. Zalesskiĭ, and E. N. Morozova, "²⁰⁹Bi NMR spectrum of BiFeO₃ in the presence of spatial modulation of hyperfine fields," Journal of Experimental and Theoretical Physics Letters, vol. 78, no. 6, pp. 389–392, 2003.
- ¹⁹² V. Rusakov, V. Pokatilov, A. Sigov, M. Matsnev, and T. Gubaidulina, "⁵⁷Fe Mössbauer Study of Spatial Spin-Modulated Structure in BiFeO₃," Journal of Materials Science and Engineering B, vol. 4, no. 10, 2014.
- ¹⁹³ A. Palewicz, T. Szumiata, R. Przeniosło, I. Sosnowska, and I. Margiolaki, "Search for new modulations in the BiFeO₃ structure: SR diffraction and Mössbauer studies," Solid State Communications, vol. 140, no. 7-8, pp. 359–363, 2006.
- ¹⁹⁴ J. F. Scott, M. K. Singh, and R. S. Katiyar, "Critical phenomena at the 140 and 200 K magnetic phase transitions in BiFeO₃," Journal of Physics: Condensed Matter, vol. 20, no. 32, p. 322203, 2008.

- ¹⁹⁵ M. Ramazanoglu, W. Ratcliff, Y. J. Choi, S. Lee, S.-W. Cheong, and V. Kiryukhin, "Temperature-dependent properties of the magnetic order in single-crystal BiFeO₃," Physical Review B, vol. 83, no. 17, 2011.
- ¹⁹⁶ H. I. Hsiang and F.-S. Yen, "Effect of Crystallite Size on the Ferroelectric Domain Growth of Ultrafine BaTiO₃ Powders," Journal of the American Ceramic Society, vol. 79, no. 4, pp. 1053–1060, 1996.
- ¹⁹⁷ A. Y. Kudzin, "Electrical conductivity of barium titanate," Soviet Physics Journal, vol. 10, no. 7, pp. 79–80, 1967.
- ¹⁹⁸ K. V. P. M. Shafi, A. Gedanken, R. Prozorov, and J. Balogh, "Sonochemical Preparation and Size-Dependent Properties of Nanostructured CoFe₂O₄ Particles," Chemistry of Materials, vol. 10, no. 11, pp. 3445–3450, 1998.
- ¹⁹⁹ B. Y. Wang, H. T. Wang, S. B. Singh, Y. C. Shao, Y. F. Wang, C. H. Chuang, P. H. Yeh, J. W. Chiou, C. W. Pao, H. M. Tsai, H. J. Lin, J. F. Lee, C. Y. Tsai, W. F. Hsieh, M.-H. Tsai, and W. F. Pong, "Effect of geometry on the magnetic properties of CoFe₂O₄–PbTiO₃ multiferroic composites," RSC Advances, vol. 3, no. 21, p. 7884, 2013.
- ²⁰⁰ D. Carta, M. F. Casula, A. Falqui, D. Loche, G. Mountjoy, C. Sangregorio, and A. Corrias, "A Structural and Magnetic Investigation of the Inversion Degree in Ferrite Nanocrystals MFe₂O₄ (M = Mn, Co, Ni)," The Journal of Physical Chemistry C, vol. 113, no. 20, pp. 8606–8615, 2009.
- ²⁰¹ G. A. Sawatzky, F. van der Woude, and A. H. Morrish, "Cation Distributions in Octahedral and Tetrahedral Sites of the Ferrimagnetic Spinel CoFe₂O₄," Journal of Applied Physics, vol. 39, no. 2, pp. 1204–1205, 1968.
- ²⁰² D. T. Margulies, F. T. Parker, M. L. Rudee, F. E. Spada, J. N. Chapman, P. R. Aitchison, and A. E. Berkowitz, "Origin of the Anomalous Magnetic Behavior in Single Crystal Fe₃O₄ Films," Physical Review Letters, vol. 79, no. 25, pp. 5162–5165, 1997.
- ²⁰³ W. J. Merz, "The Electric and Optical Behavior of BaTiO₃ Single-Domain Crystals," Physical Review, vol. 76, no. 8, pp. 1221–1225, 1949.
- ²⁰⁴ I. C. Nlebedim, J. E. Snyder, A. J. Moses, and D. C. Jiles, "Dependence of the magnetic and magnetoelastic properties of cobalt ferrite on processing parameters," Journal of Magnetism and Magnetic Materials, vol. 322, no. 24, pp. 3938–3942, 2010.
- ²⁰⁵ F. G. Brockman, P. W. Beck, and W. G. Steneck, "Magnetostrictive Ferrites with Small Change in Coupling Coefficient from 0 ° to 20 °C," Journal of the American Ceramic Society, vol. 46, no. 4, pp. 167–170, 1963.

- ²⁰⁶ S. Agarwal, O. F. Caltun, and K. Sreenivas, "Magneto electric effects in BaTiO₃-CoFe₂O₄ bulk composites," Solid State Communications, vol. 152, no. 21, pp. 1951-1955, 2012.
- ²⁰⁷ Y. S. Koo, K. M. Song, N. Hur, J. H. Jung, T.-H. Jang, H. J. Lee, T. Y. Koo, Y. H. Jeong, J. H. Cho, and Y. H. Jo, "Strain-induced magnetoelectric coupling in BaTiO₃/Fe₃O₄ core/shell nanoparticles," Applied Physics Letters, vol. 94, no. 3, p. 032903, 2009.
- ²⁰⁸ L. P. Curecheriu, M. T. Buscaglia, V. Buscaglia, L. Mitoseriu, P. Postolache, A. Ianculescu, and P. Nanni, "Functional properties of BaTiO₃-Ni_{0.5}Zn_{0.5}Fe₂O₄ magnetoelectric ceramics prepared from powders with core-shell structure," Journal of Applied Physics, vol. 107, no. 10, p. 104106, 2010.
- ²⁰⁹ V. Corral-Flores, D. Bueno-Baqués, and R. Ziolo, "Synthesis and characterization of novel CoFe₂O₄-BaTiO₃ multiferroic core-shell-type nanostructures," Acta Materialia, vol. 58, no. 3, pp. 764-769, 2010.
- ²¹⁰ V. L. Mathe, A. D. Sheikh, and G. Srinivasan, "Magnetoelectric properties of particulate and bi-layer PMN-PT/CoFe₂O₄ composites," Journal of Magnetism and Magnetic Materials, vol. 324, no. 5, pp. 695-703, 2012.
- ²¹¹ W. R. Tinga, W. A. G. Voss, and D. F. Blossey, "Generalized approach to multiphase dielectric mixture theory," Journal of Applied Physics, vol. 44, no. 9, pp. 3897-3902, 1973.
- ²¹² X. Qi, J. Zhou, B. Li, Y. Zhang, Z. Yue, Z. Gui, and L. Li, "Preparation and Spontaneous Polarization-Magnetization of a New Ceramic Ferroelectric-Ferromagnetic Composite," Journal of the American Ceramic Society, vol. 87, no. 10, pp. 1848-1852, 2005.
- ²¹³ J. V. Mantese, A. L. Micheli, D. F. Dungan, R. G. Geyer, J. Baker-Jarvis, and J. Grosvenor, "Applicability of effective medium theory to ferroelectric/ferrimagnetic composites with composition and frequency-dependent complex permittivities and permeabilities," Journal of Applied Physics, vol. 79, no. 3, pp. 1655-1660, 1996.
- ²¹⁴ G. V. Duong, R. S. Turtelli, and R. Groessinger, "Magnetoelectric properties of CoFe₂O₄-BaTiO₃ core-shell structure composite studied by a magnetic pulse method," Journal of Magnetism and Magnetic Materials, vol. 322, no. 9-12, pp. 1581-1584, 2010.
- ²¹⁵ D.-X. Chen, E. Pardo, and A. Sanchez, "Fluxmetric and magnetometric demagnetizing factors for cylinders," Journal of Magnetism and Magnetic Materials, vol. 306, no. 1, pp. 135-146, 2006.
- ²¹⁶ L. Hrib and O. Caltun, "Effects of the chemical composition of the magnetostrictive phase on the dielectric and magnetoelectric properties of cobalt ferrite-barium titanate composites," Journal of Alloys and Compounds, vol. 509, no. 23, pp. 6644-6648, 2011.

- ²¹⁷ M. Acosta, N. Khakpash, T. Someya, N. Novak, W. Jo, H. Nagata, G. A. Rossetti, and J. Rödel, “Origin of the large piezoelectric activity in $(1-x)\text{Ba}(\text{Zr}_{0.2}\text{Ti}_{0.8})\text{O}_{3-x}(\text{Ba}_{0.7}\text{Ca}_{0.3})\text{TiO}_3$ ceramics,” Physical Review B, vol. 91, no. 10, 2015.
- ²¹⁸ Y. J. Li, X. M. Chen, R. Z. Hou, and Y. H. Tang, “Maxwell–Wagner characterization of dielectric relaxation in $\text{Ni}_{0.8}\text{Zn}_{0.2}\text{Fe}_2\text{O}_4/\text{Sr}_{0.5}\text{Ba}_{0.5}\text{Nb}_2\text{O}_6$ composite,” Solid State Communications, vol. 137, no. 3, pp. 120–125, 2006.
- ²¹⁹ H. Yang, H. Wang, L. He, L. Shui, and X. Yao, “Polarization relaxation mechanism of $\text{Ba}_{0.6}\text{Sr}_{0.4}\text{TiO}_3/\text{Ni}_{0.8}\text{Zn}_{0.2}\text{Fe}_2\text{O}_4$ composite with giant dielectric constant and high permeability,” Journal of Applied Physics, vol. 108, no. 7, p. 074105, 2010.
- ²²⁰ H.-F. Zhang, S. W. Or, and H. L. W. Chan, “Electrical, magnetic, and magnetoelectric characterization of fine-grained $\text{Pb}(\text{Zr}_{0.53}\text{Ti}_{0.47})\text{O}_3-(\text{Ni}_{0.5}\text{Zn}_{0.5})\text{Fe}_2\text{O}_4$ composite ceramics,” Journal of Alloys and Compounds, vol. 509, no. 21, pp. 6311–6316, 2011.
- ²²¹ Z. Yu and C. Ang, “Maxwell–Wagner polarization in ceramic composites $\text{BaTiO}_3-(\text{Ni}_{0.3}\text{Zn}_{0.7})\text{Fe}_{2.1}\text{O}_4$,” Journal of Applied Physics, vol. 91, no. 2, pp. 794–797, 2002.
- ²²² H. J. van Hook, “Oxygen Stoichiometry in the Compound BaFeO_{3-x} ,” The Journal of Physical Chemistry, vol. 68, no. 12, pp. 3786–3789, 1964.
- ²²³ S. Mori, “Phase Transformation in Barium Orthoferrate, BaFeO_{3-x} ,” Journal of the American Ceramic Society, vol. 49, no. 11, pp. 600–605, 1966.
- ²²⁴ W. W. Malinofsky and H. Kedesdy, “Barium Iron Oxide Isomorphs of Hexagonal and Tetragonal BaTiO_3 ,” Journal of the American Chemical Society, vol. 76, no. 11, pp. 3090–3091, 1954.
- ²²⁵ S. Mori, “Magnetic Properties of Several Phases of Barium Orthoferrate, BaFeO_x ,” Journal of the Physical Society of Japan, vol. 28, no. 1, pp. 44–50, 1970.
- ²²⁶ J. Li, H. Zhang, Y. Liu, Y. Liao, G. Ma, and H. Yang, “Co–Ti co-substitution of M-type hexagonal barium ferrite,” Materials Research Express, vol. 2, no. 4, p. 046104, 2015.
- ²²⁷ R.-F. Zhang, C.-Y. Deng, L. Ren, Z. Li, and J.-P. Zhou, “Ferroelectric, Ferromagnetic, and Magnetoelectric Properties of Multiferroic $\text{Ni}_{0.5}\text{Zn}_{0.5}\text{Fe}_2\text{O}_4\text{–BaTiO}_3$ Composite Ceramics,” Journal of Electronic Materials, vol. 43, no. 4, pp. 1043–1047, 2014.
- ²²⁸ X. L. Zhong, J. B. Wang, M. Liao, G. J. Huang, S. H. Xie, Y. C. Zhou, Y. Qiao, and J. P. He, “Multiferroic nanoparticulate $\text{Bi}_{3.15}\text{Nd}_{0.85}\text{Ti}_3\text{O}_{12}\text{–CoFe}_2\text{O}_4$ composite thin films prepared by a chemical solution deposition technique,” Applied Physics Letters, vol. 90, no. 15, p. 152903, 2007.

- ²²⁹ L. Wu, B. Shen, and S. Sun, "Synthesis and assembly of barium-doped iron oxide nanoparticles and nanomagnets," Nanoscale, vol. 7, no. 39, pp. 16165–16169, 2015.
- ²³⁰ L. Amarande, C. Miclea, M. Cioangher, I. Pasuk, A. Iuga, and I. Pintilie, "Intrinsic and extrinsic effects near orthorhombic-tetragonal phase transition in barium titanate ceramics doped with small amounts of zirconium," Ceramics International, vol. 43, no. 6, pp. 4919–4925, 2017.
- ²³¹ H. Sussman and S. L. Ehrlich, "Evaluation of the Magnetostrictive Properties of Hiperco," The Journal of the Acoustical Society of America, vol. 22, no. 4, pp. 499–506, 1950.
- ²³² G. Srinivasan, E. T. Rasmussen, B. J. Levin, and R. Hayes, "Magnetoelectric effects in bilayers and multilayers of magnetostrictive and piezoelectric perovskite oxides," Physical Review B, vol. 65, no. 13, 2002.
- ²³³ V. M. Laletin, N. Paddubnaya, G. Srinivasan, C. P. D. Vreugd, M. I. Bichurin, V. M. Petrov, and D. A. Filippov, "Frequency and field dependence of magnetoelectric interactions in layered ferromagnetic transition metal-piezoelectric lead zirconate titanate," Applied Physics Letters, vol. 87, no. 22, p. 222507, 2005.
- ²³⁴ I. Chopra and J. Sirohi, Smart Structures Theory. Cambridge University Press, 2009.
- ²³⁵ G. Nabiyouni, M. Jafari Fesharaki, M. Mozafari, and J. Amighian, "Characterization and Magnetic Properties of Nickel Ferrite Nanoparticles Prepared by Ball Milling Technique," Chinese Physics Letters, vol. 27, no. 12, p. 126401, 2010.
- ²³⁶ A. Goldman, "Ferrites for Entertainment Applications-Radio and TV," in Handbook of Modern Ferromagnetic Materials, p. 32, Springer US, 1999.
- ²³⁷ J.-P. Zhou, H.-C. He, Z. Shi, G. Liu, and C.-W. Nan, "Dielectric, magnetic, and magneto-electric properties of laminated $\text{PbZr}_{0.52}\text{Ti}_{0.48}\text{O}_3/\text{CoFe}_2\text{O}_4$ composite ceramics," Journal of Applied Physics, vol. 100, no. 9, p. 094106, 2006.
- ²³⁸ G. Bordin, A. Cecchetti, G. Cecchi, M. Poppi, and F. Ronconi, "Magnetostrictive hysteresis loop of ferrites in alternating fields," Physica Status Solidi (a), vol. 35, no. 2, pp. K161–K164, 1976.
- ²³⁹ C. M. van der Burgt, "Ferrites for magnetic and piezomagnetic filter elements with temperature-independent permeability and elasticity," Proceedings of the IEE - Part B: Radio and Electronic Engineering, vol. 104, no. 7S, pp. 550–557, 1957.
- ²⁴⁰ J.-L. Mattei and M. le Floc'h, "Percolative behaviour and demagnetizing effects in disordered heterostructures," Journal of Magnetism and Magnetic Materials, vol. 257, no. 2-3, pp. 335–345, 2003.

- ²⁴¹ S. Kumar Upadhyay and V. Raghavendra Reddy, "Study of 0.9BaTiO₃-0.1Ni_xZn_{1-x}Fe₂O₄ magneto-electric composite ceramics," Journal of Applied Physics, vol. 113, no. 11, p. 114107, 2013.
- ²⁴² N. S. Sowmya, A. Srinivas, K. V. G. Reddy, J. P. Praveen, D. Das, S. D. Kumar, V. Subramanian, and S. V. Kamat, "Magnetoelectric coupling studies on (x) (0.5BZT-0.5BCT) – (100-x) NiFe₂O₄ [x=90-70wt%] particulate composite," Ceramics International, vol. 43, no. 2, pp. 2523–2528, 2017.
- ²⁴³ N. S. Sowmya, A. Srinivas, P. Saravanan, K. V. G. Reddy, S. V. Kamat, J. P. Praveen, D. Das, G. Murugesan, S. D. Kumar, and V. Subramanian, "Studies on magnetoelectric coupling in lead-free [(0.5) BCT-(0.5) BZT]-NiFe₂O₄ laminated composites at low and EMR frequencies," Journal of Alloys and Compounds, vol. 743, pp. 240–248, 2018.
- ²⁴⁴ X. Zheng, F. Li, Z. Cheng, and B. Shen, "A Structural, Magnetic and Mössbauer Study of Tb_{0.3}Dy_{0.7}(Fe_{1-x}Al_x)_{1.95} Alloys," Hyperfine Interactions, vol. 142, no. 3/4, pp. 503–511, 2002.
- ²⁴⁵ S.-H. Zhang, J.-P. Zhou, Z. Shi, P. Liu, and C.-Y. Deng, "Enhancing magnetic field sensitivity and giant converse magnetoelectric effect in laminate composite of Terfenol-D and multilayer piezoelectric vibrator," Journal of Alloys and Compounds, vol. 590, pp. 46–49, 2014.
- ²⁴⁶ T. George, A. T. Sunny, and T. Varghese, "Magnetic properties of cobalt ferrite nanoparticles synthesized by sol-gel method," IOP Conference Series: Materials Science and Engineering, vol. 73, p. 012050, 2015.
- ²⁴⁷ A. Franco Jr. and F. C. e Silva, "High temperature magnetic properties of cobalt ferrite nanoparticles," Applied Physics Letters, vol. 96, no. 17, p. 172505, 2010.
- ²⁴⁸ H. Zhang, "A theory for structural phase transitions in BaTiO₃ single crystal and PbZrO₃-xPbTiO₃ solid solution," AIP Advances, vol. 3, no. 4, p. 042118, 2013.
- ²⁴⁹ H. F. Kay, "Preparation and properties of crystals of barium titanate, BaTiO₃," Acta Crystallographica, vol. 1, no. 5, pp. 229–237, 1948.
- ²⁵⁰ A. F. Devonshire, "Theory of ferroelectrics," Advances in Physics, vol. 3, no. 10, pp. 85–130, 1954.
- ²⁵¹ A. Aubert, V. Loyau, Y. Pascal, F. Mazaleyrat, and M. LoBue, "Dynamic Magnetostriction of CoFe₂O₄ and Its Role in Magnetoelectric Composites," Physical Review Applied, vol. 9, no. 4, 2018.

- ²⁵² Y. Chen, B. Kriegermeier-Sutton, J. Snyder, K. Dennis, R. McCallum, and D. Jiles, “Magneto-mechanical effects under torsional strain in iron, cobalt and nickel,” Journal of Magnetism and Magnetic Materials, vol. 236, no. 1-2, pp. 131–138, 2001.
- ²⁵³ B. K. Bammannavar, L. R. Naik, and B. K. Chougule, “Studies on dielectric and magnetic properties of (x) $\text{Ni}_{0.2}\text{Co}_{0.8}\text{Fe}_2\text{O}_4$ + (1-x) barium lead zirconate titanate magnetoelectric composites,” Journal of Applied Physics, vol. 104, no. 6, p. 064123, 2008.
- ²⁵⁴ S. J. Lee, C. C. H. Lo, P. N. Matlage, S. H. Song, Y. Melikhov, J. E. Snyder, and D. C. Jiles, “Magnetic and magnetoelastic properties of Cr-substituted cobalt ferrite,” Journal of Applied Physics, vol. 102, no. 7, p. 073910, 2007.
- ²⁵⁵ J. A. Osborn, “Demagnetizing Factors of the General Ellipsoid,” Physical Review, vol. 67, no. 11-12, pp. 351–357, 1945.
- ²⁵⁶ W. Li, Z. Xu, R. Chu, P. Fu, and G. Zang, “Polymorphic phase transition and piezoelectric properties of $(\text{Ba}_{1-x}\text{Ca}_x)(\text{Ti}_{0.9}\text{Zr}_{0.1})\text{O}_3$ lead-free ceramics,” Physica B: Condensed Matter, vol. 405, no. 21, pp. 4513–4516, 2010.
- ²⁵⁷ X. Wang, L. Zhang, H. Liu, J. Zhai, and X. Yao, “Dielectric nonlinear properties of BaTiO_3 – CaTiO_3 – SrTiO_3 ceramics near the solubility limit,” Materials Chemistry and Physics, vol. 112, no. 2, pp. 675–678, 2008.
- ²⁵⁸ M. M. Selvi, P. Manimuthu, K. S. Kumar, and C. Venkateswaran, “Magnetodielectric properties of CoFe_2O_4 – BaTiO_3 core–shell nanocomposite,” Journal of Magnetism and Magnetic Materials, vol. 369, pp. 155–161, 2014.
- ²⁵⁹ Y. K. Fetisov, K. E. Kamentsev, A. Y. Ostashchenko, and G. Srinivasan, “Wide-band magnetoelectric characterization of a ferrite-piezoelectric multilayer using a pulsed magnetic field,” Solid State Communications, vol. 132, no. 1, pp. 13–17, 2004.
- ²⁶⁰ Y. K. Fetisov, A. A. Bush, K. E. Kamentsev, and G. Srinivasan, “Pyroelectric effects in magnetoelectric multilayer composites,” Solid State Communications, vol. 132, no. 5, pp. 319–324, 2004.
- ²⁶¹ G. Srinivasan, E. T. Rasmussen, J. Gallegos, R. Srinivasan, Y. I. Bokhan, and V. M. Laletin, “Magnetoelectric bilayer and multilayer structures of magnetostrictive and piezoelectric oxides,” Physical Review B, vol. 64, no. 21, 2001.
- ²⁶² H. Zheng, J. Wang, S. E. Lofland, Z. M. L. Mohaddes-Ardabili, T. Zhao, L. Salamanca-Riba, S. R. Shinde, S. B. Ogale, F. Bai, D. Viehland, Y. Jia, D. G. Schlom, M. Wuttig, A. Roytburd, and R. Ramesh, “Multiferroic BaTiO_3 – CoFe_2O_4 Nanostructures,” Science, vol. 303, no. 5658, pp. 661–663, 2004.

- ²⁶³ M. B. Smith, K. Page, T. Siegrist, P. L. Redmond, E. C. Walter, R. Seshadri, L. E. Brus, and M. L. Steigerwald, “Crystal Structure and the Paraelectric-to-Ferroelectric Phase Transition of Nanoscale BaTiO₃,” Journal of the American Chemical Society, vol. 130, no. 22, pp. 6955–6963, 2008.
- ²⁶⁴ D. Damjanovic, N. Klein, J. Li, and V. Porokhonsky, “What can be expected from lead-free piezoelectric materials?,” Functional Materials Letters, vol. 03, no. 01, pp. 5–13, 2010.
- ²⁶⁵ L. D. Landau and E. M. Lifshitz in Electrodynamics of Continuous Media, pp. 86–104, Elsevier, 1984.
- ²⁶⁶ S. Zhang, E. F. Alberta, R. E. Eitel, C. A. Randall, and T. R. Shrout, “Elastic, piezoelectric, and dielectric characterization of modified BiScO₃-PbTiO₃ ceramics,” IEEE Transactions on Ultrasonics, Ferroelectrics and Frequency Control, vol. 52, no. 11, pp. 2131–2139, 2005.
- ²⁶⁷ “IRE Standards on Piezoelectric Crystals: Determination of the Elastic, Piezoelectric, and Dielectric Constants-The Electromechanical Coupling Factor, 1958,” Proceedings of the IRE, vol. 46, no. 4, pp. 764–778, 1958.
- ²⁶⁸ E. W. Lee, “Magnetostriction and Magnetomechanical Effects,” Reports on Progress in Physics, vol. 18, no. 1, pp. 184–229, 1955.

List of Figures

2.1	Typical ferromagnetic hysteresis curve	6
2.2	Sublattice magnetization in magnetite	7
2.3	Mechanism of magnetostriction	9
2.4	Magnetic domain structure under tensile stress and positive magnetostriction . .	10
2.5	Magnetic field dependence of magnetostriction	11
2.6	Magnetic field dependence of magnetostriction in FeCo	12
2.7	Definition of the angles θ and ϕ	13
2.8	Magnetic field dependence of magnetization and magnetostriction in Ni	14
2.9	Different polarization processes	16
2.10	Frequency dependence of polarizability	17
2.11	Heckmann diagrams for ME coupling coefficients and product properties	28
2.12	Examples of connectivity schemes	32
3.1	Crystal structure of BFO	36
3.2	Crystal structure of CFO	37
3.3	Phase transitions of BTO	39
3.4	Crystal structure of BTO	40
3.5	Phase transitions of BCZT	41
3.6	Elastic compliance of BCZT	42
4.1	SEM measurement setup	47
4.2	AFM measurement setup	49
4.3	Sawyer-Tower circuit	51
4.4	Direct ME measurement setup	54
4.5	Decay scheme of ^{57}Co	56
4.6	Momentum transfer during γ -ray emission and absorption	57
4.7	Effects of hyperfine interactions on Mössbauer spectra	59
4.8	Standard setup for Mössbauer measurements (transmission)	67
4.9	Exemplary Mössbauer spectrum	70
4.10	Double junction SQUID overview	71
4.11	Behavior of a superconducting loop in external flux	73
4.12	Schematic representation of a DC SQUID	74
4.13	Induced circulating current in a a DC SQUID	75
4.14	Voltage as function of bias current and sample flux in a DC SQUID	76
4.15	Schematic representation of an RF SQUID	76
4.16	Behavior of the total flux in an RF SQUID	77
4.17	Peak voltages in an RF SQUID	78

4.18	Longitudinal SQUID system schematic	79
4.19	Measurement geometry of a SQUID magnetometer	80
4.20	Converse ME SQUID measurement setup	84
4.21	Converse ME SQUID sample holder	85
4.22	Overview of the converse ME SQUID setup	86
4.23	Apparent ME signal from leakage currents	93
4.24	Apparent ME signal from leakage currents in Terfenol-D - BTO 40-60	94
4.25	Frequency doubling in CFO-BTO 40-60	96
4.26	Frequency dependence of converse ME measurement signal	98
5.1	Mössbauer spectra of the CFO-BTO core-shell nanoparticles	106
5.2	M(H) curves of CFO(Al) precursor powders	108
5.3	Mössbauer spectra of CFO(Al) precursor powders	109
5.4	X-ray diffractograms of CFO(Al) precursor powders	110
6.1	Size distribution of BFO nanoparticles	114
6.2	SEM micrographs of BFO nanoparticles	115
6.3	X-ray diffractograms of BFO nanoparticles	116
6.4	M(T) curves of BFO nanoparticles	117
6.5	M(H) curves of BFO nanoparticles	118
6.6	DSC curves of BFO nanoparticles	119
6.7	AFM/PFM micrographs of BFO nanoparticles	120
6.8	Local piezoresponse on individual BFO nanoparticles	121
6.9	Mössbauer spectra of BFO nanoparticles	124
6.10	Quadrupole splitting and shift of BFO nanoparticles	126
6.11	Mössbauer spectra of BFO nanoparticles near the Néel temperature	128
6.12	Temperature dependence of the relative doublet area	129
6.13	Simulated spectra for different anharmonicities	131
6.14	Schematic representation of the spin cycloid and its effects	132
6.15	Effect of the anharmonicity on Mössbauer spectra	133
6.16	X-ray diffractograms of samples S1-S3	139
6.17	SEM micrographs of samples S1-S3	140
6.18	PFM micrographs of samples S2-S4	141
6.19	P(E) hysteresis loops of samples S3 and S4	142
6.20	M(H) hysteresis loops of samples S1-S4	143
6.21	Temperature dependence of the induced magnetic moment for S3 and S4	145
6.22	Magnetic and electric field dependence of ME magnetization for S3 and S4	146
6.23	Schematic relation between magnetization and magnetostriction	147
6.24	X-ray diffractograms of the (1-x)CFO-xBTO composite samples	151
6.25	SEM micrographs of the (1-x)CFO-xBTO composite samples	152

6.26	SEM micrograph of sample $x=0.8$	152
6.27	Temperature dependence of ϵ' of the $(1-x)\text{CFO}-x\text{BTO}$ composite samples	153
6.28	Results from $P(E)$ loops recorded on the $(1-x)\text{CFO}-x\text{BTO}$ composite samples	154
6.29	$M(H)$ curves for the $(1-x)\text{CFO}-x\text{BTO}$ composite samples	156
6.30	Total and corrected magnetization for the $(1-x)\text{CFO}-x\text{BTO}$ composites	156
6.31	Schematic representation of different sample orientations	158
6.32	Temperature dependence of the induced ME magnetization for sample $x=0.6$	158
6.33	Magnetic field dependence of the induced ME magnetization for sample $x=0.6$	160
6.34	$M(H)$ curves of sample $x=0.6$ compared to results from literature	161
6.35	ME coupling comparison for different sample geometries	163
6.36	ME(H) curves recorded with the direct ME setup	165
6.37	Comparison of ME(E) curves for poled and depoled sample	166
6.38	Comparison of direct and converse ME results for samples $x=0.6$ and $x=0.8$	167
6.39	Comparison between direct and converse ME coefficients for all samples	168
6.40	X-ray diffractogram of BCZT-CFO 85-15	169
6.41	AFM/PFM micrographs of BCZT-CFO 85-15	170
6.42	$P(E)$ hysteresis loop of BCZT-CFO 85-15	171
6.43	Temperature dependence of ϵ' of BCZT-CFO 85-15	172
6.44	Temperature dependence of ϵ'' BCZT-CFO 85-15	173
6.45	$M(H)$ curve of BCZT-CFO 85-15	174
6.46	ME(T) curve of BCZT-CFO 85-15	175
6.47	ME(H) curve of BCZT-CFO 85-15	176
6.48	ME(E) magnetization of BCZT-CFO 85-15	177
6.49	X-ray diffractograms of CFO-BTO with and without Al	179
6.50	SEM micrographs of CFO-BTO with and without Al	180
6.51	$P(E)$ hysteresis loops of CFO-BTO with and without Al	181
6.52	Vertical PFM images of BCZT-CFO(Al)	182
6.53	$M(H)$ curves of CFO-BTO with and without Al	183
6.54	ME(T) curves for CFO-BTO with and without Al	184
6.55	ME(H) curves of CFO-BTO with and without Al	187
6.56	ME(E) curves of CFO-BTO with and without Al	189
6.57	X-ray diffractograms of NFO20-NFO50	192
6.58	TOF-SIMS 3D maps of NFO20-NFO50	193
6.59	PFM micrographs of NFO30	194
6.60	$M(H)$ curves of NFO20-NFO50	196
6.61	5 T magnetization values (mass adjusted) of NFO20-NFO50	196
6.62	ME(T) curves of NFO20-NFO50	198
6.63	ME(H) curves of NFO20-NFO50	199
6.64	Comparison between ME(T) and ME(H) curves of NFO50	200

6.65	ME(E) curves of NFO20-NFO50	205
6.66	Converse ME coupling coefficients of NFO20-NFO50	206

List of Tables

6.1	Dependence of BFO particle size, unit cell parameters and Néel temperature on the calcination temperature during synthesis	122
6.2	Description of CFO-BTO samples S1-S4	139
6.3	Dielectric and magnetic properties of samples S1-S4	143
6.4	Description of the correlation between magnetostriction and magnetoelectric coupling in a CFO-BTO 60-40 sample	164

List of Abbreviations

AC	alternating current
AF	antiferromagnetic
AFM	atomic force microscope
BFO	bismuth ferrite (BiFeO_3)
BN	boron nitride
BNC	Bayonet Neill - Concelman
BTO	barium titanate (BaTiO_3)
BCZT	barium calcium zirconate titanate ($(1-x)\text{Ba}(\text{Zr}_{0.2}\text{Ti}_{0.8})\text{O}_3-x(\text{Ba}_{0.7}\text{Ca}_{0.3})\text{TiO}_3$)
CEMS	conversion electron Mössbauer spectroscopy
CFO	cobalt ferrite (CoFe_2O_4)
DC	direct current
DSC	differential scanning calorimetry
EFG	electric field gradient
ME	magnetoelectric
MFM	magnetic force microscope
MPB	morphotropic phase boundary
NFO	nickel ferrite (NiFe_2O_4)
NMR	nuclear magnetic resonance
PFM	piezoresponse force microscope
PLD	pulsed laser deposition
PM	paramagnetic
RF	radio frequency
SEM	scanning electron microscope
SPS	spark plasma sintering
SQUID	superconducting quantum interference device
TEM	tunneling electron microscope
TOF-SIMS	time of flight secondary ion mass spectroscopy
XRD	X-ray diffractometer
ZFC-FC	zero-field-cooled field-cooled

Publications

Peer reviewed articles

1. **Mössbauer Study of Temperature-Dependent Cycloidal Ordering in BiFeO₃ Nanoparticles**

J. Landers, S. Salamon, M. Escobar Castillo, D. C. Lupascu and H. Wende
Nano Letters, vol. 14, pp. 6061-6065, 2014

2. **Magnetoelectric coupling on multiferroic cobalt ferrite-barium titanate ceramic composites with different connectivity schemes**

M. Etier, C. Schmitz-Antoniak, S. Salamon, H. Trivedi, Y. Gao, A. Nazrabi, J. Landers, D. Gautam, M. Winterer, D. Schmitz, H. Wende, V. V. Shvartsman and D. C. Lupascu
Acta Materialia, vol. 90, pp. 1-9, 2015

3. **Measuring the magnetoelectric effect across scales**

D. C. Lupascu, H. Wende, M. Etier, A. Nazrabi, I. Anusca, H. Trivedi, V. V. Shvartsman, J. Landers, S. Salamon, and C. Schmitz-Antoniak
GAMM-Mitteilungen, vol. 38, no. 1, pp. 25-74, 2015

4. **Open volume defects and magnetic phase transition in Fe₆₀Al₄₀ transition metal aluminide**

M. O. Liedke, W. Anwand, R. Bali, S. Cornelius, M. Butterling, T. T. Trinh, A. Wagner, S. Salamon, D. Walecki, A. Smekhova, H. Wende and K. Potzger
Journal of Applied Physics, vol. 117, no. 11, p. 163908, 2015

5. **Local Electronic and Magnetic Properties of Pure and Mn-Containing Magnetocaloric LaFe_{13-x}Si_x Compounds Inferred from Mössbauer Spectroscopy and Magnetometry**

S. I. Makarov, M. Krautz, S. Salamon, K. Skokov, C. S. Teixeira, O. Gutfleisch, H. Wende and W. Keune
Journal of Physics D: Applied Physics, vol. 48, no. 30, p. 305006, 2015

6. **Doping of Inorganic Materials in Microreactors - Preparation of Zn doped Fe₃O₄ Nanoparticles**

M. D. Simmons, N. Jones, D. J. Evans, C. Wiles, P. Watts, S. Salamon, M. Escobar Castillo, H. Wende, D. C. Lupascu and M. G. Francesconi
Lab on a Chip, vol. 15, pp. 3154-3162, 2015

7. **Particle-Matrix Interaction in Cross-Linked PAAm-Hydrogels Analyzed by Mössbauer Spectroscopy**
J. Landers, L. Roeder, S. Salamon, A. M. Schmidt and H. Wende
Journal of Physical Chemistry C, vol. 119, no. 35, pp. 20642-20648, 2015
8. **Multiferroic Clusters: A New Perspective for Relaxor-Type Toom-Temperature Multiferroics**
L. F. Henrichs, O. Cespedes, J. Bennett, J. Landers, S. Salamon, C. Heuser, T. Hansen, T. Helbig, O. Gutfleisch, D. C. Lupascu, H. Wende, W. Kleemann and A. J. Bell
Advanced Functional Materials, vol. 26, pp. 2111-2121, 2016
9. **Reversed ageing of Fe₃O₄ nanoparticles by hydrogen plasma**
C. Schmitz-Antoniak, D. Schmitz, A. Warland, N. Svechkina, S. Salamon, C. Piamonteze and H. Wende
Scientific Reports, vol. 6, p. 20897, 2016
10. **Simultaneous study of Brownian and Néel relaxation phenomena in ferrofluids by Mössbauer spectroscopy**
J. Landers, S. Salamon, H. Remmer, F. Ludwig and H. Wende
Nano Letters, vol. 16, no. 2, pp. 1150-1155, 2016
11. **The direct and the converse magnetoelectric effect in multiferroic cobalt ferrite-barium titanate ceramic composites**
M. Etier, V. V. Shvartsman, S. Salamon, Y. Gao, H. Wende and D. C. Lupascu
Journal of the American Ceramic Society, vol. 99, no. 11, pp. 3623-3631, 2016
12. **Molecular design for tailoring single source precursor of bismuth ferrite**
G. Bendt, R. Schiwon, S. Salamon, J. Landers, U. Hagemann, C. Limberg, H. Wende and S. Schulz
Inorganic Chemistry, vol. 55, no. 15, pp. 7542-7549, 2016
13. **A new (Ba,Ca)(Ti,Zr)O₃ based multiferroic with large magnetoelectric effect**
M. Naveed-Ul-Haq, V. V. Shvartsman, S. Salamon, H. Wende, H. Trivedi, A. Mumtaz and D. C. Lupascu
Scientific Reports, vol. 6, no. 1, p. 32164, 2016
14. **Impact of lattice dynamics on the phase stability of metamagnetic FeRh: Bulk and thin films**
M. Wolloch, M. E. Gruner, W. Keune, P. Mohn, J. Redinger, F. Hofer, D. Suess, R. Podloucky, J. Landers, S. Salamon, F. Scheibel, D. Spoddig, R. Witte, B. Roldan Cuenya, O. Gutfleisch, M. Y. Hu, J. Zhao, T. Toellner, E. E. Alp, M. Siewert, P. Entel, R. Pentcheva and H. Wende
Physical Review B, vol. 94, no. 15, p. 174435, 2016

15. **Mobility Investigations of Magnetic Nanoparticles in Biocomposites**
R Müller, M. Zhou, T. Liebert, J. Landers, S. Salamon, S. Webers, A. Dellith, D. Borin, T. Heinze and H. Wende
Materials Chemistry and Physics, vol. 193, pp. 364-370, 2017
16. **Planetesimal Formation in the Warm, Inner Disk: Experiments with Tempered Dust**
C. de Beule, J. Landers, S. Salamon, H. Wende and G. Wurm
The Astrophysical Journal, vol. 837, no. 59, pp. 1-9, 2017
17. **Role of Composition and Size of Cobalt Ferrite Nanocrystals in the Oxygen Evolution Reaction**
K. Chakrapani, G. Bendt, H. Hajiyani, I. Schwarzrock, T. Lunkenbein, S. Salamon, J. Landers, H. Wende, R. Schlögl, R. Pentcheva, M. Behrens, S. Schulz
ChemCatChem, vol. 9, pp. 2988-2995, 2017
18. **Magnetic Properties of the $\text{Bi}_{0.65}\text{La}_{0.35}\text{Fe}_{0.5}\text{Sc}_{0.5}\text{O}_3$ Perovskite**
A. V. Fedorchenko, E. L. Fertmann, V. A. Desnenko, O. V. Kotlyar, E. Čížmár, V.V. Shvartsman, D. C. Lupascu, S. Salamon, H. Wende, A. N. Salak, D. D. Khalyavin, N. M. Olekhnovich, A. V. Pushkarev, Yu. V. Radyush and A. Feher
Acta Physica Polonica A, vol. 131, pp. 1069-1071, 2017
19. **Ferromagnetic Resonance of MBE-grown FeRh thin films through the metamagnetic phase transition**
A. Heidarian, S. Stienen, A. Semisalova, Y. Yuan, E. Josten, R. Hübner, S. Salamon, H. Wende, R.A. Gallardo, J. Grenzer, K. Potzger, R. Bali, S. Facsko and J. Lindner
Physica Status Solidi B, vol. 254, no. 10 p. 1700145, 2017
20. **Topotactic Synthesis of Porous Cobalt Ferrite Platelets from a Layered Double-Hydroxide Precursor and their Application in Oxidation Catalysis**
K. F. Ortega, S. Anke, S. Salamon, F. Özcan, J. Heese, C. Andronescu, J. Landers, H. Wende, W. Schuhmann, M. Muhler, T. Lunkenbein and M. Behrens
Chemistry: A European Journal, vol. 23, pp. 12443-12449, 2017
21. **Is there a temperature limit in planet formation at 1000 K?**
T. Demirci, J. Teiser, T. Steinpilz, J. Landers, S. Salamon, H. Wende and G. Wurm
The Astrophysical Journal, vol. 846, no. 1, p. 48, 2017
22. **Effect of Al^{3+} modification on cobalt ferrite and its impact on the magnetoelectric effect in BCZT-CFO multiferroic composites**
M. Naveed-Ul-Haq, V. V. Shvartsman, G. Constantinescu, H. Trivedi, S. Salamon, J. Landers, H. Wende and D. C. Lupascu
Journal of Materials Science, vol. 52, no. 23, pp. 13402-13413, 2017

23. **Adjusting the catalytic properties of cobalt ferrite nanoparticles by pulsed laser fragmentation in water with defined energy dose**
F. Waag, B. Gökce, C. Kalapu, G. Bendt, S. Salamon, J. Landers, U. Hagemann, M. Heidelmann, S. Schulz, H. Wende, N. Hartmann, M. Behrens and S. Barcikowski
Scientific Reports, vol. 7, p. 13161, 2017
24. **Strong converse magnetoelectric effect in (Ba,Ca)(Zr,Ti)O₃ - NiFe₂O₄ multi-ferroics: A relationship between phase-connectivity and interface coupling**
M. Naveed-Ul-Haq, V. V. Shvartsman, H. Trivedi, S. Salamon, S. Webers, H. Wende, U. Hagemann and D. C. Lupascu
Acta Materialia, vol. 144, pp. 305-313, 2018
25. **Moment-volume coupling in La(Fe_{1-x}Si_x)₁₃**
M. E. Gruner, W. Keune, J. Landers, S. Salamon, M. Krautz, J. Zhao, M. Y. Hu, T. Toellner, E. E. Alp, O. Gutfleisch and H. Wende
Physica Status Solidi B, vol. 255, p. 1700465, 2018
26. **The Role of Composition of Uniform and Highly Dispersed Cobalt Vanadium Iron Spinel Nanocrystals for Oxygen Electrocatalysis**
K. Chakrapani, G. Bendt, H. Hajiyani, T. Lunkenbein, M. T. Greiner, L. Masliuk, S. Salamon, J. Landers, R. Schlögl, H. Wende, R. Pentcheva, S. Schulz and M. Behrens
ACS Catalysis, vol. 8, no. 2 pp. 1259-1267, 2018
27. **Fluoride Doped γ -Fe₂O₃ Nanoparticles with Increased MRI Relaxivity**
K. Chakrapani, G. Bendt, H. Hajiyani, T. Lunkenbein, M. T. Greiner, L. Masliuk, S. Salamon, J. Landers, R. Schlögl, H. Wende, R. Pentcheva, S. Schulz and M. Behrens
Journal of Materials Chemistry B, vol. 6, pp. 3665-3673, 2018
28. **Determining the vibrational entropy change in giant magnetocaloric LaFe_{11.6}Si_{1.4} by nuclear resonant inelastic X-ray scattering (NRIXS)**
J. Landers, S. Salamon, W. Keune, M. E. Gruner, M. Krautz, J. Zhao, M. Y. Hu, T. S. Toellner, E. E. Alp, O. Gutfleisch and H. Wende
Physical Review B, vol. 98, p. 024411, 2018
29. **Nanoscale Physical and Chemical Structure of Iron Oxide Nanoparticles for Magnetic Particle Imaging**
R. Hufschmid, J. Landers, C. Shasha, S. Salamon, H. Wende and K. M. Krishnan
Small, submitted May 2018
30. **Melt-quenched cobalt and zinc imidazolate glasses from zeolitic imidazolate framework solid solutions**
M. Kloß, L. Frenzel-Beyme, S. Salamon, J. Landers, H. Wende, J. Debus and S. Henke
Journal of Materials Chemistry A, submitted June 2018

31. **Effect of substrate orientation on local magnetoelectric coupling in bi-layered multiferroic thin films**

M. Naveed-Ul-Haq, S. Webers, H. Trivedi, S. Salamon, H. Wende, M. Usman, A. Mumtaz, V. V. Shvartsman and D. C. Lupascu

Nanoscale, submitted July 2018

Conference contributions

1. **Temperature and size dependent investigation of the spin structure in bismuth ferrite nanoparticles**

S. Salamon, J. Landers, W. Keune, M. Escobar Castillo, D. C. Lupascu and H. Wende
Spring meeting of the German Physical Society, Dresden (2014), talk

2. **Multiferroic effects in nanoparticulate systems**

S. Salamon, J. Landers, W. Keune, M. Escobar Castillo, M. Naveed-Ul-Haq, V. V. Shvartsman, M. Etier, D. C. Lupascu and H. Wende
Spring meeting of the German Physical Society, Dresden (2017), invited talk

3. **Multiferroic effects in composite ceramic systems**

S. Salamon, J. Landers, M. Naveed-Ul-Haq, V. V. Shvartsman, M. Etier, D. C. Lupascu and H. Wende
3rd Seminar on Ferroic Functional Materials and 13th International Workshop on Direct and Inverse Problems in Piezoelectricity, Kassel (2017), talk

4. **Experimental characterization of magnetoelectric coupled composites (macro-nano)**

H. Wende, S. Webers and S. Salamon

3rd Seminar on the Mechanics of Multifunctional Materials, Bad Honnef (2018), poster

Acknowledgements

This comprehensive work would not have been possible if it weren't for the continuous support from a large number of colleagues and cooperation partners. In this section, I want to individually thank everyone who contributed a significant part to this thesis, by means of direct participation in our scientific endeavors, or through other means of help and support.

First and foremost, I want to thank Prof. Heiko Wende for giving me the opportunity and providing the funding to pursue the works described in this thesis, as well as many other successful projects that our group has taken on over the years.

My heartfelt thanks go to my mother, who was patient enough to support me throughout the years of my studies, and to Eric, for his valued help in creating new and improved graphics for this thesis. I thank both of them for their unfaltering belief in my ability to succeed, even in the face of my own doubts.

I want to thank Prof. Werner Keune for his invaluable expertise on Mössbauer spectroscopy, his helping hand in a large number of our studies, and for proofreading my thesis in its entirety. I wholeheartedly appreciate not only his expert scientific input, but also his unshakeable positive attitude. The exciting and successful beamtimes at the Advanced Photon Source, even amidst snowstorms, will always be among the most cherished memories of my research career.

A special thanks goes to Dr. Joachim Landers, for being the most knowledgeable mentor since the beginning of my studies, never losing his enthusiasm even in the face of overwhelming workloads. It was mainly due to his steadfast effort and work ethic that we were able to publish numerous papers in high impact journals. I highly appreciate all the time he put into proofreading several iterations of my thesis as it was being written. I also want to thank M.Sc. Samira Webers for her help in numerous measurements, proofreading, her advice regarding my thesis, and the supervision of our PLD setup while I was busy writing.

I would furthermore like to thank all other members of the Wende group, for their helpfulness and loyalty to our goals, and their willingness to tackle any unexpected challenges that we had to overcome in the past years. From the Lupascu group, I want to thank Dr. Marianela Escobar Castillo for her skilled synthesis of the BFO nanoparticles that we extensively characterized, as well as Dr. Morad Etier and Dr. Muhammad Naveed-Ul-Haq, who organized most of the work on the multiferroic composites and were the main driving forces that made our cooperative publications possible. Special thanks goes to Dr. Vladimir Shvartsman, who contributed to all of our publications on composites, and offered helpful advice regarding my thesis.

My fullest appreciation also goes to the engineers and technicians from Quantum Design, such as Thomas Beppler, Stefan Riesner and Dr. Natalia Tristan, for their readiness to help and support, despite our abuse of their highly capable devices. In this context, I also want to thank Dr. Pavel Borisov (Loughborough University), who devised and built the converse ME measurement setup that was extensively utilized in this work, and who was always ready to offer helpful suggestions regarding its use and possible improvements.

No acknowledgement would be complete without our engineer Dipl.-Ing. Ulrich von Hörsten, as our group completely depends on his decades of experience and knowledge. He is the one who keeps most of our devices operational, in addition to continuously developing and improving the "Pi" program package that we use for the fitting and evaluation of Mössbauer spectra. It was thanks to him that we were able to implement the fitting procedure for the anharmonic cycloid, which made our extensive works on BFO possible.

Funding by the DFG through FOR 1509 and SFB 1242, as well as from Stiftung Mercator (MERCUR) are gratefully acknowledged.

Last but foremost, my sincere thanks goes to Judith Fritz, not only for her generous and selfless support of me and my family, but also for teaching me that nothing in the world can take the place of persistence. In this sense, her attitude and endurance represent a role model that I will never be able to fulfill, but will always strive for. This thesis embodies the culmination of my scientific efforts that I offer as a token of appreciation for her backing.

Nothing in this world can take the place of persistence. Talent will not; nothing is more common than unsuccessful men with talent. Genius will not; unrewarded genius is almost a proverb. Education will not; the world is full of educated derelicts. Persistence and determination alone are omnipotent.

- Calvin Coolidge

Door meten tot weten (Through measurement to knowledge)

- Heike Kamerlingh Onnes